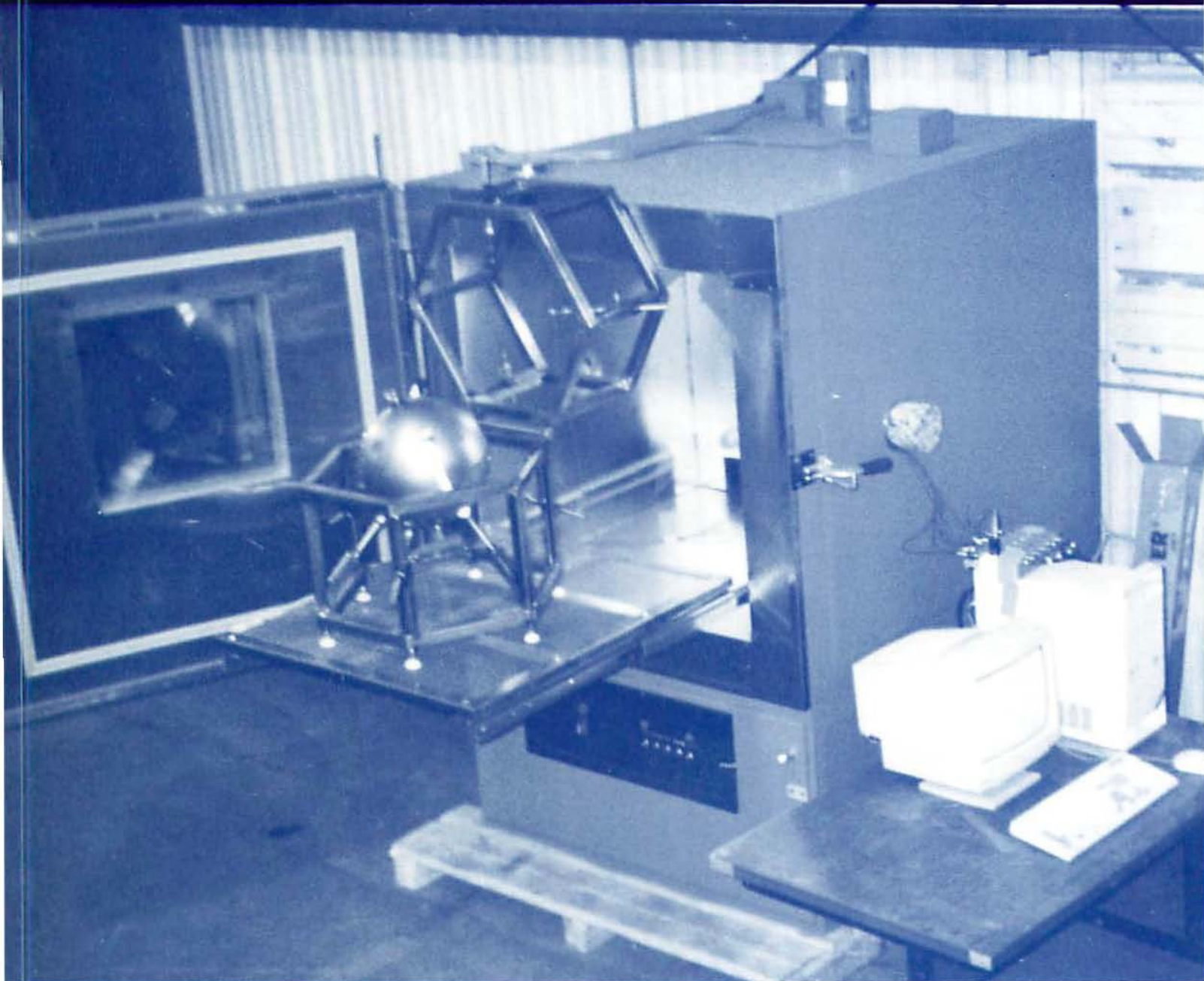


An International  
Forum For  
The AE Science  
and Technology

# JOURNAL OF ACOUSTIC EMISSION

Vol.15, No.1-4/January-December 1997



**AE Tester for Aircraft Halon Fire-Extinguisher Bottles**

Endorsed by  
AEWG, AEWGI  
CARP and  
EWGAE

Published by  
Acoustic Emission Group  
Los Angeles, CA

# JOURNAL OF ACOUSTIC EMISSION

**Editor: Kanji Ono**

**Associate Editors: A. G. Beattie, T. F. Drouillard, F. C. Beall and M. Ohtsu**

## 1. Aims and Scope of the Journal

Journal of Acoustic Emission is an international journal designed to be of broad interest and use to both researcher and practitioner of acoustic emission. It will publish original contributions of all aspects of research and significant engineering advances in the sciences and applications of acoustic emission. The journal will also publish reviews, the abstracts of papers presented at meetings, technical notes, communications and summaries of reports. Current news of interest to the acoustic emission communities, announcements of future conferences and working group meetings and new products will also be included.

Journal of Acoustic Emission includes the following classes of subject matters:

**A. Research Articles:** Manuscripts should represent completed original work embodying the results of extensive investigation. These will be judged for scientific and technical merit.

**B. Applications:** Articles must present significant advances in the engineering applications of acoustic emission. Material will be subject to reviews for adequate description of procedures, substantial database and objective interpretation.

**C. Technical Notes and Communications:** These allow publications of short items of current interest, new or improved experimental techniques and procedures, discussion of published articles and relevant applications.

**D. AE Literature section** will collect the titles and abstracts of papers published elsewhere and those presented at meetings and conferences. Reports and programs of conferences and symposia will also be presented.

Reviews, Tutorial Articles and Special Contributions will address the subjects of general interest. Nontechnical part will cover book reviews, significant personal and technical accomplishments, current news and new products.

## 2. Endorsement

Acoustic Emission Working Group (AEWG), European Working Group on Acoustic Emission (EWGAE), Committee on Acoustic Emission from Reinforced Composites (CARP), and Acoustic Emission Working Group of India have endorsed the publication of Journal of Acoustic Emission.

## 3. Governing Body

The Editor and Associate Editors will implement the editorial policies described above. The Editorial Board will advise the editors on any major change. The Editor, Professor Kanji Ono, has the general responsibility for all the matters. Associate Editors assist the review processes as lead reviewers. Mr. T.F. Drouillard is responsible for the AE Literature section. The members of the Editorial Board are selected for their knowledge and experience on AE and will advise and assist the editors on the publication policies and other aspects. The Board presently includes the following members:

S.H. Carpenter	(USA)
D.A. Dornfeld	(USA)
P. Fleischmann	(France)
L. Golaski	(Poland)
M.A. Hamstad	(USA)
H.R. Hardy, Jr.	(USA)
R. Hill	(UK)
I.V. Ivanov	(Russia)
P. Jax	(Germany)
T. Kishi	(Japan)
O.Y. Kwon	(Korea)
J.C. Lenain	(France)
S.L. McBride	(Canada)
W. Morgner	(Germany)
C.R.L. Murthy	(India)
H. Niitsuma	(Japan)
A.A. Pollock	(USA)
T.M. Proctor, Jr.	(USA)
I. Roman	(Israel)
C. Scala	(Australia)
C. Scruby	(UK)
A. Vary	(USA)
E. Waschkies	(Germany)
M. Wevers	(Belgium)
J.W. Whittaker	(USA)
B.R.A. Wood	(Australia)

## 4. Publication

Journal of Acoustic Emission is published quarterly in March, June, September and December by Acoustic Emission Group, Suite 106, 16350 Ventura Blvd, Encino, CA 91436. It may also be reached at 6531 Boelter Hall, University of California, Los Angeles, California 90095-1595 (USA). tel. 310-825-5233. FAX 818-990-1686. e-mail: ono@ucla.edu

## 5. Subscription

Subscription should be sent to Acoustic Emission Group. Annual rate for 1998 or 1999 is US \$96.00. For surface delivery, add \$8 in the U.S. and \$11 for Canada and elsewhere. For air mail delivery to South America, add \$18, Western Europe, add \$25 and add \$30 elsewhere. Overseas orders must be paid in US currencies with a check drawn on a US bank. Inquire for individual (with institutional order) and bookseller discounts.

## 6. Advertisement

No advertisement will be accepted, but announcements for books, training courses and future meetings on AE will be included without charge.

# Wideband and Narrowband Acoustic Emission Waveforms from Extraneous Sources during Fatigue of Steel Samples

M.A. Hamstad and J.D. McColskey

## Abstract

An extensive study of acoustic emission (AE) generated from extraneous sources during fatigue loading of steel samples has been performed. AE waveforms were emphasized instead of traditional AE parameters. Typically, four resonant sensors and four wideband high-sensitivity sensors were used to gather eight waveforms for each AE event. The fatigue tests were conducted in a servo-hydraulic fatigue test machine, using hydraulic grips. Specimen variables included two different thicknesses and different lateral dimensions of the plate-like samples. In addition to grip-based extraneous AE sources, artificial extraneous sources were also examined. Acoustic emission signals from both solid- and air-transmitted artificial sources were studied. The extraneous signals were contrasted to an AE event from a fatigue crack. A motivation for this research was the fact that applications of AE to monitor steel bridges encounter extensive extraneous AE. The waveform database established in this work indicates that recognition of extraneous AE is not always easy. This is due to the variety of source types, the effects of thickness changes, and dispersion effects during wave propagation. Some extraneous signal types could be easily distinguished from crack signals in the wideband AE data. Other extraneous signals are not as easily distinguished, even with wideband sensors. Using either resonant or wideband sensors, waveform-based AE analysis offers advantages to fixed-threshold approach for spatial discrimination of extraneous AE.

## 1. Introduction

Acoustic emission (AE) has been proposed as a tool to detect and locate fatigue cracks in metal structures such as steel bridges (Galambos and McGogney, 1975). Thus, AE monitoring of fatigue cracks has been the subject of numerous laboratory studies and field studies (see references in Sison et al., 1996). Both in the laboratory and in the field,

extraneous AE (signals from sources other than cracks) are a significant problem. Inspectors in the field have reported that extraneous AE can make up more than 98% of detected AE when monitoring a steel railroad bridge (Gong et al., 1992).

In a typical laboratory environment, extraneous sources of AE include:

- (1) friction or fretting in the loading pin holes of pin-type grips;
- (2) relative interfacial movement of wedges, specimen, and pistons in hydraulic grips;
- (3) other test-machine sources such as screw threads, fixturing and hydraulic servo-valves;
- (4) airborne signals from other laboratory activity; and
- (5) electrically induced AE.

Several approaches have been developed in the laboratory to remove extraneous signals from the AE of interest. These include:

- (1) frequency filtering to attenuate low frequencies;
- (2) load-gating to eliminate AE signals except those near the peak load;
- (3) source location and/or guard sensors to eliminate AE originating outside the crack region; and
- (4) rise-time analysis to eliminate slow-rise-time signals, which are considered to be extraneous AE.

Often, combinations of these approaches are used. These methods may allow the acquisition of AE data from fatigue cracks, which are not significantly contaminated by extraneous sources during careful laboratory experiments.

The application of AE to detect and monitor fatigue cracks in the field is much more complicated. The location of a crack, if it exists, is often not known ahead of time. This greatly reduces the usefulness of guard sensors and/or source location for the elimination of extraneous AE. Also, field testing usually involves an unpredictable fatigue-load spectrum without the smooth variation of a sinusoidal pattern. Maximum stresses do not occur throughout the structure at the same instant of time. This makes it difficult to apply load-gating, since strain values over the whole region monitored by the AE sensors would not likely be available. Another difficulty is that crack-induced AE sources, as well as extraneous AE sources, originate at various distances

---

Received 23 November 1996. M.A. Hamstad (hamstad@boulder.nist.gov) is affiliated with National Institute of Standards and Technology and University of Denver, Denver, CO 80208 and J.D. McColskey is with National Institute of Standards and Technology, 325 Broadway, Boulder, CO 80303. Contribution of the National Institute of Standards and Technology; Not subject to copyright in the U.S.

from the AE sensors. The dispersion of the acoustic waves makes it difficult to apply rise-time analysis techniques. The number of potential extraneous AE sources (impacts generated by vehicular traffic on bridges, friction or fretting associated with thermal-expansion design features and normal bridge load-based deflections) is much larger in field testing, as is the number of directions from which the signals propagate to the sensors. Finally, the poor accuracy of source location of typical fixed-threshold, resonant-sensor AE systems provides, at best, only the vicinity of the origin of an AE signal. This lack of accuracy makes it difficult to distinguish between real fatigue cracks and extraneous AE source regions, when the crack is near such a region.

These difficulties in the field provide encouragement for the development of wideband, flat-with-frequency, waveform-based AE approaches. Such methods provide two important benefits. First, they allow more accurate source location, since the same fixed-velocity of propagation can be used for each waveform hit of a particular AE event. This is in contrast to fixed-threshold AE systems, in which the first penetration of the threshold can come from different velocities of propagation for each hit of an event. Furthermore, these techniques provide a broader frequency window, which potentially enhances the distinction of crack-induced AE sources from extraneous sources.

Two previous studies reported waveforms from extraneous sources. Miller et al. (1984) documented waveforms from a wideband conical sensor. However, they did not filter the signals to attenuate the very low frequencies which must be removed to allow a successful AE application. Further, the extraneous AE waveforms, which they show, often lack sufficient pretrigger. Hence, they are difficult to compare with the results of the current research, as well as with real crack-induced AE, which has the signal of interest in the initial region of the AE signal. Friesel (1987) did not report the frequency response characteristics of the sensor, the bandpass, or the physical locations of the sensors. Thus, it is difficult to compare his results with this research.

In the past, wideband waveform-based testing has been hindered by insufficient sensor sensitivity. Recently, a wideband sensor with sensitivity (or signal-to-noise ratio) equivalent to that of narrowband resonant sensors, has been developed (Hamstad and Fortunko, 1995; Hamstad, 1996). This sensor provides opportunities for the development of practical application of waveform-based approaches. The purpose of this research was to examine waveforms associated with extraneous AE sources during fatigue cracking in a laboratory environment. Multiple AE channels which monitored both wideband and narrowband sensors were used. This examination has the long-range intent to develop robust field-suited techniques to distinguish extraneous AE from the AE signals caused by cracks.

## 2. Experimental Conditions

Experiments were conducted in a closed-loop, servo-hydraulic, fatigue-testing machine with a 1 MN capacity. The servo valve was isolated from the machine actuator to minimize AE from this valve. The isolation was accomplished by placing the servo valve on a manifold adapter and connecting high-pressure hydraulic hoses, 1 m long, between the manifold and the actuator. The test specimens were gripped with hydraulic wedge grips that have a 0.5 MN load capacity. A hydraulic pressure of 55 MPa was used to grip the specimen before fatigue cycling. Two different types of grips were used in this study. The first, 102 mm wide, had diamond-shaped serration that were 1 mm deep (16 pitch), and those for the second set were 204 mm wide, with diamond-shaped serration that were 0.5 mm deep (32 pitch). Since the majority of the transverse gripping forces was applied before axial loading of the sample, these grips helped decrease the amount of extraneous AE generated during the fatigue test as compared to extraneous AE generated by non-hydraulic wedge grips. Further, the gripping surfaces were only lightly serrated, to reduce the "digging-in" of the serration into the specimen and the resulting generation of extraneous AE. The grips were aligned according to ASTM Standard Practice E1012, Type A, Method 1, to minimize bending stresses (in the test specimen) and relative motion of the grip wedges and grip body (which generates extraneous AE).

Before each test, the interfaces between the grip body and wedges and also between the grip piston and wedges were cleaned. Fresh grease (described below) was then applied to minimize the introduction of foreign particles. These particles can lead to extraneous signals as a result of crushing. Several interfacial lubrication methods were evaluated, including various greases and different Teflon sheet thickness. The grease supplied by the grip-manufacturer (a molybdenum-disulfide paste/lubricant) was found to contain graphite spheres, which aid in lubricity. These spheres can rupture during fatigue testing, creating numerous extraneous AE sources. An attempt was made to use Teflon sheets (0.5 and 0.25 mm thick) between the grip body and wedges in place of the grease. The high interfacial pressure deformed the Teflon until it was too thin to be useful. Better success in reducing extraneous sources was obtained using the Teflon sheet between the wedge bottoms and the grip piston. In this case it retained sufficient thickness to isolate the grip piston from the wedge bottoms. Eventually, a combination of a molybdenum disulfide grease (without graphite spheres) and Teflon sheet, 0.5 mm thick, between the wedges and grip piston was selected. Between the wedges and the grip body, only molybdenum disulfide grease (without spheres) was used. These extraneous source suppression techniques were used because the waveform-recording instrumentation could only record events at a rate of about 10 events per second.

Table I Materials and sample configurations

Material*	Thickness,mm	Width, mm	Length, mm	Notch length, mm	Configuration**
A36	6.4	178	406	25.4	C
A36	25.4	92	406	12.7	D
A36	8	900	900	na	B†
A588	22.9	197	406	25.4	A
A588	25.4	900	1200	na	B†
A514	22.9	197	406	25.4	A, B

\*Hot rolled condition

\*\* See figure 1

† Configuration refers only to sensor spacing relative to center of sample for these specimens

A dial indicator was used to measure the relative vertical motion between the grip body and the wedges, and the grip body and the grip piston, during fatigue cycling between loads of 15 kN and 292 kN. With molybdenum disulfide grease (without spheres) as a lubricant, a typical peak-to-peak vertical displacement value of 6  $\mu\text{m}$  was measured between the grip body and wedge. Between the grip body and grip piston, a measurement of 23  $\mu\text{m}$  was made (with no Teflon between the wedge bottom and grip piston). Respective readings of 5  $\mu\text{m}$  and 10  $\mu\text{m}$  were measured with Teflon between the wedge bottom and grip piston. Presumably, the differences with and without Teflon are due to the changes in the interfacial frictional conditions and low modulus of the Teflon. These motions are suspected to be key factors in the generation of extraneous grip-based AE.

Table I shows the materials and specimen configurations used in this program. These steels (tested in their hot-rolled, as-received condition) were chosen because of their use in bridges. Some specimens were notched through the thickness (using an electrical discharge machine) and then fatigued to provide a sharp crack, representative of a crack in a bridge member. Some specimens were not notched, to evaluate extraneous sources only.

Two different types of sensors (typically coupled with vacuum grease) were used in this study. The first was a commercially available, general-purpose resonant AE sensor that, according to the manufacturer, had good sensitivity within the typical 100-300 kHz bandpass. This sensor was connected to the commercially supplied preamplifier. This preamplifier provided 60 dB of gain and 100-300 kHz bandpass filtering. Recording of the resonant sensor signals took place after preamplification. The second type sensor was a broadband, high-fidelity sensor of high-sensitivity developed at NIST-Boulder (Hamstad and Fortunko, 1995; Hamstad, 1996). It had an integral field-effect transistor and, combined with a conditioning preamplifier, had a total gain, in this application, of 51 dB. These preamplifier outputs were bandpassed from 50 kHz to 2 MHz with four-pole Butterworth bandpass filters, before waveform recording. The wideband sensors were attached to the specimens using a special holder (Hamstad and Fortunko, 1995) designed for

that purpose. The commercial sensors were attached to the specimen using silicone-rubber pads, aluminum angle bars, and rubber bands. Figure 1 shows sensor locations (four resonant and four wideband) on the different specimen geometry.

Digital storage oscilloscopes captured and stored AE waveforms sensed by the wideband and resonant sensors. The recorders had four 12-bit channels, with digitization rates of up to 10 Msamples/s. The memory depth of the digitizers was selectable up to 1 Mbyte of memory per channel per waveform. The experimental waveforms were acquired at 10 Msamples/s and had a typical length of 4001 data points. The acquired waveforms, including pre-trigger data, were displayed and analyzed using commercially available software.

### 3. Experiments and Results

Sets of eight simultaneous waveforms were gathered using one of the resonant sensors as a trigger for all the channels. The trigger threshold was set at -20 mV. The eight AE waveforms included four each from the resonant narrowband sensors and the non-resonant wideband sensors. In some cases, an additional waveform of the current load applied to the sample was also simultaneously digitized. This load waveform was used to determine the load associated with the set of waveforms. In the graphs that follow, the starting times of the waveforms were varied so that both the electrical background noise and the beginning of the AE signal were clearly displayed. In all cases, however, the displayed major time divisions were 50  $\mu\text{s}$  apart.

For the clarity of presentation, the experimental waveforms have been divided into four groups. The first group included extraneous source waveforms associated with fatigue cycling (0.3 Hz) of specimens containing growing sharp fatigue cracks or specimens without known cracks. The next group was composed of waveforms associated with deliberately generated extraneous AE, while the specimens were not under significant load. The third group was composed of waveforms generated during fatigue cycling of large plates without cracks. The fourth consisted of a set of AE

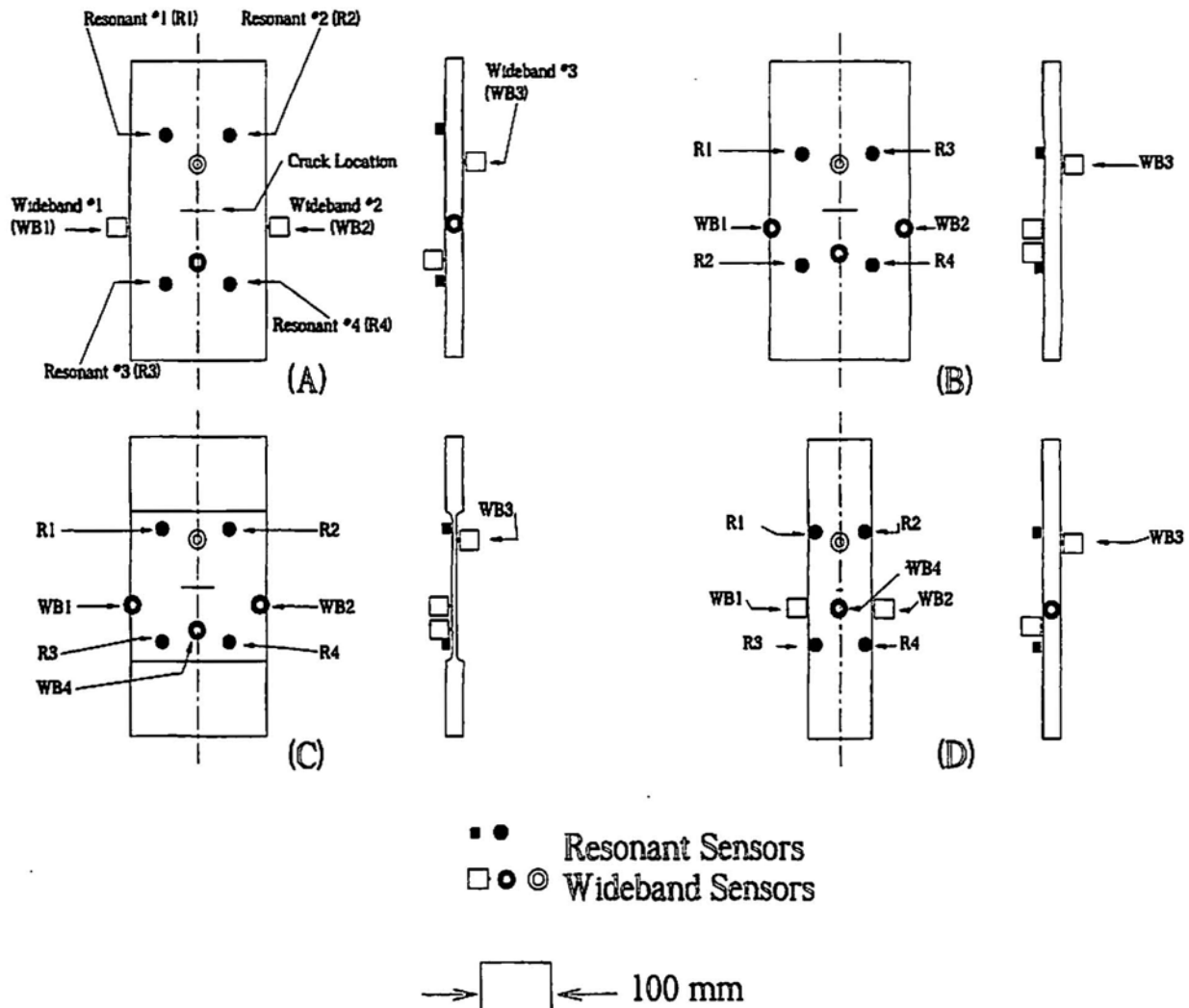


Fig. 1 Sample and sensor configurations (front and side views) drawn to the indicated scale.

waveforms from real fatigue cracks. The first group was extracted from data, which contained both extraneous and crack-induced AE. The crack-induced AE was separated from the extraneous AE based upon a careful waveform examination of the differences of arrival time at the different sensors using the known locations of the grips, crack, and sensors and the appropriate propagation velocities. General results for fatigue-crack-induced AE will be presented in a subsequent paper.

### 3.1 Cyclic Extraneous Signals from Cracked or Uncracked Samples

Figure 2 presents the signal waveforms from an electrical noise spike. These waveforms occurred during testing of a cracked A36-steel plate with reduced section (6.4 mm thick), as shown in Fig. 1C. The fact that the signal was an electrical noise spike follows from the observation that the signal appears on all eight AE channels (as well as the load channel) at exactly the same time. In other signals, which

are not shown, two additional cases of electrical noise spikes were observed:

- (1) on wideband channels only; and
- (2) on narrowband channels only.

Waveforms from extraneous AE originating at the upper grips are shown in Fig. 3. These waveforms were detected on a cracked A36-steel plate with reduced section (6.4 mm thick), as shown in Fig. 1C. The extraneous source determination is based again upon waveform-based arrival-time analysis. The first and nearly equal signal arrivals at the two top resonant sensors (R1 and R2) were followed by a progression of arrivals down the specimen to the two resonant sensors (R3 and R4) at the bottom of the sample. The waveforms show short rise times with relatively distinct peak amplitudes at the two top resonant sensors and longer rise times with no clearly defined peak amplitudes at the two bottom resonant sensors. These changes are due in part to dispersion. The wideband sensors show considerable low-frequency content in this extraneous grip source. This low-frequency content is not apparent in the resonant sensor

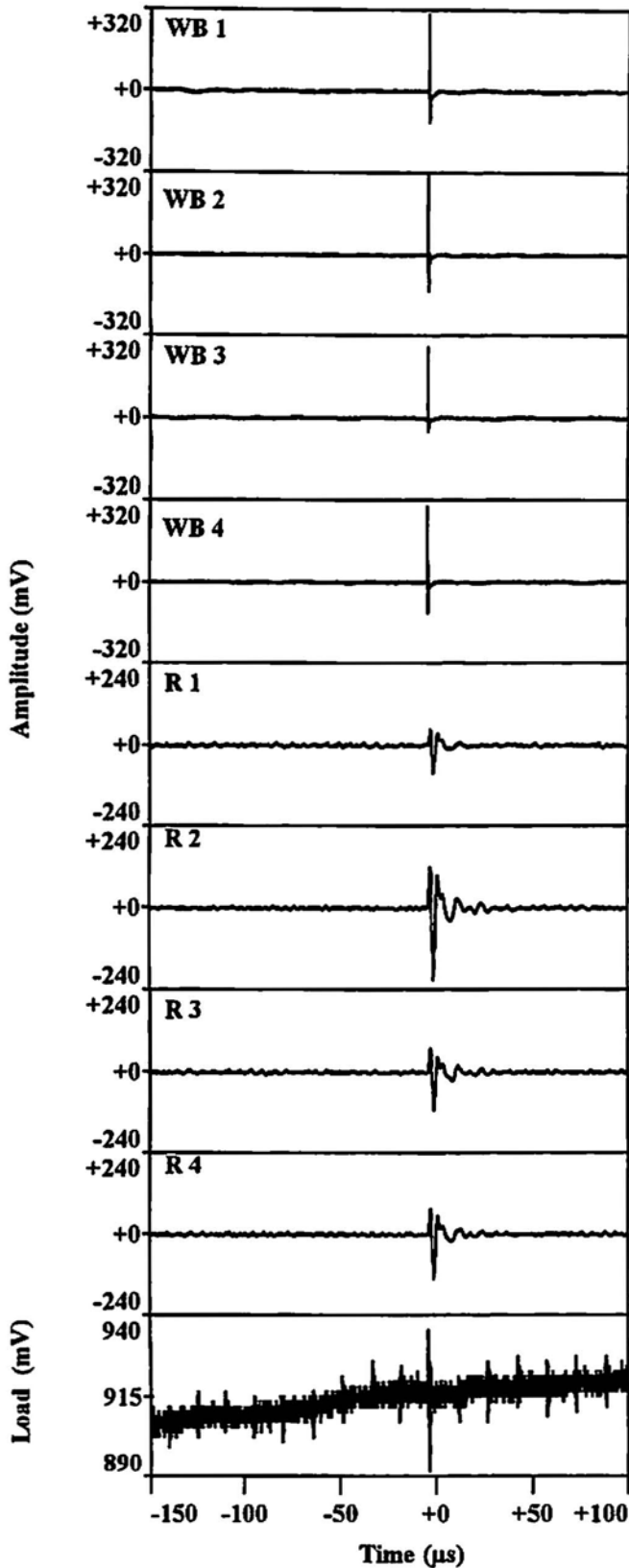


Fig. 2 Waveforms for an electrical noise spike during fatigue from wideband sensors (WB) after 51 dB gain and resonant sensors (R) after 60 dB gain. The bottom waveform shows the load-cell output.

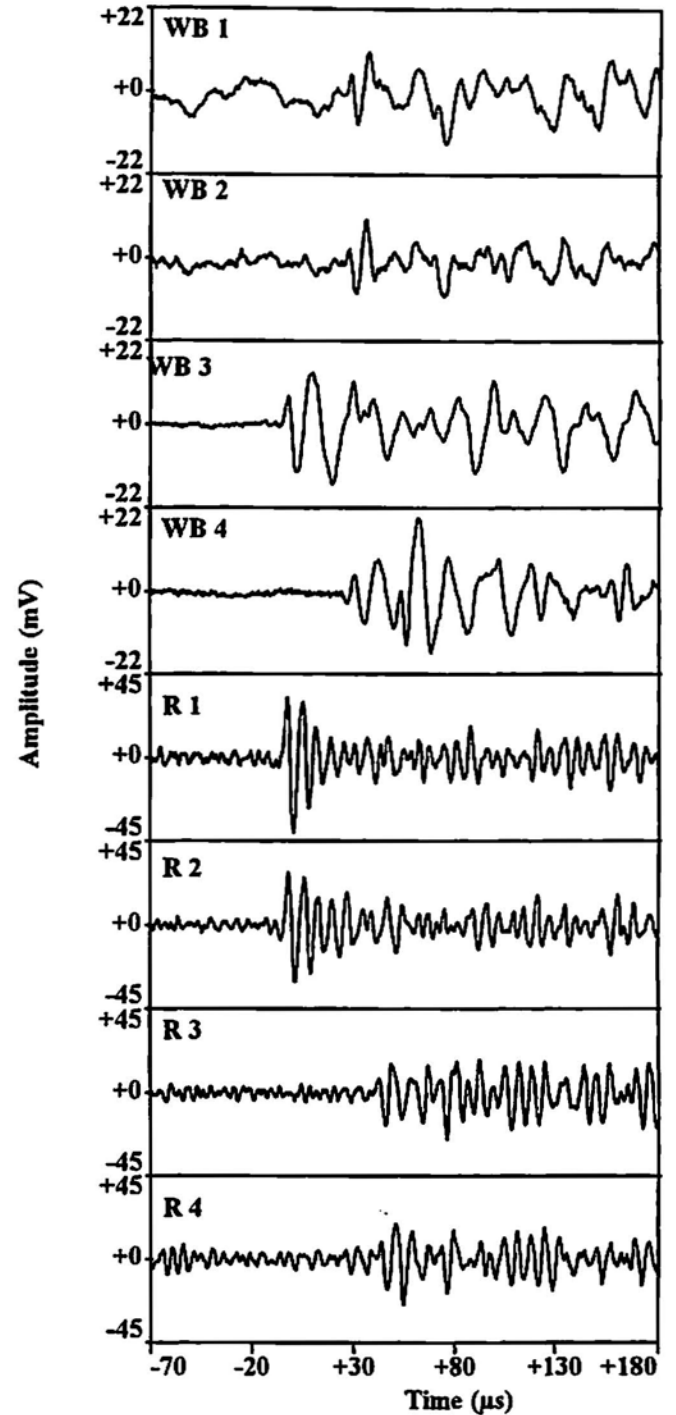


Fig. 3 Waveforms from extraneous fatigue-AE source emanating from the top grip. From specimen with a reduced section (6.4 mm) thick as shown in Fig. 1C. Gains were 51 dB for wideband and 60 dB for resonant sensors (sensor type and positions labeled on the waveforms).

waveforms. This difference is particularly interesting when compared to the signals in Fig. 4. These waveforms were detected on a cracked A514-steel plate of full thickness (22.9 mm thick) (Fig. 1A). This figure shows another extraneous source at the upper grip, which follows the same arrival

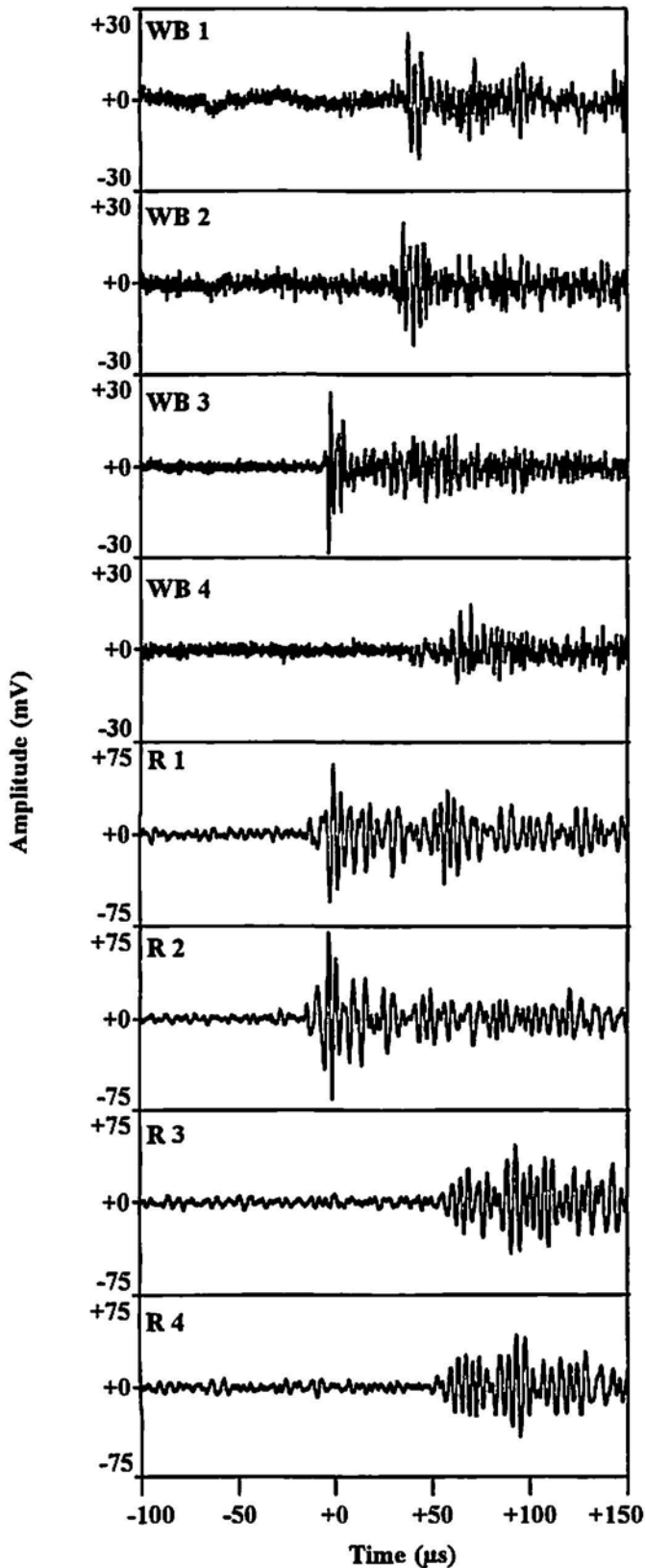


Fig. 4 Set of waveforms from extraneous fatigue-AE from the bottom grip for a specimen (22.9 mm thick) in configuration of Fig. 1B. Gains 51 and 60 dB, respectively, for wideband and resonant sensors.

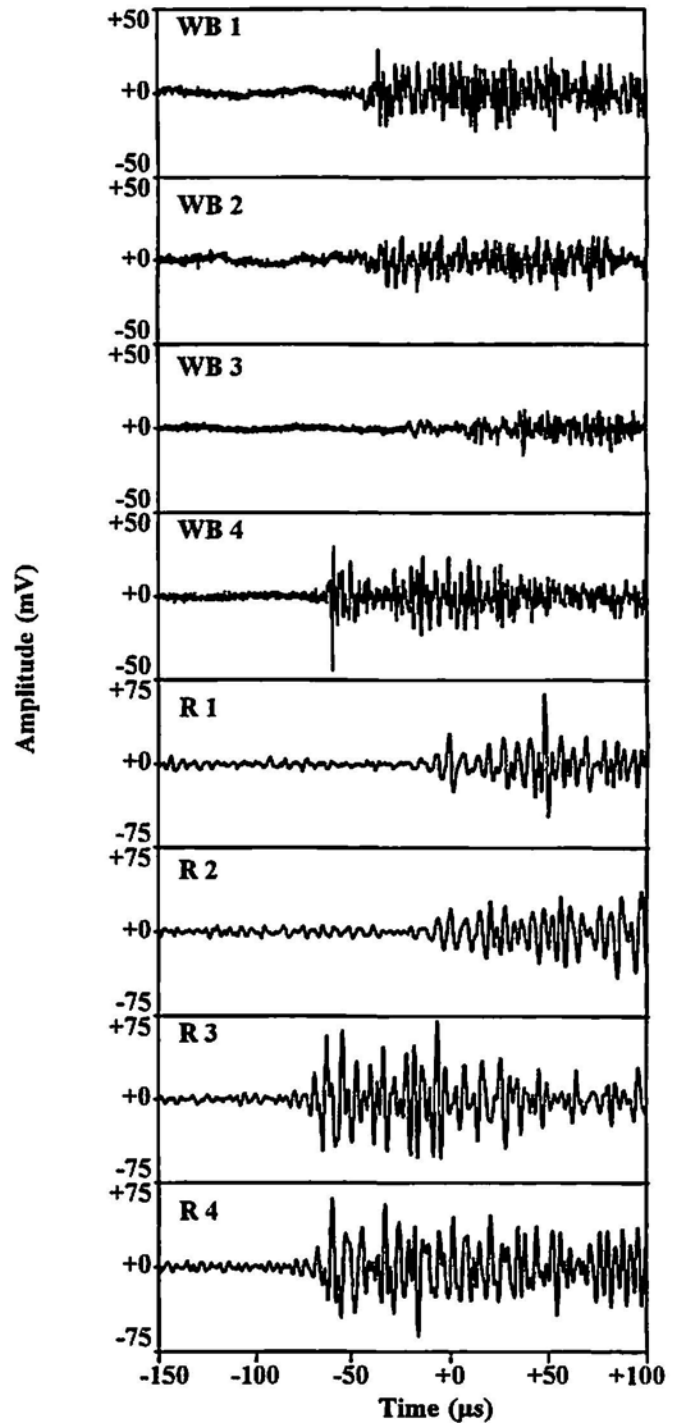


Fig. 5 Different type of extraneous fatigue-AE from the bottom grip for a specimen (22.9 mm thick) in configuration of Fig. 1B. Gains 51 and 60 dB, respectively, for wideband and resonant sensors.

pattern at the various sensors as in Fig. 3. In this case, however, the wideband sensors show a much higher frequency content, while the resonant sensors have a dominant frequency content that does not increase much from that shown in Fig. 3. Again, the dispersion effects on peak amplitude and rise time of the resonant sensor signals are ap-

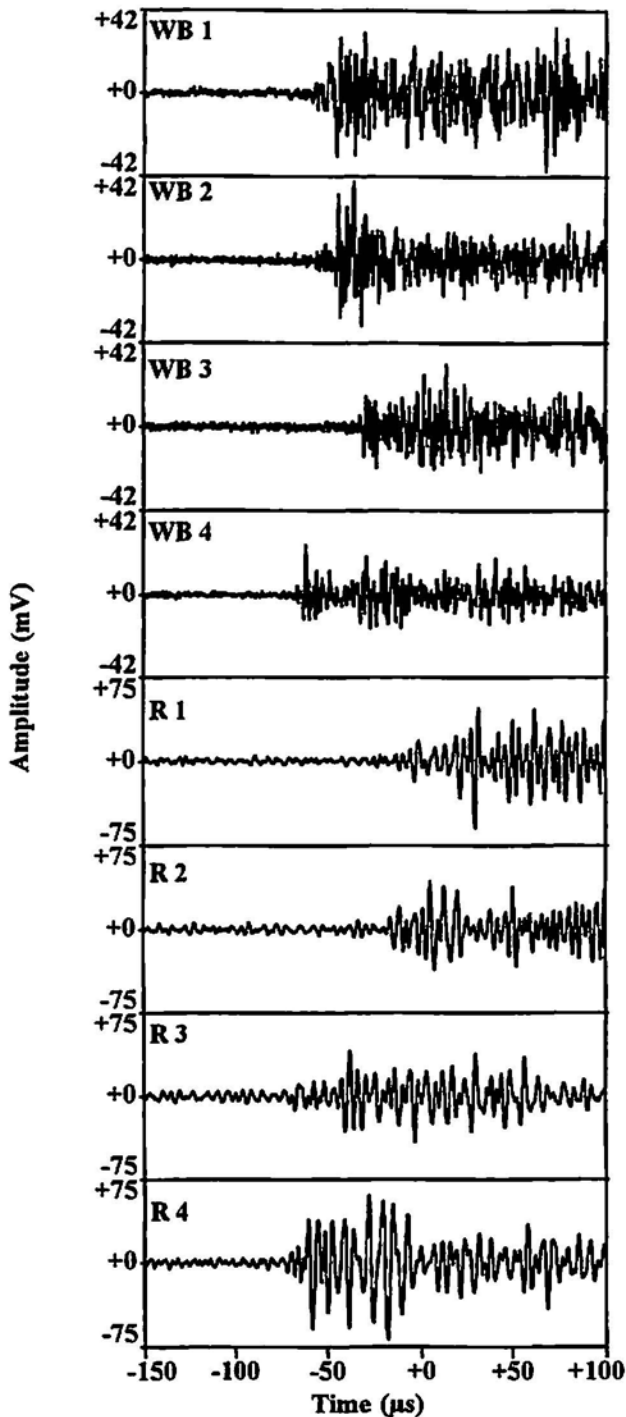


Fig. 6 Waveforms from extraneous fatigue-AE from the bottom grip, similar to Fig. 5, but for a specimen (6.4 mm thick) in configuration of Fig. 1A. Gains 51 and 60 dB, respectively, for wideband and resonant sensors.

parent. Figure 5 demonstrates an extraneous source emanating from the lower grips with characteristics different from those in Fig. 4. These waveforms occurred in a cracked A588-steel plate of uniform thickness (22.9 mm thick), as shown in Fig. 1A. The same high frequency content in the wideband waveforms as shown in Fig. 4 is present, but the

duration of the part of the signal of highest amplitude is much longer on most of the wideband sensors. Figure 6 shows that the extended high-frequency extraneous source is not limited to the thick plates. These waveforms were generated from a lower-grip extraneous source on a 6.4 mm thick steel plate of uniform thickness, as shown in Fig. 1B.

### 3.2 Artificial Extraneous Signals

Figure 7 illustrates the waveforms from a handclap about 0.5 m from the front of a steel sample mounted in the fatigue test machine. These waveforms were detected in a cracked A36-steel plate of reduced section (6.4 mm thick) as shown in Fig. 1C. This low-frequency airborne source is interesting because it displays a signal-to-noise ratio higher on the wideband sensors than on the narrowband sensors (noise refers to the background electronic noise level prior to the AE signal). It is also interesting that the low-frequency content of the source is apparent on both sensor types. Figure 8 shows a similar set of handclap waveforms detected in an A514-steel plate of uniform thickness (22.9 mm), as shown in Fig. 1B.

Figures 9 and 10 show the higher-frequency content on the wideband sensors if a short-rise-time pencil-lead break (0.3 mm, 2H) is applied to the grip body. The mechanical pencil lead break was conducted with a force parallel to the length of the specimen, on the bottom surface of the upper grip body. These sets of waveforms were detected in a cracked A514-steel plate of full thickness (22.9 mm) and in a non-cracked A36-steel plate of uniform thickness (6.4 mm) (Figs. 1B and 1C, respectively). These waveforms illustrate that extraneous sources with short-rise-times can generate high-frequency signals. They also illustrate that propagation across interfaces and longer distances (dispersion and attenuation effects) lengthens the apparent rise-time of the resulting waveforms for both types of sensors.

Figures 11 and 12 demonstrate the extraneous source waveforms for the thick and thin plates, respectively, due to airborne sound waves generated by impacting two hand-held pieces of metal together (steel rod, 32 mm dia., 152 mm long, and a steel pipe, 51 mm outside dia., 6 mm wall thickness, 914 mm long). The metal-to-metal impact was carried out at a distance of 4 m from the front of the test samples. Figures 1B and 1C, respectively, show the test configurations. In these cases, only one wideband sensor was used on the sample. Typically, the wideband sensor-location number 4 was used for this measurement. This sensor was located on the front of the sample, in the middle, below the crack. It had no internal preamplifier electronics and its output went directly to the filter and then to the waveform recorder, without any gain. Sensors with internal electronics experienced voltage saturation due to the high-amplitude, low-frequency content of this airborne sound, and hence they were not used.

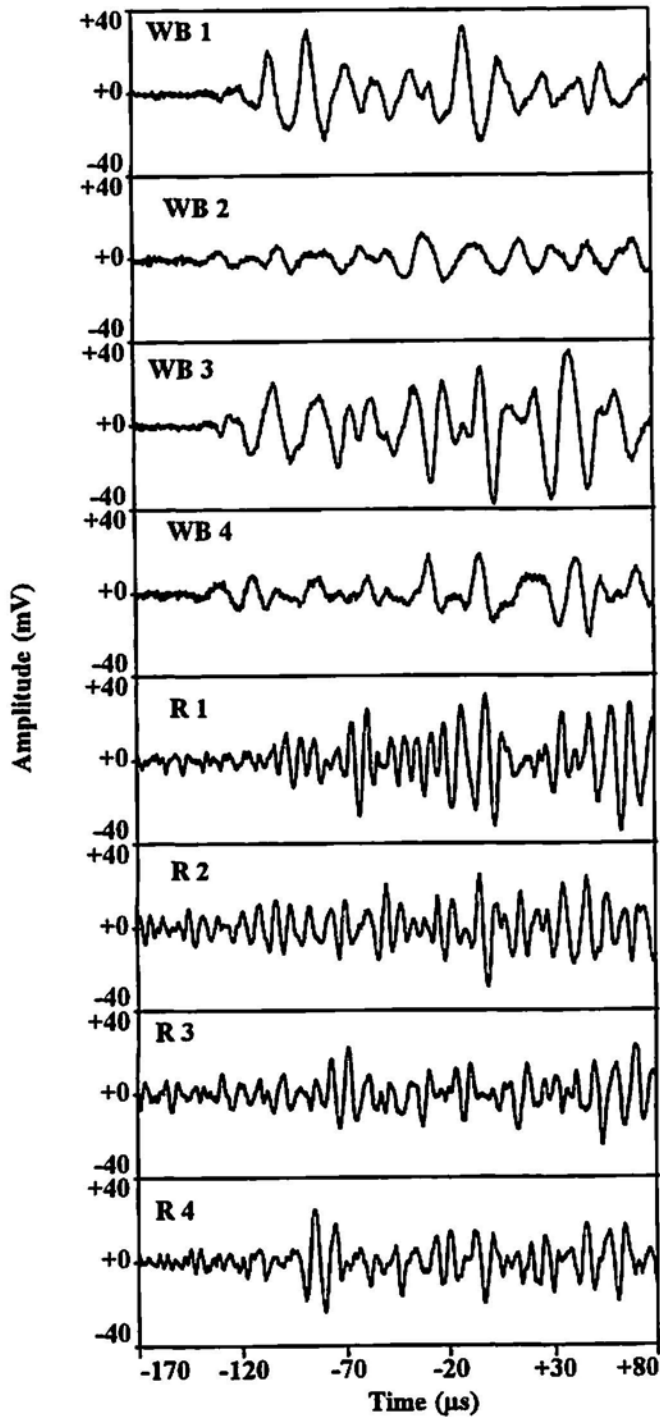


Fig. 7 Set of waveforms from handclap at 0.5 m from the front of the reduced-section sample (6.4 mm thick) in configuration of Fig. 1C. Gains 51 and 60 dB, respectively, for wideband and resonant sensors.

### 3.3 Cyclic Extraneous Signals on Non-cracked Large Samples

To provide a different perspective and one that might more closely represent field-generated extraneous AE, some waveforms were gathered from fatigue cycling of two large non-cracked steel plates. The materials were A588 and A36.

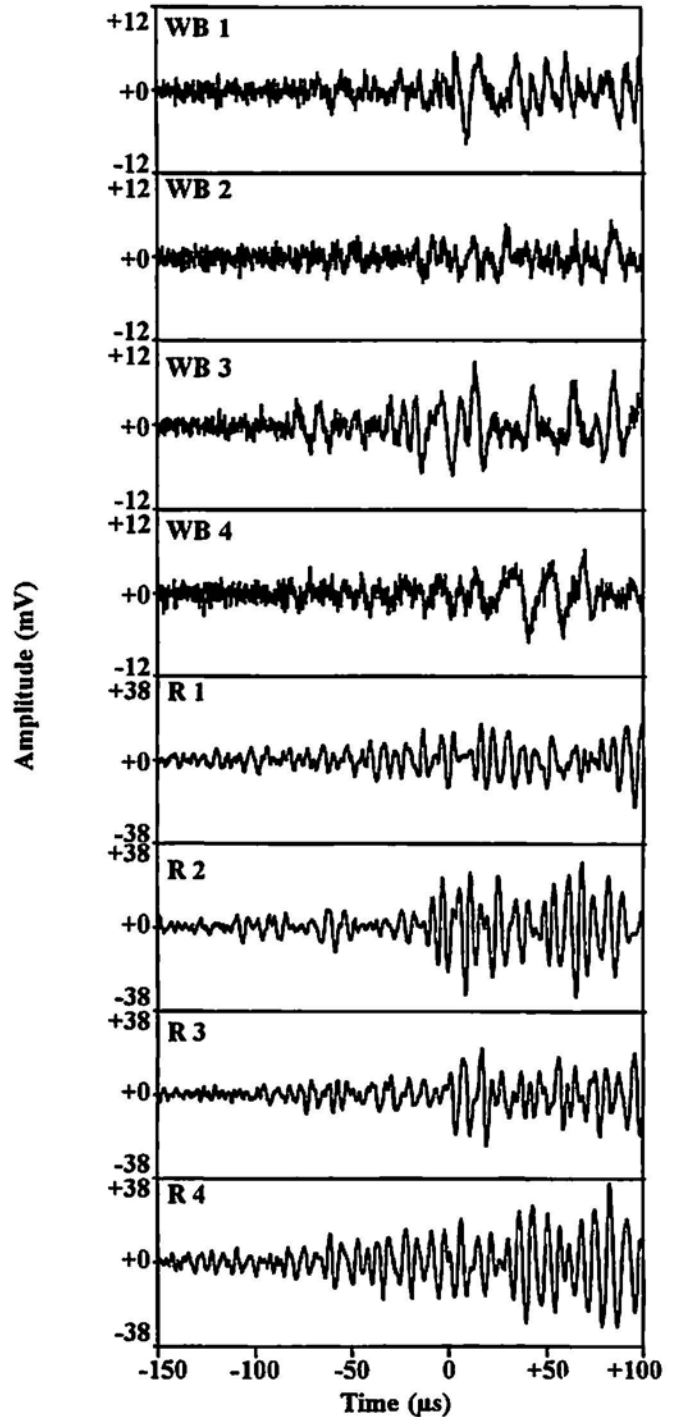


Fig. 8 Waveforms from handclap at 0.5 m position in front of specimen (22.4 mm thick) in configuration of Fig. 1B. Gains 51 and 60 dB, respectively, for wideband and resonant sensors.

The A588-steel test sample measured 0.9 m x 1.2 m x 25.4 mm, and the A36-steel test sample measured 0.9 m x 0.9 m x 8 mm. The sensor configuration and dimensional spacing, relative to the center of the plate, were the same as those used on the smaller plates, as shown in Fig. 1B. These experiments provided extraneous sources originating much farther from the sensors. Figures 13 and 14 show two

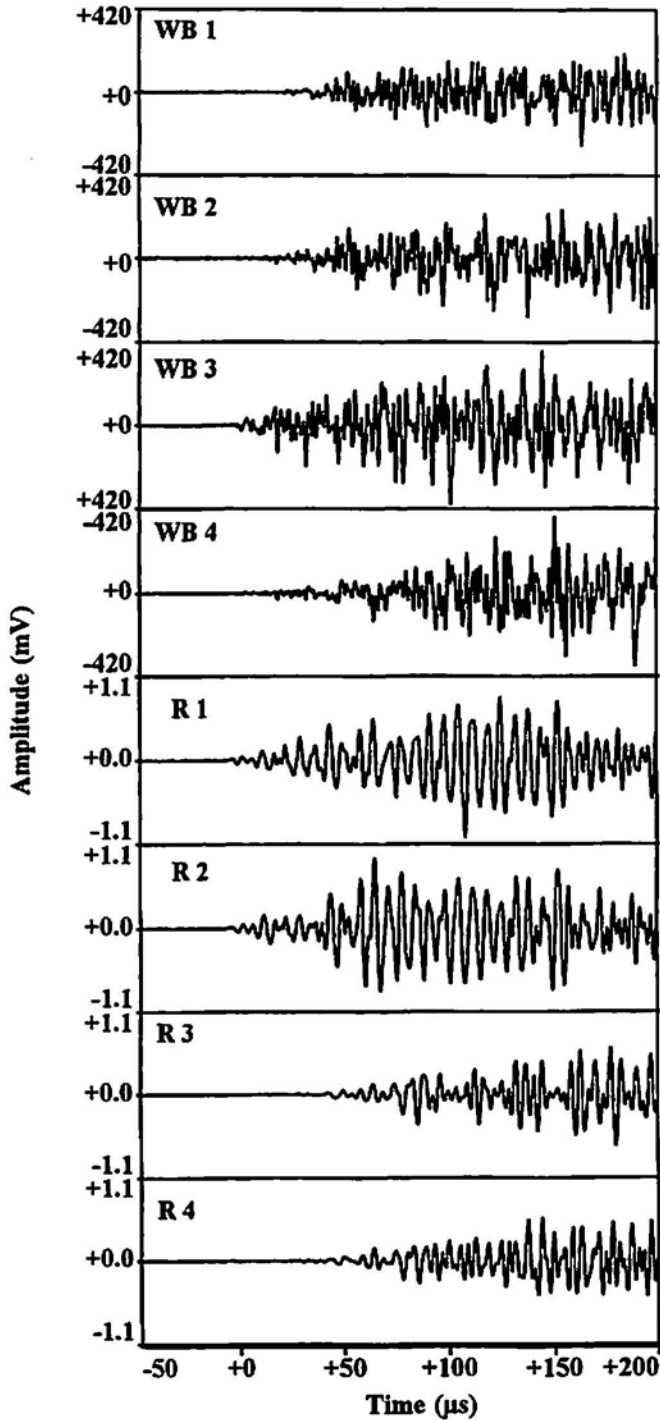


Fig. 9 Set of waveforms for lead break (force parallel to length of sample) on the upper grip housing for specimen (22.4 mm thick) in configuration of Fig. 1B. Gains 51 and 60 dB, respectively, for wideband and resonant sensors.

examples of such extraneous source waveforms. In both cases, the source was located in the bottom grip region for the thicker plate. It is interesting to note (see arrows in Fig. 13), the appearance of a Rayleigh wave (verified by velocity of propagation between sensors and the obvious high frequency spike) on three of the wideband sensor channels, but not on the fourth wideband sensor located on the other side

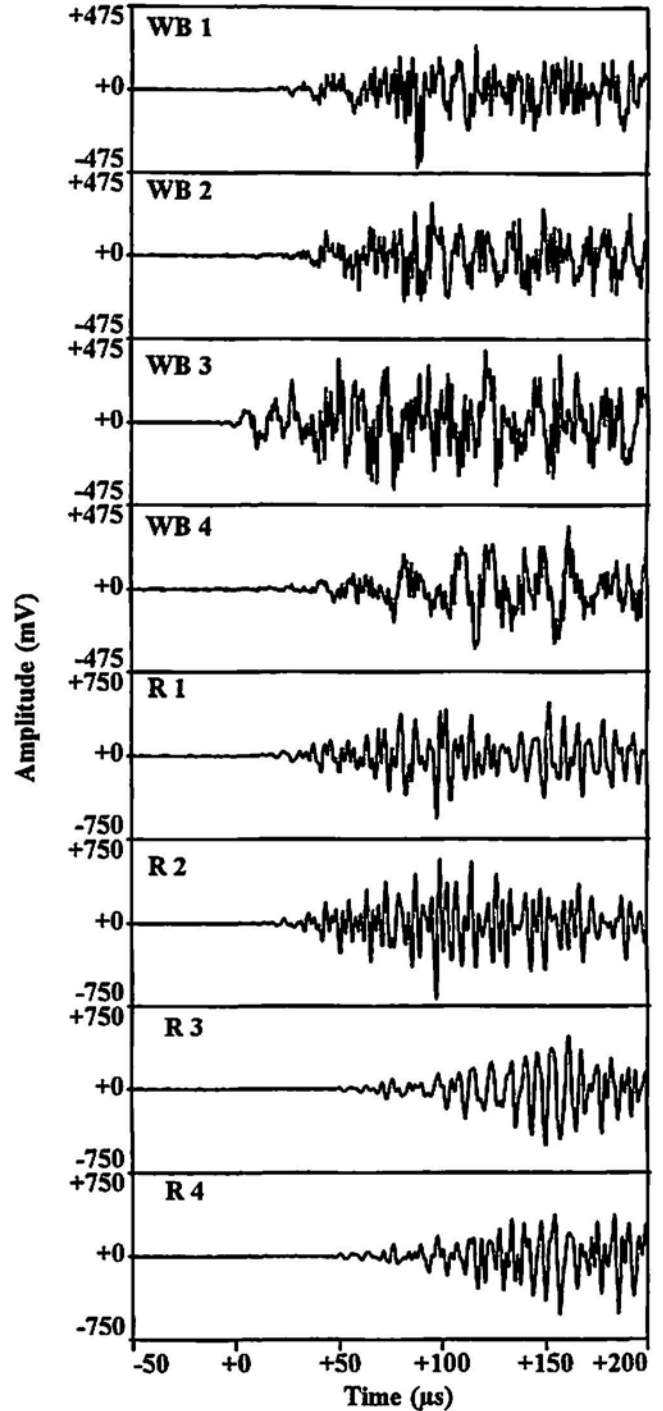


Fig. 10 Waveforms from lead break (force parallel to length of sample) on upper grip housing for reduced-section specimen (6.4 mm thick) in configuration of Fig. 1C. Gains 51 and 60 dB, respectively, for wideband and resonant sensors.

of the plate. In other cases, we observed this Rayleigh wave only on the backside sensor. Based on out-of-plane pencil-lead-break data, we believe the Rayleigh wave was generated by a grip-based surface source, as will be discussed below. Figure 13 also shows such Rayleigh wave information is not available in the resonant sensor waveforms. The extraneous AE signal in Fig. 14 occurred at the peak cyclic load.

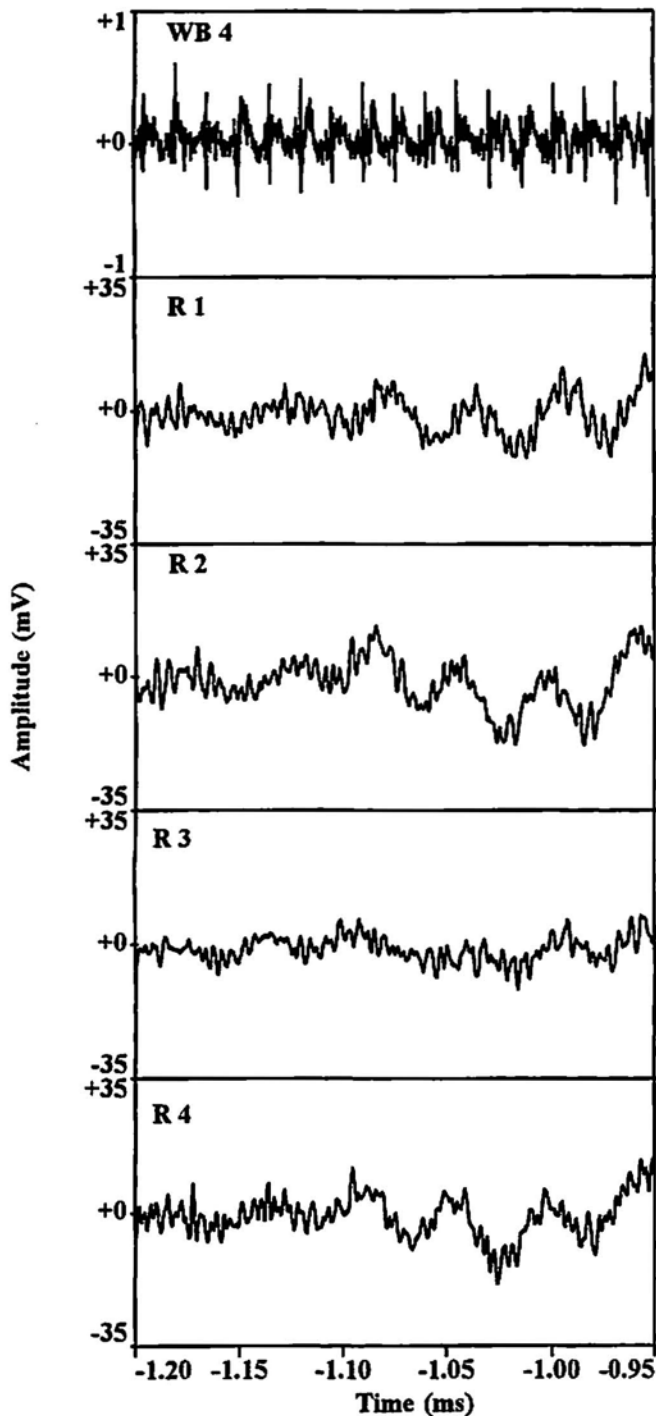


Fig. 11 Set of waveforms from impact of a pipe and bar at 4 m from the front of a 22.9 mm thick specimen in configuration of Fig. 1B. No gain for wideband sensor and 60 dB gain for resonant sensors.

Thus, load gating would have been ineffective in eliminating this signal. Figures 15, 16, and 17 provide examples of different classes of extraneous source waveforms observed during fatigue cycling of the large thin plate. The appearance of the Rayleigh wave is not as clear as it was for the thick plate. Figure 17 provides another example, in which

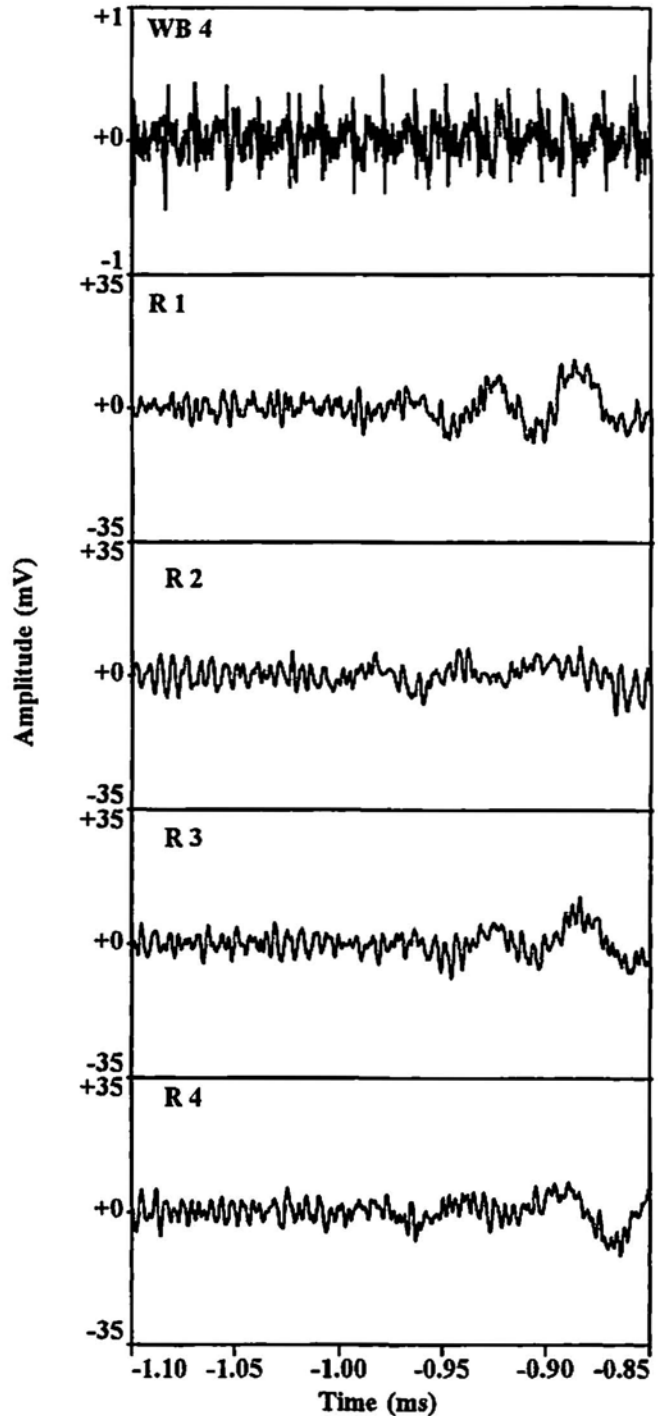


Fig. 12 Waveforms from impact of a pipe and bar at 4 m from the front of a reduced-section specimen (6.4 mm thick) in configuration of Fig. 1C. No gain for wideband sensor and 60 dB gain for resonant sensors.

load-gating does not eliminate all extraneous AE, since this source also occurred at peak load.

### 3.4 Fatigue-Crack-Induced AE

A comparison of Figs. 18 and 19 illustrates the contrast between crack-induced AE and grip-generated signals

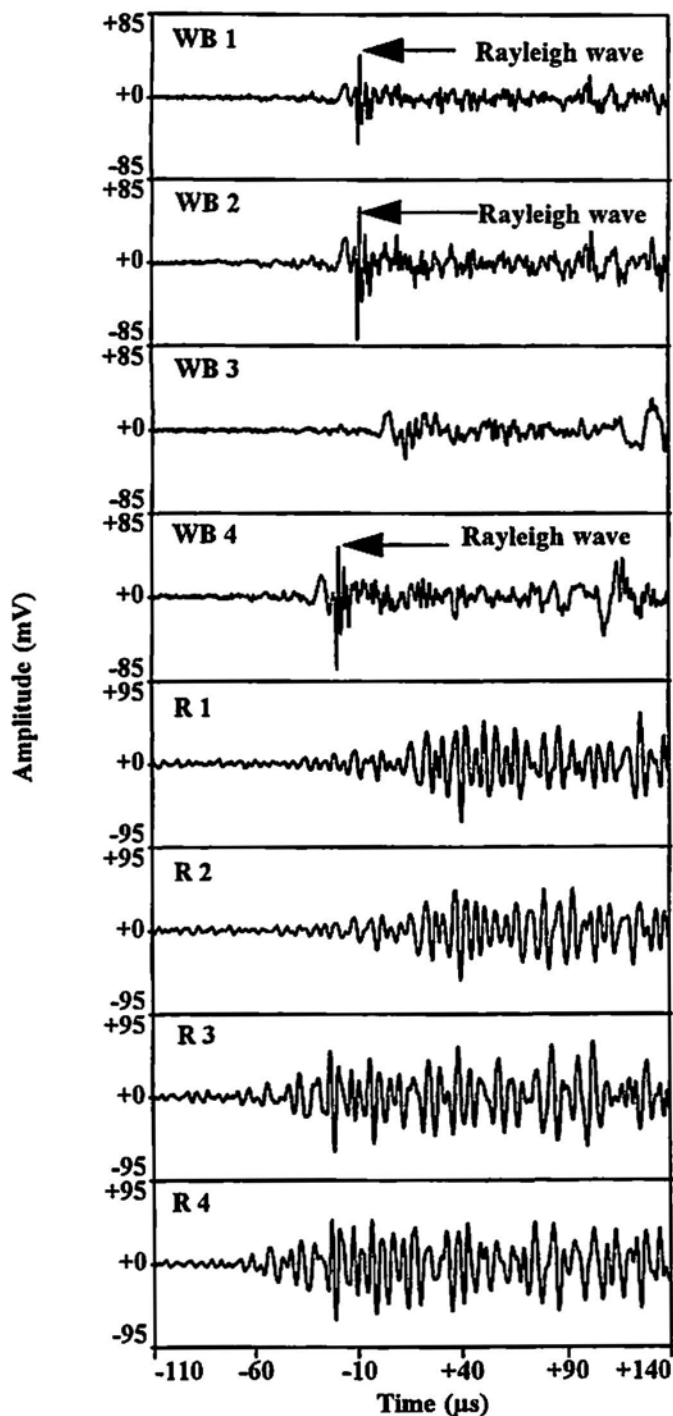


Fig. 13 Large-plate extraneous fatigue-AE waveforms from bottom grip source. 25.4-mm-thick plate. Sensors arranged as shown in the configuration of Fig. 1B. Gains 51 dB for the wideband sensor and 60 dB for the resonant sensor. Event occurred at 22% of peak load, during rising load.

during fatigue cycling of a cracked A36-steel plate of uniform thickness (25.4 mm), as shown in Fig. 1D. The fact that Fig. 18 is for a crack-induced source follows from the nearly equal values of signal arrival times at all of the sensors. Further, the crack-induced event was generated at the peak fatigue load while the lower grip signal in Fig. 19 occurred at 43% of the cyclic peak load.

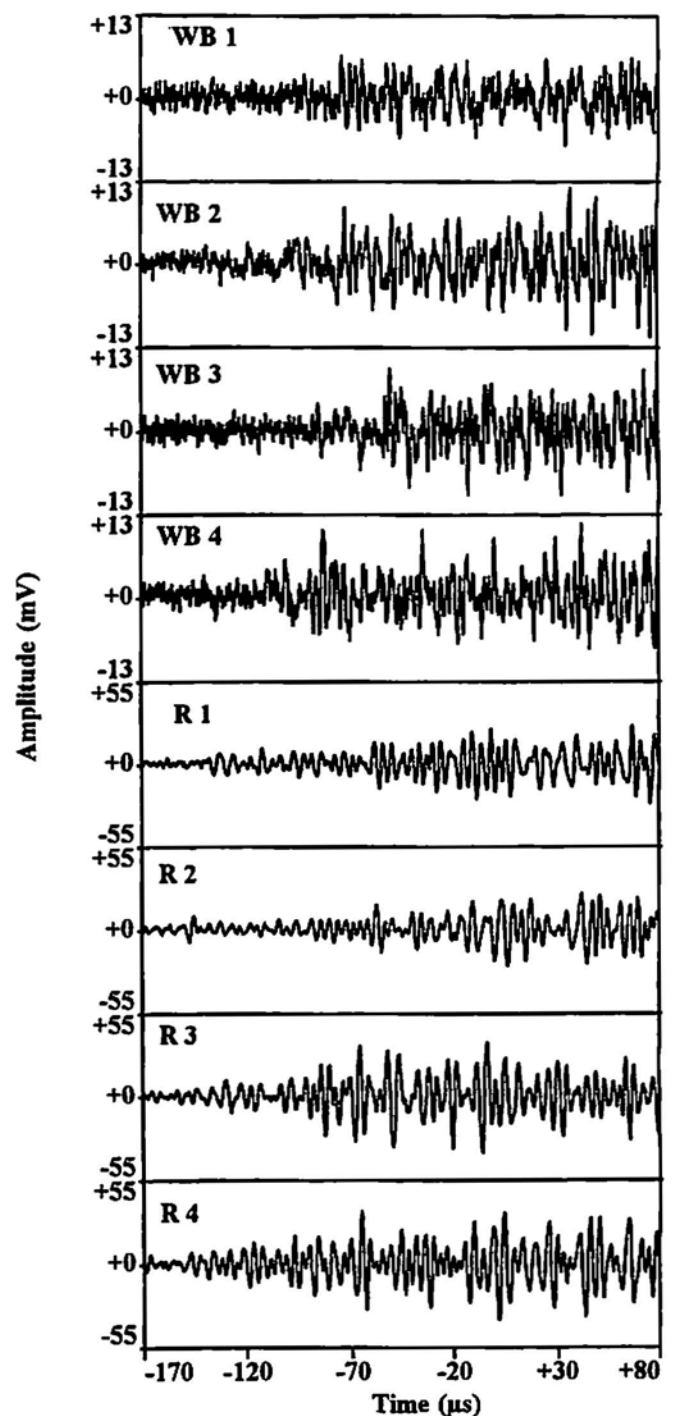


Fig. 14 Large-plate, different type extraneous fatigue-AE waveforms from a bottom grip source. Plate of 25.4 mm thickness with sensors arranged around the center as shown in the configuration of Fig. 1B. Gains 51 and 60 dB, respectively, for the wideband and resonant sensors. Event occurred at the peak load.

#### 4. Discussion of Results

The waveforms exhibited in this paper demonstrate that extraneous sources produce a wide variety of waveforms, particularly when detected with wideband sensors. Thus, in general, simple approaches to eliminating extraneous AE

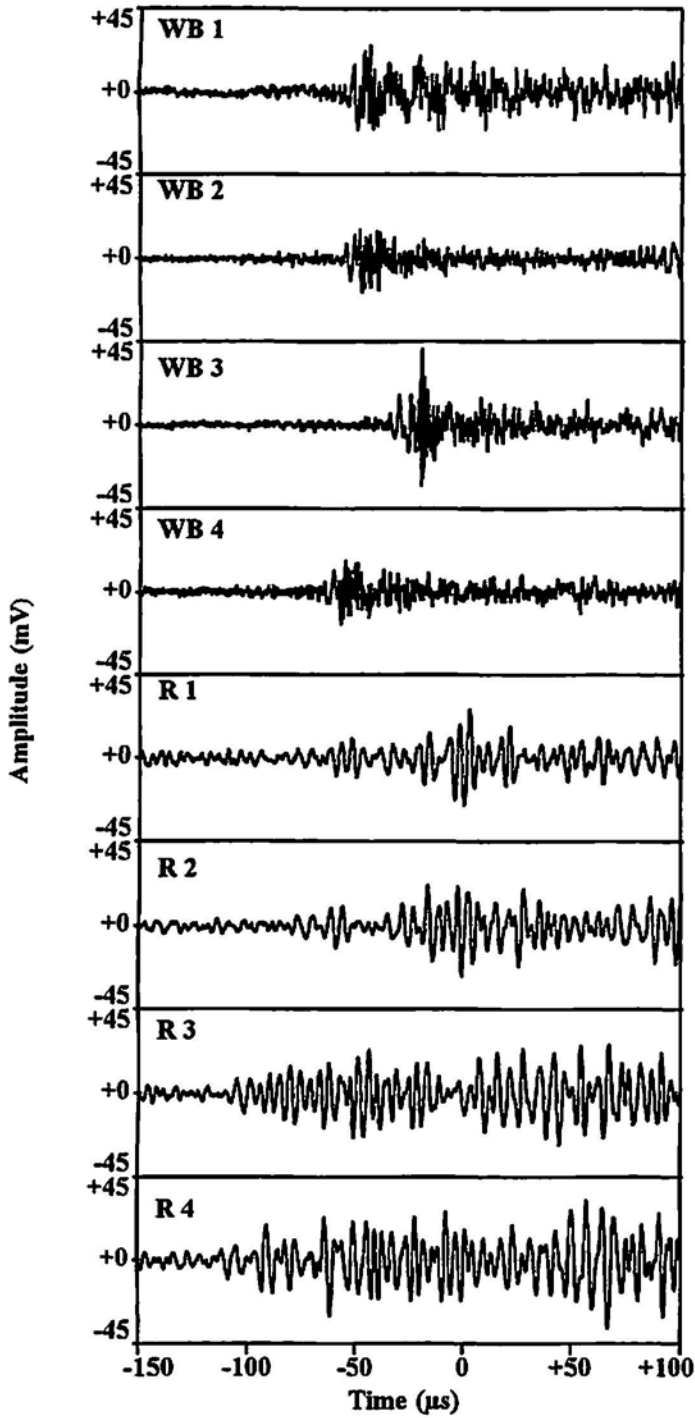


Fig. 15 Set of large-plate extraneous fatigue-AE waveforms from a bottom grip source. Plate of 8 mm thickness with sensors arranged around the center of the specimen with the same sensor spacing from the center as shown in the configuration of Fig. 1B. Gains 51 and 60 dB, respectively, for the wideband and resonant sensors. Event occurred at 50% of peak load during decreasing load.

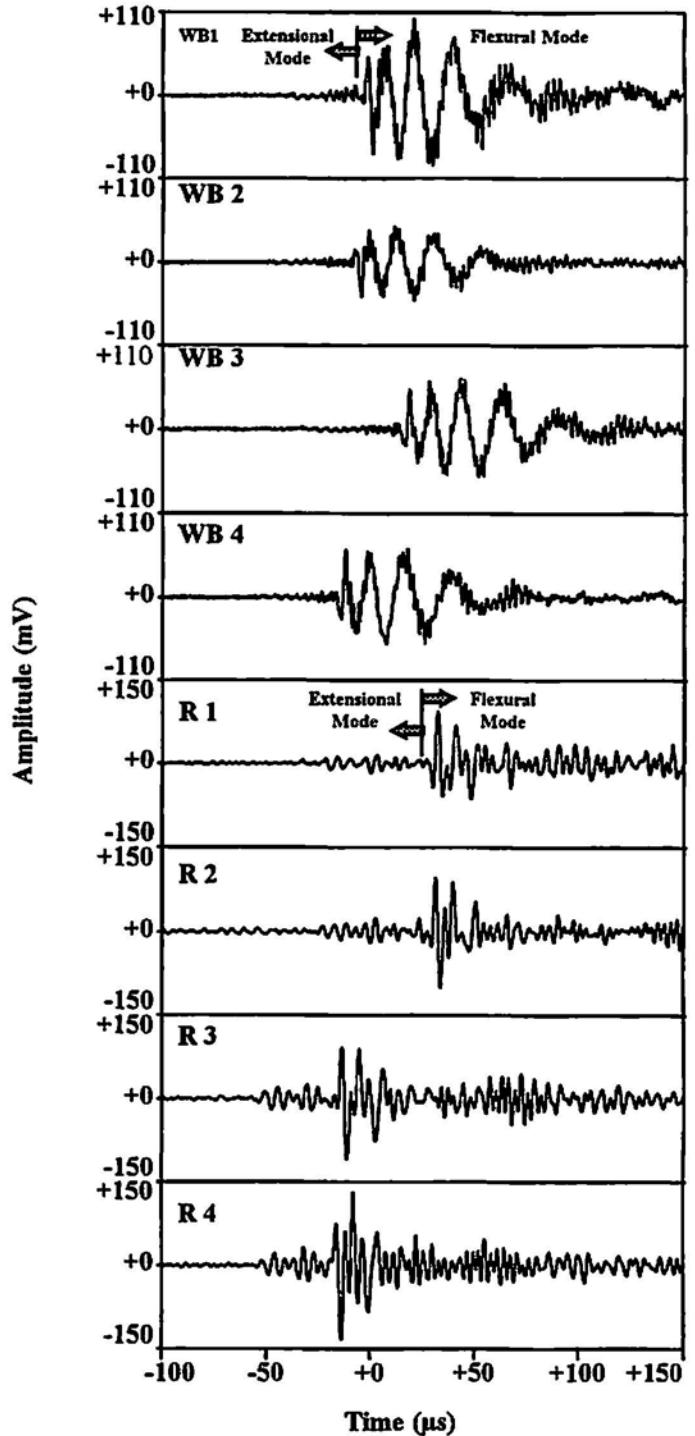


Fig. 16 Another source-type set of large-plate extraneous fatigue-AE waveforms from a bottom grip source. Plate of 8 mm thickness with sensors arranged around the center of the specimen with the same sensor spacing from the center as shown in the configuration of Fig. 1B. Gains 51 and 60 dB, respectively, for the wideband and resonant sensors. Event occurred at 14% of peak load during rising load.

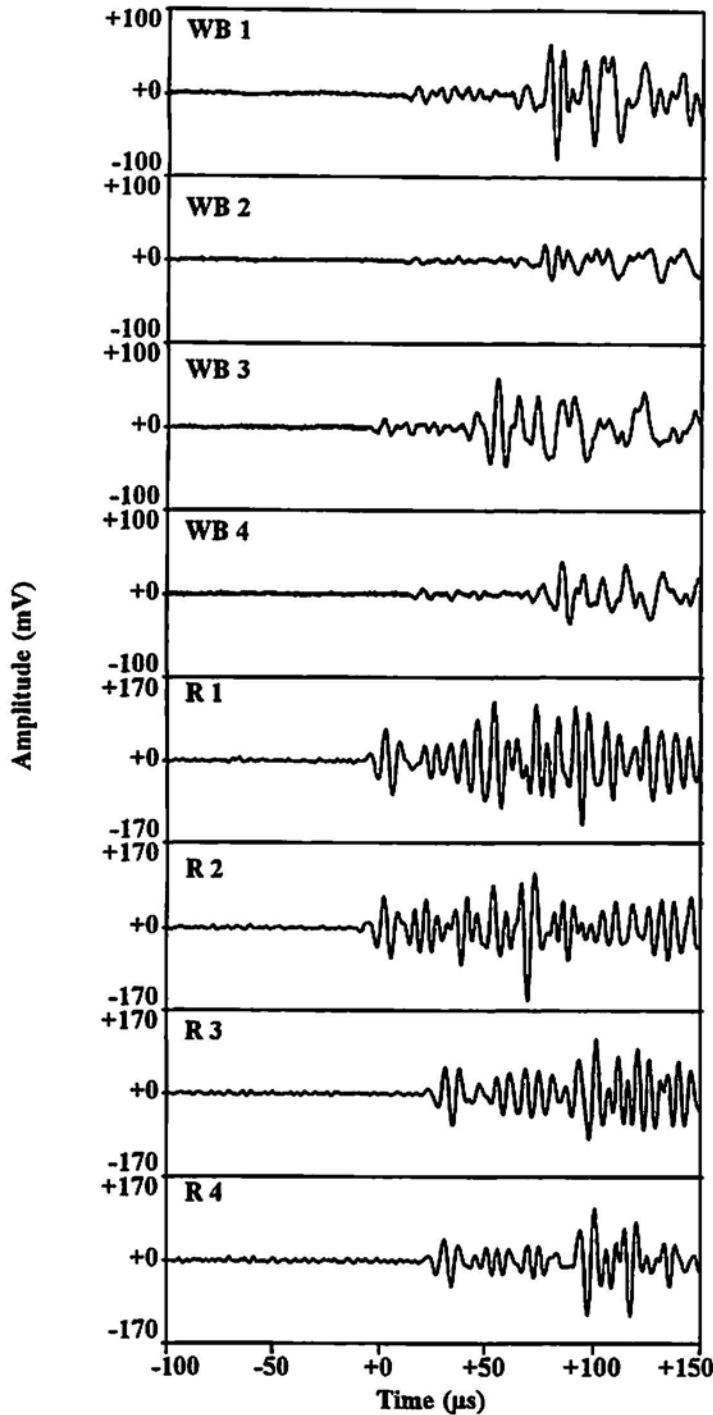


Fig. 17 Additional source-type set of large plate extraneous fatigue-AE waveforms from a top grip source. Plate of 8 mm thickness with sensors arranged around the center of the specimen with the same sensor spacing from the center as shown in the configuration of Fig. 1B. Gains 51 and 60 dB, respectively, for the wideband and resonant sensors. Event occurred at peak load.

will not be fully successful except in cases where the different types of extraneous AE are very limited. In the discussion that follows, key aspects of the different extraneous source waveforms, which were observed, will be high-

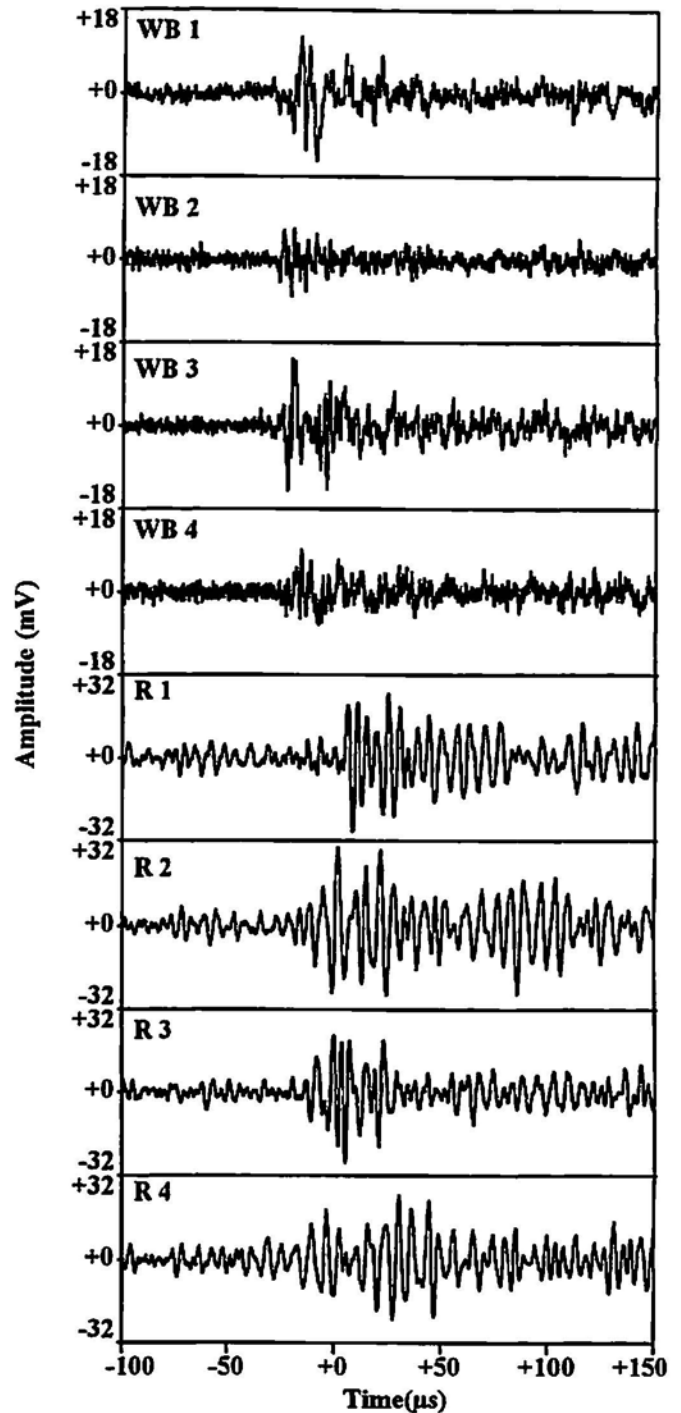


Fig. 18 Set of waveforms from crack source at peak load during fatigue of plate with 25.4 mm thickness with sensor configuration shown in Fig. 1D. Material was A36-steel with sharp crack. Gains 51 and 60 dB, respectively, for the wideband and narrow band sensors.

lighted. A focus of the discussion will be on the differences in the waveforms from the wideband sensors as compared to the resonant sensors. Since the resonant sensors and the wideband sensors were not physically located at exactly the same positions, it might be argued that some of the differ-

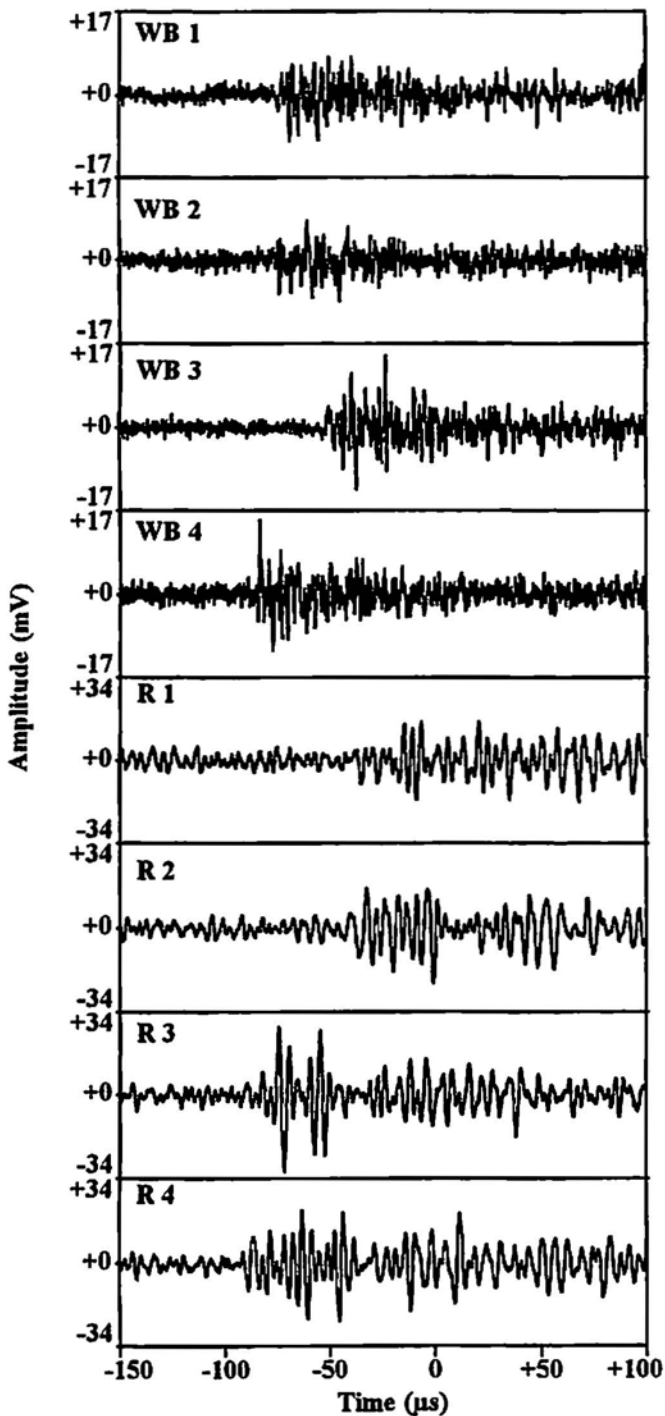


Fig. 19 Set of waveforms from extraneous source from lower grip during the same fatigue testing for Fig. 18. Extraneous AE event at 43% of peak load during the rising load.

ences between the two types of sensors could be attributed to the differences in distances of wave propagation between sensor locations, effects of radiation patterns, or differences between sensors of the same type. To provide the evidence that this is not true for the factors cited here, all the available waveforms for each extraneous AE signal are provided. Thus, readers can assess for themselves that the effects sin-

gled out between the two types of sensors are real and not a result of the differences cited above.

#### 4.1 Extraneous Signals in Large Plates

As demonstrated in Figs. 13 through 17, there are much wider variations in both the waveform shapes and the frequency content in the wideband-sensor waveforms than those of the resonant-sensor waveforms for extraneous grip-based AE. The same, or nearly the same, resonant-frequency is apparent in all the resonant-sensor waveforms in these figures. Figure 19 also illustrates, for a real crack-induced AE event in a smaller specimen (25.4 mm thick), similar resonant-frequency content. This is in spite of the wide variety of the source-frequency content (as seen in the wideband waveforms) and the two different plate thicknesses (varied by a factor of 3.2). Thus, for resonant or narrowband data, simplified post-processing frequency discrimination of extraneous AE does not appear to be a robust method to generally distinguish real crack-induced AE from all fatigue-related extraneous AE, as has been proposed (Ghorbanpoor, 1985). Furthermore, the current results, showing that resonant sensor data has similar frequency content for both crack-induced AE and extraneous AE, is consistent with later results (Ghorbanpoor and Rentmeester, 1993; Gong et al., 1992).

The wideband-sensor waveforms show much more potential for source identification in both the time and the frequency domain because of the wide variation of signal types. For example, the wideband waveforms in Fig. 16 are similar to those obtained from an out-of-plane pencil-lead break on the plate. In contrast, the wideband waveforms in Fig. 13 show Rayleigh waves at three of the sensors on the same side of the plate. This is consistent with the appearance or nonappearance of Rayleigh waves as a result of lead breaks on the two surfaces of the plate. This result indicates a means to detect, with wideband sensors, a surface-based extraneous source on a thick plate and to determine on which side it originates. Figure 13 shows no evidence of the Rayleigh wave in the waveforms from the resonant sensors, even though they were mounted on the same plate surface as the three wideband sensors which showed the Rayleigh wave. Both the 100 to 300 kHz bandpass and the large aperture (about 18 mm) of the resonant sensors would be expected to contribute to eliminating response to the high frequency Rayleigh wave.

Figures 13, 14, 15, and, to a lesser degree, Fig. 16, indicate that a long rise time can be associated with the narrowband extraneous AE waveforms. However, the measured rise-time values will clearly be a function of the particular threshold used. This clear dependence of measured rise time on threshold is contrary to other work previously reported (Ghorbanpoor and Rentmeester, 1993). These waveforms indicate that higher thresholds, or lower amplitude extraneous signals of the same type, could result in relatively short

measured rise times. Figure 16 shows that, potentially, a very short measured rise time (3 to 9  $\mu\text{s}$ ) could result if the threshold was above the apparent lower amplitude extensional mode in the resonant sensor data. Previous work for resonant sensors has claimed that extraneous sources have rise times that measure 50  $\mu\text{s}$  or more (Ghorbanpoor, 1985) and valid crack sources have short measured rise times of 1 to 15  $\mu\text{s}$  (Ghorbanpoor and Rentmeester, 1993), or less than 25  $\mu\text{s}$  (Gong, et al., 1992). The current results (Fig. 16) indicate that such approaches are not valid for all extraneous sources. Furthermore, if the propagation distance is relatively large, dispersion will increase the rise times.

Visual examination of the resonant-sensor waveforms in Figs. 13 through 17 shows whether an extraneous source originated in the lower or upper grips. Thus, it might be surmised that source location would be a valid approach to distinguish the crack-induced events from the grip-based events with threshold-based systems. To test this theory (assuming a crack was midway between the upper and lower resonant sensors), the differences in arrival times at the resonant sensors for the extraneous hits of each of several extraneous grip-based events (on a 25.4 mm-thick sample) were determined as a function of different thresholds. The different thresholds test the effects of changes in source amplitudes. Starting at a 40 dB threshold (about 3 dB above the background electronic noise) and successively raising a two-sided threshold in 3 dB increments, the time differences between the first-hit sensors (upper and lower) and the second-hit sensors (upper and lower) were determined. These time differences are compared in Fig. 20. This figure includes a line at the time difference of 47.2  $\mu\text{s}$ , which corresponds to the 152 mm spacing between the upper and lower resonant sensors based on the bulk shear-wave velocity for steel of 3.2 mm/ $\mu\text{s}$ . This velocity is commonly used for source location in conventional AE technology. Clearly, Fig. 20 shows significant errors even though the average delta time difference of 49.7  $\mu\text{s}$  is very close to 47.2  $\mu\text{s}$ . A similar study of arrival time differences was done for real crack-induced AE. The time differences as a function of a two-sided threshold are shown in Fig. 21 for several crack-induced events. This figure demonstrates substantial deviations from the expected time difference of 0  $\mu\text{s}$  (even overlapping those of the extraneous sources in Fig. 20) for these crack-induced events which had peak signal amplitudes similar to the extraneous signals used to generate Fig. 20. Examination of crack-induced events with larger amplitudes (up to nearly 100 mV peak amplitudes) resulted in the same types of deviations from the expected 0  $\mu\text{s}$ . Hence, the reliability of using source location with fixed thresholds is not always acceptable for the sensor spacing considered here. A conservative choice (a low value near 0  $\mu\text{s}$ ) of the maximum time difference allowed to distinguish a crack-induced source would result in some real crack-induced events being classified as extraneous sources, and a non-conservative maximum time (a high value near 47  $\mu\text{s}$  for the case considered above) would result in some extraneous grip sources

being classified as crack-induced. If the resonant sensors were further away from the assumed center-crack region, the concept would be expected to work more reliably. However, most experiments are not done with the required large samples. If the sensors were closer to the assumed center crack, using spatial location to distinguish the extraneous grip-based event is expected to be worse. This conclusion is based on the fact that the average time difference for grip-based sources would be smaller when the sensors are closer to each other. In this case, the errors in arrival time difference would be more likely to show that a signal originated between the sensors rather than outside the sensor array. A similar analysis of extraneous grip-based events with the large, thinner (8 mm thick) plate produced similar scatter in the arrival time differences, except that in this case, the average time difference no longer corresponded to the expected time difference for the sensor spacing, based on the bulk shear velocity. Instead, it was near the thin-plate extensional velocity (5.4 mm/ $\mu\text{s}$ ). While identification of extraneous grip sources by fixed-threshold determination of arrival times can be poor, resonant waveforms allow easy identification of grip-based sources, by using visual observation of the set of resonant waveforms.

As was noted before, extraneous signals can occur at, or near, the peak load during cyclic fatigue, as illustrated in Figs. 14 and 17. Thus, load-gating can be expected to accept some extraneous AE as well as real crack-induced AE. To account for this fact, other techniques are required to identify the extraneous AE that occurs near the peak loads.

#### 4.2 Extraneous Sources in Smaller Plates during Fatigue

Extraneous AE can also be generated by sources, which are close to the sensors mounted to monitor cracks. To study such cases, this work also included two thicknesses of smaller plates. As with the large plates, these results (Figs. 3 through 6) show a similar diversity of extraneous source waveforms captured with the wideband sensors. The waveforms detected by the resonant sensors are more similar to each other and to the resonant waveforms for the real crack-induced source in Fig. 18. Another feature demonstrated by these waveforms was that the rise time measured with a threshold-based system could result in very short rise times. This was also observed in the large plates. The resonant waveforms in Figs. 3 and 4 indicate that relatively short measured rise times (5 to 13  $\mu\text{s}$ , with a threshold slightly above the initial background noise level for the sensors nearest the source) would be determined by a threshold-based system for these extraneous source cases. This result shows that rise-time techniques are not reliable in eliminating extraneous AE.

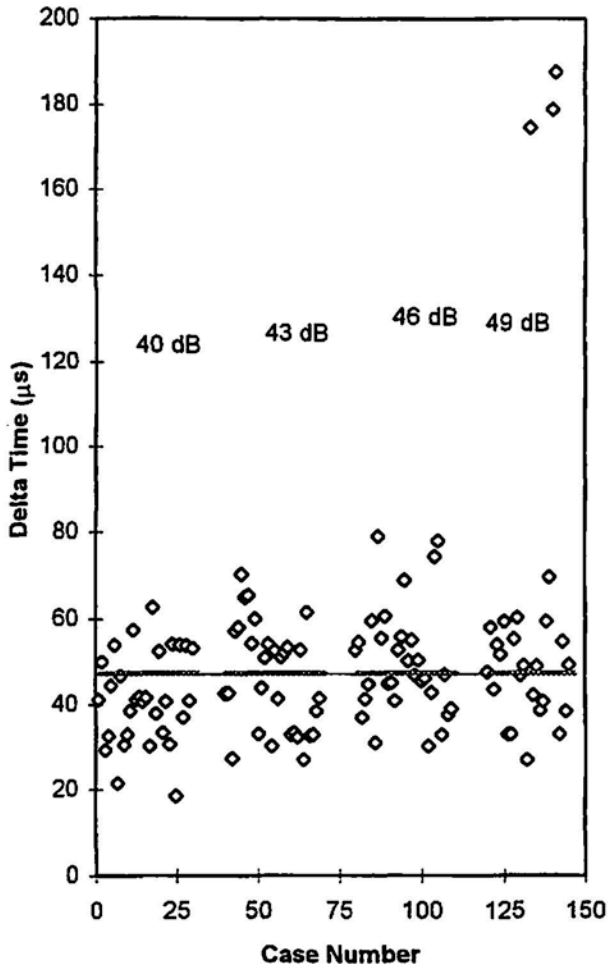


Fig. 20 Plot of arrival time differences (for different two-sided thresholds applied to recorded waveforms) between the top resonant sensor and the bottom resonant sensor on each side of the sample (sensors on the front surface). Grip-based extraneous fatigue signals on large plate of 25.4 mm thickness with the resonant sensors in a rectangular array (152 mm high by 76 mm across) centered on the sample. Horizontal line at 47.2  $\mu\text{s}$  corresponds to propagation time between upper and lower sensors, based on the bulk shear velocity for steel.

As was observed for the large plate case, the large changes in the frequency content in the wideband extraneous signals are not reflected in the waveforms of the resonant sensors. This "frequency effect" can be seen in contrasting Fig. 3 with Fig. 5. Figure 3, which has waveforms for a specimen with the sensors located on a reduced center section is also interesting. This figure shows that the measured rise time at the two resonant sensors near the top grip (origin of the source) is very fast (about 5  $\mu\text{s}$  with a threshold slightly above the initial background noise level) and, at the two bottom resonant sensors, is considerably slower (25 to 30  $\mu\text{s}$ ), due to dispersion. Again, the distinction as to which grip was the source of the extraneous AE is readily apparent from visual examination of the waveforms of the resonant sensors.

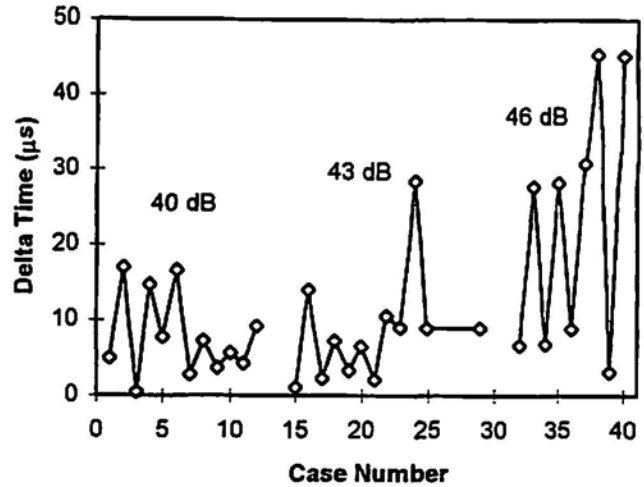


Fig. 21 Plot of arrival time differences between top and bottom sensors (like Fig. 20) for different thresholds for real crack-induced AE events during fatigue of an A36-steel plate, 25.4 mm thick, with sensor configuration shown in Fig. 1D. Theoretical time difference expected to be 0  $\mu\text{s}$ .

#### 4.3 Extraneous Airborne Signals

During field AE monitoring, airborne sound waves from other nearby mechanical processes can be "intercepted" by the metal structure, on which the AE sensors are mounted. Comparison of Figs. 7 and 8 shows that the thickness of the plate has a substantial effect on the frequencies observed with the wideband sensors for a handclap source. Thus, if frequency filtering is used to attenuate such sources, the filtering frequency range will potentially need to be altered for different sample thickness. On the other hand, the frequency content of the resonant sensors increases only slightly as the plate thickness increases.

The air-transmitted sound created from banging together two metal pieces did not result in a measurable signal (above background electronic noise) on the wideband sensor (after the 50 kHz to 2 MHz filter) in contrast to the behavior of the resonant sensors. This result is not surprising for two reasons. First, measurements have confirmed that the wideband sensor without the internal electronics loses at least 13 dB in signal-to-noise ratio or sensitivity (mostly due to sensor cable capacitance and filter input capacitance). Second, the signal-to-noise ratio (at the start of the signal), for the resonant sensor signals, is only about 8 dB. To maintain the sensitivity of the wideband sensors in a continuous, high-amplitude, noisy field environment, will require high-pass filtering before introduction of much gain. If this is not done, then the sensor with internal electronics may be saturated much of the time.

The extraneous airborne signal presents a different perspective since, as the waveforms for the resonant sensors show in Figs. 7, 8, 11 and 12, the signals typically arrive

at all the sensors at close to the same time. Thus, spatial discrimination and/or guard sensors are not useful to discriminate this extraneous source as the signal does not propagate along the test sample in a particular direction. Further, since all the resonant sensors would be hit at a similar time for a threshold-based system, it might be concluded that an AE source was active near the center of the sensor array. An examination of the metal-to-metal impact waveforms (for a time greater than that illustrated in the figures) shows that this source results in a very long duration signal. They also show continuous near-peak amplitude (presumably due to the ringing of the impacting objects, which would not occur for the handclap source) that could be used to eliminate this source, as distinguished from a real crack-induced source. Long signal duration has been recognized by others to indicate an extraneous event (Gong, et al., 1992; Ghorbanpoor, 1985). But, since the dispersion and/or reflections can increase the signal duration, care must be taken in the selection of values used for discrimination. Otherwise, real crack-induced sources may be incorrectly categorized. For example, if the sensors were on a small sample where multiple reflections would lengthen the duration of a signal, a large amplitude crack-induced source would have a long duration. Since the wideband sensors would better characterize the low-frequency content of such extraneous sources, it may be easier to use this feature to recognize them.

#### 4.4 Extraneous Solid Transmitted

A pencil-lead-break source, as demonstrated in Figs. 9 and 10, has a slow rise time and long duration (typically associated with extraneous AE), after it has passed through the two metal-to-metal interfaces in order to travel from the grip housing to the test sample. These features are present in the waveforms from both types of sensors. As expected from the discussion above, the increase in higher frequency-content is more apparent in the wideband sensors on the thick plate than the thin plate. As before, there is no discernible change in the resonant sensor's waveforms as the specimen thickness is increased. These results show that even short-rise-time sources result in long-rise-time signals if the waves must propagate across interfaces to reach the sensors. Additionally, these results indicate that crack-induced sources may be especially difficult to distinguish if the AE waves must pass through interfaces or other discontinuities in the propagation path to reach the sensors.

#### 4.5 Contrast of Crack-induced AE with Extraneous AE

Although detailed discussion of crack-induced AE will be deferred until a later paper, we note some differences between crack-induced AE and extraneous waveforms. Figures 18 and 19 demonstrate that differences in wideband AE waveform can be very large between extraneous grip-based and real crack-induced sources, while narrowband waveforms for the same two sources can have almost no difference,

except for the visual sequence of waveform arrival due to the different source locations (grips versus crack). However, even with the wideband sensors, some extraneous sources (Fig. 4) can resemble a crack-induced source (Fig. 18), where similar fast rise-time and a short-duration higher-amplitude signals are present on the wideband sensors for both of these source types.

#### 4.6 Electrical Extraneous Signals

The use of 300-kHz low-pass filtering to eliminate problems with electromagnetic interference has been proposed (Ghorbanpoor, 1985). As Fig. 2 demonstrates, that hypothesis is not always true. Clearly, in this case, the 300-kHz low-pass filter allowed a significant noise spike of amplitude up to 200 mV (66 dB) to appear on the resonant sensors. This signal is probably present due to the antenna effect of the sensor cable and/or the cable between the pre-amplifier and the waveform recorder. Since the main threshold-based AE measurement unit includes an additional 300-kHz low-pass filter, we anticipate that this signal will be attenuated further before measurement. To estimate this attenuation, the recorded signal (which experiences only the preamplifier filter) was passed through a six-pole 300-kHz low-pass Butterworth software filter. This filter reduced the signal for one channel from about 214 mV to 169 mV, which was still 18.5 dB above the threshold typically used to monitor AE in these experiments.

### 5. Current Bottom-Line Perspectives

Examination of all the recorded waveforms indicates, for known directions of propagation of extraneous AE, that visual spatial discrimination of waveforms of either sensor class can be very effective in identifying extraneous signals, except in the case of airborne extraneous AE. Since the wideband signals provide an opportunity for accurate source location (Ziola and Gorman, 1991) by an automatic, rather than a visual, inspection, the wideband-sensor approach seems to be potentially better at the present time. Further, with the diversity of wideband extraneous waveform types (and presumably source types) as compared to the resonant-sensor waveforms, advanced signal processing techniques may be developed for most wideband cases to identify the extraneous sources. This potential advantage is of great importance for cases where the location of real crack-induced AE is near the location of extraneous sources, where spatial discrimination would not likely be useful.

In the application of resonant AE sensors to monitor an existing crack, the current results indicate that a visual waveform approach or an equivalent signal-processing method combined with proper sensor placement would be effective in eliminating extraneous AE. This "visual observation" takes account of the arrival of a substantial part of the resonant waveform, not just a single feature. If an AE

measurement system with resonant sensors and fixed thresholds is used without visual examination of waveforms, then guard sensors will be effective only if they are placed along the direction of the propagation of structure-borne extraneous AE at a considerable distance away from the crack-monitoring sensors. This approach compensates for the arrival-time difference errors, which occur with such approaches. But this technique would not necessarily eliminate airborne extraneous AE, unless the data sensors were offset by large differences from being centered around the crack.

## 6. Conclusions

1. Extraneous waveforms from wideband sensors show significant differences in both shape and frequency content for different types of sources, whereas relatively small differences in shape and frequency content are seen in resonant-sensor waveforms from the same sources.

2. Techniques, which rely on using rise-time or frequency-spectrum discrimination to distinguish real crack-induced AE sources from extraneous sources, may be ineffective for resonant sensors.

3. A crack-induced AE source and an extraneous source can sometimes result in large shape and frequency-content differences in the wideband-sensor waveforms from the two sources, whereas in the narrowband resonant-sensor waveforms, these differences are typically relatively small.

4. Great care must be used in specimen design and spacing of sensors for spatial or guard-sensor discrimination of grip-based AE to be effective, when using threshold-based arrival times. Visual arrival-time determination or equivalent signal processing of recorded waveforms from resonant sensors can be used much more effectively for spatial discrimination of extraneous grip sources.

5. Approaches to distinguish extraneous AE from crack-induced AE with wideband sensors will need to account for sample-thickness variations and their effects on wave propagation.

6. Extraneous AE occurs in the peak-load region during fatigue cycling. Hence, load-gating is useful but not 100% effective in eliminating extraneous sources.

## Acknowledgments

This research was partially supported by the Federal Highway Administration (FHWA). The encouragement of Dr. Richard Livingston, FHWA, and Mr. Charles McCogney, FHWA (retired), is gratefully acknowledged. Technical support from Mr. Raymond Santoyo of NIST was essential to the testing of the samples.

## References

M.A. Friesel (1987), "Application of Pattern Recognition Techniques to Acoustic Emission from Steel and Aluminum," Review of Progress in Quantitative Nondestructive Evaluation, Vol. 6A, Plenum Press, New York, pp. 337-343.

C.F. Galambos and C.H. McGogney (1975), "Opportunities for NDT of Highway Structures," *Materials Evaluation*, 33(7), 168-175, 180.

A. Ghorbanpoor (1985), "Acoustic Emission Characterization of Fatigue Crack Growth in Highway Bridge Components," Ph.D. dissertation, University of Maryland, College Park, MD.

A. Ghorbanpoor and A. T. Rentmeester (1993), "Acoustic Emission Study For Evaluation of Highway Bridges," Final Report, Study No. 90-05, WI-06-93, University of Wisconsin-Milwaukee, Milwaukee, WI.

Z. Gong, E. O. Nyborg and G. Dommen (1992), "Acoustic Emission Monitoring of Steel Railroad Bridges," *Materials Evaluation*, 50(7), 883-887.

M.A. Hamstad and C.M. Fortunko (1995), "Development of Practical Wideband High-Fidelity Acoustic Emission Sensors," *Nondestructive Evaluation of Aging Bridges and Highways*, SPIE Proc., SPIE-2456, ed. Steve Chase, pp. 281-288.

M.A. Hamstad (1997), "Improved Signal-To-Wideband Acoustic/ Ultrasonic Contact Displacement Sensors for Wood and Polymers," *Wood and Fiber Science*, 29(3), 239-248.

R. K. Miller, H. I. Ringermacher, R. S. Williams, and P. E. Zwicke (1984), "Characterization of Acoustic Emission Signals (Final Report)," Report No. FHWA/RD-84/025, United Technologies Research Center, East Hartford, CT.

M. Sison, J. C. Duke, Jr., C. Clemena, and M. G. Lozev (1996), "Acoustic Emission: A Tool For The Bridge Engineer," *Materials Evaluation*, 54(8), 888-900.

S. M. Ziola and M. R. Gorman (1991), "Source Location In Thin Plates Using Cross-Correlation," *J. Acoust. Soc. Amer.*, 90(5), 2551-2556.

# Fracture-Mode Classification Using Wavelet-Transformed AE Signals from a Composite

Tetsuo Kinjo, Hiroaki Suzuki, Naoya Saito, Mikio Takemoto and Kanji Ono

## Abstract

With the aim of establishing a reliable method of AE signal classification, we examined the utility of classical matched filtering of given images (MF), matched filtering of Laplacian images (MF-LI) and Fourier phase correlation (FPC) of the wavelet transformed AE signals. Trial classification of three model objects revealed that the FPC method was superior to the others. We attempted to classify the wavelet-transformed AE signals from a model UD-GFRP by the three methods, and examined their discrimination capabilities. Classification was first attempted for 86 AE events, which were recorded using a resonant sensor and whose fracture modes had been identified by the source simulation analysis of simultaneously recorded displacement data. The FPC again was the best among the three. Detailed examination of similarity coefficients of the FPC results showed that 68 events were distinctly classified. Using the FPC, we classified another set of 600 AE events, which had been recorded without corresponding displacement sensor data. The relative population of signal types and their changes with strain were similar to those predicted by the source simulation analysis.

## 1. Introduction

Reliable AE signal classification is important in identifying the sequence of various micro-fracture processes in composite materials (Ono and Huang, 1994). Successful classification of AE signals can elucidate fracture mechanisms and leads to an improved design of advanced composite materials. Quantitative source simulation analysis of the out-of-plane displacement appears to be the most reliable signal classification scheme when it is jointly used with the P-wave radiation pattern analysis (Suzuki et al, 1996a, b). However, the source simulation analysis utilizes a low sensitivity displacement transducer with broad bandwidth signal processing and is vulnerable to noise interference.

The detection and analysis may be simplified if we can develop a signal classification method based on AE signals obtained by using more sensitive resonant sensors.

In our previous studies (Suzuki et al., 1993, 1996a,b), we demonstrated the validity of the source simulation analysis for the fracture mode classification in model and actual unidirectional GFRP specimens. In these specimens, the presence of four fracture modes is shown. In addition to this approach, we recently examined the pattern recognition analysis by using auto-regressive modeling and the wavelet transform (Suzuki et al., 1996b, c). The wavelet transform (WT) of AE signals represents the mapping in the frequency-time coordinates and therefore is also useful for signal classification. We reported that the contour map (or voice print) of wavelet coefficients was closely correlated to the four fracture modes classified by the source simulation analysis, but did not propose at that time any concrete method to classify the three-dimensional images of wavelet transformed AE signals (bird's-eye view of wavelet coefficients).

We believe that a reliable and automatic method of signal classification of the wavelet transformed AE signals is both desirable and feasible. As the 3-D projection of wavelet coefficients consists of an enormous amount of discrete data but also with many near-zero values, it is futile to use all the pixel data as the feature-characterizing parameters of a pattern (or signal types in case of AE). One useful and simple classification method is to utilize the reference patterns characteristic of each signal type. The wavelet transformed AE signals can be classified by computing the cross-correlation (or similarity coefficients) to the reference patterns, which can be correlated to the fracture mode by the source simulation and P-wave radiation analyses. In this study, we have examined three classification methods, i.e., classical matched filtering of given image (abbreviated as MF, hereafter), MF of Laplacian image (MF-LI) and Fourier phase correlation (FPC).

We first studied how these methods classify 3-D images using such model objects as circular, square and triangular columns. We found that MF-LI and FPC are superior to the classical MF. Using these methods, we classified 86 AE events whose fracture modes had been identified by the source simulation analysis. Actually, the fracture modes of 14 more events were identified by the source simulation analysis, but the resonant sensor data was unavailable. Of

---

Received 19 May 1997; in final form, 2 November 1997. Tetsuo Kinjo, Hiroaki Suzuki, Naoya Saito and Mikio Takemoto (takemoto@me.aoyama.ac.jp) are affiliated with Faculty of Science and Engineering, Aoyama Gakuin University, 6-16-1 Chitosedai, Setagaya, Tokyo 157, Japan and Kanji Ono (ono@ucla.edu) is with University of California, Los Angeles, 405 Hilgard Ave, Los Angeles, CA 90095-1595, USA.

the 86 events, 74 events were classified by the FPC method, which was better than the other two. Using some of the classified 74 events as reference, we next classified 600 AE signals, which had no corresponding displacement sensor data. The evolution of relative population of different fracture modes with strain coincided well with that expected from the source simulation analysis of the 100 AE events.

## 2. Classification Methods of Three Dimensional Image

### 2.1 Matched Filtering

This method evaluates the similarity between the reference and given images using full phase and amplitude. Measured image,  $f(x,y)$ , and reference images,  $h_i(x,y)$  (for  $i = 1$  to  $M$ ), which had been normalized by using the sum of squared values of each data point, have the unit integral values as equation (1)

$$\iint f^2(x,y)dx dy = \iint h_i^2(x,y)dx dy = 1 \quad (1)$$

The similarity coefficient  $g_i$  of the measured image  $f(x,y)$  to the reference image  $h_i(x,y)$  is formulated by integrating the product of corresponding values for  $i = 1$  to  $M$  as

$$g_i = \iint f(x,y)h_i(x,y)dx dy \quad (2)$$

Variables  $x$  and  $y$  in these equations represent the two-dimensional coordinate  $(x,y)$  of an object, but can be replaced by frequency and time for the wavelet transformed AE signals. In practice, discretized values, sampled at regular intervals,  $f_{jk}$  ( $j, k = 1$  to  $N$ ), are used to represent an image  $F$  (see Fig. 1).

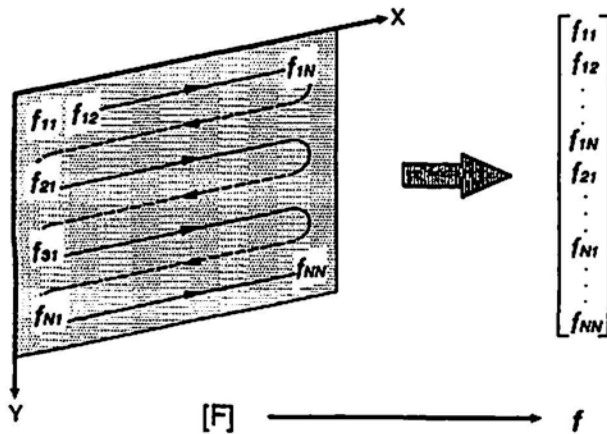


Fig. 1 Vector representation of an image.

The similarity coefficient  $g_i$  can be rewritten for  $i = 1$  to  $M$  by using a vector notation as

$$g_i = f^t h_i \quad (3)$$

Here,  $f$  and  $h$  are vectors in the  $N \times N$ -dimensional space with  $f_{jk}$  and  $h_{jk}$  as elements. From equation (1), both satisfy the following two expressions, and a superscript  $t$  indicates a transposed vector.

$$\|f\|^2 = \|h_i\|^2 = 1 \quad (4)$$

$$\|f\|^2 = f^t f \quad (5)$$

The similarity coefficient  $g_i$  is then given by equation (6), using the angle  $\theta$  between the two vectors  $f$  and  $h$  in the  $N \times N$ -dimensional space.

$$g_i = \cos \theta_i \quad (6)$$

The similarity coefficient  $g_i$  takes a value from zero to one, and becomes unity when  $\theta$  is zero, or when a given image completely matches the reference image.

We examined how simple 3-D images are classified by the MF. These objects are used as both the reference and given images, and are a circular column (represented as circle in two dimensional pattern,  $\circ$  in tables), a square column (square,  $\square$ ) and a triangular column (triangle,  $\Delta$ ), as shown in Fig. 2. The factor  $g_i$  was computed for nine combinations of these objects. Pixel number used for each image is  $30 \times 30 = 900$ . Table 1 shows the factor  $g_i$  thus determined. The  $g_i$  in the three diagonal elements are unity as expected. However, the  $g_i$  for a combination of  $\circ$  and  $\Delta$  is estimated as 0.748, and 0.875 for  $\circ$  and  $\square$  combination. The  $g_i$  for  $\Delta$  and  $\square$  combination was 0.830. The  $g_i$  values for the dissimilar objects is closer to 1.0 rather than zero, indicating that the discrimination capability of MF is poor in this example.

Table 1 The similarity coefficient  $g_i$  for simple 3-D images as classified by the MF.

		Reference image		
		$\circ$	$\square$	$\Delta$
Sample	$\circ$	1.000	0.875	0.748
	$\square$	0.875	1.000	0.830
	$\Delta$	0.748	0.830	1.000

### 2.2 Matched Filtering of Laplacian Images (MF-LI)

In this processing, Laplacian image is utilized for matched filtering. Laplacian operation of an image is expressed as equation (7), and emphasizes the edges of the original image and also islands (isolated small objects and points). This is known to be useful in classifying similar images. (Marr and Hildreth, 1980)

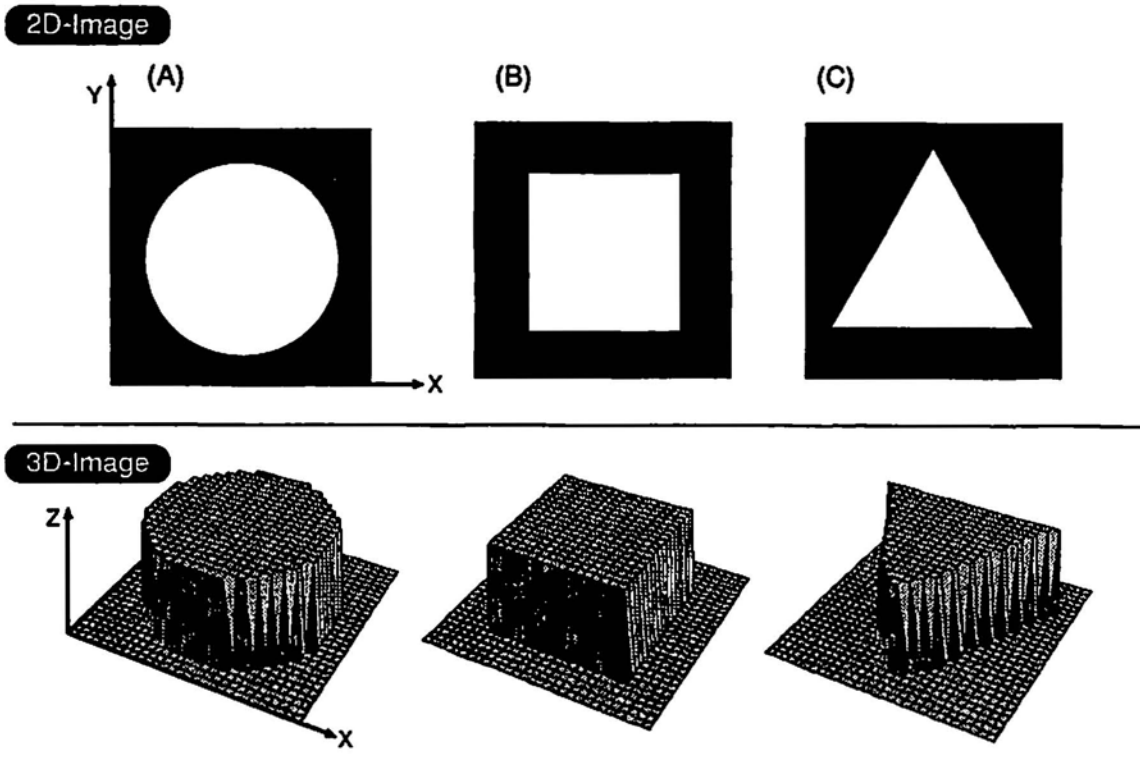


Fig. 2 2D- and 3D model objects used for comparison of classification methods.

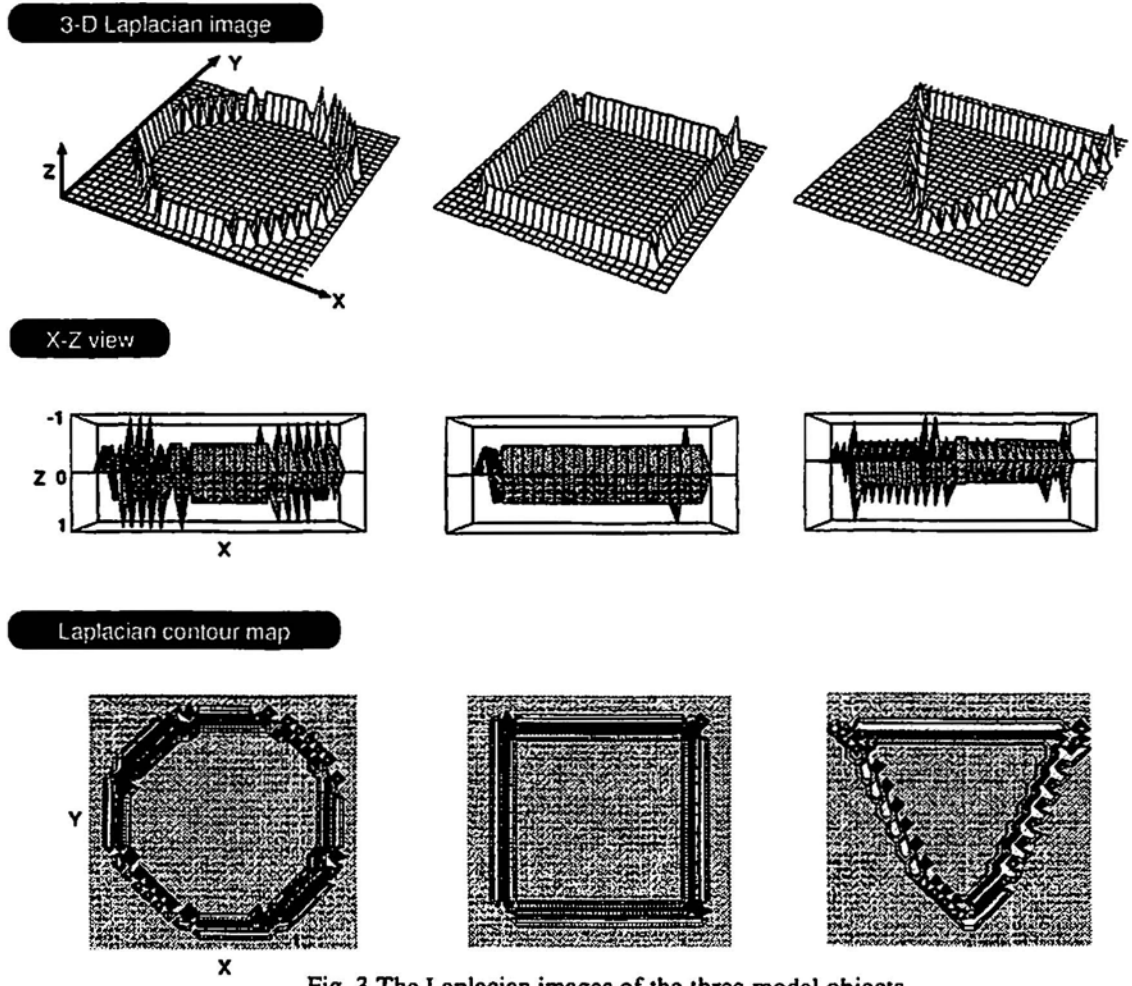


Fig. 3 The Laplacian images of the three model objects.

$$\nabla^2 f(x, y) = \frac{\partial^2 f(x, y)}{\partial x^2} + \frac{\partial^2 f(x, y)}{\partial y^2} \quad (7)$$

Shown in Fig. 3 are the Laplacian images of the three model objects. Second order differentiation gives positive and negative peaks around edges, as shown in the x-z view. Utilizing these processed images, a better classification is obtained as shown in Table 2. It is noted that the  $g_i$ 's for dissimilar objects become less than 0.2. The MF-LI appears to be superior in its discrimination capability to the classical MF method.

Table 2 The similarity coefficient  $g_i$  for simple 3-D images as classified by the MF-LI method.

		Reference image		
		○	□	△
Sample	○	1.000	0.191	0.049
	□	0.191	1.000	0.103
	△	0.049	0.103	1.000

### 2.3 Fourier Phase Correlation Method (FPC)

Horner and Gianino (1984) and Kawata et al. (1987) suggested that the phase information is significantly more important than amplitude information in preserving the features of a 3-D image. The FPC method classifies 3-D images by using only the phase information. Here, the similarity coefficient  $g_i$  is given by equation (8) using the Fourier phase images  $f^{\circ}(x, y)$  and  $h_i^{\circ}(x, y)$ .

$$g_i = \iint f^{\circ}(x, y) h_i^{\circ}(x, y) dx dy \quad (8)$$

The Fourier phase images are obtained by inverse Fourier transform ( $\mathcal{F}^{-1}$ ) of the phase terms,  $\phi_F(\xi, \eta)$  and  $\phi_{Hi}(\xi, \eta)$  by equations (9) and (10).

$$f^{\circ}(x, y) = \mathcal{F}^{-1}\{\exp[-j \phi_F(\xi, \eta)]\} \quad (9)$$

$$h_i^{\circ}(x, y) = \mathcal{F}^{-1}\{\exp[-j \phi_{Hi}(\xi, \eta)]\} \quad (10)$$

where  $j^2 = -1$  and the Fourier phase images are defined by the imaginary parts of the Fourier transformed images  $F(\xi, \eta)$  and  $H_i(\xi, \eta)$ ; i.e.,

$$F(\xi, \eta) = |F(\xi, \eta)| \exp[-j \phi_F(\xi, \eta)] \quad (11)$$

$$H_i(\xi, \eta) = |H_i(\xi, \eta)| \exp[-j \phi_{Hi}(\xi, \eta)] \quad (12)$$

The phase images are, as before, normalized according to equation (13)

$$\|f^{\circ}\|^2 = \|h_i^{\circ}\|^2 = 1 \quad (13)$$

The factor  $g_i$  takes values from  $-1.0$  to  $+1.0$ , and  $g_i = 1.0$  implies the best matching. Figure 4 shows the Fourier phase images. The top row represents the 3-D Fourier phase images of the model objects. The middle row (x-z view) represents the profile of image amplitude along x-axis. Shown in the bottom row are the contour maps of the Fourier phase images. It can be seen that the outline (periphery) is emphasized for the cylindrical and triangular columns, and the corner for the square column. Classification result by the FPC is shown in Table 3. We observed a perfect classification of  $g_i = 1.0$  for the same images (diagonal elements) and almost zero or negative for dissimilar images. The FPC is superior to the MF and appears to be better than the MF-LI method. This is expected to be valuable in classifying complicated wavelet-transformed AE images.

Table 3 The similarity coefficient  $g_i$  for simple 3-D images as classified by the FPC method.

		Reference image		
		○	□	△
Sample	○	1.000	-0.016	-0.045
	□	-0.016	1.000	0.020
	△	-0.045	0.020	1.000

Among three classification methods, the computation time for one  $g_i$  value is slightly longer for MF-LI and FPC methods than that for the MF, but even the FPC requires only 2 seconds for one pair of classification by using an engineering work station (Sun SPARC-5) for the present example.

## 3. Classification of AE Signals

We examine next the classification of actual AE signals from a composite specimen under tension using these three methods. The AE signals are separately evaluated by the source simulation analysis and identified according to their respective fracture mode.

### 3.1 AE Monitoring of a Glass-Fiber Composite Specimen

A specimen containing a bundle of 6400 E-glass fibers of 13  $\mu\text{m}$  diameter was prepared. A bundle was placed longitudinally at the center of the specimen as shown in Fig. 5. This fiber configuration is different from that of the previous specimen (Suzuki et al., 1996a) and tends to cause frequent Mode-II fiber disbonding. The epoxy matrix contains 6 parts Epicote 828 and 4 parts Epicote 878 (supplied by Shell Epoxy Co. Ltd.). We used 8 sensors and a 10-channel recording system comprised of two digitizers. Seven small resonant sensors with a small aperture diameter of 3 mm (PAC PICO) were used for channel #1 to #7. A conical element displacement sensor was used for channel #8. The displacement sensor was mounted above the reduced section

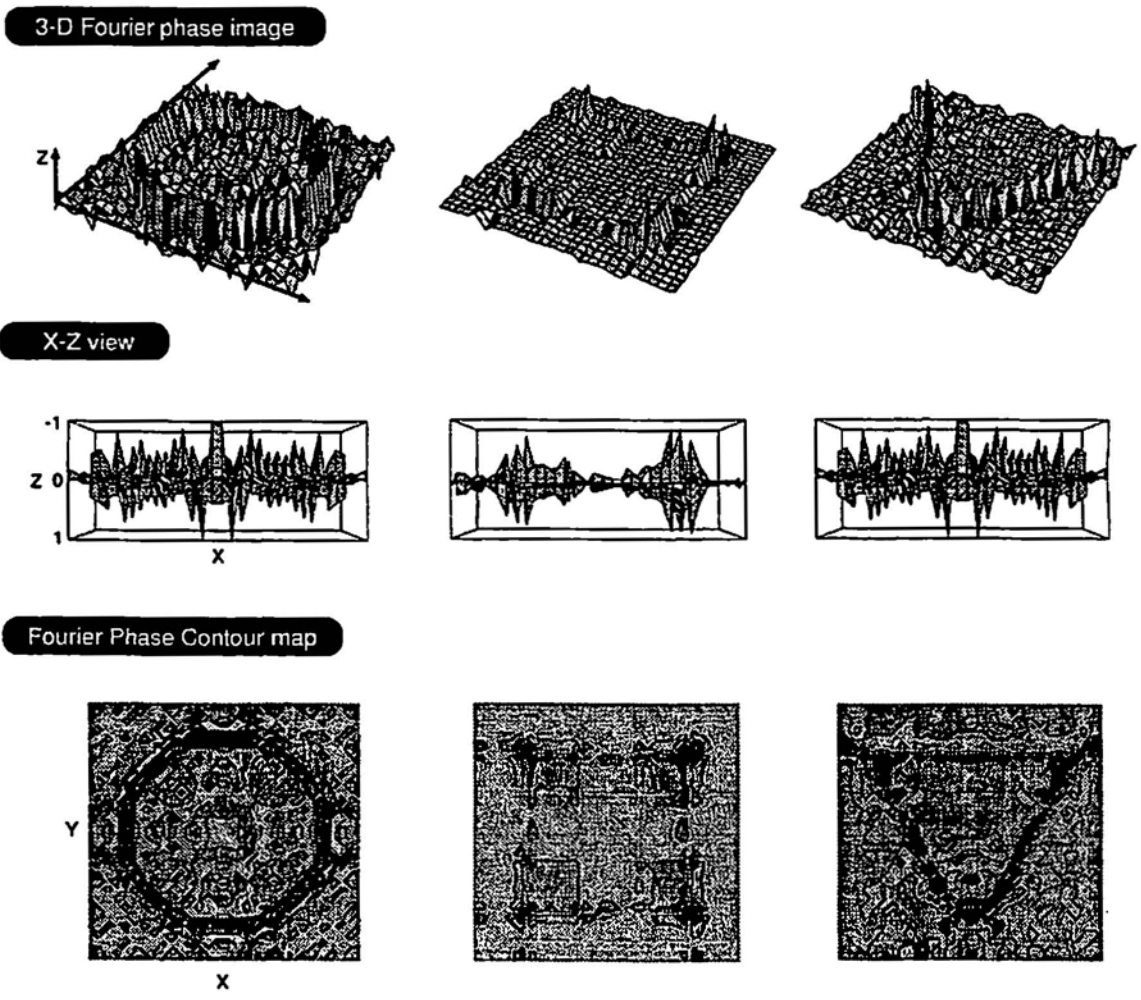


Fig. 4 The Fourier phase images of the three model objects.

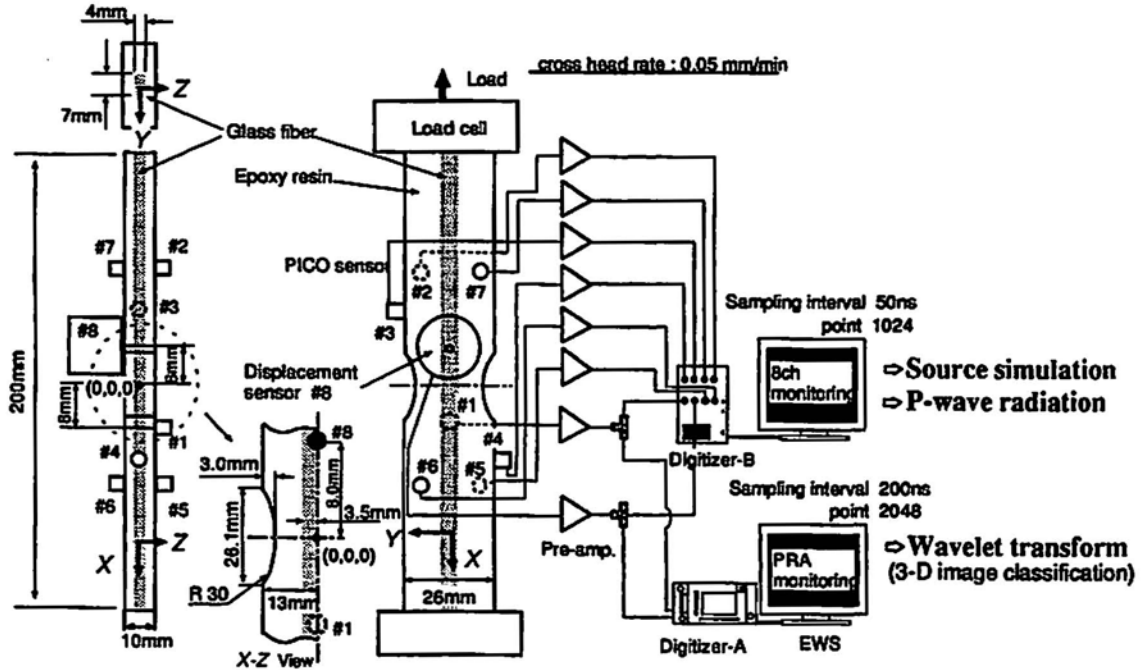


Fig. 5 The specimen configuration and experimental setup for AE signal acquisition.

while the resonant sensor #1 was placed on the opposite side, diagonally from the displacement sensor. The outputs of sensors #1 and #8 were recorded on digitizer A, following the amplification by 40-dB preamplifiers. The digitizer A operated at 200-ns sampling interval with 4096 sampling points at 8 bit. This set of data was used for the wavelet transform. The outputs from all the sensors (#1 to #8) were digitized at 50-ns interval with 1024 sampling points at 10 bit by digitizer B. The data set of digitizer B was used for the source simulation (#8) and P-wave radiation pattern analyses (#1 to #7). The system used in this research is basically the same as that reported in a previous paper (Suzuki et al., 1996b).

Signal classification by the presently proposed methods was attempted following the wavelet transformation of signals from sensor #1 (from digitizer A). Digitizer A recorded over 2,000 events. Not all these events were synchronized to those recorded by digitizer B. Of the latter, the fracture modes of 100 events were identified using the source simulation and radiation pattern analyses. 86 out of the 100 events had corresponding data for the wavelet transformation. These were examined and classified by the three proposed classification methods for 3-D wavelet-transformed signal. Subsequently, 600 events were sampled from 2000+ events. We have classified these signals using the previously classified events as reference. The results show the same trend of fracture-mode variation with strain as that of the 100 events identified by the source simulation and radiation pattern analyses

### 3.2 AE Signal Classification by the Source Simulation

Using the source simulation and P-wave radiation pattern analyses, 100 events recorded by digitizer B were classified into four types. Results of the classification as a function of strain are given in Fig. 6 along with the stress-strain

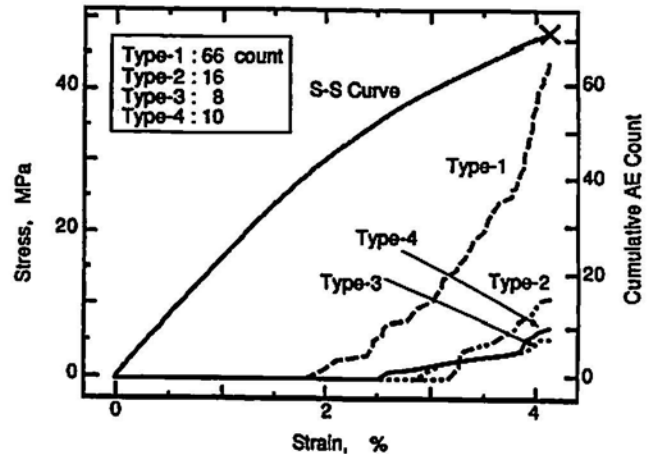


Fig. 6 The stress-strain curve and cumulative classified AE events for the 4 types of microfracture.

curve. The four fracture modes are shown in Fig. 7. Type-1 event is Mode I fracture of a fiber or the matrix, Type-2 is Mode I debonding of the fiber-matrix interface in the transverse direction, Type-3 is Mode I debonding in the thickness direction, and Type-4 is Mode II debonding, respectively. Also shown in the figure are the locations of identified AE sources. Of the 100 events, 66 events were classified as Type-1 fracture, 16 events as Type-2, 8 events as Type-3 and 10 events as Type-4 fracture.

Figure 8 compares typical waveforms for the four types detected by the displacement-sensitive sensor (#8). These are compared with the simulated out-of-plane displacement waveforms. Each was calculated following the identification of the fracture mode and source location such that the P-wave rise time ( $\Delta T_{pr}$ ) and amplitude ( $\Delta U_p$ ) as well as relative peak positions best represent the observed signal. Here, the source displacement rise time ( $\Delta T_s$ ) and source strength ( $A_b$ ) are adjusted by iteration. These values are given in Fig. 8.

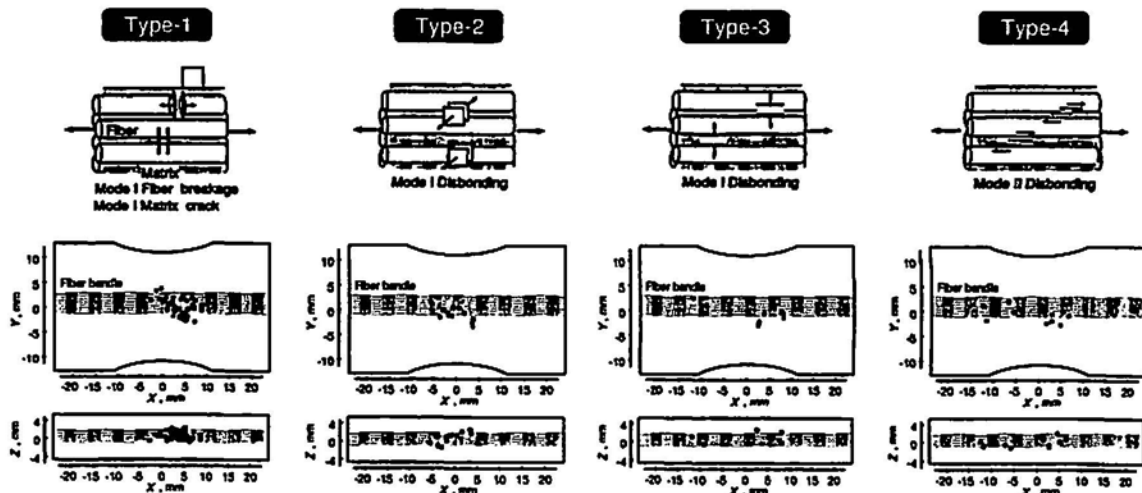


Fig. 7 Schematic representation of four fracture modes and the source location of the classified AE events.

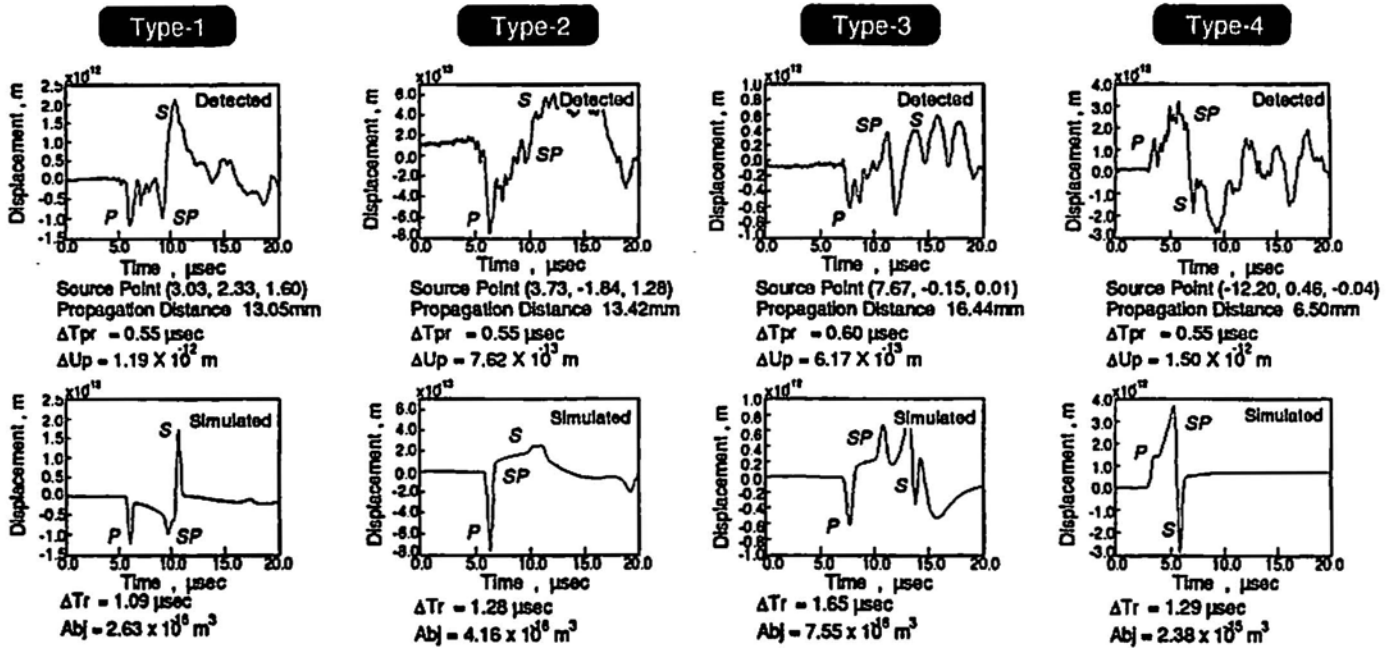


Fig. 8 Typical waveforms for the four types detected by the displacement-sensitive sensor (first row). The simulated out-of-plane displacement waveforms are shown in the second row so that the P-wave rise time ( $\Delta T_{pr}$ ) and amplitude ( $\Delta U_p$ ) as well as relative peak positions match those observed. The best fit values of source displacement rise time ( $\Delta T_r$ ) and source strength ( $Ab_j$ ) are given below the simulated waveforms.

Table 4 Three sets of the P-wave polarity (+ or -) of the 8 sensors for 9 Type-4 events.

Event No	Sensor number							
	# 1	# 2	# 3	# 4	# 5	# 6	# 7	# 8
7461	---	---	---	---	---	++-	---	+ - +
8245	+++	---	---	---	---	---	---	---
8999	---	+++	---	---	---	+++	---	+++
9560	--+	---	---	---	---	---	---	---
10771	---	---	---	---	+++	---	---	---
11114	---	+ - -	---	---	---	- - +	---	---
11137	+++	---	---	---	+++	+++	---	+++
11265	+++	---	---	---	---	- + +	---	---
11899	---	---	+++	---	---	---	---	---

The uncertainty in the classification to Type-4 fracture is larger than in the others. The most important information in classifying AE events into Type-4 or Mode-II disbonding is the four-quadrant distribution of P-wave polarity. We basically classified the events into Type-4 fracture if one of the sensors #1 to #8 indicates the P-wave polarity opposite to the other sensors. This is because the polarity changes depend on the source location and vector direction of displacement discontinuity. However, the determination of the P-wave polarity of resonant sensor output is often difficult due to low S/N ratios. Table 4 lists three sets of the P-wave polarity (+ or -) of the 8 sensors for 9 Type-4 events. The number in the left column indicates the de-

tected time in seconds and is used as signal reference number. The polarity was independently determined by three individuals. Of the nine events, they agreed completely on the polarity pattern of only four events. In the remaining cases, some differences were noted; e.g., for event 11114, only one found the polarity of sensors #2 and #6 as positive. It appears that not all the 9 events in Table 4 are really from the Mode-II disbonding. Incorrect assignments of the P-wave polarity also make an accurate source location difficult, and may result in a larger data scattering in Fig. 7. If these events can be classified correctly by wavelet transformation and 3-D image classification, a significant improvement of the signal classification accuracy is expected.

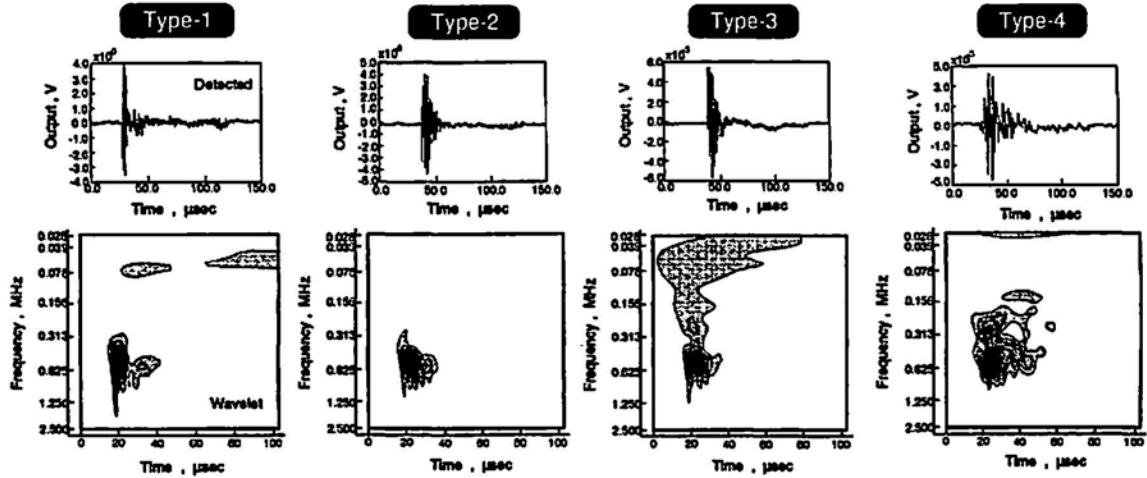


Fig. 9 Typical waveforms detected by sensor #1 and their WT images.

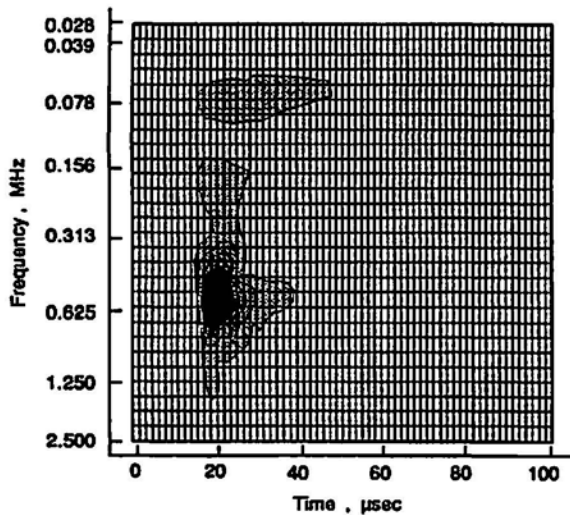


Fig. 10 The 1792 pixels used for the 3-D classification.

### 3.3 Classification of the Wavelet Transformed AE Signals by the MF, MF-LI and FPC Methods

#### 3.3.1 Reference Images

Selection of appropriate reference images is important in the proposed scheme of signal classification. AE waveforms (or their WT images) usually change with the source positions. This requires careful consideration in selecting the reference images. Typical waveforms and the WT images are shown in Fig. 9. In order to represent a range of AE signals, we selected five waveforms for each fracture mode, taking into account the time of detection and correspondence with the source simulation results. The reference images were prepared by averaging the WT images of these five. Figure 10 shows the 1792 pixels used for the 3-D classification. The pixels consist of 64 division in the time scale and 28 in the frequency scale. This level of representation appears to be adequate in characterizing the image features, although no other set of divisions has been examined.

The reference images used for the MF method are similar to the contour map of WT coefficients shown in Fig. 9. The contour maps of Laplacian images are used for the MF-LI and these are obtained by the second-order differentiation of the averaged images. The phase components are used for FPC. Examples of the images for the MF-LI and FPC classification corresponding to AE waveforms shown in Fig. 9 are shown in the middle row and the bottom row of Fig. 11, respectively. Original AE waveforms are again illustrated in the top row. Comparing the contour maps in Fig. 11 with those in Fig. 9, more small islands or craters are apparent. These may be useful in classifying the fracture modes.

#### 3.3.2 Classification of the 100 AE Events

Classification results of 100 events via source simulation analysis of the displacement data are given in the left two columns of Table 5. Signal classifications with WT were achieved for 86 events. For the remaining 14 events, the corresponding AE waveforms for WT were not recorded. Results are summarized in Table 5 (three right columns). The MF method classified 53 events into 37 as Type-1, 7 as Type-2, 4 as Type-3 and 5 as Type-4. Event percentages (shown in the parentheses) agree well with those obtained by the source simulation, but 33 events were mis-classified to other types. The MF-LI method classified 55 events, and the event counts of each fracture type are almost identical to those by MF. The FPC method classified 74 events into 53 as Type-1, 10 as Type-2, 6 as Type-3 and 5 as Type-4, with 12 mis-classified events. Percentages of the classified events by the FPC are again similar to those by the source simulation. These results indicate that the FPC method is superior to the other two methods because it classified more events of Types 1 to 3 and has less misclassification.

Even with the FPC method, however, we still have 14% misclassification. With respect to Type 4 events, the situation is worse. Thus, we further examined the corre-

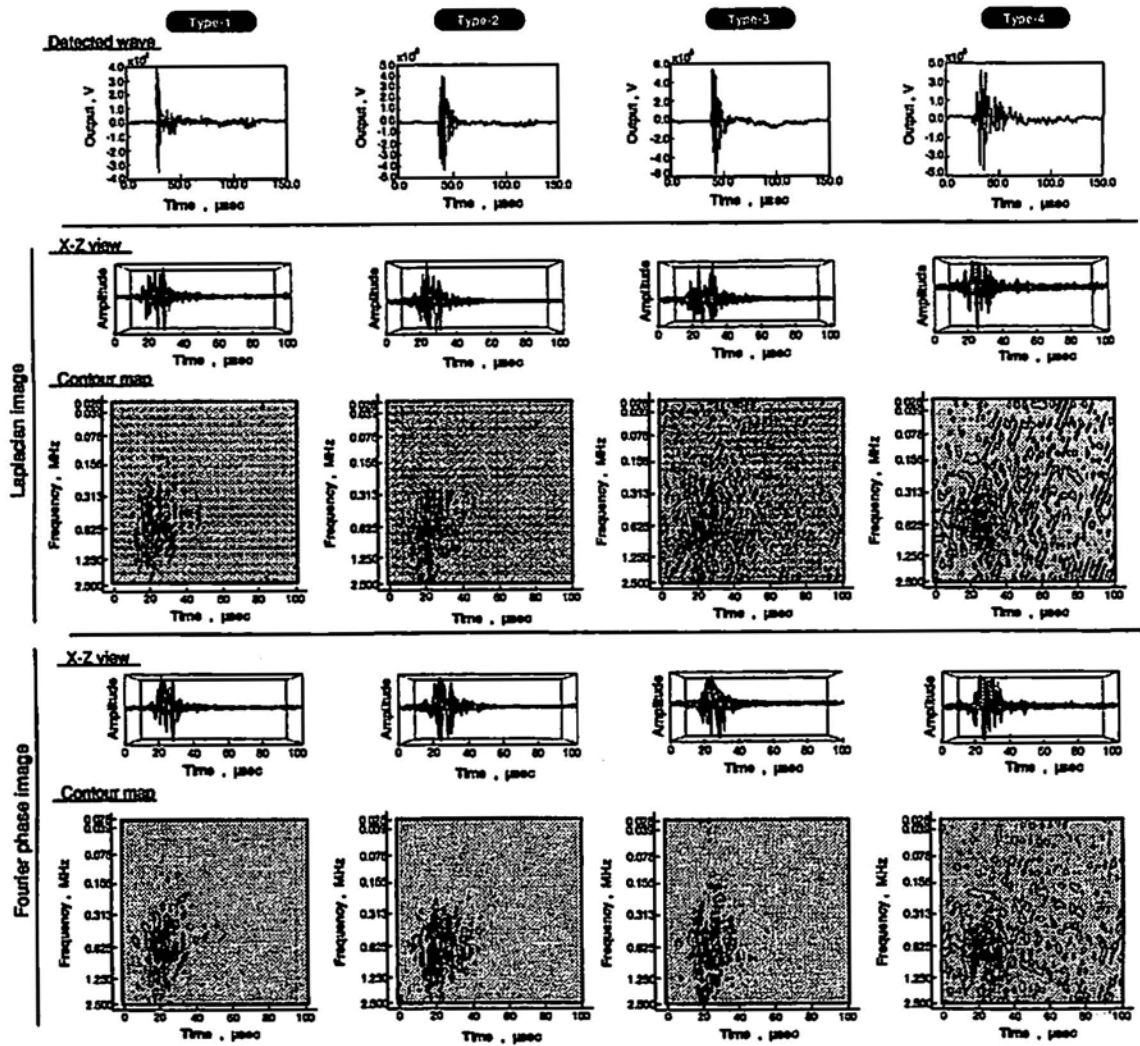


Fig. 11 Original AE waveforms from sensor #1 are in the top row. The images for the MF-LI and FPC classification corresponding to these AE waveforms are given in the middle row and the bottom row.

Table 5 Classification results of 100 events via source simulation analysis of the displacement data and three classification methods.

Source simulation	MF	MF-LI	FPC
Type-1	66 ( 66 %)	37 ( 70 %)	53 (72 %)
Type-2	16 ( 16 %)	7 ( 13 %)	10 (14 %)
Type-3	8 ( 8 %)	4 ( 8 %)	6 (8 %)
Type-4	10 ( 10 %)	5 ( 9 %)	5 (6 %)
Classified events	100 ( 100 %)	53 ( 100 %)	55 (100 %)
Others *	0	33	12
Total	100	86	86

\* events classified to another fracture type.

spondence between the source simulation and FPC. Table 6 compares the correspondence of 86 events classified by both the source simulation method (in the left column) and FPC method. The next 4 columns represent how many events,

originally classified by the source simulation, are classified to another fracture mode by the FPC. Fracture mode by FPC is shown in the top row as Type-X\*ref with X being 1 to 4. Among 57 events originally classified as Type-1 by

Table 6 Comparison of the correspondence of 86 events classified by both the source simulation method (in the left column) and FPC method.

Source simulation	Type-1 * ref	Type-2 * ref	Type-3 * ref	Type-4 * ref
Type-1 : 57	53	4	0	0
Type-2 : 13	2	10	0	1
Type-3 : 7	1	0	6	0
Type-4 : 9	3	0	1	5
Total : 86	59	14	7	6

Table 7 The FPC-determined  $g_i$  of 57 Type-1 events.

	Time, s	Type-1	Type-2	Type-3	Type-4
⊙	5512	0.591	0.088	0.292	0.244
⊙	6021	0.570	0.466	0.428	0.352
⊙	6250	0.685	0.654	0.568	0.351
⊙	6990	0.597	0.096	0.227	0.238
⊙	7093	0.287	0.169	0.128	0.044
⊙	7149	0.500	0.024	0.243	0.334
△	7159	0.418	0.411	0.257	0.263
⊙	7410	0.560	0.157	0.204	0.170
△	7417	0.424	0.412	0.241	0.267
△	7542	0.406	0.292	0.357	0.310
×	8175	0.062	0.311	-0.006	-0.003
⊙	8293	0.293	0.030	0.135	0.083
⊙	8528	0.379	0.190	0.196	0.271
R ⊙	8792	0.603	0.132	0.422	0.112
R ⊙	8794	0.430	0.082	0.171	0.125
R ⊙	8915	0.657	0.190	0.289	0.211
R ⊙	8948	0.375	0.060	0.164	0.058
×	9182	0.424	0.441	0.359	0.162
⊙	9340	0.409	0.079	0.122	0.128
⊙	9383	0.261	0.009	0.159	0.020
⊙	9584	0.520	0.405	0.228	0.341
R ⊙	9750	0.703	0.233	0.283	0.181
⊙	9768	0.721	0.114	0.386	0.133
⊙	9788	0.721	0.114	0.386	0.133
⊙	10132	0.368	0.078	0.130	0.166
⊙	10199	0.560	0.333	0.283	0.384
×	10220	0.295	0.357	0.300	0.195
⊙	10291	0.576	0.106	0.268	0.191
⊙	10358	0.527	0.227	0.320	0.210
⊙	10477	0.646	0.128	0.332	0.182
⊙	10568	0.340	0.229	0.257	0.063

the source simulation (9 more did not have the corresponding AE waveform for WT), 53 events were classified as Type-1 by the FPC method, but 4 events were misclassified as Type-2. Two or one event belonging to Type-2 or -3 was mis-classified to Type-1. Disagreement was most apparent for Type-4 (Mode-II fiber disbonding). Only

Table 7 The FPC-determined  $g_i$  of 57 Type-1 events. (cont.)

	Time, s	Type-1	Type-2	Type-3	Type-4
⊙	10874	0.393	0.276	0.245	0.196
△	10887	0.237	0.214	0.068	0.081
⊙	11004	0.538	0.130	0.311	0.194
△	11034	0.284	0.067	0.280	0.087
⊙	11084	0.585	0.172	0.304	0.222
⊙	11186	0.694	0.098	0.401	0.154
⊙	11226	0.682	0.112	0.388	0.187
⊙	11229	0.620	0.289	0.299	0.378
⊙	11281	0.644	0.077	0.453	0.190
⊙	11291	0.647	0.379	0.290	0.349
△	11349	0.496	0.428	0.314	0.344
⊙	11390	0.508	0.106	0.395	0.147
⊙	11395	0.359	0.114	0.236	0.134
⊙	11403	0.715	0.149	0.458	0.248
⊙	11437	0.672	0.204	0.320	0.260
×	11441	0.289	0.475	0.298	0.112
⊙	11452	0.505	0.102	0.340	0.311
⊙	11541	0.755	0.156	0.397	0.181
⊙	11561	0.685	0.282	0.262	0.262
⊙	11573	0.700	0.131	0.408	0.228
⊙	11596	0.521	0.113	0.346	0.302
⊙	11772	0.500	0.401	0.288	0.353
⊙	11868	0.646	0.115	0.341	0.152
⊙	11879	0.608	0.256	0.364	0.204
⊙	11929	0.465	0.322	0.171	0.402
⊙	11944	0.725	0.181	0.406	0.198

five events remain as Type-4, but 3 events were mis-classified to Type-1 and one event to Type-3.

Next, we examined the factor  $g_i$  of all events, because this data may show the reasons of mis-classification and establish the discrimination limit of the FPC. Table 7 shows the FPC-determined  $g_i$  of 57 Type-1 events. Letter "R" (for 5 events) in the left-most column implies that the signals were used as the reference image. The symbols in the second column indicate the following:

⊙ = well classified;

Δ = classified correctly, but  $g_i$  value for another type is close;

X = mis-classified to the another type.

Number in the third column indicates the signal number (detection time). The well classified ⊙-events total 47. Six Δ-events indicated Type-1, even though their  $g_i$  values were close to those of Type 2 or 3 and the highest  $g_i$  of these events were less than 0.5. Four signals indicated by X were mis-classified as Type-2. The waveforms are significantly distorted and this appears to be the cause of misclassification. The  $g_i$  values of 13 Type-2 events are shown in Table 8. Ten ⊙-events give correct classification and two X-events were mis-classified to Type-1 and one to Type-4. Table 9 for seven Type-3 fracture events indicates that one X-event was mis-classified to Type-1, but six others were classified correctly. Table 10 for the classification of Type-4 events indicates five ⊙-events with correct classification, while three X-events of Type-1 and one X-event as Type-3.

Table 8 The FPC-determined  $g_i$  of 13 Type-2 events.

		Time, s	Type-1	Type-2	Type-3	Type-4
	⊙	9448	0.276	0.566	0.226	0.060
	⊙	9468	0.210	0.548	0.168	0.051
R	⊙	9488	0.399	0.487	0.303	0.126
	⊙	10249	0.222	0.556	0.194	0.072
R	⊙	10521	0.019	0.735	0.064	0.026
	⊙	10782	0.190	0.355	0.102	0.044
	X	10982	0.737	0.168	0.418	0.179
R	⊙	11057	0.138	0.423	0.087	0.070
	X	11241	0.115	0.335	0.139	0.350
	X	11505	0.679	0.174	0.372	0.176
R	⊙	11636	0.434	0.502	0.286	0.381
R	⊙	11636	0.038	0.665	0.107	-0.067
	⊙	11884	0.107	0.257	-0.019	-0.001

The detailed examination of these  $g_i$  values indicates more cases of potential misclassification or uncertain classification. Excluding marginal events, 47 Type-1, 10 Type-2, 6 Type-3 and 5 Type-4 events can be unambiguously classified; i.e., 68 out of 86 events. The main reason appears to be the small number of events for each type (with the possible exception of Type 1). It is also possible that the results of classification based on the source simulation analysis of the displacement data contain uncertainty. Thus, the limit of the FPC method needs to be tested with a larger data population.

In order to eliminate the marginal event classification (as in the case of six Δ-events indicating Type-1), an additional step of setting the lower limit of acceptable  $g_i$  values can be used. The ratio of the highest to the second highest

Table 9 The FPC-determined  $g_i$  of 7 Type-3 events.

		Time, s	Type-1	Type-2	Type-3	Type-4
R	⊙	8438	0.436	0.193	0.500	0.247
	⊙	8762	0.311	0.252	0.464	0.078
R	⊙	9006	0.115	0.112	0.332	0.199
R	X	9917	0.433	-0.046	0.345	0.122
R	⊙	10823	0.175	0.110	0.442	0.262
	⊙	11393	0.249	0.049	0.303	0.110
R	⊙	11679	0.312	0.082	0.701	-0.017

Table 10 The FPC-determined  $g_i$  of 9 Type-4 events.

		Time, s	Type-1	Type-2	Type-3	Type-4
	X	7461	0.598	0.144	0.281	0.248
R	⊙	8245	0.191	0.025	0.111	0.399
	X	8999	0.742	0.681	0.586	0.344
R	⊙	9560	0.231	0.043	0.210	0.685
R	⊙	10771	0.179	0.094	0.102	0.497
	X	11114	0.349	0.145	0.355	0.028
R	⊙	11137	0.114	0.084	0.042	0.306
R	⊙	11265	0.094	0.078	0.062	0.431
	X	11899	0.773	0.192	0.428	0.180

$g_i$  values may also be useful. In regard to the larger scatter in Type-4 analysis, the UD-GFRP sample used in this study emitted only a limited number of Type-4 events and with lower S/N ratios. The source positions were also distributed more than the other types. These made correct classification difficult. In another study using a UD-GFRP sample with a different fiber arrangement, we observed more frequent Type-4 events with higher S/N ratios. In that case, the proposed FPC method classified all types of events better including Type-4. This result will be reported elsewhere.

### 3.3.3 Classification of 600 Events by FPC Method

From 2000 events recorded by digitizer A, we selected 600 events by picking one event from every 3 (or 4 when the third event is evidently noise) events in time sequence. This is because of the limitation in the signal processing capability. The same reference images as those used in the previous section are employed except that for Type-3. As the signal 9917 (Table 9) was found to be inappropriate as a reference pattern, we omitted this signal.

By using the FPC method, these 600 events were classified to 364 Type-1, 151 Type-2, 44 Type-3 and 41 Type-4 events. Due to the pre-selection process, no noise event

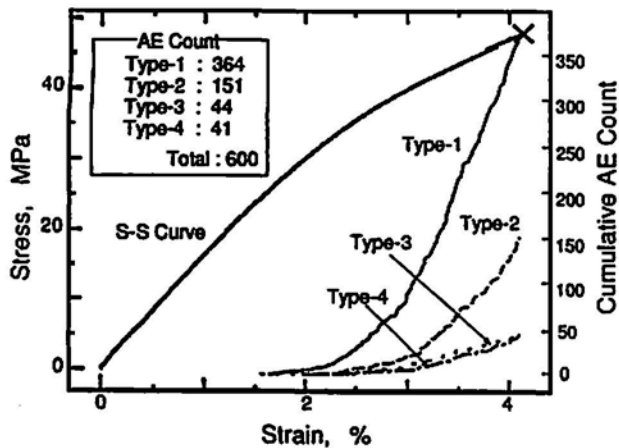


Fig. 12 Cumulative AE counts of each fracture mode as a function of strain. Classified by the FPC method using sensor #1 data. The stress-strain curve is also given.

was included. Cumulative AE counts of each fracture mode are shown in Fig. 12 as a function of strain. Comparing this figure with Fig. 6, we find the general strain dependence of each fracture mode is similar to that revealed by the analysis of 100 events. However, the present FPC analysis of 600 events showed higher occurrence of Type-2 fracture (25% of the total) than previously found (15-16%). This resulted from the reduction of Type-1 (70% down to 60%). Since the number of events analyzed is larger, the present results are probably more representative.

The variation of  $g_i$  values for the four types are shown in the percentage histograms of Fig. 13. Histogram peak for Type-1 event is located at higher  $g_i$ , compared to those of other types. We found only 19 Type-1 events (5%) whose  $g_i$  values were lower than 0.4. For Type 2, the  $g_i$  distributed over a wider range from 0.3 to 0.8. Type 3 appears to be well classified because of their relatively higher  $g_i$  values. For Type 4, most  $g_i$  values are lower than 0.5. This may be due to the fact that the waveform of Type 4 (Mode-II disbonding) is significantly affected by the source location as noted previously.

In classification, the relative  $g_i$  values are more important than the absolute values; i.e., how is a given  $g_i$  value different from the nearest  $g_i$  value(s) of other types. Figure 14 compares the change of the maximum  $g_i$  value for Type-4 (the upper solid line) and nearest  $g_i$  (the lower broken line) with the time of detection. In the figure, the numbers (1 to 3) next to the nearest  $g_i$  indicate the other fracture types. Although the absolute value of the maximum  $g_i$  slightly decreases with time, the ratio of the maximum  $g_i$  to the nearest  $g_i$  is higher than 1.4 for 15 of 41 events. These events are indicated by  $\odot$  and undoubtedly are of Type-4.

Changes of the  $g_i$  values for Types-1, -2 and -3 with test time are shown in Fig. 15. The events with  $g_i$  values lower than 0.3 (8 events for Type-1, 10 events for Type-2

and 2 events for Type-3) should basically be omitted because of their ambiguous discrimination. However, these events constitute only 7% of the classified events and do not affect the general conclusion. The ratio of the maximum to the nearest  $g_i$  is usually higher than 1.4 for Types-1 to -3. This implies that the classification for Mode-I fracture is reliably performed by the FPC method. This is expected as the source positions of Mode-I fracture are more localized.

#### 4. Conclusion

In order to classify AE signals from composite materials, we examined their wavelet transforms as images via three methods; i.e., the matched filtering of a given image (MF), that of the Laplacian image (MF-LI) and that of the Fourier phase correlation (FPC). Results are summarized below:

1) Eighty six (86) AE events from a resonant sensor were classified by the three proposed methods. These were compared with the fracture modes determined by the source simulation analysis, which classified a larger set of 100 events. The FPC method was superior to the others in its higher classification counts and discrimination capability. Most AE events were successfully classified to the fracture modes deduced by the source simulation; however, classification was difficult for Type-4 events with a small population and varying source positions.

2) Classification of 600 events, monitored by a resonant sensor but had no corresponding recordings of the displacement-monitoring system, revealed that the occurrence of each fracture mode agrees reasonably well with that predicted by the source simulation analysis of 100 events. Similarity coefficients,  $g_i$ 's, are generally above 0.5 and/or far from the nearest  $g_i$ 's (with ratios of 1.4 or more). The FPC method was demonstrated to be capable of classifying the complicated fracture modes in composite materials. However, the present method needs a faster computer processing speed with a large memory capacity. Faster wavelet-transform algorithms and more efficient processing of WT data are desirable for near real-time analysis of AE data.

#### Acknowledgment

We gratefully acknowledge the assistance Mr. Y. Haruoka. The authors also thank Showa Highpolymer Co. for providing us with epoxy resin and to Teitsu Densi Co. for a special PZT sensor.

#### References

Joseph L. Horner and Peter D. Gianino (1984), "Phase-only Matched Filtering", *Applied Optics*, 23(6), 812-816.

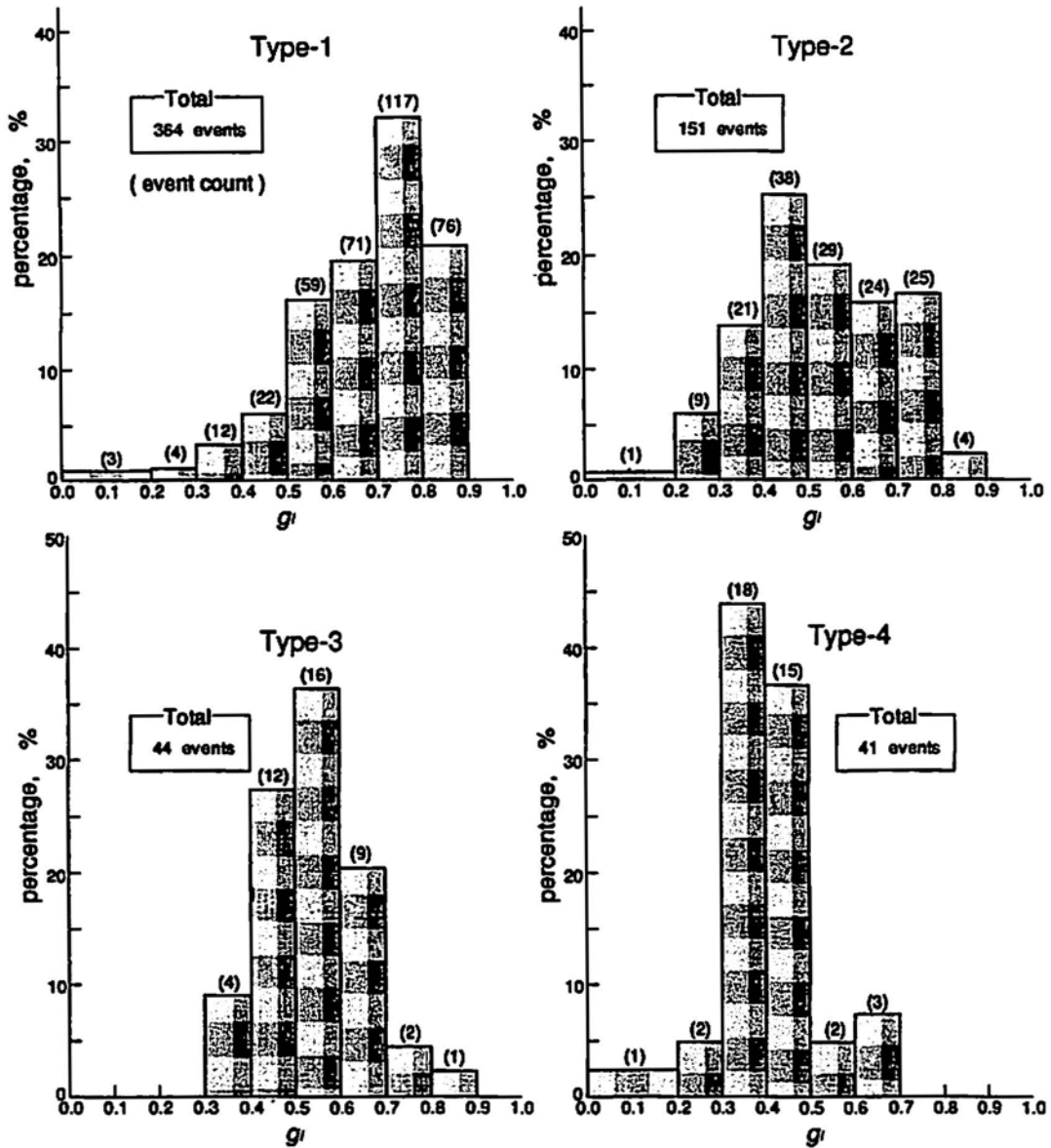


Fig. 13 Percentage histograms of  $g_i$  for the four fracture modes.

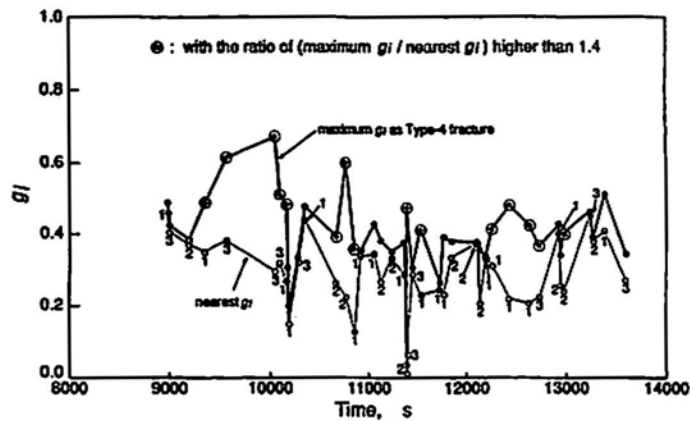


Fig. 14 Temporal variation of the maximum value of  $g_i$  (thick line) and the nearest values for Type-4 fracture.

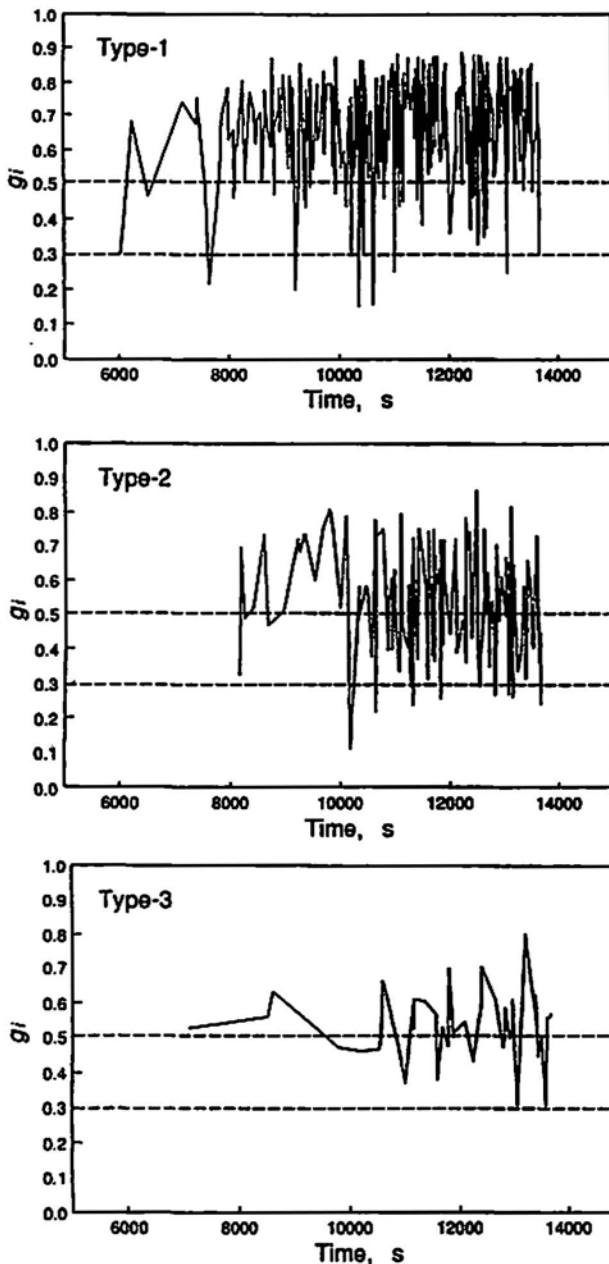


Fig. 15 Change in time of  $g_i$  values for Types 1-3 fracture.

S. Kawata, T. Noda and S. Minami (1987), "Spectral Searching by Fourier-Phase Correlation", *Applied Spectroscopy*, 41(7), 1176-1182.

D. Marr and E. Hildreth (1980), "Theory of Edge Detection", *Proc. Roy. Soc. London, Ser. B*, B207, 187-217.

Hiroaki Suzuki, Mikio Takemoto and Kanji Ono (1993), "A Study of Fracture Dynamics in a Model Composite by Acoustic Emission", *J. Acoustic Emission*, 11(3), 117-128.

Hiroaki Suzuki, Mikio Takemoto and Kanji Ono (1996a), "The Fracture Dynamics in a Dissipative Glass-Fiber/Epoxy Model Composite with AE Source Wave Analysis", *J. Acoustic Emission*, 14(1), 35-50.

Hiroaki Suzuki, Tetsuo Kinjo, Mikio Takemoto and Kanji Ono (1996b), "Fracture-mode determination of glass-fiber composites by various AE processing", *Progress in Acoustic Emission VIII*, eds. T. Kishi et al., JSNDI, Tokyo, pp. 47-52.

Hiroaki Suzuki, Tetsuo Kinjo, Yasuhisa Hayashi, Mikio Takemoto and Kanji Ono, with Appendix by Yasuhisa Hayashi (1996c), "Wavelet Transform of Acoustic Emission Signals", *J. Acoustic Emission*, 14(2), 69-84.

# Nondestructive Evaluation of Fiberglass-Reinforced Plastic Subjected to Localized Heat Damage Using Acoustic Emission

H. Nayeb-Hashemi, P. Kisnomo and N. Saniei

## Abstract

Fiberglass-reinforced composites are extensively used in electronic and aerospace applications due to their high specific strength. In these applications, they are often subjected to localized heat damage due to various sources such as electronic over heating, electric arcing, and laser beams. In order to ensure their reliability, it is important to predict their residual properties using nondestructive evaluation techniques. Unidirectional fiberglass composite specimens were manufactured using three layers of a fiber-glass prepreg. Some of the specimens were subjected to a localized heat damage using a heated copper tip with a diameter of 12.5 mm at 360°C and other specimens were subjected to a laser beam operated at 0.64 W/mm<sup>2</sup> for various exposure time. In addition, the number of laser-damaged spots varied among similar specimens. The specimens were then subjected to tension tests while acoustic emission (AE) activities of specimens were collected.

The AE activity of all specimens showed three distinct regions. An early activity, followed by a relatively dormant activity period and a high exponential activity before final failure. The period of the dormant activity was independent of the contact heat duration of less than 15 min. However, the dormant period for the laser-damaged specimens was a function of the number of laser-damaged spots. The majority of the early activities for all specimens were related to mechanisms other than fiber fracture. The activity in the dormant period for contact heat damage was mainly controlled by the fiber fracture, while for the undamaged and laser-damaged specimens was still by the interfacial failure. This could be justified since laser-damaged specimens contained numerous damaged fibers leading to a significant interfacial shear stress. The failure modes of specimens further supported this conclusion. The state of the damage in the composite was predicted using the AE-stress delay concept.

Received 20 May 1997; in final form, 20 February 1998. H. Nayeb-Hashemi (hamid@coe.neu.edu) and P. Kisnomo are affiliated with Department of Mechanical, Industrial and Manufacturing Engineering, Northeastern University, Boston, MA 02115 and N. Saniei is with Department of Mechanical and Industrial Engineering, Southern Illinois University, Edwardsville, Illinois, USA.

## 1. Introduction

Fiberglass-reinforced plastics have been used extensively in manufacturing components used in aerospace applications, electronic boards, pressure vessels, etc. In these applications they may be subjected to undesired localized heat damage. In order to ensure the reliability of these components, their residual properties should be investigated using an effective nondestructive evaluation technique.

Nondestructive evaluation of fiber composites using wave propagation has resulted in a variety of techniques for intrinsic property determination. In addition to typical examples of wave propagation velocity and attenuation measurements and the use of these values to compute elastic and damping constants (Kraui, 1963; Achenbach, 1973), the work by Vary and coworkers (1979a,b), Vary (1987a,b) and Nayeb-Hashemi et al. (1985, 1994) have indicated that because the presence of micro-flaws reduces the wave propagation efficiency of composites, it may be possible to correlate efficiency parameters with strength parameters. Their initial efforts have focused on an ultrasonically measured quantity called stress wave factor. Henneke and co-workers (1987, 1990) introduced several moments of the frequency spectrum as wave propagation efficiency. They related these parameters to the composite properties.

Acoustic emission is another nondestructive evaluation technique, which has been shown to have potential for predicting the structural integrity of composites. Possible AE sources are fiber fracture, fiber matrix debonding, fiber/fiber rubbing, matrix deformation and failure etc. In addition to predicting the residual strength of the composite, acoustic emission can indicate the source of the energy emission and thus the damage mode. Williams and Lee (1978) have provided an extensive review of the literatures on the early AE studies of fiber reinforced plastics. They concluded that events corresponding to the fiber fracture have high amplitude with small event duration. In contrast, events corresponding to fiber pull out and fiber/fiber rubbing have low amplitudes with long event duration.

Laksimi et al. (1994) investigated the damage and failure mechanisms in a glass-fiber/epoxy composite specimens with and without a hole under monotonic tensile loading. The damage initiation and failure mechanisms were studied

by means of scanning electron microscopy and AE monitoring. It was found that the amplitude distribution of AE signals is an efficient tool for identifying damage mechanisms such as micro-cracking in the resin, fracture and friction of the interface between fiber and matrix, and fiber pull-out.

Despite this body of information, there is relatively little research on the applicability of the above techniques in evaluating the residual properties of composites subjected to heat damage. Kerr and Haskin (1984) studied the effects of prolonged aging at temperature of 394-561K on the mechanical properties of unidirectional S3501 graphite/epoxy and HT-S/710 graphite polyamide composites. The results showed that the loss in mechanical properties during thermal aging are related to both degradation of the resin matrix and to a lesser extent to the graphite reinforcing fiber. Since tensile strength is a fiber-dominated property, a post-exposure tensile test was probably not the best choice for evaluating the effects of thermal aging. A test that measured the matrix strength would undoubtedly have given results more indicative of the degree of the material degradation.

Carrol et al. (1993) investigated the effect of 1-min.-contact exposure at temperature of 427°-650°C on the flexural properties of a graphite/epoxy composite. Four different techniques were used to evaluate the residual properties of the composite specimens. It was found that C-scan ultrasonic testing is the most accommodating to variations in response to heat exposure within a specimen.

In a recent paper, Fisher et al. (1995) evaluated the damage caused by subjecting graphite fiber reinforced polymer composite to high temperatures, using a laser-induced fluorescence technique. They showed that the heat damaged material exhibits significant changes in fluorescence intensity and in the wave length of maximum fluorescence intensity. The extent of thermal damage was quantified by measuring the shift in the high intensity wavelength.

The above investigations have all focused on the degradation of composites when the entire composite was subjected to high temperature. The purpose of this paper is to evaluate the degradation of the composite specimen subjected to a localized heat damage using both mechanical testing and acoustic emission.

## 2. Experimental Procedures

### 2.1 Material

The material used in this investigation is an E-glass fiber-reinforced epoxy provided in the form of prepreg by the 3M company. Three layers of prepreg was laid in a mold to form a unidirectional composite plate of 0.64 mm thickness. The composite was cured at 78°C under 96 kPa pressure for 1 hr and air cooled under pressure before being removed from the mold. The volume fraction of the fiber was

evaluated and found to be 52-57%. The composite plate was then cut in the direction of fibers to make specimens of 12.5 mm width. Aluminum end-tabs were attached to the specimen with a Loctite 404 adhesive.

To produce the heat damage, some specimens were exposed to 0.64 W/mm<sup>2</sup> laser beam for 5 min. This produced a damage spot of about 2 mm in diameter. The number of laser-damaged spots varied from 1 to 5. Some of the specimens were subjected to the contact heat damage using a heated copper tip with the contact diameter of 12.5 mm. The temperature of the copper tip was maintained during contact at 360°C using a temperature controller. The contact time was varied from 1 to 60 min. Figure 1 shows a schematic diagram of specimens.

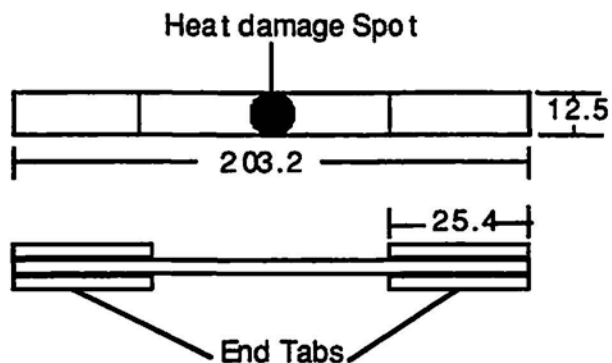


Fig. 1 Schematic diagram of composite specimens. All dimensions in mm

### 2.2 Acoustic Emission Experiment

Acoustic emission experiments were conducted using an AET 5500 system. Two AE transducers, each with the center frequency of 175 KHz (AC-175L), were utilized to detect the events emitted from the specimen at a distance of 25.4 mm apart with the damage center located at the mid distance. Each sensor was coupled with the workpiece through a couplant and held in position with the aid of 4 stiff spring as shown in Fig. 2. Data collection was focused on the damage region only and all other AE activities were discarded. AE event locations were established using the difference in the arrival times of the signals received by the two sensors. Calibration was performed using pencil-lead fracture according to the ASTM standard (ASTM, 1994). Some of the parameters measured during the tensile tests were as follows; peak amplitude in decibels, events duration and rise time in  $\mu$ s, AE (ring-down) counts, and AE energy. The detected signals were pre-amplified 60 dB with a total system gain of 70 dB. A floating threshold of 0.3 V was chosen to eliminate the background noise.

All tensile tests were performed using a servo-hydraulic tensile machine under stroke control of 2.5  $\mu$ m/s. This slow loading rate was in order to increase AE sensitivity and to

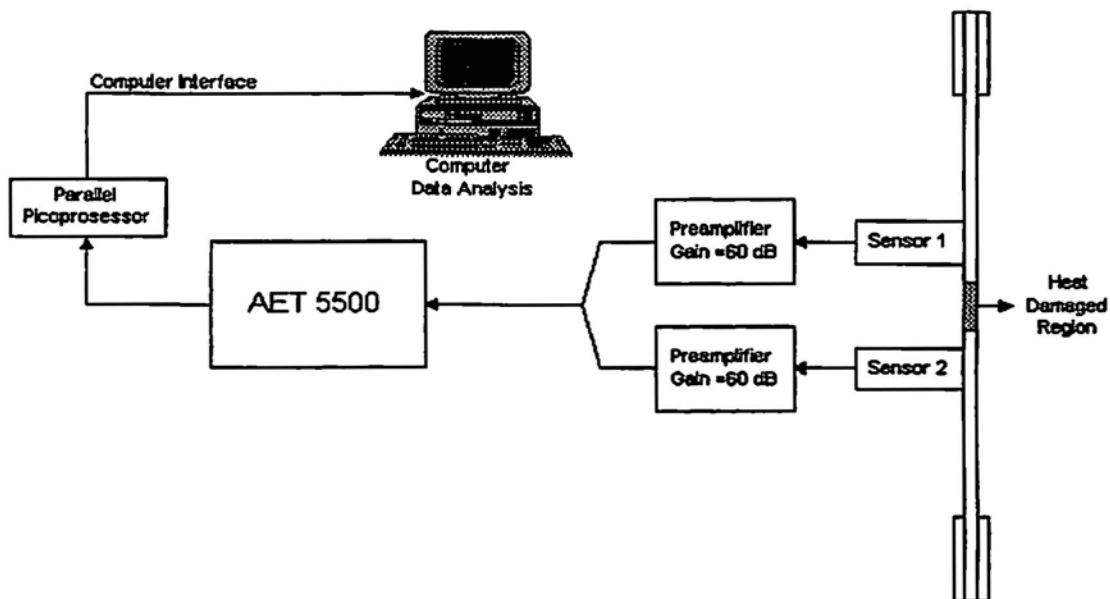


Fig. 2 Schematic diagram of AE data acquisition system.

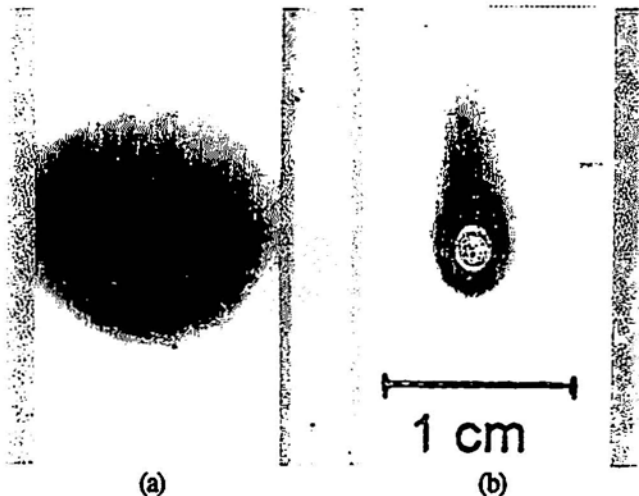


Fig. 3 Photograph of two damaged specimens: (a) contact heated and (b) laser damaged.

prevent AE event pile-up. It is possible that several simultaneous events to appear as one or several subsequent events to be missed if the loading rate is too high.

### 3. Results and Discussions

Figure 3 shows a typical composite with laser- and contact-heat damage. Although visual examination may show more discoloration of specimens with the contact-heat damage, the scanning electron microscopy of the damaged area revealed that the damage was mostly confined to the matrix material while for the laser-damaged specimens both matrix and fibers were damaged, as shown in Figs. 4 and 5. Specimens subjected to prolonged contact-heat damage showed extensive char formation and blistering, while this was not observed in the laser-damaged specimens.

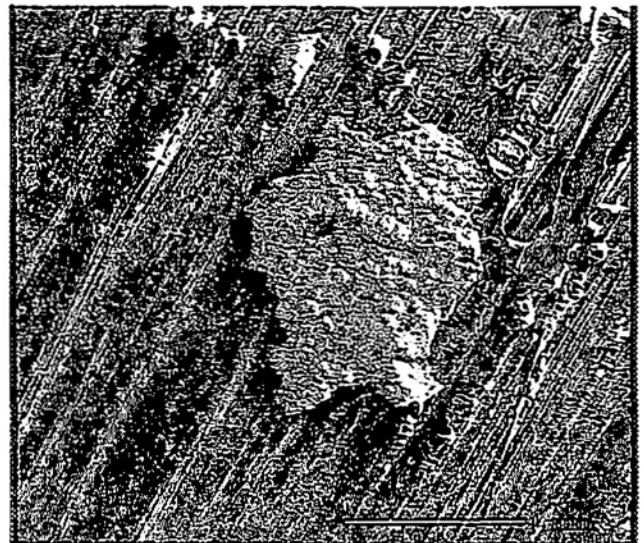


Fig. 4 SEM photo-micrograph of a contact heat damaged specimen. White bar indicates 1 mm.

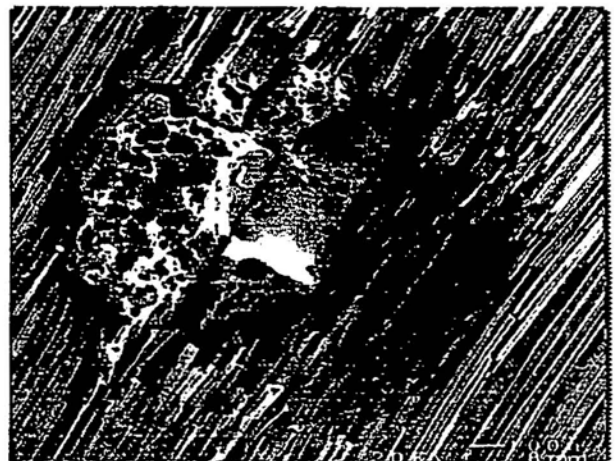


Fig. 5 SEM photo-micrograph of a laser-heat damaged specimen. White bar indicates 100 μm.

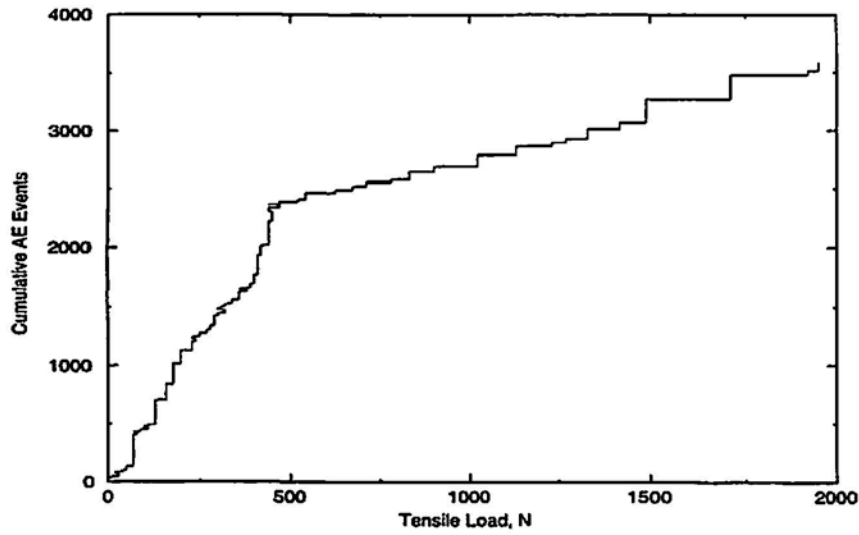


Fig. 6 Typical initial data of cumulative events vs. tensile load with initial exponential rise, followed by a linear behavior.

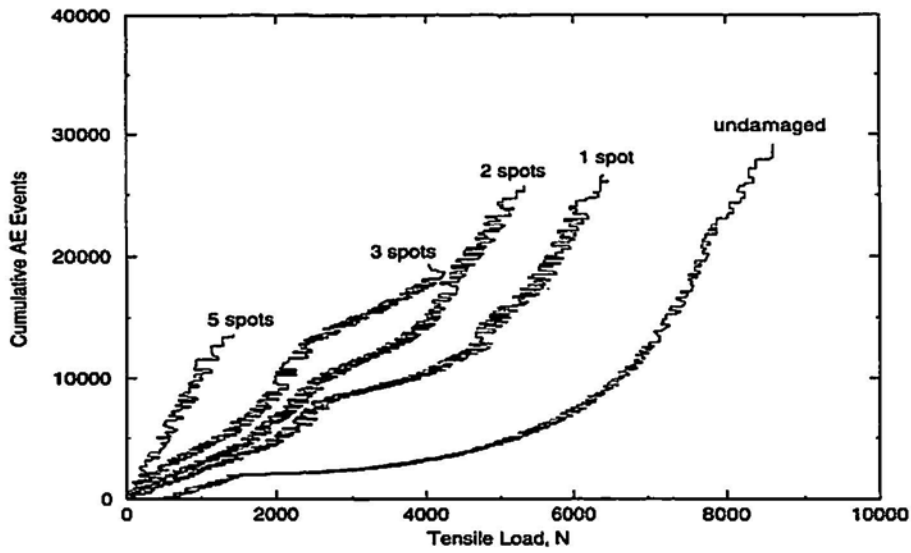


Fig. 7 Cumulative events vs. applied load for specimens with different number of laser damage spots.

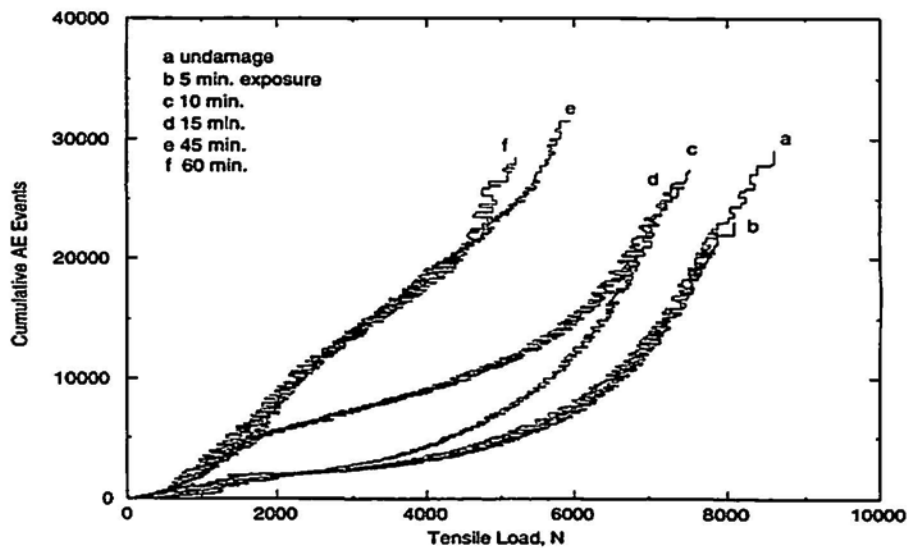


Fig. 8 Cumulative events vs. applied load for specimens with various contact heat duration.

A typical initial cumulative AE-event data versus the tensile load is shown in Fig. 6. This behavior was independent of the damage state and was similar to those reported by Fang and Berkovits (1995) and Pocecho et al. (1997). The activity rose exponentially with the increase of the applied load. The cumulative events then followed a linear relation until specimen failed. Such a behavior indicates that the collected data may have been influenced by the experimental setup.

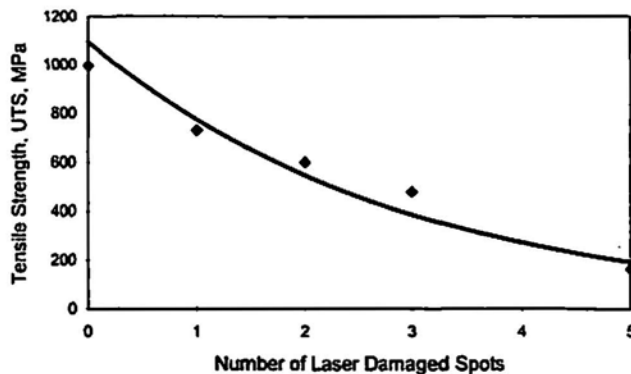


Fig. 9 Tensile strength as function of number of laser damage spots.

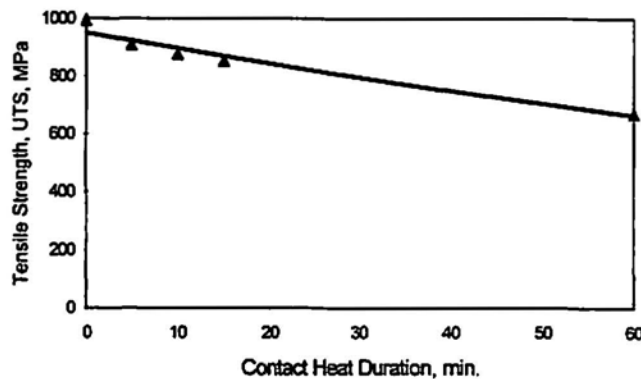


Fig. 10 Tensile strength as function of contact heat damage duration.

Fiber-glass composite has a fairly high AE-event rate when tested in tension. Such a high rate can easily saturate the AET 5500 buffer. The AE events will be then collected at the rate of data transferred from the buffer to the hard disk, which is constant. In order to collect the total AE activities, tests were periodically halted and all pre-recorded data were transferred to the hard disk. Tests were then resumed with the full available buffer. Following this procedure, the linear region of the cumulative events versus applied load did not appear. Figures 7 and 8 show the cumulative AE events versus load for composites with laser-damaged spots and contact-heat damages.

Figures 7 and 8 show that the AE activities of the specimens rose with the applied load. This was followed by a relatively dormant activity period and an exponential increase in the number of AE events before specimen failure.

The period of the dormant activity was independent of the contact-heat damage of less than 15 min. However, this period was a function of the number of damage spots in the laser-damaged specimens. The strength of the composite with the contact heat damage again did not change significantly compared to undamaged specimen, for the contact heat damage of less than 15 min. However, the composite strength was a function of number of laser-damage spots (Figs. 9 and 10). This could be attributed to preserving and not preserving the fibers integrity in these two damage modes. In the laser-damaged specimens, a significant number of fibers are damaged, while in the contact heat no fibers were damaged. The reduction of the composite strength after 45 min.-contact-heat damage could be related to the lack of matrix material to transfer the load uniformly to fibers.

In order to understand the micro-mechanisms of damage growth upon tensile loading in these composites, the AE events corresponding to the three regions in the cumulative event curves were analyzed for their peak amplitude, AE event duration and AE counts. Figure 11 shows the three regions used to analyze the events. Figure 12 shows AE events versus event duration for undamaged composite, laser-damaged and contact-heat damaged specimens. Since fiber fracture produces events with the lowest event duration, events with less than 70 ms was assumed to be due to fiber fracture. This assumption may be justified since the majority of AE activities are due to fiber fracture with event duration of less than 70 ms in region 3. Figure 12 shows that, in region 1, the majority of AE events have event duration of more than 70 ms. Therefore, in region 1, the dominant micro-mechanisms of the damage growth is other than fiber failure. This mechanism could be fiber-matrix debonding, delamination, matrix cracking, and fiber pull-out. The majority of the AE activities in region 2 of the contact-heat damaged and undamaged specimens could be attributed to the fiber fracture, while for laser-damaged specimens they are still due to interfacial failure. The AE events in region 3 are mainly controlled by the fiber fracture. These results were further justified by considering AE events versus AE counts in the three regions. Events corresponding to the lowest AE counts were attributed to fiber fracture, as shown in Fig. 13. Figure 14 shows the failure mode of a contact-heat-damaged specimen and a laser-damaged specimen. This figure indicates fiber fracture in the contact-heat-damaged specimen was the dominant damage mechanism, while the laser-damaged specimen contained numerous interfacial delamination prior to final failure.

Williams and Lee (1983) have introduced a methodology that allows one to predict the residual structural properties using AE data. An AE-delay parameter was defined as a parameter value that was required to produce a specified low-base-line level of cumulative AE measure. The [parameter] can be load, stress, strain, temperature, etc. Using this concept, the load corresponding to total cumulative AE-events

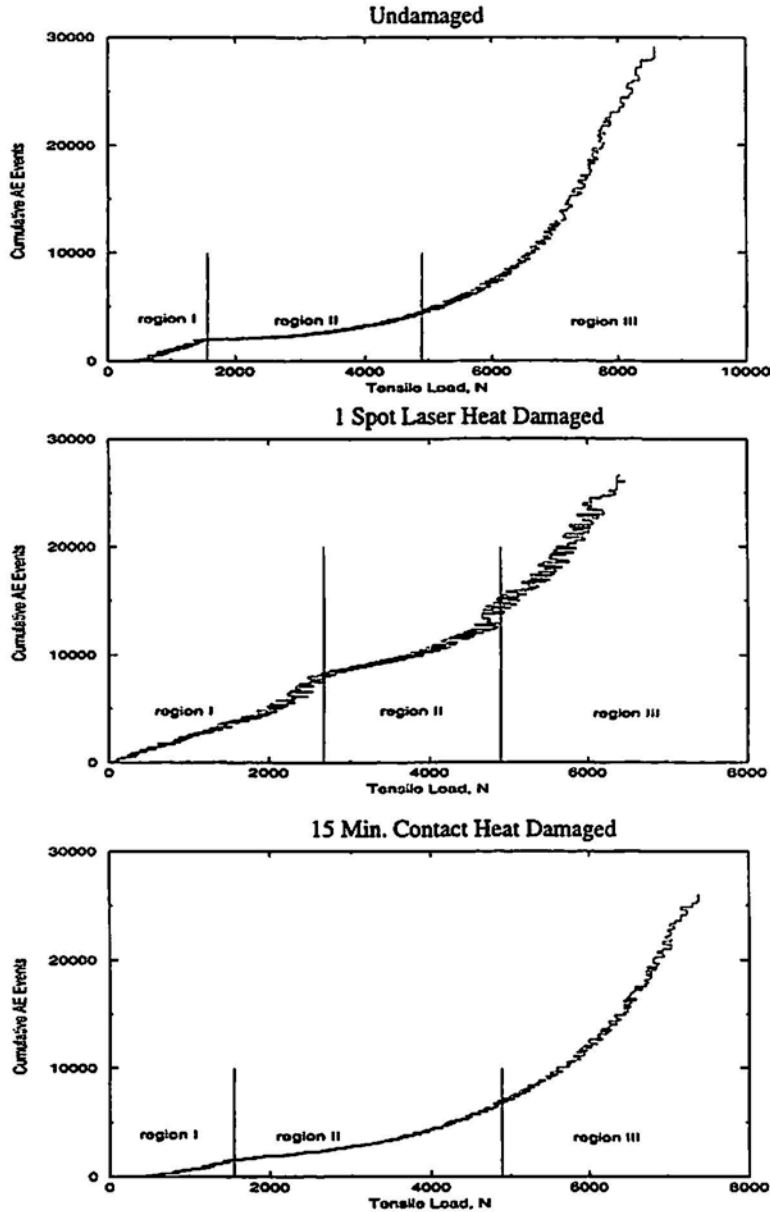


Fig. 11 Three regions of cumulative events vs. tensile load, used to further study the damage growth mechanism.

of 5000 were collected from Figs. 7 and 8. The composite damage state was defined as

$$\eta = 1 - (UTS)_r / (UTS)_{ud} \quad (1)$$

and the normalized load parameter required to produce 5000 AE events relative to undamaged specimen was defined as

$$NP = (\text{load parameter})_d / (\text{load parameter})_{ud} \quad (2)$$

where  $(UTS)_r$  is the residual strength of the damaged specimen and  $(UTS)_{ud}$  is the strength of the undamaged specimen. Figures 15 and 16 show the damage state versus normalized load parameter for the contact- and laser-damaged specimens. The results show that this technique can be used to predict the residual strength of the laser-damaged specimens, while the data for the contact-heat-damaged specimens are somewhat scattered.

#### 4. Conclusions

Acoustic emission technique was used to assess the structural integrity of the composite subjected to localized heat damage from contact heating and laser beam. It was found that

- 1) contact heating produced significant discoloration, char and blistering compared to the laser-damaged specimens. Despite this, the strength of the composite did not change significantly because fibers were left intact during contact heating. In contrast, the strength of the laser-damaged specimens was changed and reduced with the increase of the laser-beam exposure.

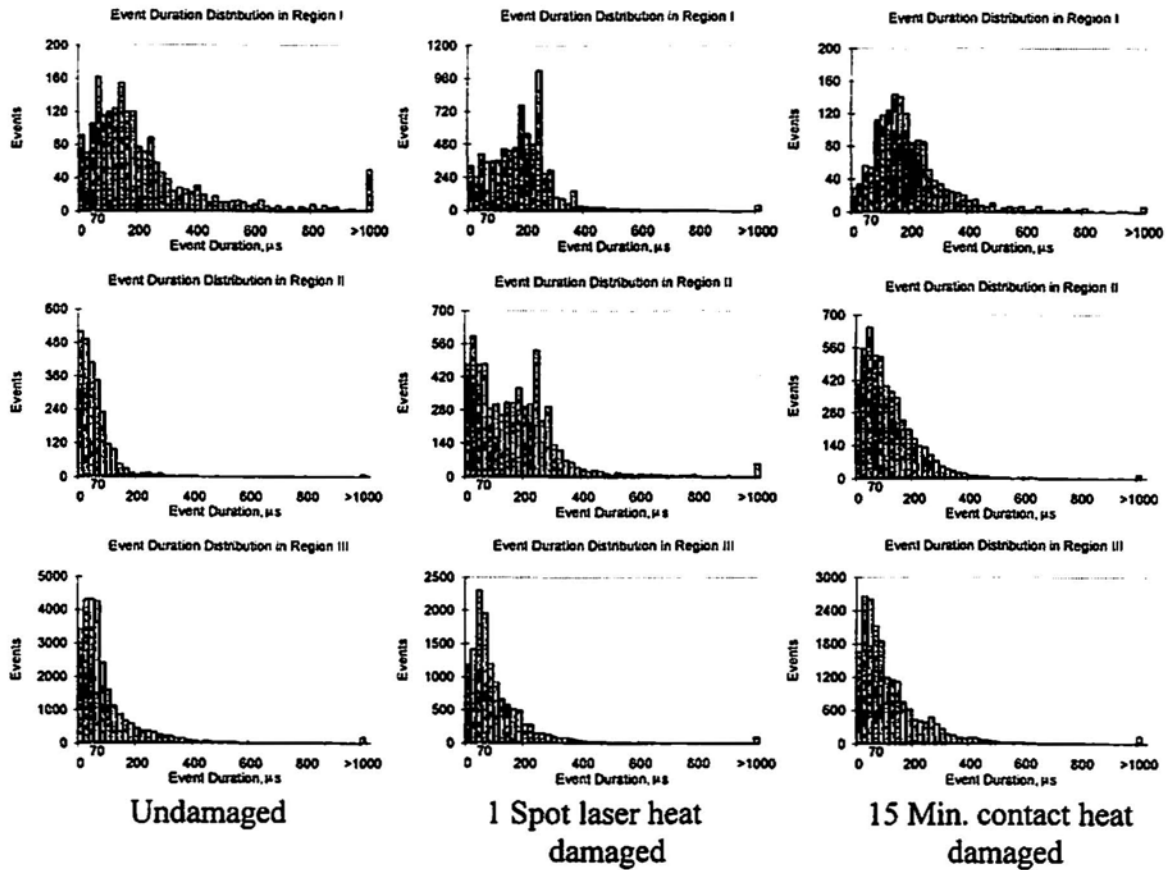


Fig. 12 Distribution of events by event duration for an undamaged, a laser heat damaged and a contact heat damaged specimen.

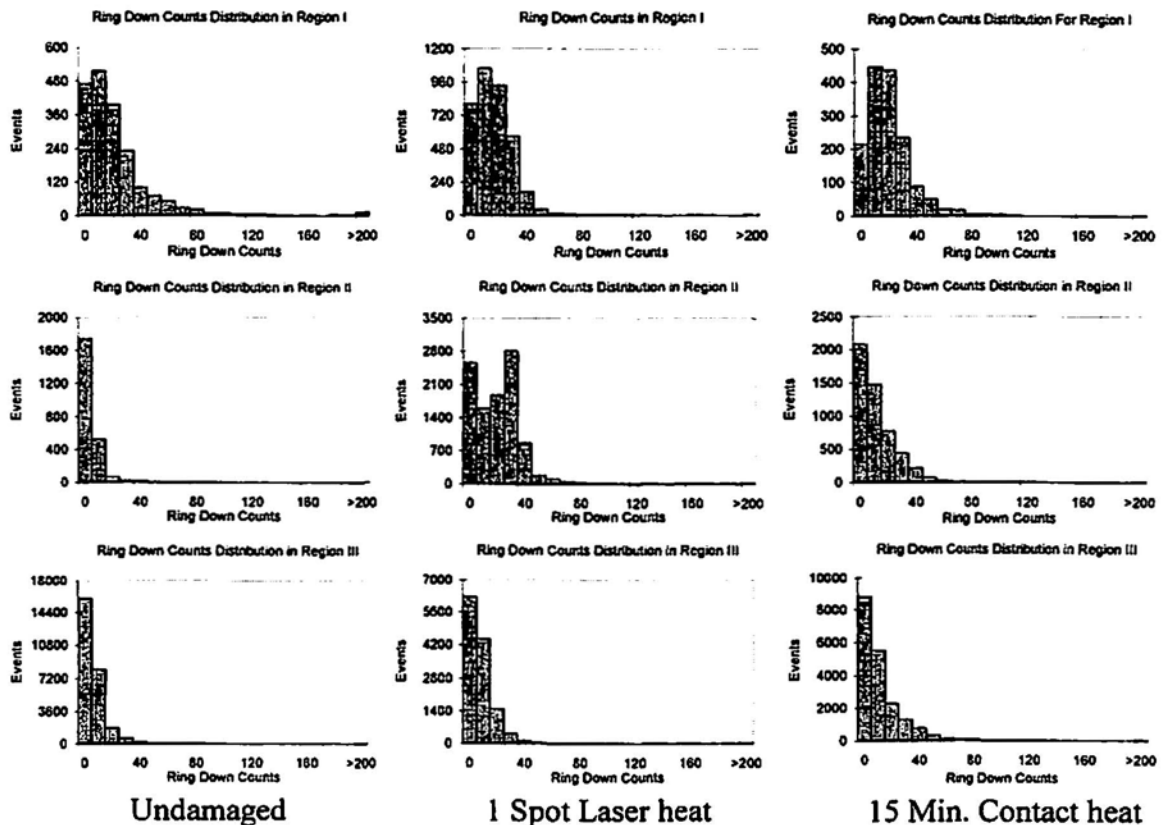


Fig. 13 Distribution of events by AE count for an undamaged, a laser heat damaged and a contact heat damaged specimen.

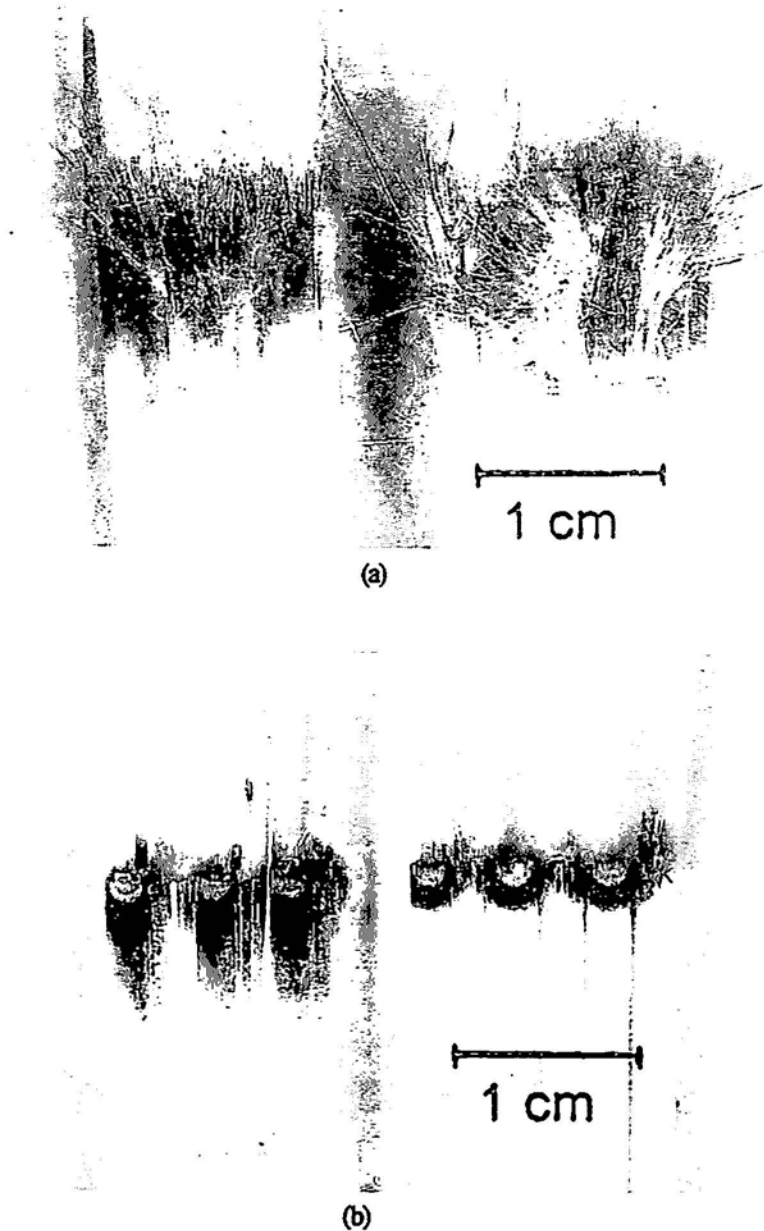


Fig. 14 Photograph of the failure modes of composites with (a) contact-heat damaged and (b) laser-heat damaged.

- 2) Post-damage growth of heat-damaged composites subject to tensile load were evaluated by collecting the AE activities. The cumulative AE events curve showed three distinct regions. An early activity, followed by a relatively dormant activity, leading to an exponential increase in AE event activities prior to specimen failure. The period of the dormant activity was independent of contact heat duration, but was a function of number of laser-damaged spots.
- 3) The early AE activity was related to failure mechanisms other than fiber fracture. However, the majority of AE activities in the third region were related to fiber fracture.
- 4) Fracture mode of specimens damaged by the contact heat was different from the specimens having laser heat damage. In the laser-burned specimens, there were significant number of cracks (delamination) running along the specimens prior to specimen failure. These were absent in the contact-heat-damaged specimens.
- 5) AE delay parameter seems to indicate a trend in the residual strength of composite subjected to heat damage. This trend may be used to predict the residual strength of the composite.

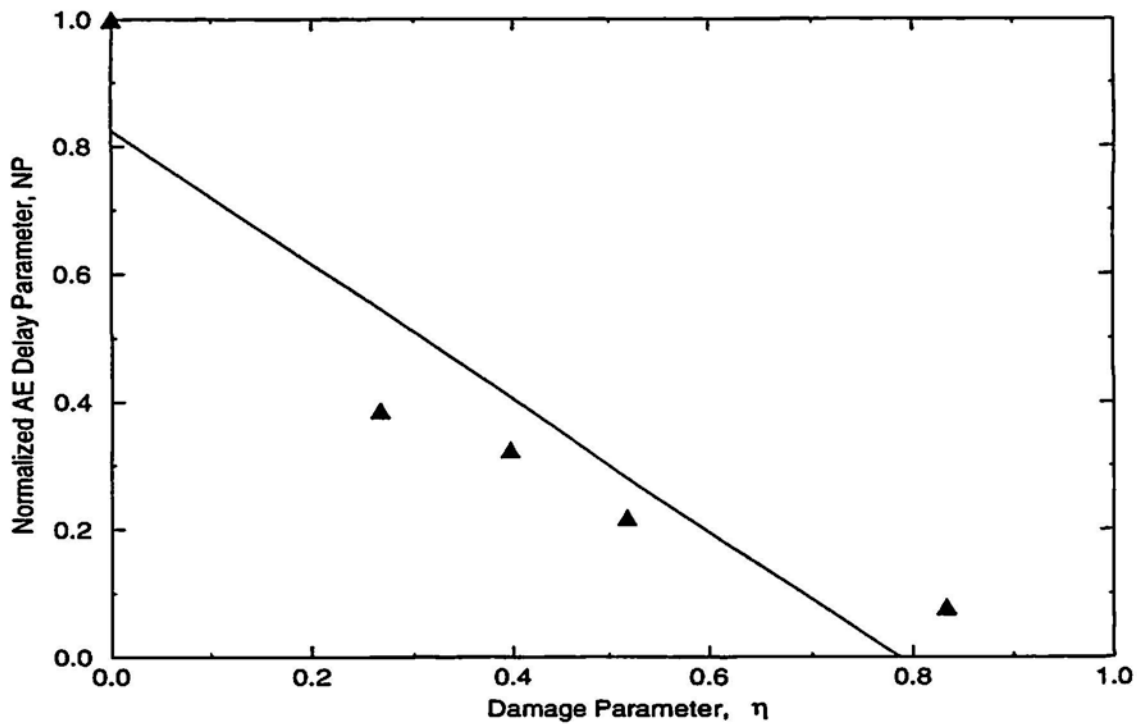


Fig.15 Normalized stress delay, NP, as function of damage parameter,  $\eta$ , for laser heat damaged specimens.

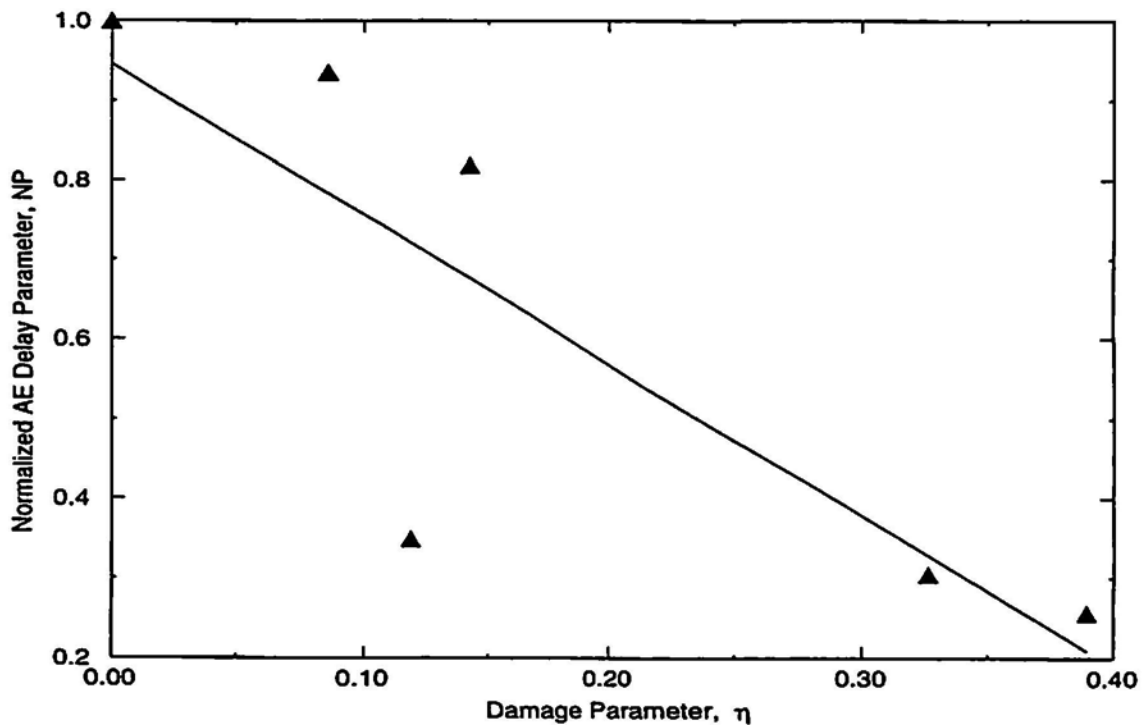


Fig.16 Normalized stress delay, NP, as function of damage parameter,  $\eta$ , for contact heat damaged specimens.

#### References

J. D. Achenbach (1973), "Wave Propagation in Elastic Solids," North-Holland Publishing Co., Amsterdam, London.

ASTM (1994), ASTM Standard Guide for Determining the Reproducibility of Acoustic Emission Sensor Response, E976-94, ASTM, Philadelphia, PA.

E. A. Carrol, P. A. Mehrkam and R. Cochran (1993), "Heat Damage Evaluation of Painted Graphite /Epoxy Composites," *Proc. Conf. on Characterization and NDE of Heat Damage in Graphite Epoxy Composites*, April 27-28, Orlando, Florida, pp. 113-124.

J. C. Duke, Jr., E. G. Henneke, M. T. Kiernan and P. P. Grosskopf (1986), "Ultrasonic Stress Wave Characterization of Composite Materials," NASA CR 4187, May.

D. Fang and A. Berkovits (1995), "Acoustic Emission During the Tensile Deformation of Incoloy 901 Superalloy," *J. of Materials Science*, 30, 3552-3560.

W. G. Fisher, J. M. E. Storey, S. L. Sharp, C. J. Janke, and E. A. Wachter (1995), "Nondestructive Inspection of Graphite-Epoxy Composites for Heat Damage Using Laser-Induced Fluorescence," *Applied Spectroscopy*, 49(9), 1225-1231.

E. G. Henneke (1990), "Ultrasonic Nondestructive Evaluation of Advanced Composites," *Nondestructive Testing of Fiber Reinforced Plastic Composites*, ed. J. Summerscales, Vol. 2, Elsevier Applied Science, London, pp. 55-159.

E. G. Henneke, J. C. Duke, Jr., and R. C. Stiffler (1987), "Characterization of the Damage State of Composite Laminates via Acousto-Ultrasonic Technique," eds. J. D. Achenbach and Y. Rajapakse, Martinus Nijhoff Publishers, Dordrecht, Netherlands, pp. 217-235.

J. R. Kerr and J. F. Haskins (1984), "Effects of 50,000 Hours of Thermal Aging on Graphite/Epoxy and Graphite/Polyamide Composites," *AIAA Journal*, 22, 96-102.

A. Kraut (1963), "Advances in the Theory of Anisotropic Elastic Wave Propagation," *Review of Geophysics*, 1(3), 401-448.

A. Laksimi, X. L. Gong and M. L. Benzeggagh (1994), "Analysis of Damage Mechanism in a Centrally Notched Glass-Fiber / Epoxy Plate," *Composite Science and Technology*, 52, 85-91.

H. Nayeb-Hashemi and J. Rossettos (1994), "Nondestructive Evaluation of Adhesively Bonded Joints by Acousto-Ultrasonic Technique and Acoustic Emission," *J. of Acoustic Emission*, 12(1/2), 1-14.

H. Nayeb-Hashemi, M.D. Cohen and T. Erturk (1985), "Evaluation of Fatigue Damage on the Mechanical Properties of Fiber Reinforced Cement Pastes," *J. of Cement and Concrete Research*, 15, 879-888.

T. Pocheco, H. Nayeb-Hashemi and H. M. Sallam (1996), "Acoustic Emission in a Nextel 440 Fiber Reinforced 6061 Al Composite," *J. of Acoustic Emission*, 14(2), 85-95.

A. Vary (1987a), "Acousto-Ultrasonic," *Nondestructive Testing of Fiber-Reinforced Plastic Components*, Vol. 2, ed. J. Summerscales, Elsevier Applied Science, London, pp. 25-54.

A. Vary (1987b), "The Acousto-Ultrasonic Approach," NASA Technical Memorandum 89843, April.

A. Vary and R.F. Lark (1979a), "Correlation of Fiber Composites Tensile Strength with Ultrasonic Stress Wave Propagation Factors," *J. of Testing and Evaluation*, 7(4), 185-191.

A. Vary and K.J. Bowles (1979b), "Use of an Ultrasonic Acoustic Technique for Nondestructive Evaluation of Fiber Composite Strength," NASA TM 73813, Feb.

J. H. Williams and S.S. Lee (1978), "Acoustic Emission Monitoring of Fiber Composite Materials and Structure," *J. of Composite Materials*, 12, 348-370.

J. H. Williams and S. S. Lee (1983), "Acoustic Emission Characterization Using AE [Parameter] Delay," *Materials Evaluation*, 41, 961-966.

## Appendix

Properties of fiber and matrix used in this study

	Elastic Modulus		Tensile Strength		Poisson's ratio
	GPa	(Msi)	GPa	(ksi)	
Fiber	72.4	(10.5)	3.45	(500)	0.2
Matrix	10.5	(1.53)	---	-----	0.28

# An Investigation of Lüders Band Deformation and the Associated Acoustic Emission in Al - 4.5% Mg Alloys

D. L. Armentrout and S. H. Carpenter

## Abstract

We have conducted a detailed investigation of non-uniform plastic deformation and acoustic emission (AE) associated with the initiation and motion of Lüders bands in aluminum-magnesium alloys. A series of Al-4.5%Mg alloys with increasing amounts of Fe, Si and Mn was investigated during deformation in uniaxial tension. The elements of Fe, Si and Mn are common non-soluble impurity elements that form constituent particles in aluminum alloys. Increasing the impurity elements concentration produced a refinement of the grain size of the test materials, resulting in changes in the mechanical properties. All of the samples tested, irrespective of the impurity concentration, exhibited unstable Lüders-band deformation, as characterized by multiple yield points. High-speed digital instrumentation was used to capture and analyze the stress, strain and AE behavior in detail during individual yield points. From careful analysis of these data, the following has been determined: 1) three separate and distinct regions during the drop in stress associated with a yield point have been identified, 2) a distinct burst of AE activity is associated with each yield point, 3) the AE activity actually begins a short time before any decrease in stress is observed, 4) the strain rate during a drop in stress of a yield point is estimated to be as high as  $30 \text{ s}^{-1}$  and 5) an excellent correlation exists between the magnitude of the drop in stress and the AE generated for a given impurity concentration.

## 1. Introduction

The focus of this investigation was to examine in detail the non-uniform plastic deformation associated with Lüders deformation in aluminum-magnesium alloys. In addition to the mechanical properties, the acoustic emission (AE) generated during Lüders deformation was measured and analyzed to aid in the characterization and understanding of the non-uniform plastic deformation. Lüders deformation has different appearances on the surface that are effected by the grain size and the sample shape. Lomer (1952) showed that for fine grain, stiff tensile specimens with a length-to-

breadth ratio of 12 or less and with a breadth of 5 mm or more, the shear stress in a stiff tensile machine is best accommodated by nucleating a series of Lüders bands characterized by multiple yield points. Under Lomer's stiff specimen conditions, Lüders-band deformation reveals a surface characterized by narrow depression bands that form at roughly  $45^\circ$  to the direction of the applied stress. With each sudden drop in stress or yield point, a single depression band forms. As the sample deforms, many depression bands form, evenly spaced across the gage section of the sample.

A large number of metallurgical variables strongly influence Lüders-band deformation. At least fifteen different experimental test and material variables have been investigated and reported on in the literature (Armentrout, 1991; Hall, 1970; Morris, 1974; Sperry, 1963; Pink, 1989; Tabata et al., 1980). Of the material variables investigated, the grain size of the test material appears to have the largest effect on whether or not Lüders deformation occurs (Hall, 1970). In order to have a well-defined planar front established and propagated uniformly along the gage section, the ratio of the minimum specimen dimension to the grain size must be greater than 25:1 (Moon, 1971). McReynolds (1949) found the Lüders front becomes more distinct as the grain size decreases. In the present investigation, the concentration of Fe, Si and Mn was increased to produce a refinement of the grain size in the test materials.

In a sample with multiple yield points, the AE generated during yield deformation can be compared and studied many times in the deformation of a single sample. Multiple yield points in the same sample can be more easily compared than a single yield point in multiple samples. At sufficiently low strain rates, Lüders bands are distinct. When the Lüders band forms, the deformation rate in the band is significantly higher than the applied strain rate. Digital signal instrumentation was used to capture and analyze the stress, strain and AE behavior in detail during individual yield points. The digital data allows enhanced analysis and additional understanding of the Lüders-band deformation phenomena. Certain characteristics of the generated AE and characteristics of the individual stress drops were investigated to provide a better understanding of Lüders deformation, the mechanisms involved and the sources of AE operational during Lüders deformation.

---

Received 9 September 1997; in final form, 12 December 1997. D. L. Armentrout is affiliated with Metallurgical and Analytical Instrument Consultant, Golden, CO and S. H. Carpenter (scarpent@du.edu) is with Physics Department, University of Denver, Denver, CO 80208.

## 2. Equipment and Experimental Procedure

The materials used in this investigation were obtained from the Alcoa Aluminum Co. The samples were supplied originally in the H19 condition and were annealed for 1 hr at 616 K prior to testing. Tensile specimens were machined to dimension, as shown in Fig. 1 and then deformed in uniaxial tension at a constant displacement rate. Table 1 lists the chemical composition and grain size of the test materials. The sample materials have a relatively constant Mg concentration (approximately 4.5%) with increasing concentrations of Fe, Si and Mn. At room temperature, Fe, Si and Mn are essentially insoluble in aluminum (Moffatt, 1995). Optical microscopy of the test materials revealed constituent particles on the order of 1  $\mu\text{m}$  in diameter separated by distances larger than the average grain size. The addition of impurity elements caused a refinement of the grain size through formation of constituent particles, see Table 1. A linear relationship between the inverse square-root of the grain size with impurity concentration was found as shown in Fig. 2.

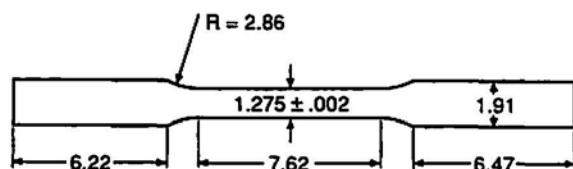


Fig. 1 Schematic diagram of tensile specimens used in this investigation. All measurements are in centimeters. The sample thickness was 0.51 mm.

An MTS testing machine with a mechanical stiffness of  $2.5 \times 10^5$  N/mm (many times greater than the stiffness of the test samples) was used for the uniaxial deformation tests. A 25-kN load cell was used, which allowed for good resolution of the load and a quick response time. The maximum resolution of the load was 0.05 N with an overall accuracy of better than  $\pm 0.3\%$ . A 100-mm-long strain gage was used with a resolution of at least  $3.2 \times 10^{-7}$ . The accuracy of the strain gage was better than  $\pm 0.1\%$  over the entire range of  $1.27 \times 10^{-2}$  after calibration.

The AE equipment used was standard, commercially available equipment. Figure 3 shows a block diagram of

both the AE and mechanical test equipment. A Dune-gan/Endevco S9204 resonant transducer (140 kHz) was chosen primarily because of its high sensitivity. The output of the pre-amplifier was divided into an amplifier and a signal acquisition module (Acoustic Emission Associates; also known as a Phoenix system). The amplifier (60 dB gain) also filtered the signal between 100-300 kHz, output of which was then fed into two rms voltmeters (Hewlett Packard 3400A), and a digital recorder. The signal acquisition module is a device that measures input signal characteristics and other test parameters, recording the data in a personal computer. The digital recorder offers a wide selection of voltage ranges and capability of recording over a million digital values. Two channels of data on the digital recorder were used to record the AE signal and the applied stress. Two completely different setups of the digital recorder required during the investigation to effectively capture with sufficient accuracy each of the two different inputs. For a more accurate AE signal measurement, the setup recorded 514,288 (512K) samples per channel with the sampling interval of 1  $\mu\text{s}$ . For a complete measurement of a stress serration, the setup was 512K samples per channel with the sampling interval of 22  $\mu\text{s}$ .

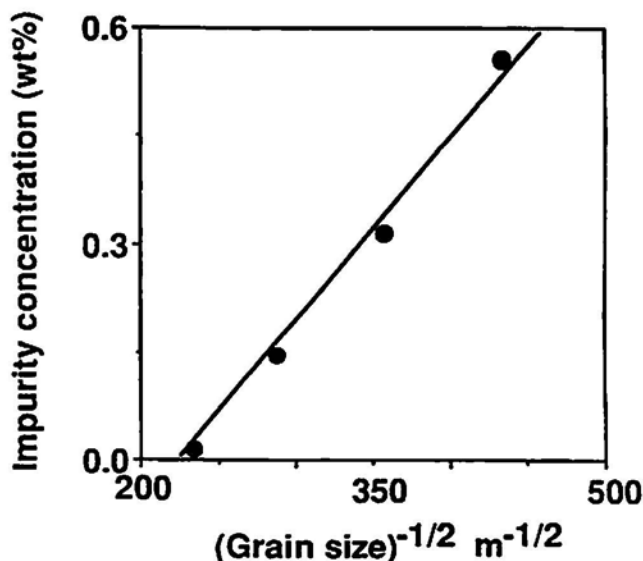


Fig. 2 Plot of impurity concentration in wt% versus the inverse square-root of grain size.

Table 1 Grain Size and Chemical Composition of Alloys by Weight Percent

Sample type	Mg	Si	Fe	Mn	Grain size ( $\mu\text{m}$ )
I	4.56	.00	.00	.00	18.4
II	4.47	.000	.00	.14	11.9
III	4.45	.06	.11	.15	7.9
IV	4.47	.13	.28	.15	5.3

Table 2 Properties of Alloys with ~4.5%Mg

Sample type	Mg %	% impurities	$\sigma_U$ (MPa)	$\epsilon_L$ (%)	d ( $\mu\text{m}$ )
I	4.56	<0.02	101.6	0.738	18.4
II	4.47	.14	112.1	1.13	11.9
III	4.45	.32	144.0	1.94	7.9
IV	4.47	.56	150.4	2.17	5.3

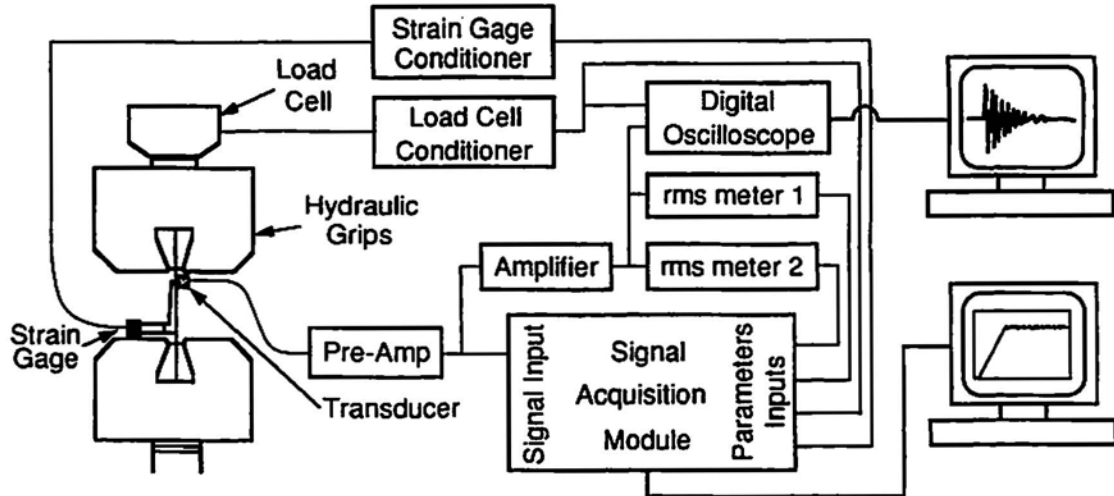


Fig. 3 Schematic diagram of experimental setup and equipment used in this investigation.

The AE equipment was carefully calibrated before performing the uniaxial tensile tests. A measurement of the system noise was made using a stainless steel specimen known to generate essentially no AE, with similar dimensions to the test samples. In all cases, the background and machine noise were maintained at a low level compared to the AE generated in the test specimens during deformation.

### 3. Experimental Results

Figures 4a-d show the applied stress and the AE, in terms of the rms voltage (voltage referenced to the transducer output), as a function of strain for increasing concentrations of Fe, Si and Mn. Multiple yield points were observed for all samples tested, as seen in the figures. Table 2 lists average mechanical properties of the different test materials. The value  $\sigma_U$  is the average value of the upper yield stress,  $\epsilon_L$  is average value of the total plastic strain during Lüders deformation (Lüders strain), and d is the average grain diameter of the test material. A review of the data shown in Table 2 indicates that the upper yield strength and the Lüders strain increase with increasing impurity concentration. The grain size of the test material, as expected, decreases as the impurity concentration increased, as shown earlier in Fig. 2. An examination of Fig. 4 reveals that for each individual yield point there is a corresponding burst of AE activity. Figure 5 is a plot of the AE, given as the peak value of the rms voltage burst, versus the corresponding

stress drop for a number of tests of the different alloys. Table 3 provides a summary of the data displayed in Fig. 5. The values given under  $\langle \Delta\sigma \rangle$  are the average magnitude of the drop in stress and the values given under  $\langle V_{rms} \rangle$  are the average peak values of the rms voltage burst during the Lüders deformation. The linear least-squares fit of the data is plotted in Fig. 5. The slope of the lines and the linear correlation coefficient,  $L_c$ , of the fit are also given in Table 3.

The data shown in Fig. 5 and Table 3 indicate a direct proportionality between the magnitude of the stress drop and the resulting AE; i.e., the larger the stress drop the larger the resulting AE. However, the proportionality constant and the scatter in the data between the stress drop and the AE are strongly effected by increasing impurity concentrations. For the binary Al-Mg alloy (sample I, impurity concentration <0.02 wt%, Fig. 5a), an excellent correlation between the AE and the stress drop is observed. The addition of 0.14 wt% Mn increases the magnitude of the stress drop slightly and decreases the average AE slightly (Fig. 5b). The addition of 0.06 wt% Si and 0.11 wt% Fe produces larger average stress drops and smaller average AE (Fig. 5c). The scatter of the data increases markedly from Fig. 5a to 5c. Doubling of the Si and Fe concentration has only a slight effect on the average stress drop, but causes a decrease in the rms voltage peak and enhances the scatter, as shown in Fig. 5d. A weak correlation between the AE

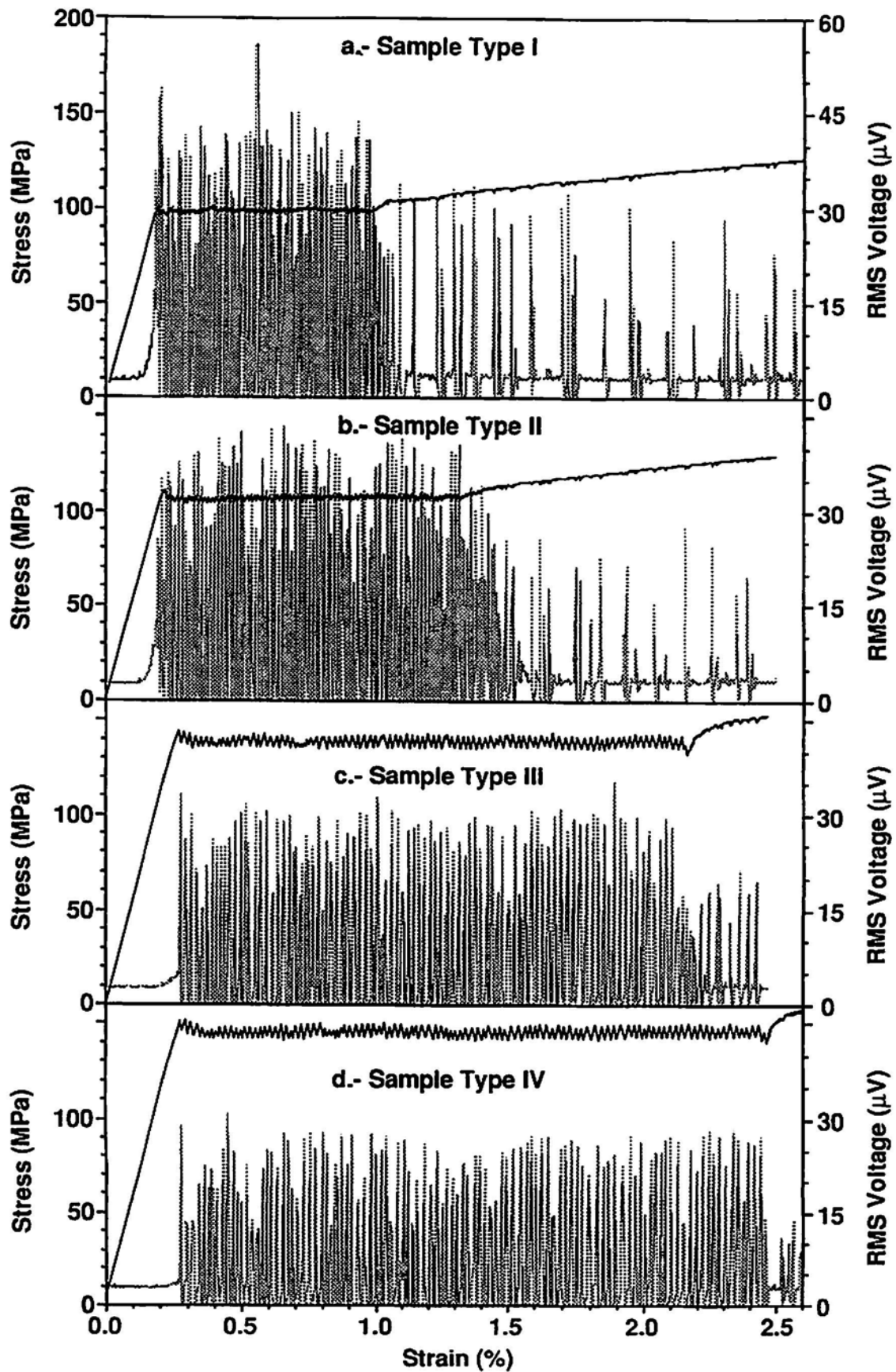


Fig. 4 Plots of applied stress and AE versus strain for increasing impurity concentrations: a) type I sample, b) type II sample, c) type III sample, d) type IV sample.

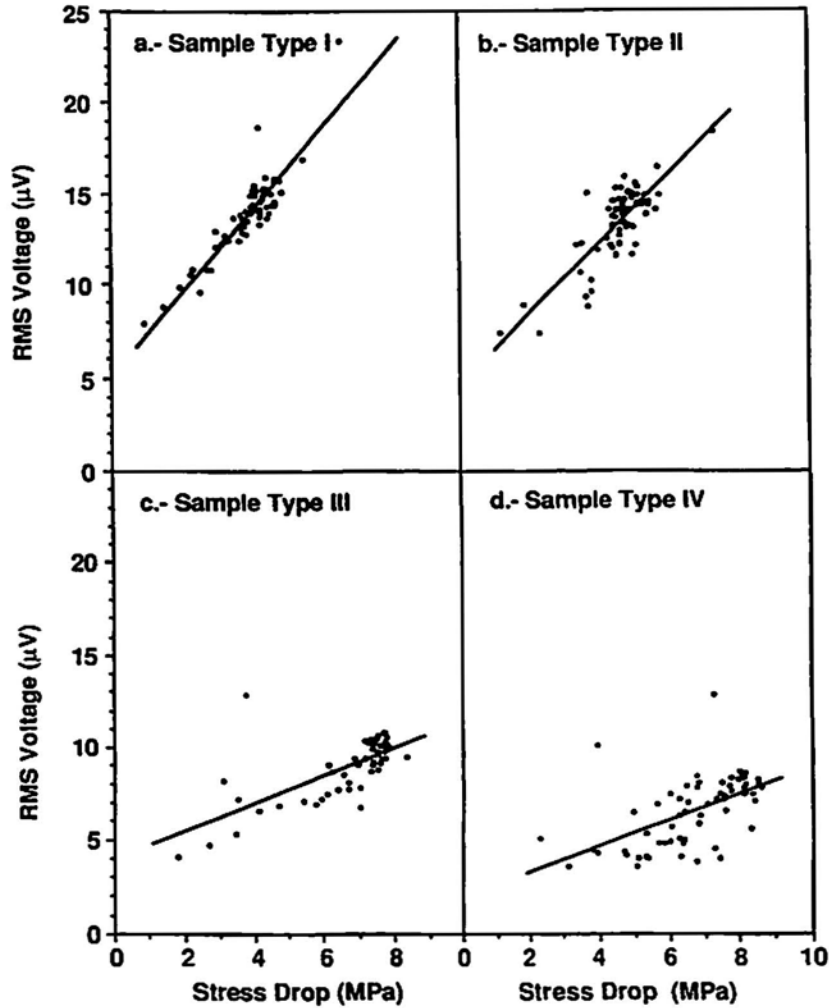


Fig. 5 Plots of the peak values of the rms voltage versus the magnitude of the corresponding stress drop for increasing impurity concentrations; a) type I sample, b) type II sample, c) type III sample, d) type IV sample.

Table 3 Statistical Properties of Stress Drops of Alloys with ~4.5% Mg

Sample type	Mg %	% impurities	$ \langle \Delta \sigma \rangle $ (MPa)	$\langle V_{rms} \rangle$ ( $\mu V$ )	Slope	$L_c$
I	4.56	<0.02	3.91	13.8	2.23	0.822
II	4.47	0.14	4.62	13.4	1.91	0.652
III	4.45	0.32	6.63	8.95	0.75	0.469
IV	4.47	0.56	6.60	6.55	0.72	0.310

and magnitude of the stress drop has been reported in an earlier work on 3004 Al alloy with higher impurity concentrations (Armentrout and Carpenter, 1991). Figure 6 shows the percentage change of both the average stress drop and the associated average rms voltage peak as a function of total impurity concentration.

Using the digital recording system, the time sequence of the stress drop and AE behavior can be studied in detail. The stress and the resulting AE (rms voltage in reference to the transducer output) are plotted, as a function of time, for a yield point with a double drop in stress from

a type III sample in Fig. 7. A double drop in stress occurred in less than 10% of the stress drops. The signal voltage scale is enlarged to show details of the signal. The graph insert in Fig. 7 shows the AE signal plotted on scale. The stress has been corrected for the time delay, as will be discussed later, and processed to remove 30 and 60 Hz signals from the load-cell conditioner. Examination of Fig. 7 reveals that the major part of the stress drop occurs in less than 10 ms. The higher frequency oscillations that begins after the steepest portion of the drop in stress are mechanical resonance of the system excited by the stress drop.

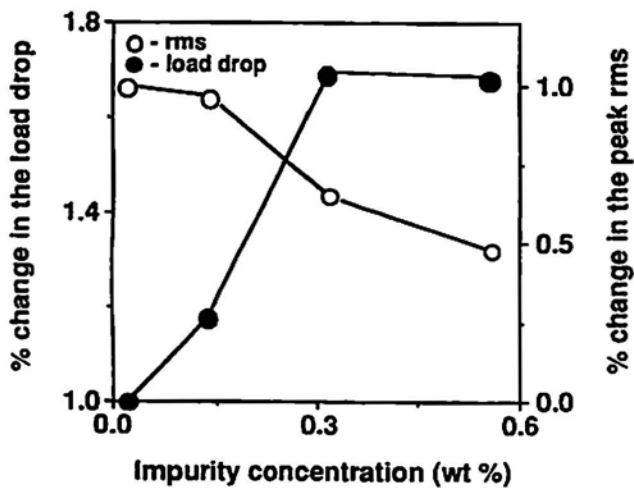


Fig. 6 A plot of the percent change in the load drop and the percent change of the peak AE as a function of impurity concentration.

An expanded view of another stress drop from type III sample is shown in Fig. 8. This stress drop can be separated into three distinct regions or zones. The first region, arbitrarily called band initiation, occurs first over a short interval of time. The initiation region begins as the AE signal increases above the noise level. The stress slightly decreases in the initiation region. The second region, called the band-slip region, corresponds to the short time interval characterized by the rapid decrease in stress. This region has been called the band-slip region because the primary deformation mechanism of a stress serration is slip. The peak amplitude of the AE signal occurs during the band-slip region. A third region, called the kink-resolution region, is characterized by a slower decrease in stress to a minimum value. For a sample that is constrained at the grips, a stress or kink develops that opposes slip. The kinking force builds during slip until it is large enough to stop the slip band. The duration of the AE signal closely corresponds to the time required for the stress to drop to its minimum value.

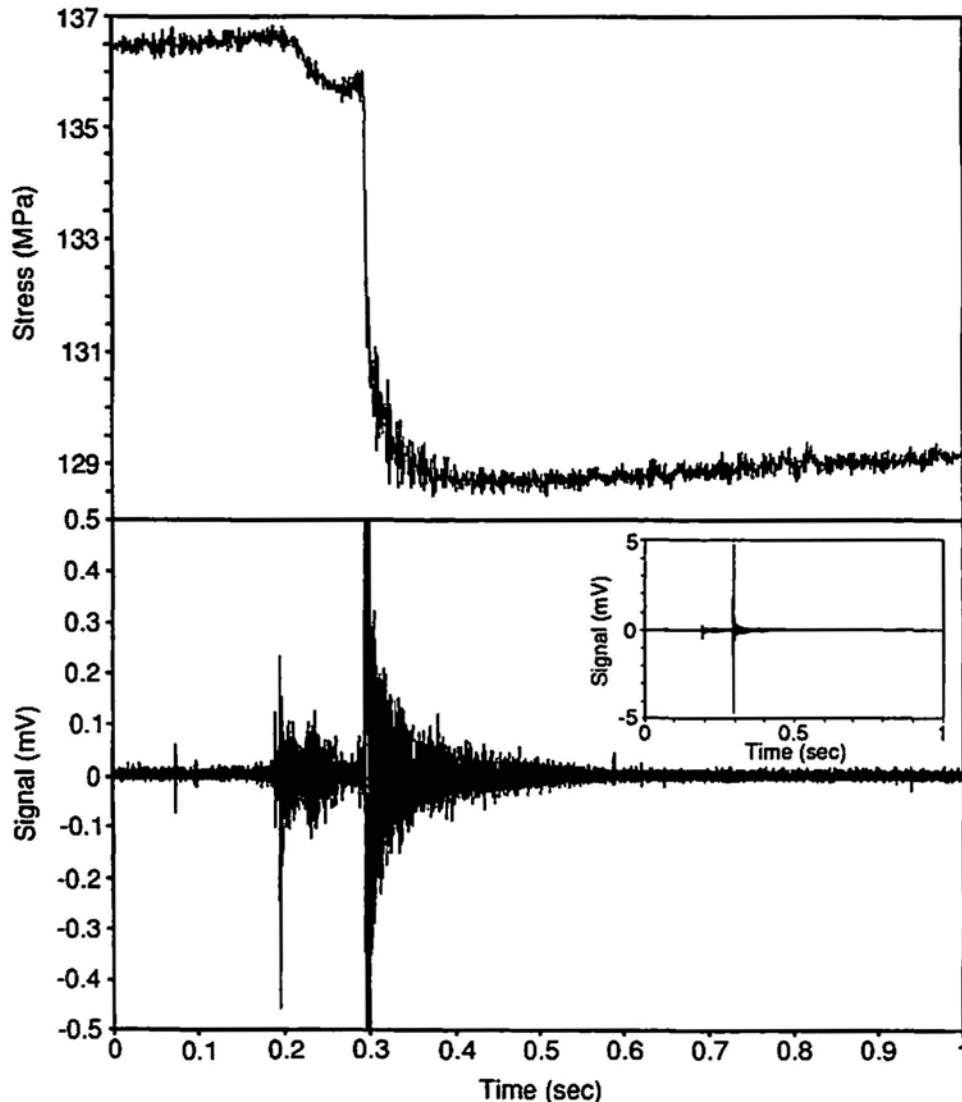


Fig. 7 Plot of a double stress drop and associated AE as a function of time for a type III sample, recorded at a sampling interval of 11  $\mu$ s.

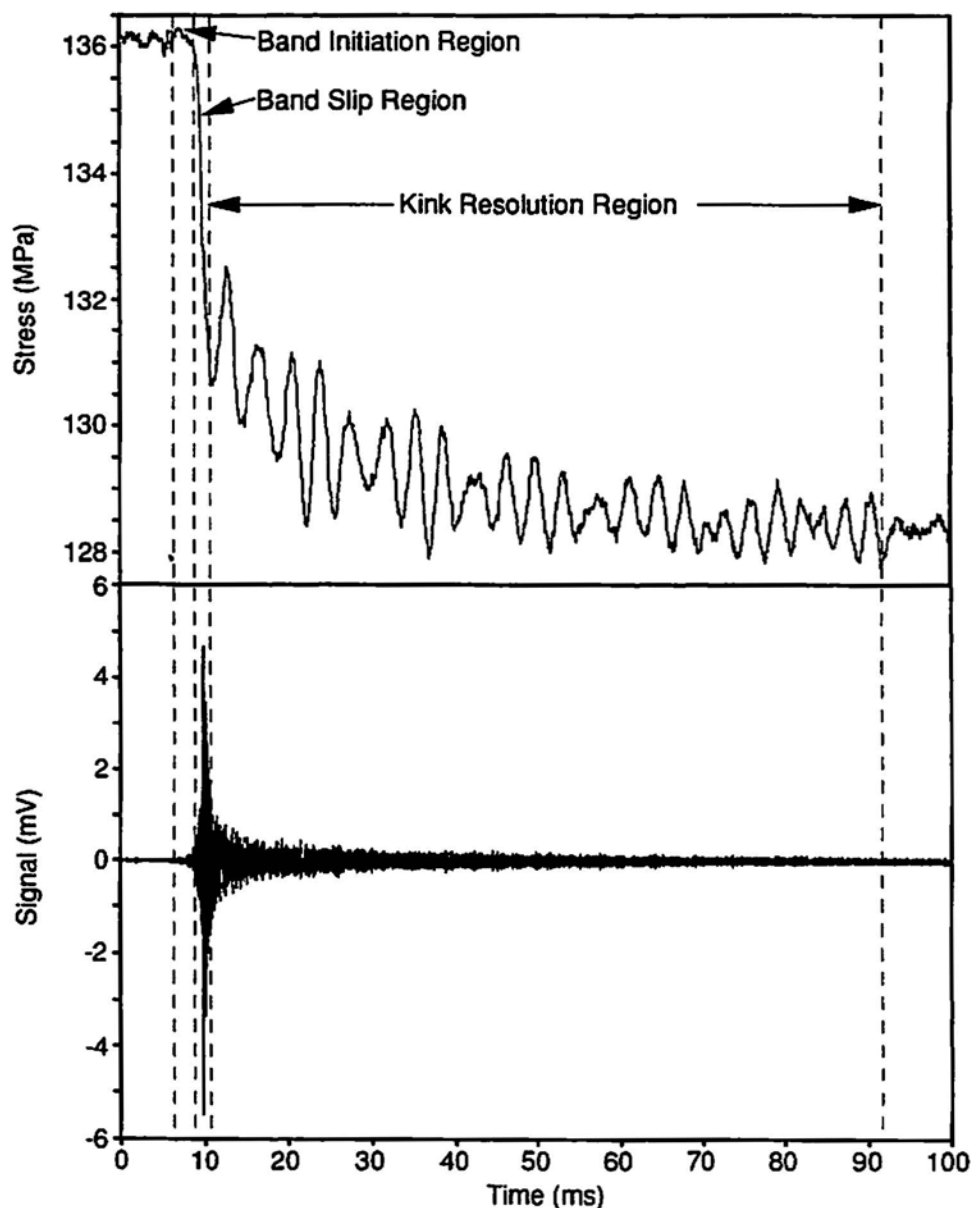


Fig. 8 An expanded view of a single stress drop from a type III sample.

Because both the AE signal and the impulse from the load drop can be delayed by a certain amount of time until they were measured, the relative time delay of the AE signal and impulse needed to be measured. This relative time delay was measured using a sharp hammer blow to one of the hydraulic grips to simulate a stress drop. A value of  $860 \pm 150 \mu\text{s}$  was obtained for the time delay of the initial change in slope of the load cell from the rise out of noise of the AE transducer signal due to the hammer blow. A correction has been made in Figs. 7 and 8 for the time delay of the load cell. Figure 9 shows data for the load drop as a function of the duration of the load drop for a number of tests recorded using the digital recording system. Notice that as the concentration increases, the magnitude of the load drop increases, in agreement with data reported earlier (Armentrout and Carpenter, 1991). The duration of the

load drop decreases as the impurity concentration increases. A larger drop in stress also means a faster resolution of the kink stress.

As shown above, the stress drop takes place rapidly, and is also confined to a small volume of material. Hence, the strain rate during a stress drop is expected to be much higher than the applied strain rate of the test machine. The volume of material deforming during one stress drop can be inferred from the size of the depression band that forms on the surface of the sample. The amount of deformation can be obtained from the magnitude of the drop in stress. From these data, a rough estimate has been made for the strain rates occurring during a stress drop. Table 4 provides results from limited transient recorder data for three different stress drops from two different specimens. The value  $|\Delta\sigma|$

Table 4 Transient Recorder Data and Calculated Strain Rates

Sample type	$ \Delta\sigma $ (MPa)	$t_d$ (ms)	$E^*$ ( $V^2ns$ )	$\epsilon_s$ ( $s^{-1}$ )	$\epsilon_k$ ( $s^{-1}$ )
III	7.26	175.7	181	18	0.17
III	7.66	109.1	226	20	0.18
III	7.69	82.4	255	22	0.19
IV	3.46	135.1	109	23	0.26
IV	8.94	67.1	122	30	0.21
IV	9.19	68.4	138	24	0.25

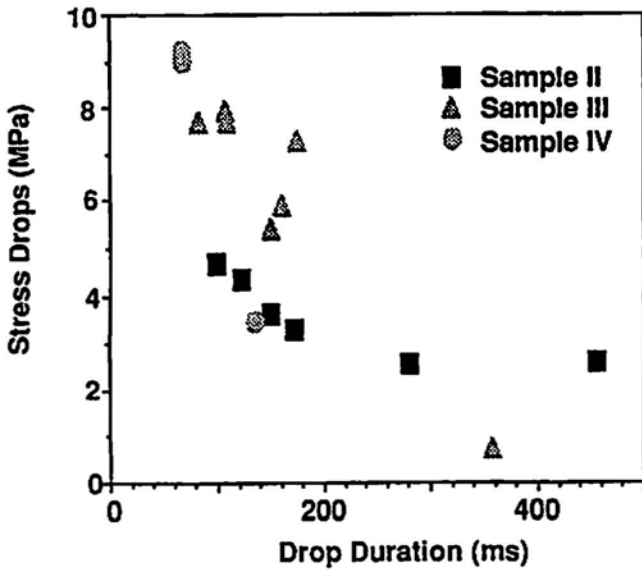


Fig. 9 Magnitude of the measured stress drop as a function of the time duration of the stress drop for sample types II, III, and IV.

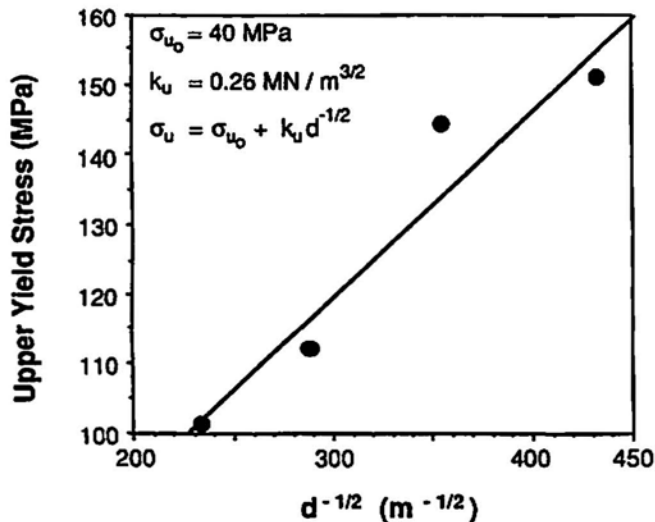


Fig. 10 Hall-Petch plot of the upper yield stress versus grain size.

is the magnitude of the stress drop,  $t_d$  is the duration of the stress drop,  $\epsilon_s$  is the estimated strain rate during the band slip region and  $\epsilon_k$  is the estimated strain rate during kink resolution, and  $E^*$  is the relative energy of the AE waveform. The response of the load cell limited the strain rates that could be measured during the band-slip region. Since the applied strain rate was  $2.6 \times 10^{-5} s^{-1}$ , the values of band-slip strain rate, ranging from 18 to  $30 s^{-1}$ , are six orders of magnitude larger than the applied strain rate. The values for the kink-resolution strain rate are four orders of magnitude larger than the applied strain rate.

#### 4. Discussion of Results

All of the mechanical properties, i.e., the upper yield strength, Lüders strain and magnitude of the load drop, were found to increase as the impurity concentration was increased. The changes in the mechanical properties could be due to changes in the grain size or hardening effects due to the impurities inside the grains. Changes in the upper yield strength due to changes in the grain size is given by the Hall-Petch relationship (Hall, 1970) as

$$\sigma_u = \sigma_o + k_u d^{-1/2} \quad (1)$$

where  $\sigma_u$  is the upper yield strength,  $\sigma_o$  and  $k_u$  are constants and  $d$  is the grain size. Figure 10 is a plot of equation (1). A linear fit of the data yields values of  $k_u = 0.26 MN/m^{3/2}$  and  $\sigma_o = 40 MPa$ . Using the data of Phillips et al. (1953), Hall (1970) obtained values of  $k_u = 0.26 MN/m^{2/3}$  and  $\sigma_o = 49 MPa$ , for an Al-3.5%Mg alloy with the Fe, Si and Mn concentration similar to the sample IV material tested here. The value of  $k_u$  is not very sensitive to the concentration, but  $\sigma_o$  should be concentration dependent. The agreement of our data with that of Phillips et al. (1953) is good. The agreement of the experimental data to the theoretical linear line implies that the increase in strength measured in the test materials is primarily due to the reduction in grain size and not significantly effected by any hardening mechanism from increasing the Fe, Si and Mn concentration. The magnitude of the average stress drop was found to be linearly dependent on the magnitude of the upper yield stress, i.e., the higher the upper yield stress the larger the average stress drop. A plot of the average stress drop versus the upper yield stress is given in Fig. 11, where an excellent

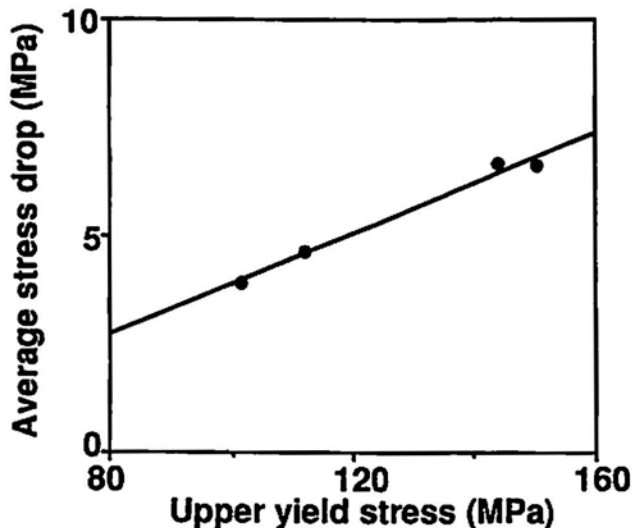


Fig. 11 Plot of the average stress drop versus the upper yield stress

straight line is obtained with a correlation coefficient of 0.985. This result indicates that the average stress drop is also determined primarily by the grain size of the test material.

Since the stress drop occurs in a short time interval and the machine displacement is negligible, the plastic deformation in the Lüders band causes elastic relaxation in the rest of the sample and the tensile machine. The magnitude of the stress drop is directly proportional to the amount of plastic deformation of the Lüders band. Smaller grain size produces higher yield stress and larger magnitude of stress drops. This, in turn, means that a smaller grain size produces more plastic deformation per Lüders band on average. For there to be greater plastic strain, the product of the mobile dislocation density and the average dislocation displacement must increase.

The effects of grain size and impurity concentration on the AE are more difficult to analyze, since there exists a fundamental difference in the dislocation motion required to produce plastic strain and that required to produce measurable AE (Heiple and Carpenter, 1987). The dislocation motion required to accommodate a given amount of plastic strain needs neither be a uniform or coordinated motion nor needs it to occur in a short interval of time. On the other hand, the dislocation motion required to produce a measurable AE event requires that the dislocation motion be coordinated and that it must occur in a short duration; i.e., an avalanche motion of dislocations. It is reasonable to surmise that a smaller grain size with a higher dislocation density would limit the avalanche motion of the dislocations, resulting in lower values of the average rms voltage peak, as is observed in the present study.

The above arguments assume that the additional impurities are not effective in the pinning or locking of the dislo-

cations in the individual grains. However, the presence of the additional constituent particles will present obstacles to the avalanche motion of the dislocations and should decrease the average rms voltage peak, as was observed. A distinct feature of the data shown in Fig. 5 is the increase in scatter of the data as the impurity concentration is increased. We believe that the increase in scatter is directly related to the fact that the Lüders deformation is localized to small volumes and to the differences in the local impurity concentration. With no constituent particles to block the avalanche motion, the AE and the load drops should be closely correlated regardless of where the deformation occurs. However, as the concentration of constituent particles increases, there will be regions where deformation may occur and there will be significant obstacles to coordinated motion while there will also be localized area with low constituent particles and no obstacles to avalanche motion. Hence, the larger deviation of stress drops and AE should be expected as the constituent particle concentration is increased.

## 5. Conclusions

A detailed investigation of non-uniform plastic deformation and AE associated with the initiation and motion of Lüders bands in aluminum-magnesium alloys has been carried out. Increasing the concentration of constituent particles produced a refinement of the grain size of the test materials, resulting in changes in the mechanical properties. Digital instrumentation was used to capture and analyze the stress, strain and AE behavior during individual yield points. From the data generated and analysis of the same, the following conclusions are possible:

1. It is possible to identify three separate and distinct regions when a stress drop is measured as a function of time.
2. A distinct burst of AE is generated during every yield point.
3. Careful time resolution of the data reveals that the AE activity starts before there is any indication of a drop in stress.
4. The calculated strain rate during the stress drop of a yield point was found to be as high as  $30 \text{ s}^{-1}$ , or  $10^6$  times larger than the applied strain rate.
5. For a given impurity concentration, there exists a correlation between the magnitude of the drops in stress and the AE generated.
6. As the impurity concentration increases, the correlation between the stress drop and the magnitude of the AE deteriorates.

## References

D. L. Armentrout (1991), Ph. D. Dissertation, University of Denver, Denver, CO.

D.L. Armentrout and S.H. Carpenter (1991), *Proc. 4th World Meeting on Acoustic Emission and 1st International Conference on Acoustic Emission in Manufacturing*, ASNT, Columbus, OH, p. 50.

E. O. Hall (1970), *Yield Point Phenomena in Metals and Alloys*, Plenum Press, New York, NY.

C.R. Heiple and S.H. Carpenter (1987), *J. Acous. Emis.*, 6, 171.

D. Hull (1975), *Introduction to Dislocations*, 2nd ed., Pergamon Press, New York, NY.

W.M. Lomer (1952), *J. Mech. and Phys. of Solid*, 1, 64.

A.W. McReynolds (1949), *Trans AIME*, 185, 32.

W.G. Moffatt (1995), *The Handbook of Binary Phase Diagrams*, vol. 1, Genium Pub. Corp., Schenectady, NY.

D.W. Moon (1971), *Mater. Sci. Eng.*, 8, 235.

J.G. Morris (1974), *Mater. Sci. Eng.*, 13, 101.

V.A. Phillips, A.J. Swain and R. Eborall (1953), *J. Inst. Met.*, 81, 625.

E. Pink (1989), *Acta Metall.*, 37, 1773.

P. R. Sperry (1963), *Acta Metall.*, 11, 153.

T. Tabata, H. Fujita and Y. Nakajima (1980), *Acta Metall.*, 28, 795.

# Modal Analysis of Acoustic Emission Signals

H.L. Dunegan

## Abstract

This report shows the results of a continuing study to determine the type of waves present in plates of different thickness created by breaking pencil leads in-plane (IP) and out-of-plane (OOP) on the plates and by detecting the resulting stress waves with a high fidelity acoustic-emission transducer mounted on the edge and surface of the plates. The results show that the extensional velocity over the range of plate thickness from 3.13 to 12.5 mm does not change, and the flexure wave is dispersive in accordance with plate wave theory. The procedure in this work split the signal into two frequency ranges, a high frequency range with a 100 kHz high-pass filter and a low frequency range with a 20-70 kHz bandpass filter. This frequency split provided an easy method of measuring the velocity of the low frequency flexure wave. A bulk shear wave, not predicted by plate wave theory was observed along with the extensional wave in the high frequency channel. In order to confirm the presence of the shear wave, two shear plates, one with particle motion vertical to the plane of the plate and the other parallel to the plane of the plate were attached to the end of one of the bars. These transducers were used as receivers for IP and OOP pencil-lead breaks, and also as transmitters excited by a 150-V spike pulse. Both the Sv and Sh waves, created with pulsing, could be detected with a transducer mounted on the surface with petroleum jelly. The Sh wave had a much higher amplitude than the Sv wave. The results show that mode conversion of the Sv wave to a flexure wave occurs, as it propagates down the bar, which partially accounts for its loss of amplitude. From this study, it is suggested that the crack growth signal detected by most AE tests on large thin-wall structures utilizing 100 kHz high-pass filtering, resonant transducers, and large transducer spacing, is the Sh wave created by crack propagation.

## 1. Introduction

Over three decades ago, Worlton (1961) published his paper, "Experimental Confirmation of Lamb Waves at Megacycle Frequencies". This work was received with great enthusiasm by researchers using ultrasonic techniques

for nondestructive testing (NDT), and the results of this work find continuing use today in ultrasonic NDT applications. Researchers in acoustic emission (AE) testing, who began a few years later, largely ignored applications of Lamb's theory to analyzing AE data. One reason this occurred is due to the fact that most of the early AE experiments were conducted on small specimens, where the theory is not applicable. The second reason is that ultrasonic researchers can transmit a harmonic wave to select the mode desired for a given plate thickness, while AE researchers are faced to deal with waves generated by a transient event and therefore such selection is denied.

Gorman (1990) discussed the use of plate wave theory to the AE testing of thin plate-like specimens. According to the theory, there are two modes of propagation. One is called the extensional and the other the flexural mode. The extensional mode is non-dispersive and the flexural mode is dispersive. This work and the following work by Gorman and Prosser (1991) sparked a great interest on the part of the author in starting an experimental program to study the wave modes in plates. Most of the prior published experimental data was obtained from thin composite plate specimens. This author's primary interest was in finding out if the theory was applicable to thicker plates constructed from steel and aluminum. Experiments were conducted on 6.25 mm and 12.5 mm thick steel bars, 1.2 m in length (Dunegan, 1996). It was discovered from the start that a signal traveling at the shear velocity of steel was present in most of the data. It was also found in this study that analog filtering of the signal into two frequency bands; 100 kHz - 1 MHz and 20 - 70 kHz would allow for separation of the extensional and flexure modes. The extensional-mode wave and shear wave always appear in the high frequency passband and the flexure wave in the low frequency passband. The purpose of this report is to show results of a more intensive study on the presence and detectability of shear waves in plates, as well as the results of a study to determine the dispersive nature of plate waves in the thickness range between 3.13 mm and 12.5 mm.

## 2. Procedures

The specimens chosen for the study (see Fig. 1) were three steel bars 1.05 m in length, by 75 mm in width, with three different thickness; 12.5 mm, 6.25 mm and 3.13 mm. The first experiment conducted on these steel bars was to bond a high fidelity broadband transducer (DECI SE 1000-

Received 23 October 1997. The author (hal@deci.com) is affiliated with Dunegan Engineering Consultants Inc., PO Box 1749, San Juan Capistrano, CA 92693.

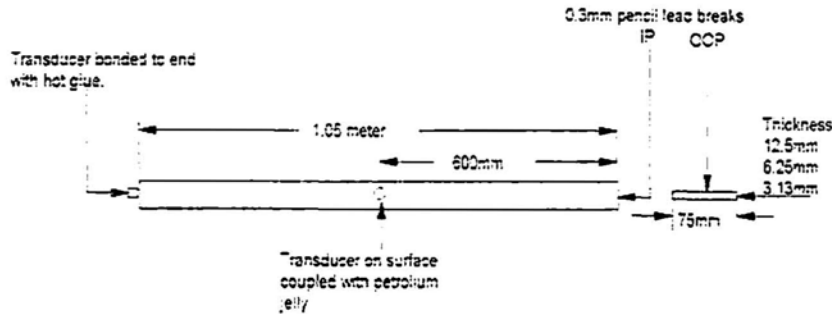


Fig. 1 Schematic of the placement of transducers on steel bars, and location where pencil-lead breaks are made on bars.

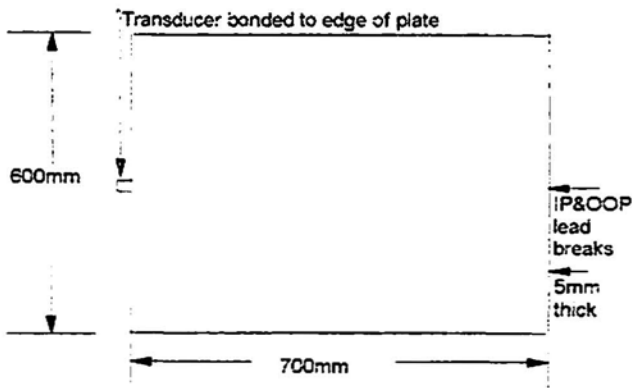


Fig. 2 Schematic of aluminum plate used in experiments.

H) to one end of each bar and make 0.3 mm pencil-lead breaks both in-plane (IP) and out-of-plane (OOP) at the other end of the bar.

Per prior experimental results (Dunegan, 1996), different modes present in plates can be observed by splitting the signal from the AE transducer into two frequency components: 100 kHz-1 MHz and 20-70 kHz. We used AE-SMART 2000 instrument designed to split the AE signal into these two frequency bands. Amplified and filtered AE signals from these high and low frequency channels were recorded by a digital oscilloscope and Paintbrush software was used to present the data. For the 12.5-mm-thickness plate used in the previous study, the arrival time of the high-frequency shear wave very closely matched the arrival time of the low frequency flexure wave and it was initially thought that the high frequency wave was simply the high frequency components of the flexure wave. What seemed to contradict this scenario was the fact that the high-frequency wave traveling at the shear velocity was still present when pencil-lead breaks were made in the exact center of the edge of the plate. The symmetry produced by this condition does not produce flexure-wave components in the plate. Consideration was given to the finite width of the bars being used, as a possible reason for the presence of this high-frequency wave. Therefore, another experiment was chosen using a large aluminum plate. The dimensions of the plate are 600 mm x 700 mm x 5 mm, as shown in Fig. 2. Again,

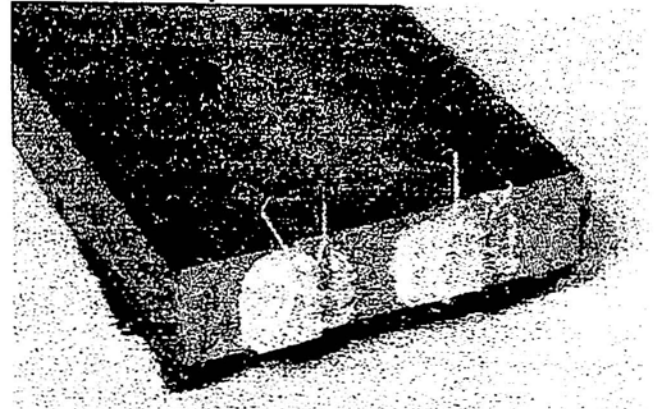


Fig. 3 Horizontal and vertical shear elements bonded to the end of a 12.5 mm thick steel bar.

an SE 1000-H high fidelity transducer was bonded to the center of the 600-mm edge and both IP and OOP pencil-lead breaks were made at the opposite center of the other 600-mm edge, giving 700 mm of travel for the simulated AE signal.

A third experiment was conducted in order to determine the efficiency of a transducer coupled to the surface of the plate in detecting shear waves of different polarization traveling in the plate. Two piezoelectric shear elements were bonded to the end of a 12.5-mm-thick steel bar, 1.2 m in length (Fig. 3). The bar had damping material on the bottom side. One of the shear elements was oriented such that particle displacement was vertical to the plane of the bar and the other with particle displacement parallel to the plane of the bar. OOP- and IP-type 0.3-mm-pencil-lead breaks were made at the opposite end of the plate, and the signals from each of the shear elements were recorded. The shear elements were then used as transmitters by connecting a 50-V spike pulse to each in turn. Receiving transducers were placed at 600 mm on the surface of the bar and coupled with petroleum jelly.

### 3. Experimental Results

#### 3.1 Edge-mounted High-fidelity Transducer

Figure 4 shows the data obtained from the high-fidelity transducer, which was bonded to the end of three steel bars

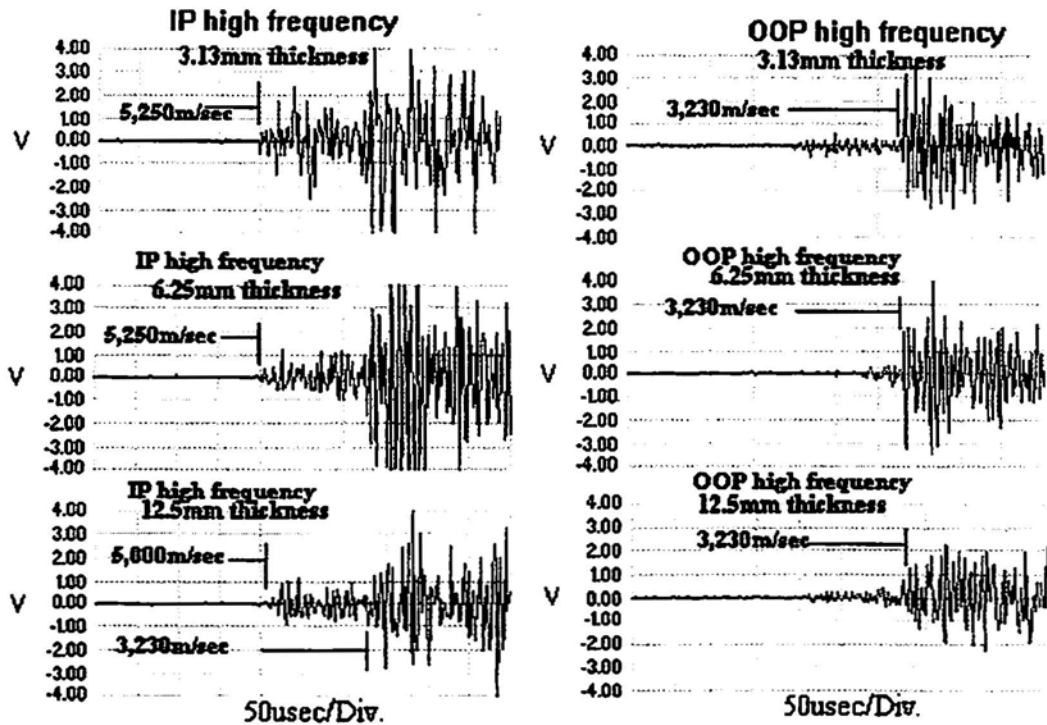


Fig. 4 SE 1000-H transducer bonded to the end of 3 steel bars 1.05 m in length and varying thickness as indicated above. IP- and OOP-type 0.3-mm-pencil-lead breaks were made at the opposite ends of the bars. Note that a signal arriving at a velocity of 3,230 m/s is present in all the data regardless of thickness.

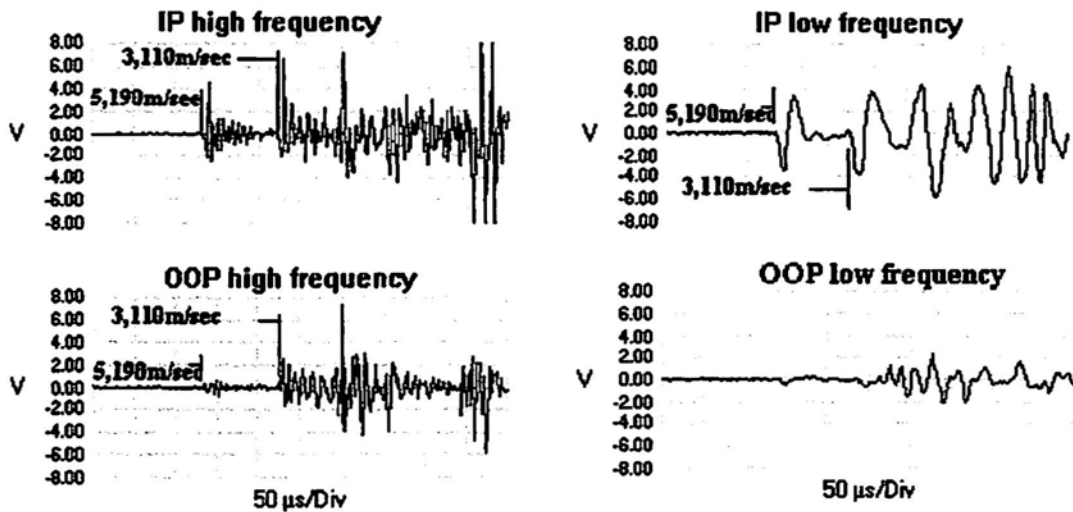


Fig. 5 SE 1000-H bonded to center 600-mm edge of a 600 mm x 700 mm aluminum plate, 5 mm in thickness. IP- and OOP-type 0.3-mm-pencil-lead breaks at opposite edge from the transducer with 700 mm of wave travel. 60 dB gain, AESMART 2000.

of different thickness. OOP- and IP-type 0.3-mm-pencil-lead breaks were made at the opposite end of each bar. Note that some dispersion is observed in the first arrival signal (extensional wave) in the high-frequency in-plane (IP) channel as a function of thickness of the bars. Also note the presence of a large signal arriving at approximately 325  $\mu$ s from each of the bars. Since this signal arrives at the same time regardless of the thickness of the bar and exhibits a velocity equal to the shear velocity of steel, one must as-

sume that it is a shear wave and not a high-frequency flexure wave. Note that only faint evidence of the extensional wave is present from the OOP high frequency channels, and, similar to the IP channels, a large signal traveling at the shear velocity in steel is observed from each of the bars. An OOP-type pencil-lead break apparently produces a vertically polarized shear wave in addition to the large amplitude flexure wave more clearly observed at lower frequencies. Again, argument for this wave being a shear wave

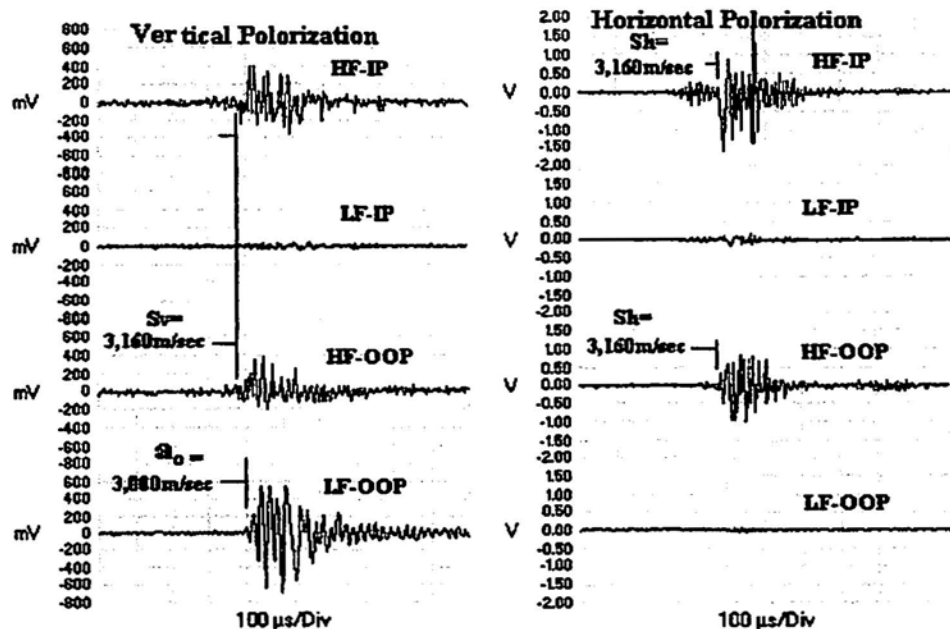


Fig. 6 Vertical and horizontal shear elements were bonded to the end of a 1.2 m steel bar, 12.5 mm thick. Out of plane (OOP) and in-plane (IP) 0.3-mm-pencil-lead breaks were made at the opposite end. Signals recorded in two frequency ranges, HF=100-1000 kHz, LF=20-70 kHz. Trigger transducer for the digital scope was adjacent to lead breaks. Note vertical scale difference. 40 dB gain.

comes from the fact that the arrival time of the signal is the same regardless of the thickness of the bar. If this were a high frequency flexure wave, which is dispersive, one would expect to see arrival times that differ as a function of plate thickness.

All of the steel bars were 75 mm in width. In order to test whether or not the arrival of what appears to be a shear wave was not an artifact due to side reflections from the finite width of the bar, the large aluminum plate shown in Fig. 2 was utilized. It is wide enough to prevent any side reflections from reaching the transducer prior to the arrival time for the shear wave. The data from the aluminum plate is shown in Fig. 5. Note that the IP- and OOP-high-frequency channels, and the IP-low-frequency channel show the arrival times of an extensional wave and the shear wave. Note the lack of signal strength from the OOP-low-frequency channel. Apparently, the small aperture, high-fidelity transducer (SE 1000-H) bonded to the edge of the plate is fairly unresponsive to the large low frequency flexure wave generated by an OOP source, but is responsive to the low frequency components of the shear wave from the IP source.

Further confirmation of the presence of a shear wave in the steel bars, and the ability of AE transducers in detecting the shear waves of different polarization was the motivation for conducting experiments on the bar shown in Fig. 3. Two shear elements were fabricated from PZT-5 material and bonded to the end of a 12.5-mm-thick steel bar 1.2 m in length. The bottom side of this bar was coated with a

damping material. IP- and OOP-type 0.3-mm-pencil-lead breaks were made at the opposite end. A trigger transducer was located adjacent to the pencil-lead-break region in order to provide a time trace to measure velocities. Figure 6 shows the response of the shear elements to the pencil-lead breaks. First of all, note the difference in vertical scale. The horizontally poled element gave more than twice the signal as the vertically poled element. One reason for this is the damping material on the bottom of the bar attenuated the Sv wave, but had minimal influence on the Sh wave as would be expected. Another reason is that some of the energy of this shear wave is mode-converted into a low-frequency flexure wave as indicated by the large signal detected in the low frequency channel. Note the lack of signal in the low frequency (LF) channel of the element with horizontal polarization. The OOP source created a low-frequency flexure wave in the bar, which was detected by the vertically poled element as would be expected. The LF-OOP channel from the horizontally poled crystal was not responsive to this flexure wave since the particle motion was 90° from the poling direction. A slight hint of a shear-wave arrival is present in both LF-IP channels. Most of the Sh wave energy is displayed in the high frequency (HF-IP) channel for the horizontally polarized element. Note that the anti-symmetrical wave (LF-OOP) from the vertically poled element has a velocity very close to the shear velocity measured by both the vertically and horizontally poled high frequency channels. Also note that a small signal traveling at the extensional velocity precedes the arrival of the Sh wave in the HF-IP horizontally poled channel. It is almost impossible to

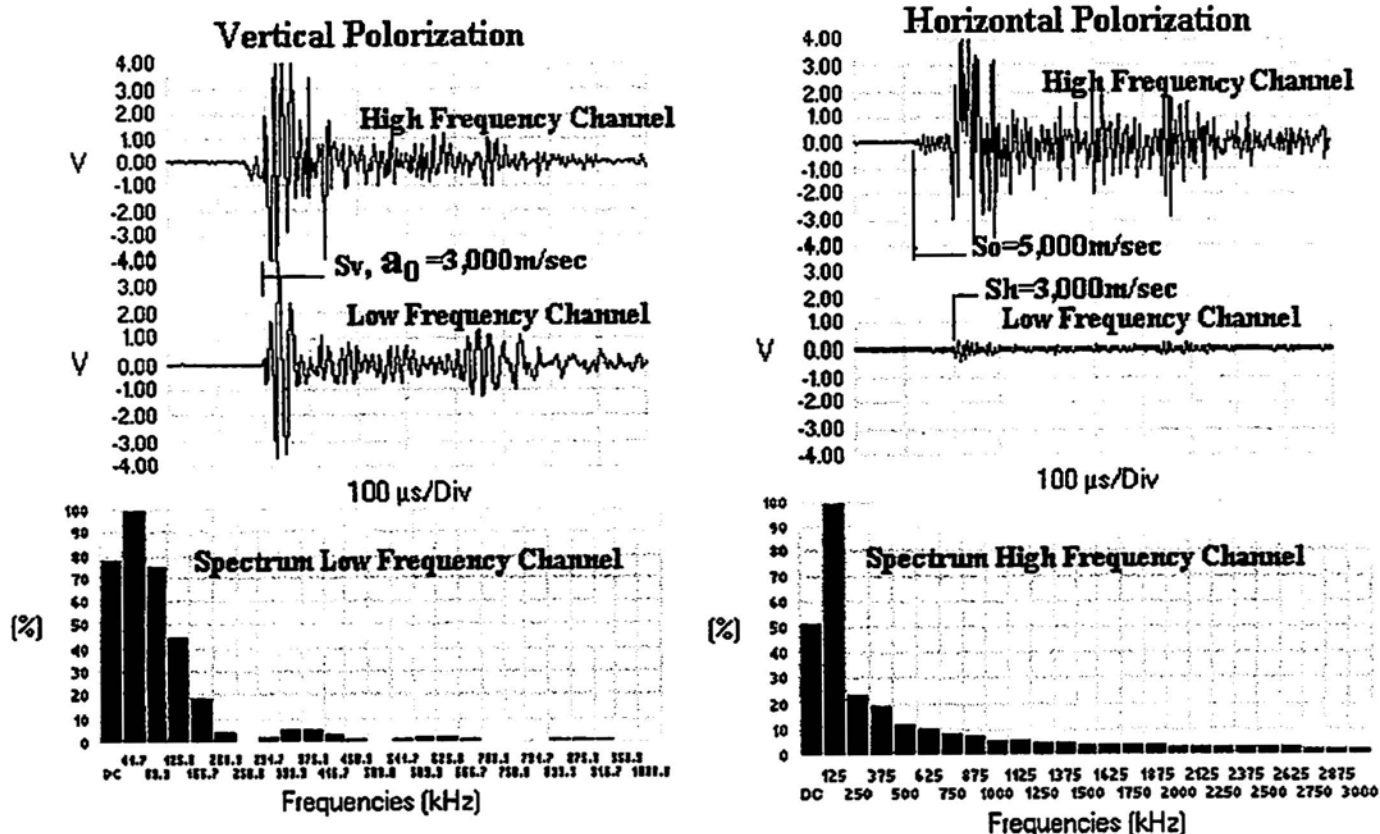


Fig. 7 Vertically and horizontally polarized shear elements were bonded to the end of a 1.2 m steel bar, 12.5 mm thick with damping material on the bottom side. A high fidelity transducer was coupled to the bar with petroleum jelly at 600 mm distance from the shear elements. Each shear element was excited with a 50-V spike pulse.

fabricate a "pure" shear element from PZT plates, so a certain amount of cross coupling is to be expected.

### 3.2 Surface-mounted Transducers

It is shown in Fig. 6 that both IP- and OOP-pencil-lead breaks produce shear waves in the steel bars. The next step in the experimental program was to determine how effectively an AE transducer mounted on the surface can detect shear waves having polarization parallel to the plate. Again a high fidelity transducer (SE 1000-H) was coupled with petroleum jelly at 600 mm on the 1.2-m bar, on which the shear PZT plates were bonded. Each of the shear PZT plates was pulsed with a 50-V spike pulse and resultant signals were detected by the SE 1000-H. Figure 7 shows the results of this experiment. One of the surprising results of this experiment was the presence of the high amplitude signal from the horizontally poled PZT plate. Since the particle motion is parallel to the surface, on which the transducer is mounted, it was expected that not much signal would couple through the petroleum jelly. The low frequency channel in Fig. 7 did not detect the  $S_h$  wave very effectively. A hint of a signal is present in the low frequency channel with arrival time corresponding to the  $S_h$  wave, but it is insignificant compared to the amplitude of the high frequency  $S_h$  wave. Again, a hint of an extensional wave arrival is

present in the high frequency channel. The frequency spectrum of this channel shows a predominant peak at 125 kHz.

The transducer responded to signals from the vertically poled PZT plate in both the high frequency and low frequency channels. It is apparent that the  $S_v$  wave excites the low frequency flexure wave as would be expected. The data suggests that the high frequency response is a direct measure of the  $S_v$  wave. As seen previously, both the  $S_v$  wave and the low frequency flexure waves have approximately the same arrival time (or velocity) for this plate thickness. The frequency spectrum of the low frequency channel shows maximum response in the 50 kHz range, which correlates with previously observed frequencies of the low frequency flexure wave.

The next experiment involved attaching a transducer at 800 mm on each of the three bars of different thickness. (This longer distance was used in order to obtain more accurate velocity measurements). IP- and OOP-pencil-lead breaks were made at the ends of each bar. Figure 8 shows the high and low frequency response on the three bars to OOP-pencil-lead breaks. A voltage range on the oscilloscope was set at a high sensitivity in order to detect the leading edge of the signals for the purpose of making velocity measurements on the different waves. Note that on

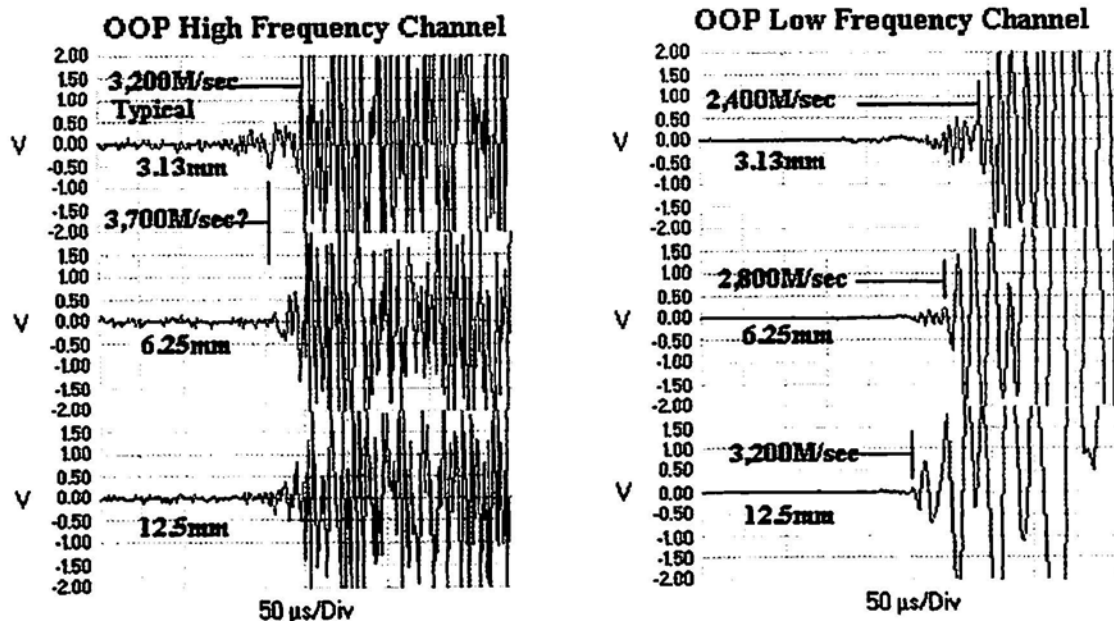


Fig. 8 A high fidelity transducer (SE 1000-H) at 800 mm on three steel bars of varying thickness. Out-of-plane (OOP) 0.3-mm-pencil-lead breaks were made at the end of each bar. 40 dB gain.

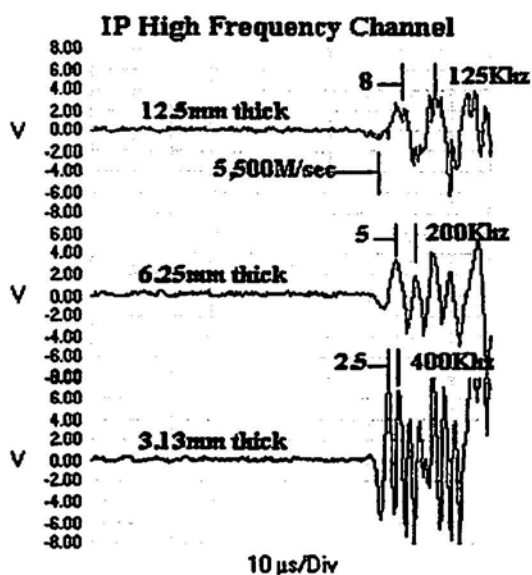


Fig. 9 A high fidelity transducer (SE 1000-H) at 400 mm on three different thickness bars. Showing a response to IP 0.3-mm-pencil-lead breaks at the end of the bar. High frequency channel of AESMART 2000, 60 dB gain.

the high frequency channel for each bar a signal with a velocity of 3,200 m/s is observed from all three bars. This constant velocity regardless of thickness along with a value of 3,200 m/s shows these waves to be shear waves. Note in the high frequency data a small amplitude signal having a velocity of 3,700 m/s. The question mark following the velocity value indicates that the mode for this wave is unknown. It might possibly be a first order anti-symmetrical Lamb wave. The signals observed on the low frequency channel have a varying velocity, which is dependent on

plate thickness. This is the type of results one would expect from the zeroth order anti-symmetrical Lamb wave.

There was also an interest in determining if the primary frequency content of the IP- and OOP-source signals could be determined easily. The transducer was re-positioned to 400 mm on the bars and the time base was expanded in order to show more detail of the leading few cycles of the signals. Figure 9 shows the response of the high fidelity transducer to IP-pencil-lead breaks at the opposite end of each bar. One can see from this data that there is no apparent change in the extensional velocity as a function of plate thickness. There is a definite difference in the frequency content of the signals. The frequency of the signal was estimated by measuring the time in  $\mu\text{s}$  between the first two positive going peaks and dividing this value into 1. Note that the thinner the plate, the higher the frequency content, and the higher the amplitude of the signal of these extensional waves. The primary frequencies measured in this manner were:

- 125 kHz for the 12.5 mm bar,
- 200 kHz for the 6.5 mm bar, and
- 400 kHz for the 3.13 mm bar.

The same procedure was repeated with the exception that OOP-pencil-lead breaks were made at the end of the bar in order to create a low frequency flexure wave in each bar. Again, the time in  $\mu\text{s}$  was measured between the first two positive peaks in order to estimate frequency content. This data is shown in Fig. 10. Observe that the frequency content and amplitude of the signals increases as the bar gets thinner. This is similar to results for extensional waves. The primary difference in the low frequency data is the velocity dispersion, which was not present in the high fre-

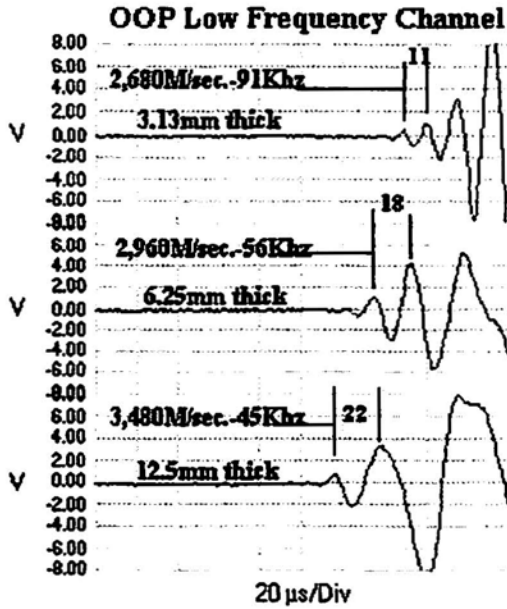


Fig. 10 A high fidelity transducer (SE 1000-H) at 400 mm on three different thickness steel bars. Response to OOP 0.3-mm-pencil-lead breaks at the end. Low frequency channel of AESMART 2000, 40 dB gain.

quency extensional wave data. This increase in amplitude as the bar gets thinner for both the extensional waves and flexure waves is an indicator that the surface displacement is greater in the thinner bars. The velocity dispersion of this low frequency wave as a function of thickness, shown in Fig. 8, is repeated in this data. The velocity measurements

in Fig. 10 differ from those in Fig. 8 by approximately 200 m/s, but the relative differences remain in the same proportion. Note at this sensitivity that the high frequency precursor for the two thinner plates that was present in Fig. 8 are absent from this data. The primary frequencies measured for the data were:

- 45 kHz for the 12.5 mm bar,
- 56 kHz for the 6.5 mm bar and
- 91 kHz for the 3.13 mm bar.

Figure 11 shows the group velocities for the first three modes of the symmetrical (So) and anti-symmetrical (Ao) Lamb waves against thickness-frequency in mm-MHz. Below these curves are corresponding values in kHz for the three steel bars used in these experiments. The smaller numbers on the ordinate are group velocities measured in this study (Figs. 8 and 9). These values were projected horizontally until they intersected with the proper wave mode. Projections (small dotted lines) from these intersections were then made vertically until intersection was made with the bar, from which the velocities were measured. Some interesting observations can be made from this data. Note that the zeroth order symmetrical mode velocity (So) for all three thickness plates is constant and its projection to the three different plate thickness results in a frequency of approximately 70 kHz for the 12.5 mm plate, 140 kHz for the 6.25 mm plate and 280 kHz for the 3.13 mm plate. These values favorably compare with the measured values in Fig. 9 considering the possible errors present in only measuring the time between the first two cycles of the signals. Observe that the zeroth order anti-symmetrical mode (Ao) for the

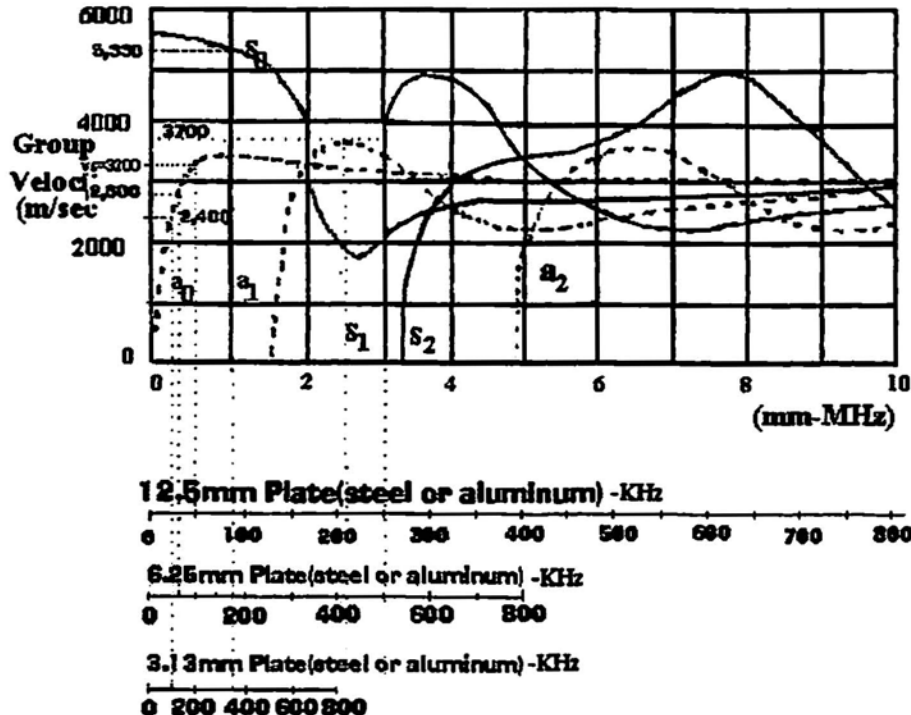


Fig. 11 The group velocities for the first three modes of the symmetrical (So) and anti-symmetrical (Ao) Lamb waves against thickness-frequency in mm-MHz.

same bars decreases in velocity such that projection onto the respective bars yields a frequency of 50 kHz for the 12.5 mm bar, 60 kHz for the 6.5 mm bar and 100 kHz for the 3.13 mm bar. These results also compare favorably with the measured results in Fig. 10.

#### 4. Discussion of Results

The stress wave produced in a plate by an impulse source such as breaking of a 0.3-mm pencil lead appears to partition the majority of its energy into three primary waves: The  $S_0$  symmetrical Lamb wave (extensional), the  $A_0$  anti-symmetrical Lamb wave (flexural) and a shear wave. The amount of energy carried by the extensional and flexure waves depends strongly on whether or not the source direction is in-plane or out-of-plane with respect to the plate dimensions. The amplitude of the shear wave is not so dependent on source orientation, since it can travel in the plate with different polarization. For OOP sources, a strong flexure wave is produced with little extensional component, and for IP sources a strong extensional wave is produced with lesser amounts of the flexure-wave component depending on the depth in the plate where the source originates (Hamstad et al., 1994).

Figure 4 shows the dependence of the extensional wave on source orientation. For the OOP case, the extensional wave components are very weak, but note that the shear-wave amplitude is approximately the same for both source inputs in the high frequency range. Another example of the effect of orientation is shown by Fig. 8, which shows a lack of extensional component in the OOP-high-frequency range and a strong shear wave. The OOP-low-frequency range for this figure shows a strong flexural wave and a lack of extensional- and shear-wave components. This is further indication that the extensional and shear waves are high frequency phenomenon and do not have frequency components below 100 kHz in plates of the thickness used in this study. Note here that the above test utilized a high-fidelity displacement transducer (SE 1000-H) coupled to the surface of the plate with petroleum jelly. Surprisingly, this arrangement detects the displacement due to high-frequency shear waves.

The above statement is contradicted by the data shown in the IP-low-frequency range of Fig. 5. Both extensional and shear waves having low frequency components were detected in this example. However, the test utilized a high-fidelity displacement transducer (SE 1000-H) bonded to the edge of the plate. It was capable of detecting low-frequency extensional waves, and apparently shear waves as well, in the plate due to its high sensitivity to displacement and broad frequency response. From a practical standpoint, it would be rare that access to the edge of a plate would be available, since in most instances the transducer is placed on the surface of the plate.

It has been observed throughout this study that the shear wave is present for both IP and OOP sources and its amplitude is much higher than the amplitude of the extensional wave. This leads to the following hypothesis. For IP sources both  $S_h$  and  $S_v$  shear waves are launched by the pencil-lead break at the edge of a plate. The  $S_v$  wave will lose energy due to any damping material on the surfaces and due to transfer of energy through mode conversion to a flexural wave. The  $S_h$  wave, which has particle motion parallel to the plate surface, will propagate without mode conversion. This is indicated by the data in Fig. 6, which shows that the  $S_h$  wave has more than three times the amplitude of the  $S_v$  wave. For the OOP source in Fig. 6, a strong flexural wave is detected by the vertically poled PZT element in the low-frequency channel, while no such wave is detected by the horizontally poled PZT element in the same frequency band.

Further evidence of this partitioning of energy between modes is shown in Fig. 4. For an IP source at the center edge of the plate, a partitioning of energy is shown by the IP-high-frequency channel between the extensional and shear waves (no low-frequency flexural wave is created by this source). The OOP-high-frequency amplitude of the shear wave is less than the IP-high-frequency amplitude due to energy partition to a low frequency flexural wave (not shown). Therefore, it appears that one can expect higher amplitude shear waves from IP sources than from OOP sources. If one assumes that the IP-pencil-lead break truly represents the growth of a crack, the  $S_h$  wave is the strongest high-frequency wave produced and is probably the predominant wave detected in most field tests using AE instrumentation with high-pass filtering above 100 kHz, resonant sensors, and large transducer spacing. The data in Fig. 7 shows that it does not matter whether or not a displacement at the surface is present in order to detect stress waves, a shear wave with polarization parallel ( $S_h$ ) to the surface will excite the transducer as well as a displacement of the surface if the coupling material has enough stiffness to couple the shear wave to the transducer. Apparently a thin layer of petroleum jelly is sufficient to transfer the energy to the transducer for higher frequency/shorter wavelength signals but not for signals having frequencies below 100 kHz, as indicated by a lack of data in the low frequency channel. The same transducer was used for the data in Fig. 7 and in Fig. 5 where a low-frequency shear wave was apparently detected. For the situation of Fig. 5 where the transducer was on the end of the bar as opposed to being on the surface of the bar (Fig. 7), the detected wave corresponding to the shear-wave velocity could have been mode-converted signals that created a displacement at the end of the bar.

The data in Figs. 4 and 5 show a comparison of the high fidelity transducer bonded to the end of three steel bars and the large aluminum plate. Both sets of data show the arrival of the extensional wave and shear wave. The data

from the aluminum plate is "cleaner", due to a lack of any edge reflections prior to approximately 500  $\mu$ s. There is some evidence of side reflections from the bar data, but it occurs after the arrival of the shear wave. Therefore, if one is only interested in studying the extensional and shear wave arrival in the high frequency range, and the flexure mode in the low frequency range, the finite width bars are suitable subjects for investigating plate waves. The width-to-thickness ratio for the three bars used in this study ranged from 12 for the thicker bar to 48 for the thin bar. There is no obvious difference in the appearance of the signals in Fig. 4 due to this wide difference in ratio.

The data in Fig. 9 shows that the extensional wave velocity remains constant for the three thickness bars used in this study. This is only obvious when increasing sensitivity to view the leading edge of the signals. When viewing the signals such that the shear wave signal remains on scale, there is an "apparent" decrease in velocity when going from the 6.25 mm to the 12.5 mm bar (Fig. 4). The data in Fig. 10 shows the frequency and velocity variation of the Ao wave as a function of bar thickness. The frequency differences are small and are only measurable due to the high fidelity response of the transducer used in these measurements. Favorable correlation of these frequencies to those obtained from the measured velocities and projection from the group velocity curves to each bar in Fig. 11 further shows that splitting the signal into a high and low frequency range prior to making velocity measurements allows a high degree of accuracy in measuring the velocity of the slower flexure waves.

## 5. Conclusions

Results of this investigation have shown that for transient signals produced by breaking of 0.3-mm pencil lead on plates of thickness ranging from 3 to 12.5 mm, useful signals from the acoustic emission standpoint are only present from extensional waves, zeroth order anti-symmetrical Lamb waves, and a shear wave. For plate thickness greater than 3.1 mm, the first two zeroth order Lamb modes are predominant at frequencies below 200 kHz. Plate wave theory only predicts two waves for thin plates: A non-dispersive extensional wave, and a dispersive flexure wave. This study shows that a strong shear wave is generated in a plate by both OOP and IP pencil-lead breaks. This signal unlike the normal Lamb modes associated with wave propagation in plates is non-dispersive and therefore travels at a constant velocity regardless of plate thickness and frequency. It is consistently higher in amplitude than the extensional wave, and is the primary wave detected by AE transducers in field testing of large structures when working at frequencies above 100 kHz.

This report has shown that an AE transducer is capable of detecting both Sv and Sh waves and that the Sv waves lose energy due to mode conversion and damping material

on the plate surface while the Sh wave is not affected by either. It is further shown that the detected shear wave has very little frequency content below 100 kHz. Therefore, it is postulated that it is the Sh wave that is detected from crack growth as well as noise from impact and friction (since it is generated by both IP and OOP sources) on large plate-like structures such as pressure vessels, piping, and bridges by AE transducers with large spacing. Since the larger aperture resonant AE transducer has a higher sensitivity in detecting the high frequency shear wave over a smaller aperture high fidelity sensor (Dunegan, 1995, 1996), its use for field testing of large structures is justified. Since the shear wave is generated by both OOP (or noise) sources and IP (or crack growth) sources, the resonant transducer alone will not provide the type of data needed to separate crack-like signals from noise. Best identifier of OOP (noise) sources is the zeroth order anti-symmetrical Lamb wave (Ao). It is further shown that finite width bars can be used effectively for the study of the zeroth order plate modes and the shear mode without influence from side reflections since they arrive later than the shear wave in the high frequency channel and higher order Lamb wave modes are not present in the low frequency channel.

## References

- Harold L. Dunegan (1995), "The Effects of Aperture Size and Mass Loading on the Response of AE Transducers to Plate Waves," presented at the 38th AEWG Conference, NASA Langley Research Center, May 1-4.
- Harold L. Dunegan (1996), "Use of Plate Wave Analysis in Acoustic Emission Testing to Detect and Measure Crack Growth in Noisy Environments", Proceedings of Structural Materials Technology - An NDT Conference, Feb. 20-23, San Diego, California.
- Michael R. Gorman (1991), "Plate Wave Acoustic Emission", J. Acoustical Society of America, **90**(1), July, 358-364.
- Michael R. Gorman and William H. Prosser (1991), "AE Source Orientation by Plate Wave Analysis", J. Acoustic Emission, **9**(4), 283-288.
- M.A. Hamstad, S.L. Quarles and R.L. Lemaster (1994), "Experimental Far-field Wideband Acoustic Waves in Wood Rods and Plates", 9th International Symposium on Nondestructive Testing of Wood, organized by Roy Pellerin and Kent A. McDonald, Sep. 22-23, 1993, Forest Products Soc., Madison, WI, pp. 30-44.
- D.C. Worlton (1961), "Experimental Confirmation of Lamb Waves at Megacycle Frequencies", J. Applied Physics, **32**(4), June, 967-971.

# Meeting Calendar

## **Ninth Annual Symposium on Nondestructive Characterization of Materials**

June 28 - July 2, 1999, Novotel Hotel at Daring Harbor, Sydney, Australia  
Contact: Robert E. Green Jr., The Johns Hopkins University, Baltimore, MD; Don Price  
CSIRO, Sydney, Australia  
Abstracts due: December 4, 1998  
E-mail: [cnde@jhu.edu](mailto:cnde@jhu.edu); [www.cnde.com](http://www.cnde.com); phone (410) 516-7126

## **Acoustic Emission '99**

An international conference commemorating the 150<sup>th</sup> anniversary of Technical University in Brno  
Sponsored by Technical University of Brno and Czech Society for Nondestructive Testing.  
CONTACT: Pavel Mazal, Technical University, Faculty of Mech. Engineering, Institute of Design  
Technická 2, Brno, CZ 616 69  
Abstracts due: September 30, 1998  
E-mail: [mazal@cms.fme.vutbr.cz](mailto:mazal@cms.fme.vutbr.cz); <http://cmspro.fme.vutbr.cz>

## **The 41<sup>st</sup> AEWG Meeting**

September 1999, Princeton, NJ  
Contact: S.J. Vahaviolos, [sales@pacndt.com](mailto:sales@pacndt.com)

# Recent Books on AE

## **Progress in Acoustic Emission IX**

the Proceedings of 14th International Acoustic Emission Symposium & 5th Acoustic Emission  
World Meeting, *Transitions in AE for the 21st Century*.

Proceedings volume (480 pages, 1998): Published jointly by the Acoustic Emission Working  
Group (AEWG) and the Acoustic Emission Group (Suite 106, 16350 Ventura Blvd, Encino, CA  
91436 USA). For ordering copies (\$120 each + applicable sales tax (CA only, 8.5%) and  
shipping), contact Acoustic Emission Group (fax 818-990-1686) or send e-mail to [ono@ucla.edu](mailto:ono@ucla.edu).

Shipping: US: \$5; All other countries: \$7; Air mail to S. America: \$18; Air to Europe: \$27; Air to  
other contries: \$35.

Proceedings of previous International Acoustic Emission Symposia can be purchased from  
Japanese Society for Non-Destructive Inspection, Natsume No. 5 Building, 67 Kanda-  
Sakumagashi, Chiyoda, Tokyo 101, Japan.

## **Proceedings**

22nd European Conference on Acoustic Emission Testing, Aberdeen, Scotland : May 1996

Order to be sent to: Meg Thain, Univation, The Robert Gordon University, Kepplestone, Queen's  
Road, ABERDEEN AB9 2PG UK. Cost: £40 including shipping.  
Fax: 01224 263323 / Tel: 01224 263322

# An Acoustic Emission Tester for Aircraft Halon-1301 Fire-Extinguisher Bottles

Alan G. Beattie

## Abstract

An acoustic emission test for aircraft Halon-1301 bottles has been developed, a prototype acoustic emission test system constructed, and over 200 used bottles tested at the repair facilities of the two manufacturers of these bottles. The system monitors a bottle with six acoustic emission sensors while its pressure is raised by heating it in an oven. The sensors are held in position with a fixed relationship between them by a special fixture. This fixture was designed to fit spheres with diameters between 127 and 406 mm (5" and 16"). Results of the tests on used bottles indicate that over 95% of the bottles showed no indication of significant defects. The rest had some indication of flaws or corrosion. However, all bottles tested to date have passed the hydrostatic test required by the U.S. Department of Transportation.

## 1. Introduction

Many of the world's commercial jet aircraft use spherical bottles containing pressurized Halon 1301 (CF<sub>3</sub>Br) to extinguish fires of an engine, an auxiliary power unit, and cargo hold. The regulations of the U.S. Department of Transportation (DOT) require periodic testing of these bottles for structural integrity. The only test method currently approved by the DOT regulations is a hydrostatic test for inelastic expansion of the bottles.

To perform a hydrostatic test, the permanently sealed bottle is first cut open and the halon removed. The bottle is then hydrostatically pressurized to twice its marked service pressure in a water bath. The displacement of the water is measured both at the maximum pressure and after the release of the pressure. The elastic and inelastic expansion are determined from the data. If the inelastic expansion exceeds 10% of the total expansion, the bottle is rejected. After testing, the bottle is then refilled with Halon 1301, resealed, and returned to service. The test primarily detects thinning

of the wall due to corrosion, not flaws in the bottle. Gross corrosion has not been a problem in recent years. The few bottles that have failed the hydrostatic test recently (aside from experimental error) exploded during the test. Thus, the hydrostatic test has effectively become a go/no-go proof test. Another problem is that the procedure of cutting open a bottle and then resealing it by welding removes metal and can introduce new weld defects.

The production of Halon 1301 was banned in January 1994 by international agreement due to the ozone depleting properties of halon. At this time, no substitute material exists, which combines both Halon 1301's outstanding fire extinguishing effectiveness and low toxicity. The U.S. airline industry has been granted an exemption by the DOT to continue using Halon 1301 through the year 2000. The cost of halon from existing stores has rapidly increased even though halon from the bottles undergoing a hydrostatic test is recovered, purified, and reused. A test of the bottle's integrity, which does not require the opening of the bottle, would save time and expense for the airline industry as well as eliminating one source of loss of the world's Halon-1301 supply.

In the past, the DOT has granted exemptions, which allow acoustic emission (AE) testing in place of the hydrostatic test of gas cylinders for gas transportation trailers (ASTM, 1992). This procedure is now widely used throughout the United States. In this test, these cylinders are individually monitored by an AE system while being pressurized to 110% of their service pressure. This extra pressure is applied during the normal filling procedure and bled off after the test. An extensive testing program was conducted to determine the AE failure criteria for these cylinders. The extension to a similar AE test for aircraft halon bottles appeared to be a viable solution to the problems associated with the hydrostatic test.

## 2. Principles of Acoustic Emission Testing

An acoustic emission is generated in the form of a transient burst of acoustic energy. Acoustic waves propagate through the material until they reach the surface where they can be detected by a piezoelectric sensor. In a thin sheet of material, the waves travel along the sheet, generally in one of two different modes of motion. The two modes are an extensional wave, where the particle motion is

---

Received 1 March 1998. The author (pacabq@worldnet.att.net) was affiliated with Department 9742, Sandia National Laboratories, Albuquerque, NM 87105-0615; now is at Physical Acoustic Corp., PO Box 572, Corrales, NM 87048. This is based on a U.S. Department of Transportation/Federal Aviation Administration report, DOT/FAA/AR-97/9.

parallel to the propagation direction in the sheet, and a flexural wave, where the particle motion is perpendicular to the direction of propagation. Both of these modes have frequency dependent velocities and are thus dispersive. The flexural velocity is about half the extensional velocity and both modes are usually seen in an emission burst. The dispersion of the two modes results in the shape of the acoustic waveform continually changing over time. Both modes are detected by conventional piezoelectric sensors with the flexural mode usually having the largest amplitude (Beattie, 1983).

As the burst signal propagates away from the source, the locus of maximum energy is an expanding circle in isotropic materials. The wave will excite the surface mounted sensors at different times as it passes under them. The measured time of arrival is proportional to the wave velocity and the distance from source to sensor. Knowing the wave velocity and the sensor locations, one can then use these arrival times to triangulate back to the source and thus calculate its location. Because the time of origin of the wave is not known, three sensors are needed for location on a surface and four for location in a solid.

In general, a single AE burst only indicates that something happened in the test object. The large number of possible generating mechanisms usually prevents the determination of the source mechanism for a single emission. On the other hand, several emissions from the same location usually is evidence of a growing flaw. Another significant piece of information is the occurrence rate of the detected emissions as a function of load. If the rate of emissions from one region increases more than linearly with respect to the load value, there is a strong probability that unstable crack growth is occurring and failure is imminent.

### 3. Design of the Acoustic Emission Test

The main problem in the design of a safe, practical AE test for halon bottles was how to apply an overpressure in the sealed bottles. The most viable method to increase the pressure appeared to be heating the bottle and its contents. The bottle is filled with a measured charge of Halon 1301 and then charged with dry nitrogen gas to a pressure of 2.5, 4.1 or 5.5 MPa (360, 600, or 800 psi). Most of the halon bottles currently in use have been restricted by their manufacturers to temperatures below 71°C (160°F). Theoretical curves such as the one shown in Fig. 1 show that a temperature of approximately 63°C (145°F) will produce a pressure in most halon bottles about 30% over the bottle pressure at 43°C (110°F). This is a temperature, which industry members have estimated that a bottle will seldom exceed in normal commercial service. Therefore, heating a halon bottle to 63°C will exceed the 110% criterion developed for gas trailer bottles and should provide a valid test.

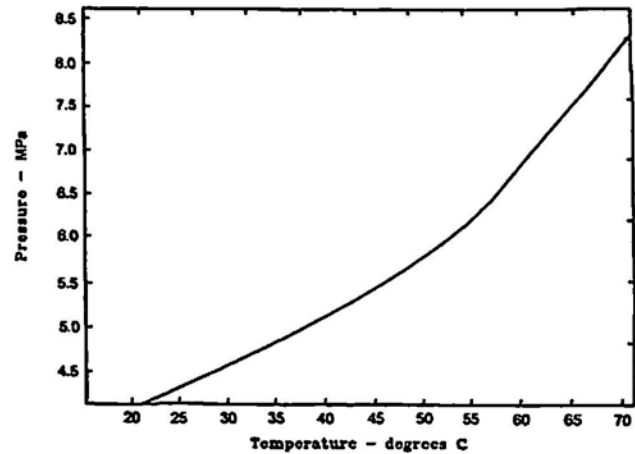


Fig. 1 Pressure - temperature curve for a halon bottle.

A completely quiet AE test of a pressure vessel is a rarity. Acoustic emission can be generated by the spalling or cracking of oxides or other corrosion products. Grit in threads can fracture with a change in the overall strain in the bottle. There are also different types of electrical interference which can be detected as emissions. A source location test was chosen since emission produced by corrosion or grit usually will not repeat themselves and do not show several emissions from the same location. A growing crack will usually show a cluster of sources around one location.

Most of the Halon-1301 bottles in commercial aircraft are spheres. The mathematics for the location of a point on a spherical surface have long been known. If the sensors are positioned on the ends of the same spherical radii for different size spheres, the only parameter which has to be changed in a location calculation is the value of the radius. Therefore, a fixture which runs the sensors in or out on the tip of a rod located on a radii will allow the use of the same mathematics for a variety of sphere sizes. Such a fixture, shown in Fig. 2, was designed to hold spheres from 127 and 406 mm (5" and 16") in diameter and to fit in an industrial oven.

### 4. Description of the Prototype Test System

The AE system uses the Physical Acoustics Corporation (PAC) AEDSP-32/16 digital AE board. Three boards are mounted in a 66-MHz 486 computer. These boards have two separate channels, each containing a digital processor with a 16-bit word and a maximum digitization frequency of 8 MHz. The large dynamic range of the 16-bit word (up to 90 dB) allows triggering at a very low signal level without losing high-amplitude data. The system is triggered at a 25 dB level (17 μV out of the sensor).

The board uses a dedicated signal processing chip to calculate various AE signal parameters in real time from the digital record. In this application, the following parameters

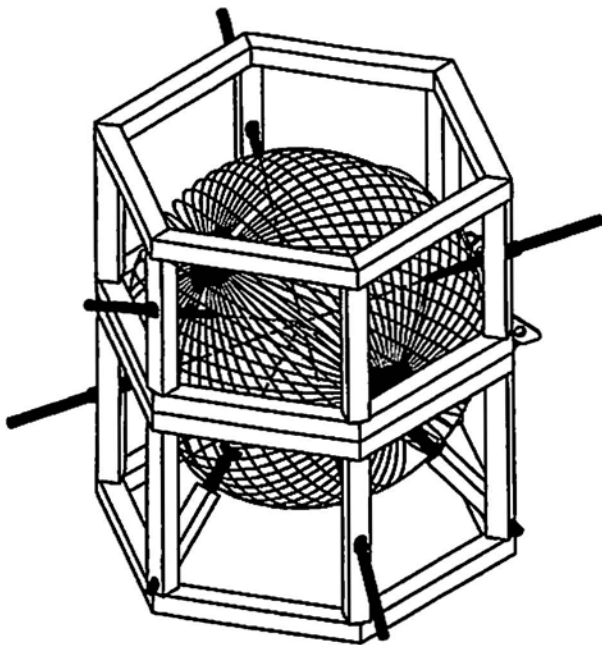


Fig. 2 Drawing of the fixture.

for each AE hit are recorded: the test time to within 0.25  $\mu$ s, the AE count, the peak signal amplitude, the signal rise time, the signal length, the area under the voltage time curve (called variously signal strength, energy, or MARSE), and finally, the digitized waveform for each hit. This digital record contains 2048 words digitized at a 4-MHz rate and is recorded for every hit on each sensor. This data set allows a test engineer to examine a bottle test in great detail, including the AE waveforms, if the test results are not clear. The detectors are PAC Nano-30 sensors with a response peak between 300 and 350 kHz. The 40-dB preamplifiers have a frequency bandpass set at 250 to 1200 kHz. This restriction to higher frequencies is necessary to reduce the effect of low-frequency sound waves reverberating through the halon inside the bottle.

The prototype test system (see cover photograph) combines the AE system described above with a Russell industrial oven having a 730-liter internal volume. The oven has a slide-out shelf, which supports the test fixture. The fixture supports the bottle and positions the sensors on it. The shelf with the fixture is shoved back into the oven and the door closed to heat the bottle. The oven has encased heating elements with a surface temperature limit of 427°C (800°F). This will prevent thermal decomposition of the Halon 1301 in the event of an accidental release. The oven air temperature is limited to a maximum of 93°C (200°F). Relays are installed in the oven to allow the computer to operate the heaters and circulation fan. The computer reads the skin temperature of the bottle using a thermocouple taped to the bottom of the bottle.

Initially, the system was controlled by the operator, who initiated all operations from the keyboard or the oven

controller. This required a relatively skilled operator to run and to constantly monitor the system. Since it was intended that the system be run by aircraft mechanics in maintenance facilities, it was decided to automate as much of the system as possible. A computer program was developed to control the AE system and the oven, and to decide upon the health of the bottle in almost all cases. The operator is required only to mount and dismount the bottle and to enter information about the bottle into the computer. This turnkey system was used for the second half of the tests at Walter Kidde and all of the tests at Pacific Scientific.

The system operates as follows. The operator first loads a bottle into the fixture and attaches the thermocouple to its lower skin. Next the bottle's identification number is entered into the computer with the keyboard. When this is verified, the computer starts an auto sensor test. Each sensor is excited several times with a voltage pulse. This generates an acoustic burst which is received at each of the other five sensors. The peak amplitude of each received signal is measured. If the average of the peak amplitudes of all signals received by each sensor lies within  $\pm 4$  dB of the average of all signals received by all sensors, the test is passed. This shows that all the electronics are working and that each sensor has good acoustic coupling to the bottle. If the test fails, the operator is instructed to reseat the sensors and try again. After the auto sensor test is passed, the system turns on the oven and the circulation fan and starts taking data. When the bottle wall temperature reaches 66°C, the heaters and fan are turned off and the bottle sits for 5 min. to allow the halon inside to reach equilibrium with the bottle wall. The equilibrium temperature is usually between 63° and 66°C. Throughout the test, the computer calculates the locations of every event. It checks each located event to see whether it is a member of a cluster or whether to start a new cluster. If a cluster size exceeds a preset criterion, the computer will conclude that the bottle has failed the test and may be close to structural failure. It will shut off the heater and circulating fan and signal the operator. The operator will then open the door to allow the bottle to cool before removing it from the oven. At the end of a test, the auto sensor test is again performed to insure that all sensors are still working. A brief report is printed after the test identifying the bottle and stating that it has either passed or failed the test.

## 5. Discussion of Analysis

While the mathematics of location of points on a spherical surface are not new, the problem is complicated because bottles are not smooth spheres. Fill ports, discharge ports, and mounting lugs are welded onto the bottle. These cause distortions of the acoustic waves traveling along the bottle wall. The largest amplitude signals are usually flexural waves, which are easily distorted as they pass under a mounting or positioning lug or through the base of a port. The lugs are often mounted on a doubler

plate which is fillet welded to the surface of the sphere. At the relatively low signal amplitudes (35 to 50 dB) seen in these spheres, the distortion of the waves can produce triggering on either the extensional or the flexural portion of the wave, making the calculation of the exact source position difficult. To achieve reasonably accurate location of the source of the detected signals, only over-determined data sets are used in the calculation (an event where the emitted acoustic wave excites 4 or more sensors). A nonlinear least-squares program was written in FORTRAN to calculate the most probable location of the event on the sphere. It was then modified by PAC for their hardware. This location program first tries the extensional wave velocity (5.21 mm/ $\mu$ s). If that does not produce a good fit to the data, the flexural velocity (3.00 mm/ $\mu$ s) is tried. The computer ignores the event if it cannot locate the source position with a relatively good fit to the data by using one of these two wave velocities. Approximately 80% of all the events are located. This percentage approaches 100% as the peak amplitude of the wave exceeds 316  $\mu$ V (50 dB) out of the sensor.

To estimate the significance of the events, an algorithm was written, which searches for spatial clusters of event sources. A cluster is arbitrarily defined here as all events, which fall within a circle on the surface of the sphere. The radius of this circle is 15° of the arc of a great circle on the bottle. The 15° radius corresponds to a circle about 75 mm in diameter on a 280-mm-diameter sphere. This cluster radius was based on data from a flawed bottle. Extensive testing indicates that it is a reasonable choice for the spherical halon bottles used in the aircraft fleet.

Analysis of the Pacific Scientific data showed that the usual AE signal parameters (AE count, signal strength, signal energy or signal length) are not ideal indicators for the cluster severity. The acoustic impedance ratio between the Halon 1301 and the bottle wall is different for different metals. This changes the damping of the acoustic wave, which affects these parameters. For example, an AE signal for a titanium bottle has an AE count about 50% greater than the same amplitude signal for one made of ferrous alloys. Therefore, it was decided that the failure criteria should be based solely on the density of the located emissions in the cluster and the change in slope of the AE curve with temperature (or pressure). The program keeps a record of the location coordinates and the temperature for each member of a cluster. From the data it was determined that bottles with identified flaws showed most of located events above a temperature of 54°C. Here, we calculate the slopes of the located AE event versus temperature curves between 43 and 54°C and between 54 and 66°C. We use as the failure criterion, a factor of 3.0 or more increase in the slope above 54°C in comparison to that below 54°C.

While corrosion has not appeared to be a problem in recent years, some of the bottles showed high cluster densi-

ties with AE event rate curves typical of corrosion. Even in stainless steel bottles, a small amount of liquid impurity, such as water, sitting on the bottom of the sphere for long periods of time could cause corrosion in a small area if the Halon 1301 decomposed in the liquid. It was decided that a second failure criterion based upon cluster density might be appropriate, depending upon the results of the bottle tests at the commercial repair stations.

## 6. Results of Bottle Tests

Both current manufacturers of these halon bottles maintain test and repair facilities. It was arranged to perform the AE test on used Halon 1301 bottles as they were returned to these facilities for repair or testing. The test was run on the arriving bottles before emptying them for the hydrostatic test. The prototype system was first installed in the Walter Kidde testing facility in Wilson, NC. Because these bottles were owned by customers and some had tight scheduling requirements, not all of the desired NDT procedures could be performed on those questionable bottles found by the AE tests. However, all bottles tested with the AE system subsequently passed the hydrostatic test. A total of 147 bottles were tested at the facility while the prototype system was there. The system was then moved to Pacific Scientific Corporation in Duarte, CA. Here another 60 bottles were tested. This gave a data set of 207 bottles. Table 1 shows the number of the tested bottles made of each material. Table 2 shows the number of the tested bottles as a function of size. A majority of the bottles were made of Nitronic steel and had a volume of 10.3 liters (630 cubic in.), but a wide selection of bottles were tested.

Table 1 Bottles Tested Versus Composition

Material	Number
Nitronic (21-6-9)	125
Almar	40
4130 Steel	26
Titanium	7
300 Series Stainless	9

Table 2 Bottles Tested Versus Volume

Bottle Volume (liters)	Number Tested
1.17	1
2.45	1
3.66	23
6.18	24
6.87	4
8.76	14
10.3	123
13.1	13
22.9	5

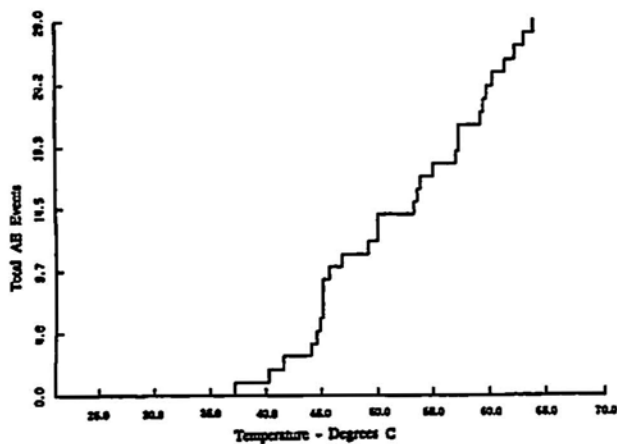
Table 3. Summary of Acoustic Emission Data for The 207 Bottle Tests

Number of Bottles	Results
7	no AE observed
56	random AE hits but no located events
77	AE hits and located events - no clusters with over 4 located events
48	clusters with 5 to 17 located events
19	at least one cluster with 18 or more located events

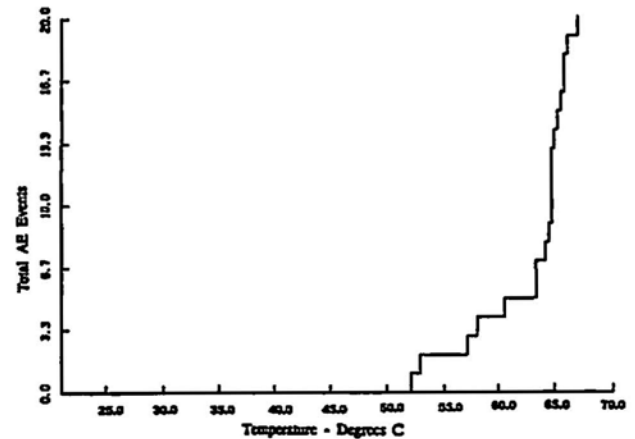
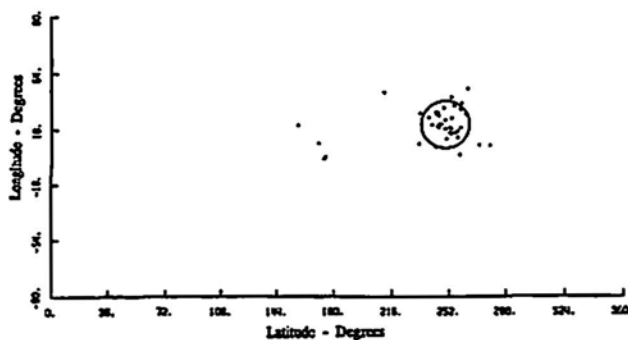
The acoustic emission results are given in Table 3. Seven bottles had no emissions, 56 bottles had emissions but no located events, and another 77 had located events and possibly small clusters, which contained less than 5 events. Thus, about 68% of the bottles showed no significant AE. The rest had clusters of moderate to large number of events.

Based on the data from Walter Kidde tests, it appeared that the bottles could be graded according to whether AE clusters contained low or high numbers of events. However, 25% of the Pacific Scientific bottles showed clusters containing 18 or more events, although none failed the hydrostatic test. A more thorough examination was then made of

the data. Most pressure vessels, which fail an AE test, show a distinct knee in the data where a relatively steady rate of emission as a function of the load suddenly starts to increase. This is indicative of continuous crack propagation, which ends in the failure of the vessel if the loading is not at least stopped, if not reversed. Of the 19 bottles with 18 or more located events in a cluster, 15 of them showed a relatively constant rate of emission between 43°C and the end of the test at 66°C. Only 4 of them showed a much higher emission rate between 54° and 66°C than between 43 and 54°C. However 5 of the remaining 15 had 35 or more located events in a cluster. This high density in a cluster with a constant slope of the event versus temperature curve was probably due to the cracking or spalling off of corrosion products at a localized region inside the bottle. After discussions with the DOT technical staff, it was decided to set two failure criteria. First, any bottle with a cluster containing 35 or more located events would fail the AE test. Second, any bottle with a cluster containing 18 or more events and which had a significantly increased AE rate above 43°C would also fail the AE test. The actual criterion used in the computer program was to divide the number of AE events in the cluster, which occurred at temperatures above 54°C by the number of cluster events, which occurred in the range between 43 and 54°C. If this ratio is 3.0 or



HPA12569



HKA19355

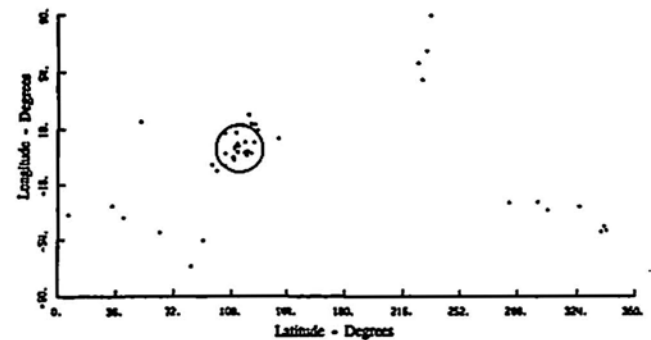


Fig. 3 Event versus temperature curve and location plot. The slope of the event curve for the cluster is constant with increasing temperature.

Fig. 4 Event versus temperature curve and location plot. The slope of the event versus temperature curve for the cluster shows a significant increase at high temperatures.

higher, the bottle will fail the AE test. Of the 207 bottles tested, two failed both criteria, two failed the slope criterion and 5 failed the cluster density criterion.

Location diagrams and event versus temperature data are shown in Figs. 3 and 4. In Fig. 3, a serious appearing cluster containing 29 events is shown on the location plot. However, the event rate is constant as the temperature, and thus the pressure, increases. In contrast, Fig. 4 shows a cluster containing 20 events, but 18 of the 20 events occurred above 54°C. The cluster in Fig. 4 is located partially over a doubler plate on the bottle. An x-ray of this plate showed a tungsten inclusion in the fillet weld holding the plate on the bottle. The fact that the emission did not start until a relatively high temperature and the rapid emission rate above 64°C is strong evidence that a crack is propagating in the weld, starting from the tungsten inclusion. Because the bottle passed a hydrostatic test the crack is probably not in the vessel wall but instead is propagating in the doubler plate fillet weld parallel to the wall. Thus, it is a real flaw but one, which may not result in the failure of the bottle.

These results show that 4 of the 207 bottles in the data set produced AE data, which indicated the possibility of serious flaws. Five more of the bottles had cluster densities, which indicated the possible presence of areas with at least moderate corrosion products inside the bottles. All nine bottles passed the hydrostatic test, which primarily means that they did not blow up at pressures twice the nominal pressure at 21°C. The other 198 bottles passed the AE test based on the failure criteria described above. It was noticed that two sets of identical bottles with closely grouped serial numbers contained the majority of moderate to high density clusters. It is not known whether these belonged to two distinct batches of old bottles, whether they had been somehow mistreated by their owners or whether this observation was just a statistical anomaly.

The time that it takes to run a test on a bottle depends upon the size of the bottle, its surface condition (paint slows down the heat transfer), and the condition of the oven. Total test times including the five-min. hold at the end, ranged from 15 min. to over an hour. The first test of the day is always longer due to the heating of the mass of the oven. Handling the 66°C bottles is no problem if a little care with gloves and long sleeves are used. The turn-around between tests is quite short, even when the fixture has to be reset for a new bottle size. At Walter Kidde, the average time was about 25 min. per bottle. This data indicates that an average test time of around 30 min. per bottle should be quite feasible.

## 7. Conclusions

The AE Halon Bottle Tester has shown its ability to detect small flaws in Halon 1301 bottles. None of the flaws seen yet has caused the rejection of a bottle by the hydrostatic test. Conservative AE rejection criteria have been set for commercial use of the system. The test data reported in this paper show that over 95% of the tested bottles passed this criteria. There was no indication that any specific bottle design or construction was more prone to failure by this AE test than the rest of the test set.

Based on the data presented here, the Air Transport Association applied for an exemption, which would allow its members to use the AE Halon Bottle Tester described here in place of the hydrostatic test. This exemption (DOT-E 11850) was granted on 11 December 1997. The system is now available commercially.

## Acknowledgment

This project was funded by the Federal Aviation Administration (FAA) William J. Hughes Technical Center and the Air Transport Association (ATA). The author would like to thank Michael Bucks of American Airlines and Steve Jeung of United Airlines for supplying the halon bottles used in the experiment. Kamran Ghacmmaghmi of Federal Express provided both aid and encouragement. Steve Erickson, formerly of the ATA, was instrumental in getting this project started. Steve Lamb and Junior Bunn of Walter Kidde enthusiastically conducted the tests of user bottles at their facility as did John McNeese at Pacific Scientific Corporation. Finally, Wayne Roney of Physical Acoustics Corporation (PAC) worked many extra long days to adapt the Sandia program to PAC hardware on schedule.

## References

ASTM (1992), "Standard Test Method for Examination of Seamless, Gas Filled Pressure Vessels Using Acoustic Emission," ASTM Standard E 1419, Annual Book of ASTM Standards, Section 3, 1992 and later, ASTM, Philadelphia, PA.

A.G. Beattie (1983), "Acoustic Emission, Principles and Instrumentation" J. Acoustic Emission, 2, 96.

## Cover Photograph

Prototype test system is depicted in this photograph, with the top fixture open and a halon bottle placed in the middle. This demonstration was conducted on 12 December 1995.

# AE Detection of Cracking in Pipe Socket Welds

Bryan C. Morgan

## Abstract

Small-bore pipe socket welds in fossil and nuclear power plants are prone to vibration induced cracking. This is particularly a problem for small-bore pipe vents and drains that are cantilevered from large diameter pipes. It has been found that fluctuations in flow and attached rotating equipment resonate with the natural frequencies of the small-bore pipe cantilever. Typically, the small-bore pipe is attached to main large-bore pipe using a socket weld. This type of weld can have a high stress concentration, which may result in cracking at the weld root. The socket's geometry makes a non-destructive inspection using either ultrasonics or radiography very difficult. In the laboratory, stainless steel pipe specimens with socket weld cracks were stressed to the plastic yield while monitoring for acoustic emission (AE). This showed that a significant amount of AE was generated during elastic bending, and could be used to differentiate between specimens with cracks and without cracks. The cumulative AE signal energy at relatively low stress levels provided a means of identifying the cracked specimens.

## 1. Introduction

Behavior of power-plant piping systems during dynamic loading, particularly from flow-induced vibration, can lead to a degraded condition and a safety concern. One pipe component of special concern is the socket weld connecting a cantilevered small-bore pipe to a large-diameter main run pipe. The flow drives the low frequency response of the cantilever to generate high stresses in the weld. This is aggravated when the cantilever supports a heavy isolation valve. Inherently, the socket-weld geometry and any weld undercutting exhibits high stress intensification. Figure 1(a) shows a typical cantilevered pipe with a large valve. In this case, an instrument tube is connected to the valve, but it provides little structural support or influence on the cantilever's natural frequency. Figure 1(b) shows another typical configuration, where the cantilevers are drain lines with end caps.

Received 7 October 1997. The author (BXM0.TesMs.Gsv@bangate.pge.com) is affiliated with Technical & Ecological Services Laboratory, Pacific Electric and Gas Company, 3400 Crow Canyon Road, San Ramon, CA 94583.

The end result of the vibration is the initiation and growth of weld cracks, potential fluid leakage and ultimately a pipe break. Figure 2 shows examples of discovered cracks. In Fig. 2(a), the crack originates at the weld root. Due to the loose socket fit-up to pipe, the root is prone to exhibit lack of weld penetration, and correspondingly higher stress concentration and intensification. Figure 2(b) shows cracks growing above the weld root pass. However, the figure also shows a lack of weld root penetration.

Stainless steel small-bore (19 mm and 25 mm (3/4" and 1") nominal diameter) pipe has been particularly of concern for leakage. This is a concern for both safety and for potential to shut down a power plant. It is particularly an issue with nuclear power plants where leaks or breaks in socket welds may require immediate shutdown of the plant. Inspections to identify the cracks are difficult, as many socket welds are in plant areas not accessible during normal power operation. In some plants, the access may only be every 18 months. This provides time for a small crack to propagate to leakage before loss of fluid sounds an alarm. As such, a small leak can go unnoticed until a pipe break occurs.

Another problem is the difficulty in detecting cracks. The socket-fitting geometry complicates the inspection. Radiography will show clearly the fitting material and the gap between the socket fitting and pipe, but generally misses the root cracking. Likewise, ultrasonics will show the gap between socket fitting and pipe wall. A shallow crack will generate a reflector that is obstructed by the gap's reflector signal. As such, using ultrasonics for inspection is not likely to detect cracking in the bottom one-third of the material thickness. Thus, the crack in Fig. 2(b) would be detected, but not the cracking in Fig. 2(a).

To address these concerns, an inspection procedure was developed using the detection of acoustic emission (AE) as an indicator of the socket weld's structural integrity. The expectation is that a significant amount of AE is generated by applying a nominally elastic stress level. Degraded and cracked welds will exhibit higher concentrated stress levels and higher AE activity.

## 2. Mechanical Testing

Laboratory mechanical testing was conducted to quantify the AE generated by socket-welded specimens. Testing

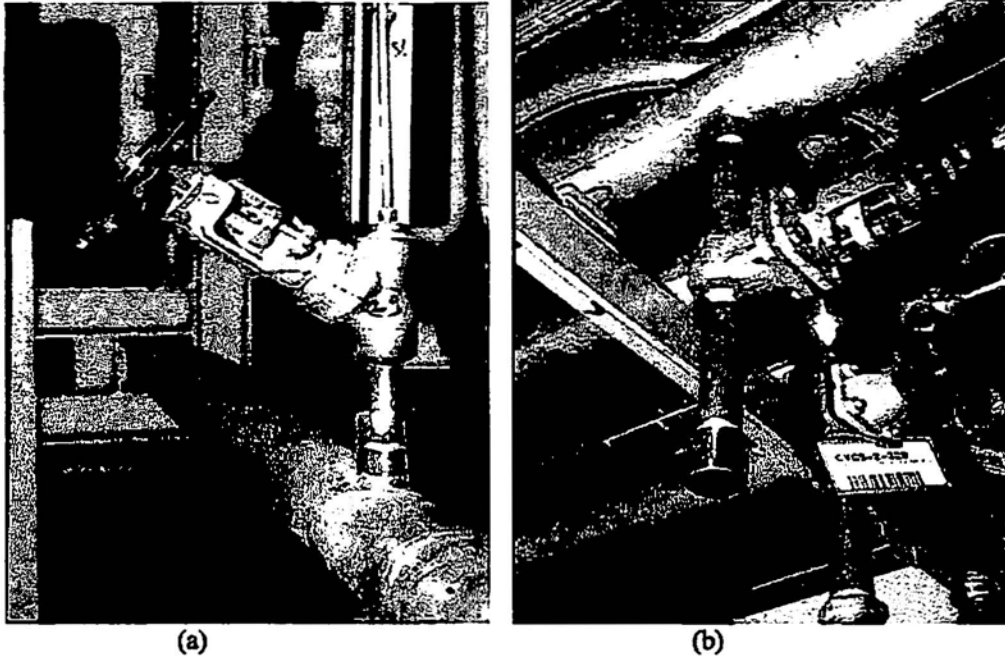


Fig. 1 (a) Small-bore (19-mm diameter) cantilever pipe with instrument connection. The socket weld of concern connects the socket fitting to the small-bore pipe. [Note, a metal name plate tag is tied around the weld] (b) Three small-bore cantilever drain lines with straight pipe sections. In many cases, the cantilever has an elbow between the valve and large-bore pipe. This tends to increase flexibility and lowers the cantilever's natural frequency; making it more susceptible to resonance with flow-induced vibration frequencies.

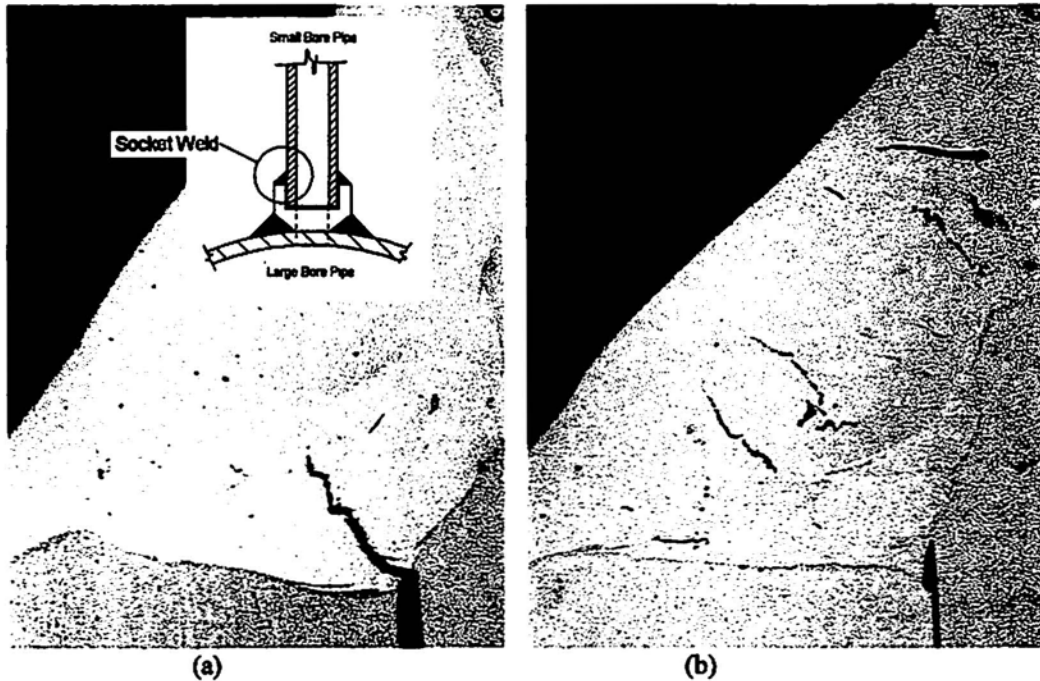


Fig. 2 (a) Crack initiated and growing from the weld root. The crack has extended almost to the top of the weld root pass. The socket weld indicated is the weld most of concern for cracking. (b) Service induced cracks above the weld root pass. Note lack of weld penetration at root, the typical initiation point for mechanical fatigue cracking.

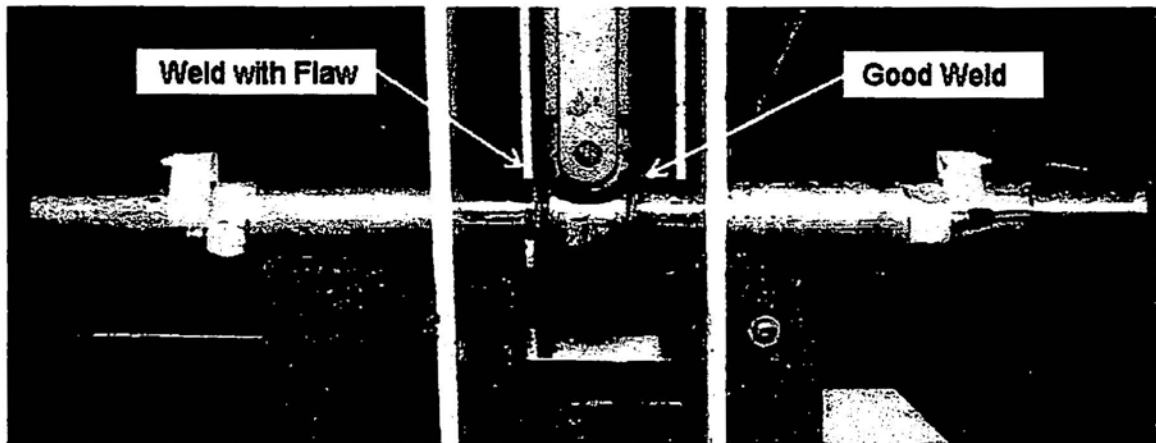


Fig. 3 Pipe specimen in the 3-point bender. Specimen is pipe socket coupling with pipe welded to both sockets. The photos show two linear arrays of sensors, one with a 150 kHz resonance (Physical Acoustics R15) and the other with a broadband response (Digital Wave B1025). The broadband response was limited with 100 to 1200 kHz bandpass filtering.

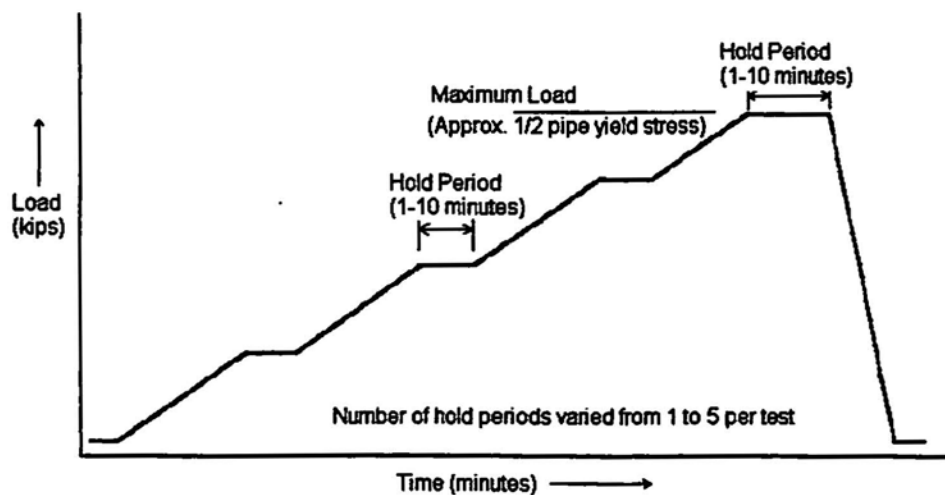


Fig. 4 Load histogram. Ramp loading has hold points at 4.45 kN (1 kip) increments.

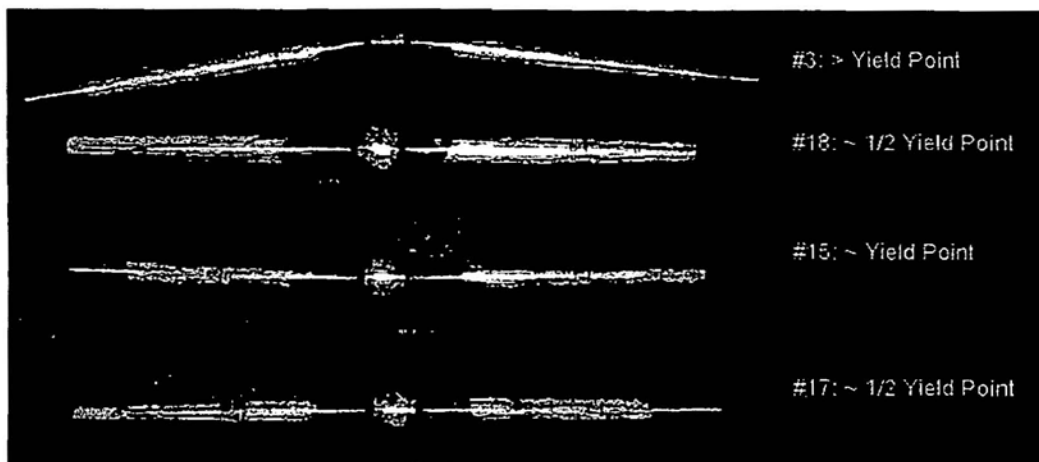


Fig. 5 – Four socket weld specimens (#3 is 13 mm diameter; all others are 19 mm diameter.)

was performed at Pacific Gas & Electric Company's Technical & Ecological Services Laboratory. Loading was applied in stages up to yielding, in order to determine if the generated AE that occurs during elastic loading can act as an identifier of weld cracks. To be a usable technique the applied loading must be significantly lower than the yield point to prevent damage to non-cracked specimens.

A 10-ton hydraulic 3-point bender was used for loading. 13 mm, 19 mm, and 25 mm (1/2", 3/4" and 1") nominal diameter pipe specimens of Type-304 austenitic stainless steel were tested. Each specimen consisted of a pipe coupling with a pipe socket welded to each end. Figure 3 shows a typical specimen in the 3-point bender. Flaws were induced in the weld root, by preventing weld penetration in the weld root pass. The welder could control, to an extent, the lack of penetration circumferentially around the pipe length and correspondingly the flaw length. This induced various flaw lengths in the specimens. Typically for each specimen, one weld would contain a flaw; the other weld would be without any significant flaw.

Piezoelectric sensors were attached to the specimen, as shown in Fig. 3, to provide a linear location array. Both broadband (DWC B1025) and resonant (PAC R15) sensors were used. The array setup provided the pipe axial location of generated AE: i.e., at the welds, bend points, and other locations. AE monitoring was performed for both transient waveforms and signal feature values utilizing a Vallen AMS3 system. This setup provided a direct comparison between emission generated at the flawed and good welds.

Both tension and compressive loads were applied to the socket welds across the flaw surfaces. The specimen was ramp loaded as indicated by Fig. 4, to a maximum load equivalent to one-half the yield point. Then unloaded, circumferentially rotated 90° and reloaded. The specimen was loaded four times at each 90° orthogonal direction. The orientation generating the greatest amount of AE was selected to continue loading to the yield point. Figure 5 shows four specimens after loading.

Figure 6 shows the cumulative number of AE events, energy and counts as a function of axial position; for a flawed specimen loaded past yield stress. Energy was recorded as the true energy of the waveform (the integrated area under the waveform). The figure shows most emission was located at the flawed weld and at one of the bender support points. Emission was initiated first at the flaw location, and then at the support point. After bending, the specimen visually showed a localized pipe deformation occurring at the support point. The figure provides two plots comparing the broadband (top) and resonant (bottom) sensor responses. These show similar event locations. The major difference is likely a result of the different circumferential locations of the two sensor arrays, resulting in dissimilar wave path lengths.

The broadband sensor's signal waveforms show a broad frequency response, with maximum amplitudes at the lowest frequencies within the filtering pass-band. Figure 7 shows an example for a wave originating at the flawed weld of Specimen #2. This was typical of waves generating at one-half yield stress. At lower loads, signals showed lower amplitude and a reduced spectral content with just the lowest frequencies. It was observed that the surface mounted sensors on the pipe OD detected predominately the flexural wave mode.

One reason for comparing the sensor types, broadband and resonant, was to determine which would be better in the field testing. Considering the short distances between weld and sensor, the lower sensitivity of the broadband sensor does not appear to be an issue. The primary difference may be in their ability to deal with background flow noise. Previous experience with power-plant piping noise (Morgan and Foster, 1997) has suggested that high-pass filtering above 200 kHz will eliminate a significant amount of flow noise. As such, when noise is present the broadband sensor with high-pass filtering should be preferred over a low frequency resonant sensor.

The effects of filtering using signal feature values are displayed by Fig. 8. It shows for a specimen loaded past yielding, cumulative number of events, energy and counts. A count filter was used to remove events with very small number of counts. A comparison of the two plots shows that the filtering removes events that locate near the good weld, but not at the flawed weld. It is expected that many of these events were associated with rubbing from the bender's middle load point, which is located between the two welds.

A major concern exists that water or steam flow in the large main pipes will generate a substantial amount of background noise. While pipe flow was not simulated in the lab, it is known that this type of count filter is also proficient in removing flow background noise. As such, this filter was used in the laboratory data evaluation.

In comparing the plots, filtering shows differences between cumulative event, energy or counts. Using counts as an indicator of flaw location is less effective than energy or number of events. This was found in common for a number of specimens. Overall, using energy as the indicator of flaw location showed the best correlation.

The Specimen #3 (shown in Fig. 8) was loaded past the yield point into gross bending. Figure 9 shows the cumulative AE versus load history for just the specimen's flaw location. The specimen was initially loaded to approximately one-half yield stress, unloaded then reloaded to check the felicity ratio. This showed a ratio of approximately 80%, thus indicating material instability.

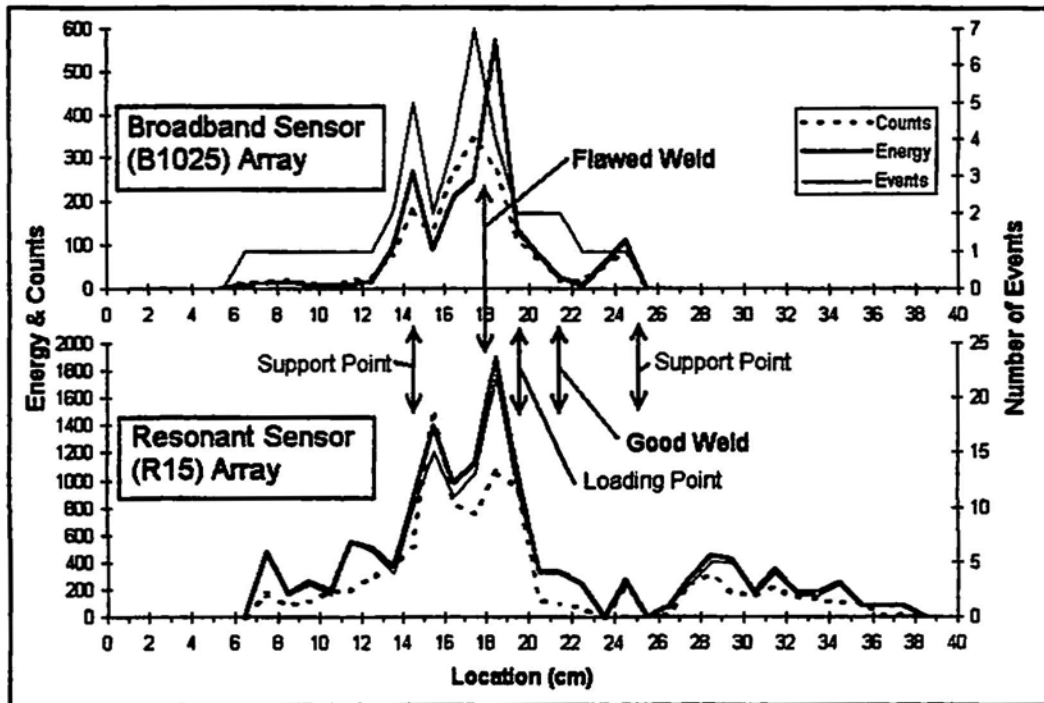


Fig. 6 -- Axial location of AE from specimen #2 (1" schedule 80 pipe). Top plot shows linear located AE from the broadband sensor (B1025) array. Bottom plot shows linear location from the resonant sensor (R15) array.

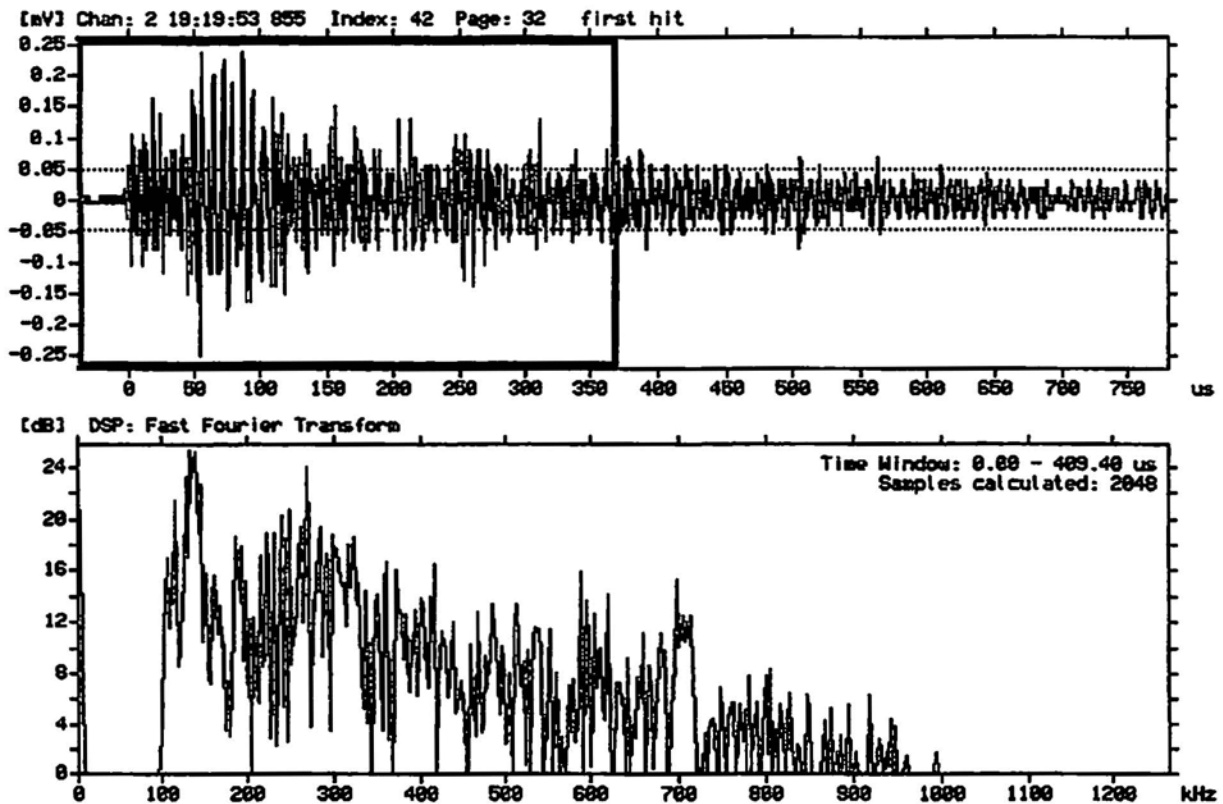


Fig. 7 Transient waveform and FFT spectrum of broadband sensor from specimen #2. Top plot shows waveform with windowed time period used in FFT spectrum calculation. Wave originated at flawed weld location with loading at approximately one-half yield stress. Bottom plot shows associated spectrum.

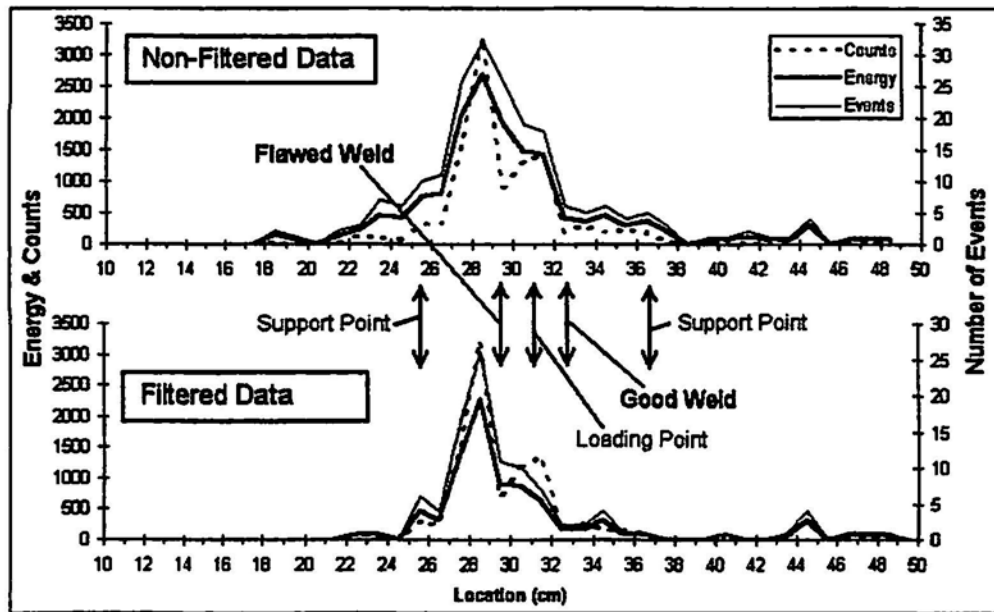


Fig. 8 Filtered vs. non-filtered AE from specimen #3 (1/2" schedule 80 pipe). Both plots show linearly located AE from the resonant sensor (R15) array. Restricting data to first hit sensors  $\geq 25$  counts provides the filter.

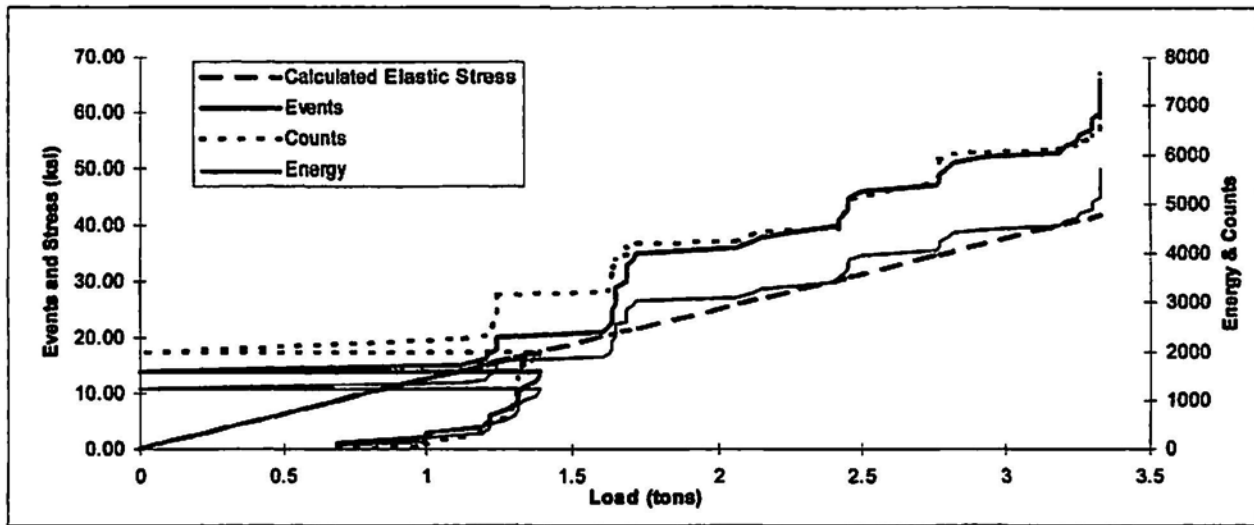


Fig. 9 Cumulative events at flaw location from specimen #3. Plot shows emission versus 3-point bender load. Specimen was loaded to 1.4 t, completely unloaded, and reloaded to 3.3 t. Plot is for filtered ( $\geq 25$  count filter) resonant sensor array data at the flaw (within  $\pm$  one pipe diameter from flaw location). The specimen's minimum yield stress is stated to be 210 MPa (30 ksi) per the ASTM A312 TP304 standard.

To identify the main load direction that was generating flaw AE, results from each 90° orthogonal loading was compared. Tensile strain is created on the side of the pipe opposite the loading point, and compressive strain on the loading side. Cumulative energy, events, and counts for both Specimens #2 and 3 were compared in Figs. 10 and 11. Both specimens were loaded to approximately one-half the yield stress. They indicate that most emission is being generated from tensile loading of the flaw. Note the graph for cumulative counts in Fig. 11, which shows a high number of counts for the non-flawed locations. This is

consistent with the result in Fig. 8, where a high number of counts are seen at the good flaw location.

In order to help confirm the presence and circumferential location of the flaws; some flawed specimens were ultrasonically scanned. As noted before, there is difficulty in interpreting ultrasonic signals at the weld-root area. It helped that specimens were scanned after loading to better detect any crack enlargement. Figures 12 and 13 compare the signal amplitudes of ultrasonic test (UT) and AE energy measurements. Figure 12 shows three specimens loaded to

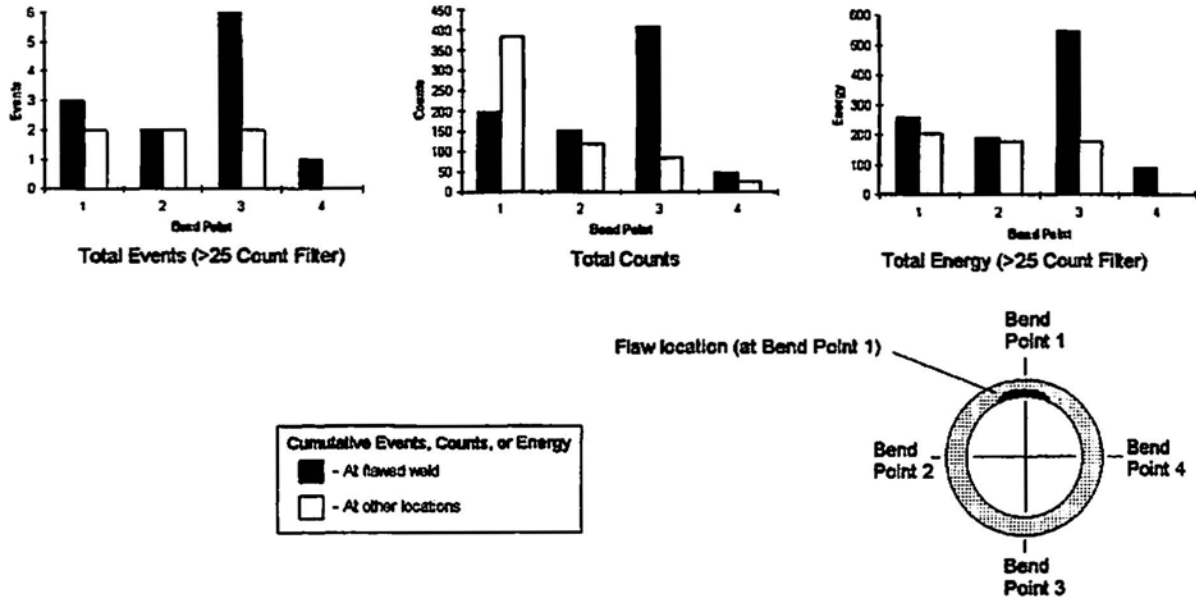


Fig. 10 Circumferential location of AE from specimen #2. Graphs are for the resonant sensor array data with filtering as shown. Black bars show data from the flawed weld location. White bars show data from all other locations combined. The flaw length is short as indicated by the cross-sectional view. Its location is centered at bend point 1. Loading at bend point 3 puts the flaw at bend point 1 in tension.

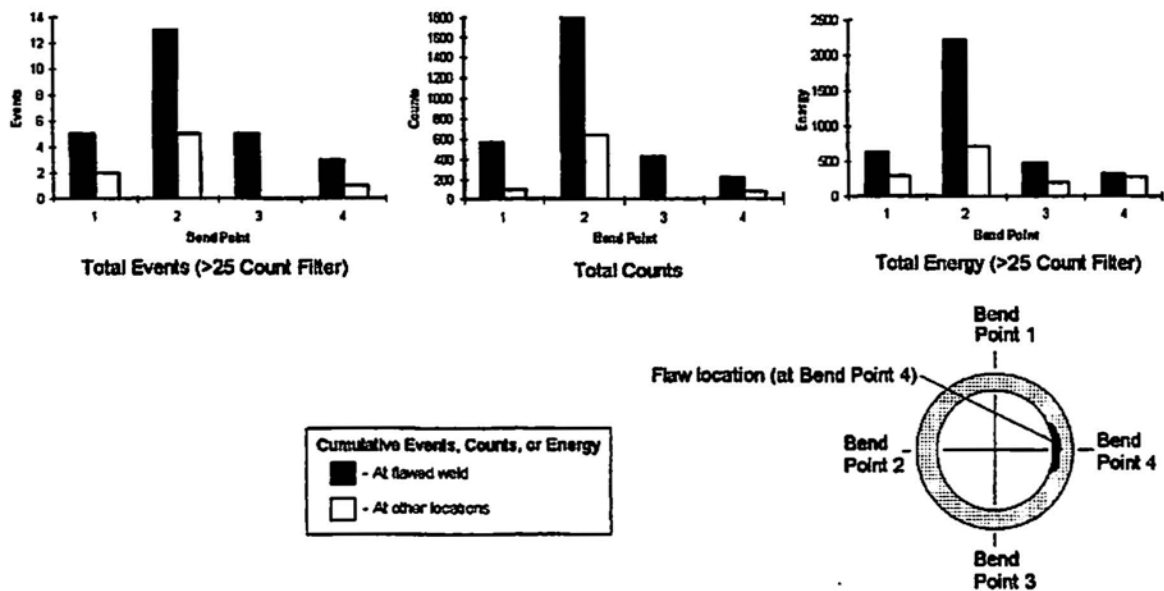


Fig. 11 Circumferential location of AE from specimen #3. Graphs are for the resonant sensor array data with filtering as shown. Black bars show data from the flawed weld location. White bars show data from all other locations combined. The flaw length is short as indicated by the cross-sectional view. Its location is centered at bend point 4. Loading at bend point 2 puts the flaw at bend point 4 in tension.

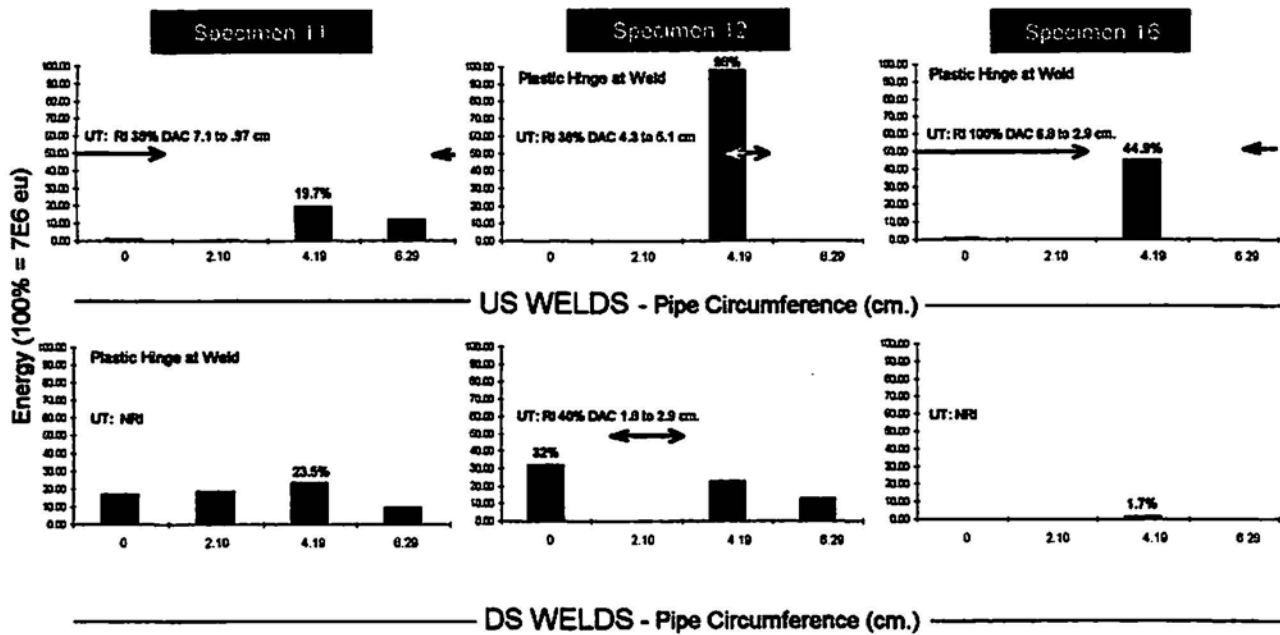


Fig. 12 Circumferential location of AE from specimen #2. Graphs are for the resonant sensor array data with filtering as shown. Black bars show data from the flawed weld location. White bars show data from all other locations combined. The flaw length is short as indicated by the cross-sectional view. Its location is centered at bend point 1. Loading at bend point 3 puts the flaw at bend point 1 in tension. Top: Upstream welds; Bottom: Downstream welds.

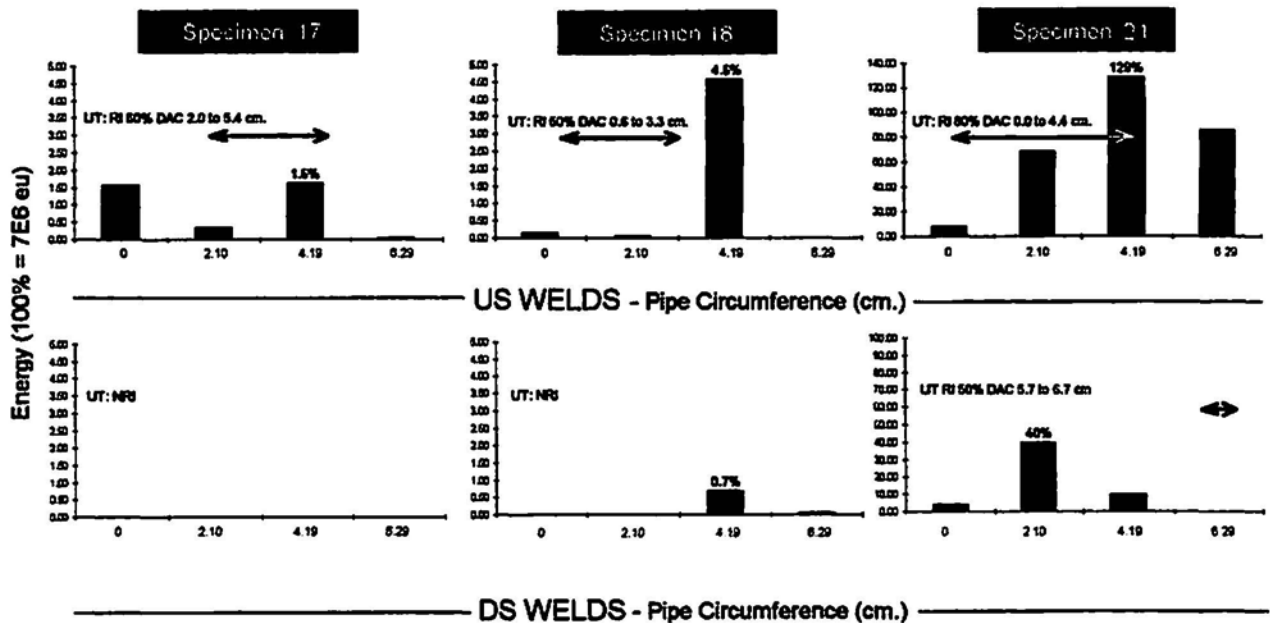


Fig. 13 Correlation of AE and UT data from specimens loaded to one-half yield stress. Format of the figure is the same as for Fig. 12.

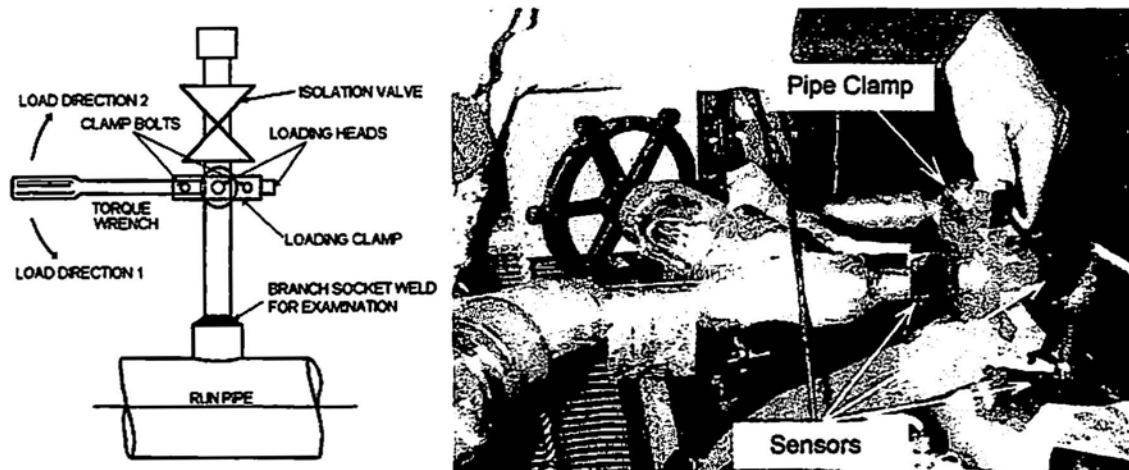


Fig. 14 (a) Torque wrench and clamp loading. (b) Field test of socket weld. Bolt heads are provided on all four side of clamp to allow for torque loading in different orientations without rotating clamp.

the yield point. Figure 13 shows three different specimens loaded to just one-half the yield point. As such, specimens loaded to yielding include the initially induced flaws, and any material damage generated by the yielding.

The figures provide comparisons for both the specimen welds. The welds are identified as the upstream-side and downstream-side welds. The specimens in Fig. 12 were loaded to yielding to identify a baseline cumulative energy level. It was selected to be  $7 \times 10^6$  energy unit (eu) to match the energy generated by specimen #12. [Note, this energy unit (eu) is as measured by the Vallen AMS3 AE system.] The UT peak signal amplitudes are shown as a percentage of the UT DAC, with the identified UT signal end-points; i.e., distance-amplitude corrected echo. Correlation shows the AE energy peak locations matching the UT signal end-points. This is expected, as the crack tip extension is a known source for generation of AE. For each specimen in Fig. 12, a visible plastic hinge formed.

Specimen #11 is of interest as the visible plastic hinge formed on the downstream weld, where significant AE energy was emitted, but no UT indication was identified. Generally, plastic yielding is not a good UT reflector. More typically, plastic hinges would be expected to form at the induced flaw locations, as occurred with Specimens #12 and #16.

A comparison was made of the AE energy measurements generated by the specimens loaded to one-half yield stress (Fig. 13) and the yielded specimens (Fig. 12). The energy level for the former exceeds  $7 \times 10^5$  eu (10% of the baseline level) for all specimens at the flawed weld. This level was found to indicate a flaw in these specimens, as well as others not shown in the figure. Specimen #21 showed a level that exceeded 100% of the baseline energy associated with yielding. This specimen demonstrated material instability even at low loads; by continued emission at constant load hold.

### 3. Field Application

To demonstrate the technique, cantilevered small-bore socket welds in use at the power plant were tested. To strain the socket weld, a pipe clamp with a bolt head for torque wrench loading was attached to the pipe, as shown in Fig. 14(a). The desired torque wrench load was calculated to provide a stress level at one-half the yield stress. That load is a function of the pipe configuration, pipe diameter, loading direction, and the placement point of the clamp.

Figure 14(b) shows a test in progress. Four 150-kHz resonant sensors were attached to the pipe using vacuum grease and tape. Three sensors are shown in the figure, on the socket coupling, elbow, and small-bore pipe. Not visible is a sensor on the bottom of the large-bore main run pipe. These sensors were aligned in a linear array to clearly distinguish emission from specific locations. Identifying any emission associated with the pipe clamp rubbing, and water/steam flow through the main run pipe was particularly of interest. As expected, it was found that the count filter ( $\geq 25$  counts) eliminated most emissions from the clamp and fluid flow. Consequently, a simpler two-sensor array could have been used.

Inspections were performed for three welds. AE was recorded and UT scans were performed. No reportable UT indications were identified. No acoustic emission was recorded that exceeded the energy level of  $7 \times 10^5$  eu.

### 4. Conclusions

The mechanical testing showed that the AE generated during elastic stressing of the socket weld provided a precursor to identifying flaws. Three classical AE signal features; i.e., cumulative number of events, (true) AE energy, and AE counts, were utilized as an indicator. Best fit was found with the measured energy. An energy criteria level was established to separate flawed welds from non-flawed welds.

However, both lab and field experience demonstrated that most good welds generated very little emission when loaded up to one-half the yield point, certainly much lower than the energy criteria level.

Evaluation of the waveform showed the frequency response from the flawed welds to be of broadband allowing detection by either resonant or broadband sensors. The presence of field background noise and the different susceptibility of the sensors should dictate the best sensor type.

Correlation was shown between AE energy levels and UT scans. The flaw ends, as located by the UT scans, typically crack tips, were found to be strong AE emitters. As such, the AE monitoring is demonstrated to be a method of identifying the crack extension point.

Most AE was generated with the flaw under tensile loading. Very little emission was produced during compressive loading. As such, loading direction for detection is critical. This requires that a tensile load be applied in all four 90° orthogonal directions from the weld's axial direction.

## References

B.C. Morgan, and C.L. Foster (1997), "Acoustic Emission Monitoring of High Energy Steam Piping, Volume 2: Basis for Acoustic Emission Monitoring", EPRI Report TR-105265-V2.

# Feature Extraction of Metal Impact Acoustic Signals For Pattern Classification by Neural Networks

Shahla Keyvan and Rodney G. Pickard

## Abstract

Acoustic emission (AE) impact signals are created in nuclear reactors when a loose part strikes the wall of a pressure vessel, steam generator tube sheet, or other object within the reactor coolant system (RCS). According to the US Nuclear Regulatory Commission (NRC) Regulatory Guide 1.133, any reactor licensed after 1978 must have systems to detect loose parts within reactor vessels and primary coolant systems. As part of a continuous effort to improve Loose Parts Monitoring System (LPMS) effectiveness the feasibility of using artificial neural networks to recognize and classify AE signals has been and continues to be explored. In searching for the ideal means of exploiting neural network technology for this particular problem much attention has been devoted to using feature extraction to preprocess AE signals prior to presenting them to a neural network. The goal of this research was to perform various types of feature extraction on AE signals created in the laboratory and examine the effectiveness of a Fuzzy ARTMAP neural network in classifying these signals. The results of this study indicate that feature extraction do not increase network effectiveness. However, artificial neural networks still have a high potential for successful application in LPMS using raw acoustic data.

## 1. Introduction

The primary purpose of the loose parts monitoring system, as the name implies, is simply to detect the presence of parts that have become loose (and possibly completely unattached) within the reactor coolant system (Keyvan and King, 1992). Although the purpose is simple enough, it is rather difficult to accomplish. Loose parts are detected based upon their acoustic emission (AE) as they strike other objects. The colossal background noise indigenous to power reactors inhibits accurate detection of the acoustic signature of loose parts, and much of the technology used to this end has proven to be inadequate. The result of this unfortunate pairing is that present loose parts detection methods simply do not provide adequate identification and diagnosis of loose parts.

---

Received 24 May 1998. The authors are affiliated with Nuclear Engineering Department, University of Missouri-Rolla, 102 Fulton Hall, 1870 Miner Circle, Rolla, MO 65409-0170 (keyvan@umr.edu).

The feasibility of using neural networks to recognize and classify AE signals for improvement of LPMS performance has been and continues to be explored (Olma and Wach, 1994; Khan, 1995; Nagaraj, 1995; Pickard, 1997). Past research has already proven neural networks to be a capable tool well suited for the loose parts monitoring problem, but their full potential has yet to be realized (Keyvan and Nagaraj, 1997).

One postulated means of realizing this potential is to extract certain key features from the raw AE data and using these features as neural network input data. In cases where numerous independent features can be extracted from a set of raw data, this process is proven to be quite effective (Keyvan et al., 1997), but extracting independent features from AE data is a challenge undertaking.

It is a common practice to extract features from acoustic signals for signature analysis (Edmonds et al., 1992). Many researchers have even utilized neural networks for extracting features from acoustic signals (Yang and Dumont, 1991; Szyszko and Payne, 1991).

The objective of this paper is to present the development of representative features from metal-impact AE signal, and examine their effectiveness in pattern classification using a Fuzzy ARTMAP neural network (Carpenter and Grossberg, 1992). All principle aspects of this process from the generation of the raw data to the testing results will be discussed.

## 2. Neural Networks and Fuzzy ARTMAP

It is appropriate to define some neural network related terminology used in this work.

**Features-** A feature is a unique measurable attribute of a pattern. A feature vector is a collection of features that completely describe a pattern. This feature vector is presented to the artificial neural network as input during the training process.

**Feature Space-** Feature space is a set of feature values that determines a pattern class, from which the feature vector is determined.

**Vigilance parameter-** Vigilance parameter  $\rho$  ( $0 \leq \rho \leq 1$ ) is used by the adaptive resonance theory family of neural networks in order to determine if an input pattern is "similar" to the existing prototype. The vigilance parameter ( $\rho$ ) sets the criterion for matching, under the exact same conditions, lower vigilance leads to coarser categories and higher vigilance to finer categories. The optimum  $\rho$  is obtained by trial and error.

Fuzzy ARTMAP (FAM) neural network is selected for this application due to its capability of handling nonstationary stochastic data, as well as, its supervised learning characteristics. It is beyond the scope of this paper to describe the intricate details of the functionality of the Fuzzy ARTMAP algorithm. Nevertheless, it is useful to discuss briefly the general operation of the FAM network.

Adaptive Resonance Theory (ART) represents a family of neural networks which self-organize categories in response to arbitrary sequences of input patterns in real time for pattern recognition (Carpenter and Grossberg, 1988). ART network architecture consists of two major subsystems called the attentional subsystem and orienting subsystem. The attentional subsystem as shown in Fig. 1 consists of two layers of processing elements, the F1 layer (input layer) and the F2 layer (output layer). The Gain Control in ART networks is a mechanism which acts to adjust overall sensitivity to input patterns and to coordinate the difficult functions of the ART subsystems.

The orienting subsystem acts as a novelty detector. The orienting subsystem in ART networks is responsible for controlling the fineness or coarseness of the pattern being recognized. It has only two input signals and one output signal. The two inputs are the input data pattern and the overall activity in F1. The single output of the orienting system goes to F2 as a reset wave (see Fig. 1). The resonance and reset is accomplished in the orienting subsystem through a very important parameter called the vigilance " $\rho$ ". The vigilance is a parameter which points to the degree to which the system discriminates between different classes of input patterns. It can have any decimal value between 0 and 1.

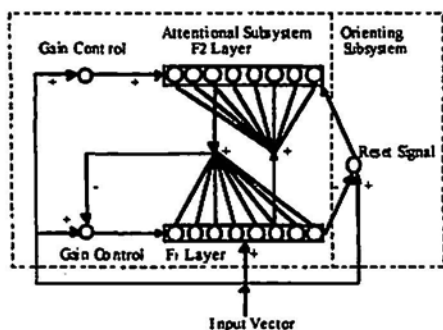


Fig. 1 General ART network.

Fuzzy ARTMAP (see Fig. 2) is built with a pair of fuzzy ART modules, Fuzzy ARTa and Fuzzy ARTb. These networks are designed as generalized ART except the set-theoretic operation of intersection ( $\cap$ ) is replaced by the fuzzy set theory conjunction ( $\wedge$ ). This fuzzy set operator makes fuzzy ARTMAP capable of handling both analog and binary data and makes the ART neuro-dynamic equations much simpler (Carpenter and Grossberg, 1992). As shown in Fig. 2, the two fuzzy ART modules a and b are connected with an inter-ART module called the Mapfield Layer. The Mapfield associates the fuzzy ARTa recognition categories with the fuzzy ARTb recognition categories. If a match occurs at the Mapfield layer then learning takes place. If a mismatch occurs, then the match tracking process is initiated. Match tracking is a method of forcing the mismatched fuzzy ARTa winning node to reset by incrementing  $\rho_a$  (vigilance parameter) by a small value, such that the current winning node fails the resonance condition in the subsequent trial.

During the supervised learning the FuzzyARTa module receives a stream (a) of input patterns and FuzzyARTb receives a stream (b) of input patterns, where (b) is the correct prediction given (a). These modules are linked by an associative learning network and an internal controller that ensures autonomous system operation in real time.

The FuzzyARTa complement coding preprocessor transforms the  $M_a$ -vector a into a  $2M_a$ -vector  $A = (a, a^c)$  at the FuzzyARTa field  $F_0^a$ , where  $a^c$  is the complement of vector a (i.e.,  $a_i^c = 1 - a_i$  for each normalized element i of the vector a).  $A_j$  is the input vector to FuzzyARTa field  $F_1^a$ .

The input to  $F_1^a$  like FuzzyARTa is the  $2M_b$ -vector  $B = (b, b^c)$ , where  $b^c$  is the complement of vector b. For each input (I) in the 0 to 1 range presented to the network, the net value at the output is compared as

$$net_j(I) = |I \wedge W_j| / (\alpha + |W_j|)$$

where  $\alpha = 0.00001$ ,  $I$  = input vector,  $W_j$  = adaptive weights or LTM traces (initialized to 1),  $\wedge$  = the fuzzy And operator. The maximum of  $net_j(I)$  is selected. For this node J, it is checked if the vigilance ( $\rho$ ) parameter is met, that is:

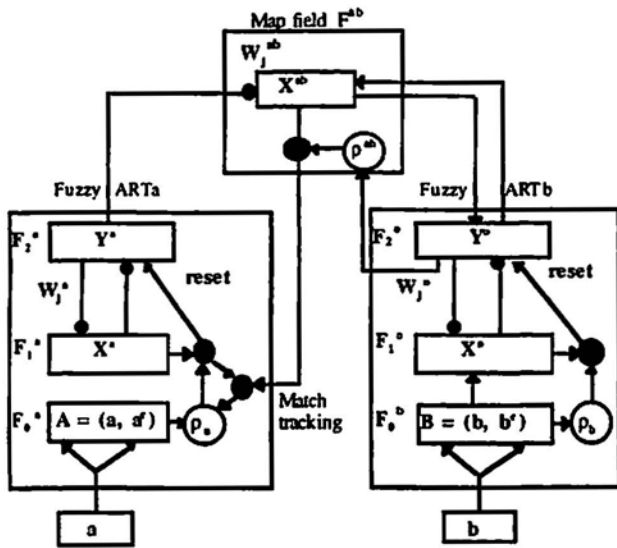
$$|I \wedge W_j| / |I| \geq \rho$$

resulting in node J being committed, else reset occurs at the selected output node and is inhibited for further competition for input I. This process is repeated until the vigilance criteria equation is satisfied. If the output node satisfies the vigilance criteria then learning takes place using

$$W_j^{new} = (I \wedge W_j^{old}).$$

### 3. Data Acquisition

The impact signals were generated by striking metal tubes with small metallic masses. The tubes were open at



$X^a$  and  $X^b$  represent activity of the F1 layer  
 $Y^a$  and  $Y^b$  represent activity of the F2 layer  
 $W_j$ 's are two top-down adaptive weights  
 $\rho$  is the vigilance parameter  
 $X^{ab}$  represent the activity of the mapfield layer  $F^{ab}$

Fig. 2 Architecture of fuzzy ARTMAP neural network.

one end and plugged at the other with a metal pipe cap. The striking was accomplished by way of pendulum action in which the pendulum was formed by attaching a mass to a string that was in turn attached to the top of the tube itself (see Fig. 3). The pendulum would be held roughly perpendicular to the side of the tube with the string taut and released such that it swung approximately  $90^\circ$  before striking the side of the tube at its approximate midpoint.

The piezoelectric accelerometer output was routed to a signal conditioner which applied a 10 kHz low-pass filter to the signal and sent it to a PC-based high-speed data acquisition board. Signals were digitized at a rate of 50 kHz. Examining the plot of each data set revealed that 700 data points were sufficient to capture the first waveform envelope for each data set. Hence, the first 700 data points of each data set were selected for this study.

Signals were created using either a long or a short tube in conjunction with either a 100g or a 50g mass. These two variables produce a net of four possible combinations (e.g., long tube, 100g mass; long tube, 50g mass; short tube, 100g mass; and short tube, 50g mass). An additional variable was the placement of the sensor that collected the signals. The sensor was initially placed at the bottom of the tubes, and then the experiments were repeated with the sensor at the top of the tubes. Introduction of this variable creates the following eight possible combinations:

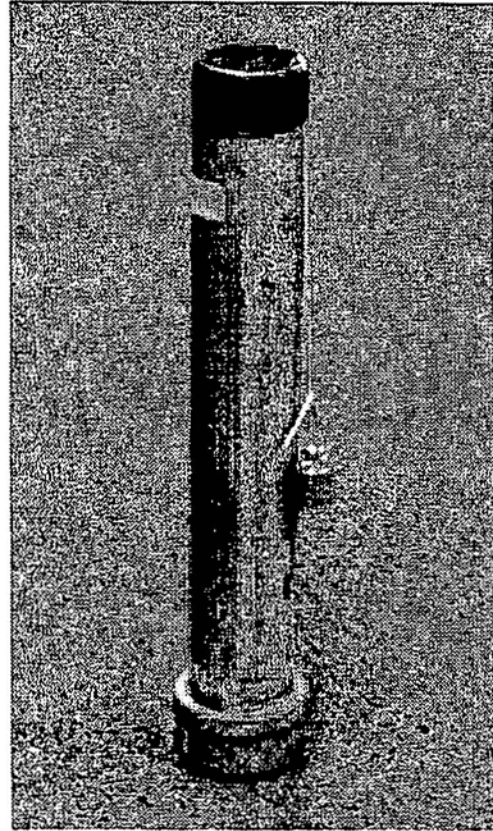


Fig. 3 Short tube with pendulum.

- Long Tube, 100 g Mass, Top Sensor (LT100GT)
- Long Tube, 100 g Mass, Bottom Sensor (LT100GB)
- Long Tube, 50 g Mass, Top Sensor (LT50GT)
- Long Tube, 50 g Mass, Bottom Sensor (LT50GB)
- Short Tube, 100 g Mass, Top Sensor (ST100GT)
- Short Tube, 100 g Mass, Bottom Sensor (ST100GB)
- Short Tube, 50 g Mass, Top Sensor (ST50GT)
- Short Tube, 50 g Mass, Bottom Sensor (ST50GB)

For each of these eight categories or classes, 60 signals were generated to produce a net of 480 signals. From this population of signal, 10 from each category were selected for neural network training, and 10 others from each category were selected for testing. Thus, from this population of 480 signals, 160 were randomly selected for use in this project.

For the purpose of these experiments, a certain degree of randomness in generating the signals was preferable to extreme consistency simply because the varied signals provide a more realistic sorting challenge for the neural network. Thus, only minimal effort was made to consistently reproduce the set of signals for a certain class. For example, visual inspection was considered an adequate means of determining that the pendulum was perpendicular to the tube prior to its release. Similarly, sensor placement was unlikely to be exact when the sensor was moved from top to bottom and tube to tube.

#### 4. Feature Extraction

Among the more obvious features that describe an acoustic signal are its frequency components. Figures 4 and 5 illustrate the relationship of the frequency to time domain for a particular signal. Figure 5 is the frequency spectrum of the time domain signal shown in Figure 4. Transforming a time domain signal to the frequency domain produces a data set that contains no more or no less information than the time domain, but; for many applications, the frequency domain signal is more useful. For example, the human ear is designed to function in the frequency domain. People can easily recognize familiar voices based upon the frequency spectrum of the voices.

The same is true of impact signals. Each region in a nuclear power plant (steam generators, reactor pressure vessel, etc.) has its own unique set of resonance which, when struck by a loose part, manifest themselves in the frequency spectrum of the resultant acoustic impact signal. Information in the frequency spectrum of impact provides valuable information for sorting signals by their point of impact.

Using the fine-bin frequency spectrum obtained from performing a Fourier transform on the original time-domain signal as input to a neural network is unlikely to be the optimal method for extracting the useful information contained therein. Since the aforementioned frequency shifts are typically macroscopic, the efficiency of using the frequency spectrum is, in some cases, enhanced by using a coarse histogram of the spectrum as input to the neural network. Of course, this potentially introduces a new variable into the optimization process since varying bin widths should result in varied network performance.

Figure 6 is an illustration of a frequency histogram. In this case, the frequency spectrum depicted in Fig. 5 has been converted into a ten bin histogram. For this project, the histograms were created by breaking a frequency spectrum such as the one shown in Fig. 5 into  $N$  equal bins. The average frequency is then calculated for each bin.

Another means of capturing the macroscopic behavior of a signal in the frequency domain is to simply note the peaks in a frequency spectrum. Indeed, this may be a very effective means of extracting useful information from the frequency spectrum since it quickly identifies characteristic resonance and fundamental frequencies specific to an object. In this project, These peaks are identified by simply locating the largest spikes that appear in a frequency spectrum. If two peaks are identified and are determined to be too close together (i.e., below the resolution threshold), the peaks are deliberately identified as the same peak.

One simple feature that can be useful in sorting AE signals is to note the mean frequency of the signal. This

information is certainly contained in some of the other frequency-related features discussed thus far. Average frequency can often be estimated from knowing the frequency peaks, it can be easily approximated from a frequency histogram, and it can be calculated exactly from the unabridged frequency spectrum. Since the point of feature extraction is, among other things, to provide information to a neural network that is directly useable rather than forcing the network to discover for itself the relevant characteristics of its input data, calculating the average frequency up-front can be extremely useful. The average frequency for each signal was calculated similar to the average frequency calculation for a histogram bin.

All other things being equal, impacts of greater energy produce measurably higher frequency impact signals (Mayo et al., 1988); so the frequency spectrum may also contain information that will assist the neural network in sorting impact events by their impact energy. A more obvious feature for sorting by impact energy is the root mean square (RMS) amplitude of the entire impact signal. Since, higher energy impacts will produce larger acoustic signal amplitude, clearly this feature should be valuable for sorting impacts by energy.

Signal RMS is calculated next. Like the frequency spectrum, the time-domain signal may be broken into bins and the RMS value computed for each bin. Doing so enables one to see the macroscopic behavior of the signal over time. Macroscopically, a metal impact signal is an example of damped harmonic motion. The initial impact sets the material in motion. Then, inertia and the restoring force of the metal lattice attempt to keep the material in motion; but the oscillations are exponentially damped by forces which oppose the motion. Mathematically, this is expressed as:

$$\text{RMS}(t) = \text{RMS}_{t=0} \exp(-\lambda t). \quad (1)$$

By calculating the signal RMS over equally spaced bins, the results may be used to calculate the exponential damping factor ( $\lambda$ ). Because  $\lambda$  is a function of the physical system where the impact occurred, this feature also contains information that is useful for sorting signals by impact location.

Figure 7 illustrates graphically how this damping factor is calculated. Mathematically, the damping is factored by breaking the time domain signal into a number of bins, the RMS for each bin is calculated and the logarithm is taken for each of these RMS values. Finally, a linear least-squares fit is performed on these values using a standard least-squares algorithm to find a linear equation that best fits the log of the RMS values as a function of time. The slope of this equation is the damping factor,  $\lambda$ .

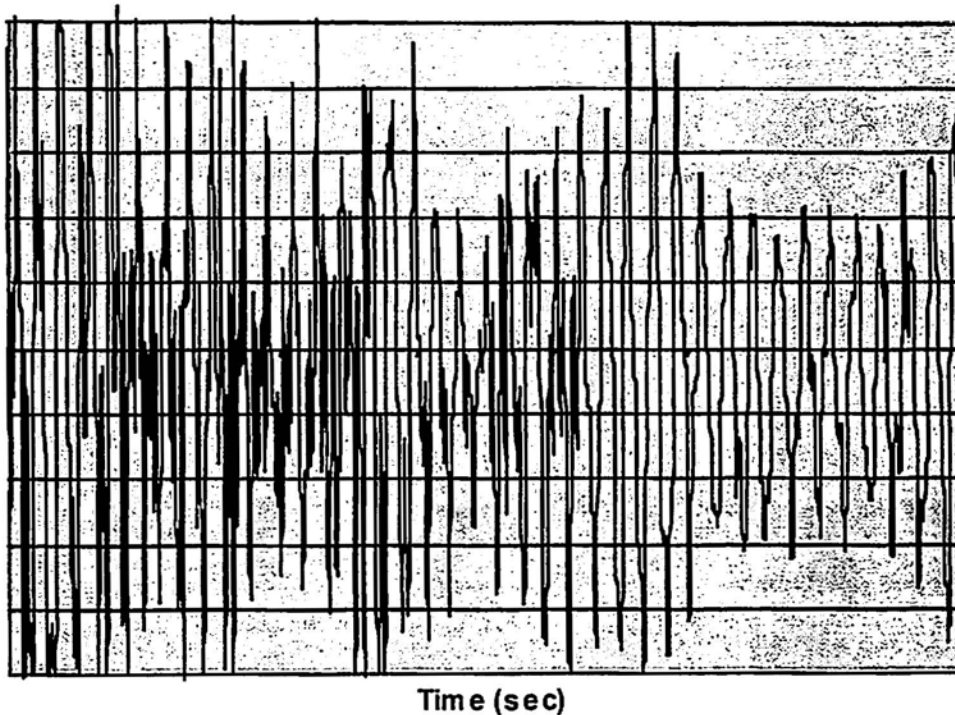


Fig. 4 Time domain signal.

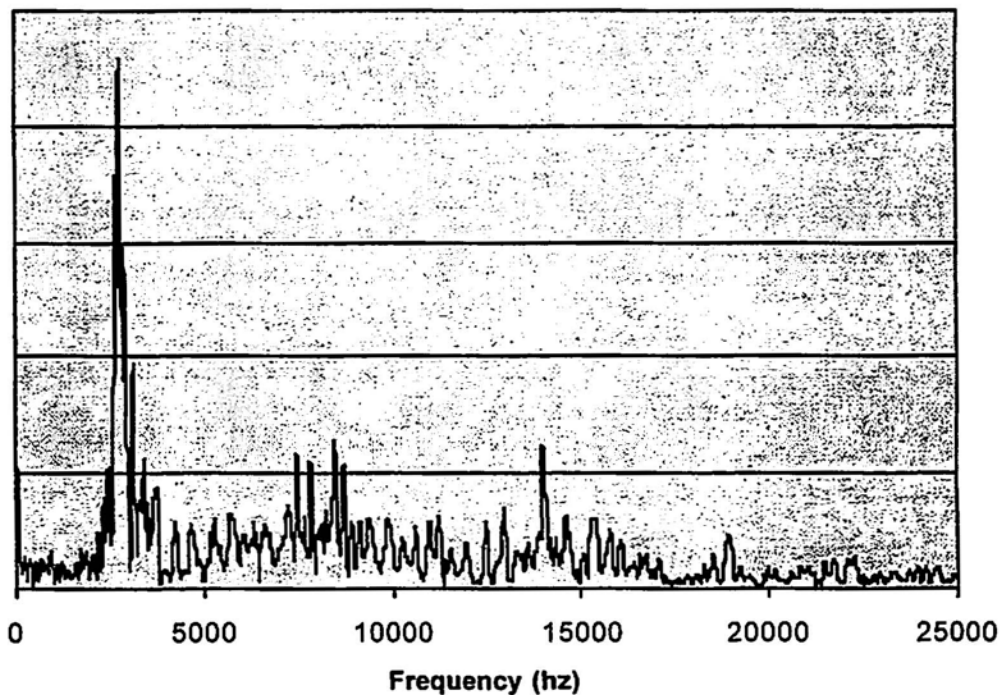


Fig. 5 Frequency domain signal.

As a matter of practicality, calculating this damping factor in the manner described is a rather simple process, but the results can be somewhat misleading if DC bias was present in the signal. In this case, the entire signal is shifted such that it is no longer centered about the x-axis; and, as a result, the calculated damping factor, while

mathematically accurate, may no longer describe the signal in the same manner. Additionally, material anomalies may prevent the oscillations from following equation (1) exactly; and, in such a case, the signal can be significantly asymmetric with respect to the x-axis.

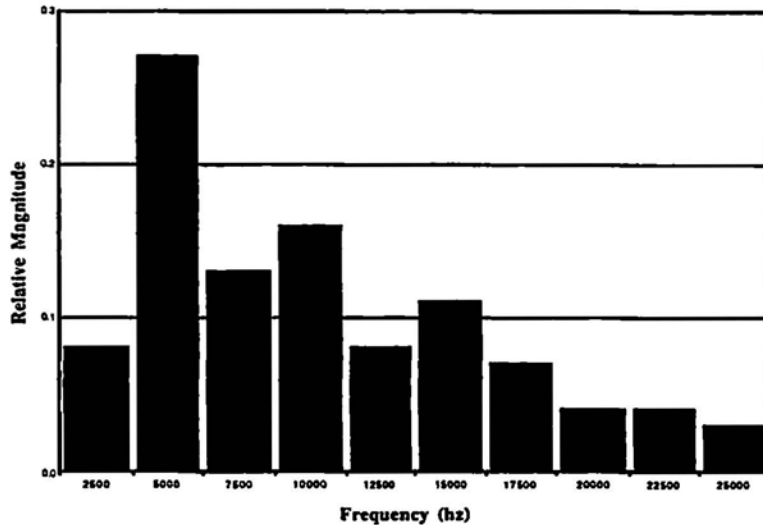


Fig. 6 Frequency spectrum histogram.

Fortunately, a simple solution was developed, implemented, and found to be quite effective. For any given signal, the damping factor was calculated using the previously described method. Next, a similar damping factor was calculated using only the positive portion of the signal; and, finally, a damping factor was calculated using the negative portion of the signal.

Table 1 List of various features extracted.

Feature Description	Data Points
Raw Time-Domain Data	700
Unabridged Frequency Spectrum	512
Frequency Spectrum Histogram	10
Frequency Peaks	5
Positive Damping Constant	1
Negative Damping Constant	1
Net Damping Constant	1
Average Frequency	1
Signal RMS	1

If the signal has no DC bias and is essentially symmetric about the x-axis, the positive damping factor, negative damping factor, and net damping factor will be nearly equal in magnitude. For signals with DC bias or appreciable asymmetry, these factors will be significantly different.

Table 1 provides a summary of the various features used in this project and the number of data points associated with each particular feature. While raw time-domain data represents no feature extraction at all, it is included in the table for comparison.

## 5. Testing

Eight basic tests were run with four different types of feature data set. Generally, a test would use two or four categories of signals and attempt to sort them into their appropriate two or four categories. For each test several sets of signals were used. Ten signals from each of these categories were used for training data. Similarly, another ten signals from each category, separate from those used for training, were used as test data.

The one exception to these generalizations is a particular test that, for reasons that will be discussed later, attempted to sort four categories of signals into only two groups. Like the others, this test used ten signals from each category (for a total of 40 signals) for training and another 40 signals for testing data, but these 40 testing signals were to be classified into two groups. Table 2 summarizes the various tests performed.

The types of feature extraction and the abbreviations that will be used to reference them throughout the remainder of this work are listed below.

- **Raw Data:** No feature extraction at all, just the raw time domain signal.
- **Frequency Spectrum:** The complete frequency spectrum obtained from converting the time domain signal to the frequency domain.
- **Standard Feature Set:** The frequency histogram, frequency peaks, damping factors, average frequency, and signal RMS features described in Section 4.
- **Scaled Feature Set:** Same as the standard feature set, but the feature values are scaled such that all are on the same order of magnitude.

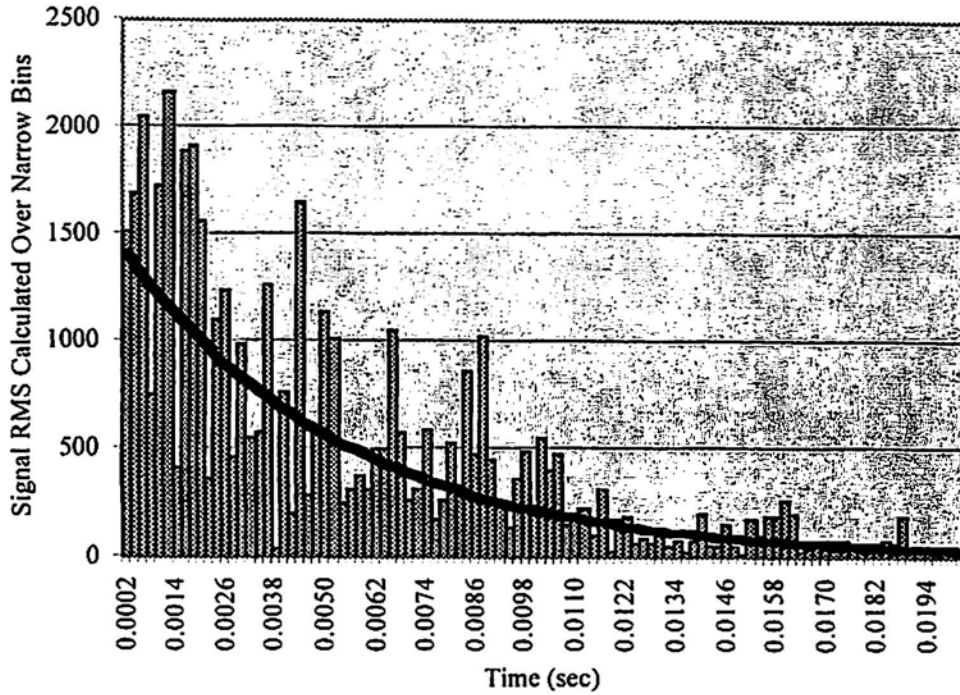


Fig. 7 Exponential signal damping trend.

Table 2 General tests performed.

Test number	Data Sets Used				Categories
Test 1	LT100B	LT100T			2
Test 2	LT50B	LT50T			2
Test 3	ST100B	ST100T			2
Test 4	ST50B	ST50T			2
Test 5	LT100B	LT100T	ST100B	ST100TB	4
Test 6	LT50B	LT50T	ST50B	ST50TB	4
Test 7	LT100B	LT50B	ST100B	ST50B	4
Test 8	LT100B	LT50B	ST100B	ST50B	2

Since it has not been previously mentioned, the "scaled feature set" is deserving of some additional description. There was some concern about the wide range of values between different types of features. This concern seems particularly valid given that a FAM input data file must be normalized prior to use. This could result in small feature values to lose their significance completely. To remedy this situation, the values of the standard feature set were scaled such that all features have values on the same order of magnitude, thus producing the "scaled feature set".

Recalling the labeling convention discussed in section 3, one can see from Table 2 that in Tests number 1-4 the Fuzzy ARTMAP network is called upon to differentiate between top and bottom sensor mounting.

Similarly, Tests number 5 and 6 call upon the network to distinguish between top and bottom sensor mounting while simultaneously differentiating between short and long tubes. Test number 7 also calls upon the network to separate data into four categories, but does not include sensor placement as a variable. Rather, the network is to sort long and short tubes (as in Tests 5 and 6) as well as sorting by the mass of the pendulum. Because Tests number 5-7 have four possible outcomes, it is to be expected that, all other things being equal, they represent a greater challenge for the network than do Tests 1-4.

Test number 8 is comparatively unusual in that four categories of input data must be sorted into only two categories of output. This test was arranged such that the network was to sort only by the mass of the pendulum used. In so doing, the network would be required to ignore the significant

Table 3 Success rate summary for each test in %.

Feature Type	TEST # 1-8							
	% success rate							
Raw Data	100	100	100	80	83	85	85	83
Frequency Domain	80	85	95	75	93	65	53	80
Standard Features	65	85	95	85	78	83	78	70
Scaled Features	100	95	80	75	75	78	78	78

difference between using short and long tubes. It was the intent of this test to observe the ability of the network to ignore certain stimuli, because doing so provides another means of gaining insight into network response to various features. Table 3 summarizes the results achieved for each feature set on each test.

## 6. Conclusions

From Table 3 it may be concluded that, overall, the best results were obtained using raw data as input. In Tests number 1-3, the network actually achieved 100% correct classification using raw data input.

Although the network performed well when using the scaled feature set, this work does not support the assumption that feature extraction will improve neural network performance in classifying acoustic signals of this type. It is, of course, recognized that new features may be developed that could potentially lead to higher success rates than those obtained using raw data. Given the challenge of developing independent features for acoustic signals and the remarkable results achieved using only raw data, the incentive for developing such features seems less than overwhelming.

The results from this study as well as a prior work (Keyvan and Nagaraj, 1997) indicate that artificial neural networks indeed have high potential for successful application in pattern recognition of loose part acoustic emission signals. In addition, there is no need for extra effort of feature extraction in pre-processing of network input data, the raw acoustic data will do the job.

## Acknowledgments

This work was supported by the National Science Foundation (Grant # ECS-9415004).

## References

G. A. Carpenter and S. Grossberg (1992), "Fuzzy ART-MAP: A Neural Network Architecture for Incremental

Supervised Learning of Analog Multidimensional MAPs", *IEEE Transactions on Neural Networks*, 3(5), 698-713.

G. Carpenter and S. Grossberg (1988), "The ART of Adaptive Pattern Recognition by a Self-Organizing Neural Network", *Computer*, 21(3), 77-88.

M. B. Christopher (1995), *Neural Networks for Pattern Recognition*, Clarendon Press, Oxford.

E. A. Edmonds, L. Y. Pam, and S. M. O'Brien (1992), "Automatic Feature Extraction from Spectrograms for Acoustic-Phonetic analysis", *Proceedings of the 11th IAPR International Conference on Pattern Recognition*, vol. II, pp. 701-704.

S. Keyvan and R. King (1992), "The Role of Acoustic Monitoring as a Diagnostic Tool in Nuclear Reactors" *Journal of Acoustic Emission*, 10(3-4), 91-95.

S. Keyvan and J. Nagaraj (1997), "Pattern Recognition of Acoustic Signatures Using ART2-A Neural Network". *J. Acoustic Emission*, 14(2), 97-102.

S. Keyvan, X. Song, and M.L. Kelly (1997), "Feature Extraction for Artificial Neural Network Application to Fabricated Nuclear Fuel Pellet Inspection," *Nuclear Technology*, 119, 269-275.

W. Khan (1995), "Application of AI Techniques to the Diagnosis of Nuclear Reactor System", M.S. Thesis, University of Missouri-Rolla.

C. W. Mayo, D. P. Bozarth, G. N. Lagerberg and C.L. Mason (1988), "Loose-Parts Monitoring Systems Improvements", Electric Power Research Institute, EPRI NP-5743.

J. Nagaraj (1995), "A Prototype Diagnostic Monitoring System Using Artificial Neural Networks", M.S. Thesis, University of Missouri-Rolla.

B. Olma and D. Wach (1994), "On-line Classification of Acoustic Burst Signals by a Neural Network Application to Loose Parts Monitoring in Nuclear Power Plants", *Proceed-*

*ings of the IEEE Conference on Control Applications, Piscataway, NJ, pp. 1133-1138.*

R. G. Pickard (1997), "Application of Artificial Neural Network Technology to Loose Parts Monitoring Systems", M.S. Thesis, University of Missouri-Rolla.

S. Szyszkko, P.A. Payne (1991), "Artificial Neural Networks for Feature Extraction from Acoustic Emission Signals", *Proceedings of IEE Colloquium on measurement, Modeling, and Imaging for Non-destructive Testing*, 6, 1-6.

J. Yang and G.A. Dumont (1991), "Classification of Acoustic Emission Signals via Hebbian Feature Extraction", *Proceedings of IEEE International Joint Conference on Neural Networks (IJCNN)*, vol. I, pp. 113-118.

## Conferences and Symposia

### **Fourth Far East Conference On NDT (FENDT '97)**

October 8-11, 1997, Cheju-Do, Korea, sponsored by Korean Society of Nondestructive Testing. The following articles are reprinted from its Proceedings.

- Source Location in Highly Dispersive Media by Wavelet Transform. of AE Signals  
Oh-Yang Kwon and Young-Chan Joo S1-S10
- Acoustic Emission Monitoring of the Fatigue Crack Activity in Steel Bridge Members  
Dong-Jin Yoon, Seung-Seok Lee, Philip Park, Sang-Hyo Kim, Sang-Ho Lee and Young-Jin Park S11-S18
- Acousto-Ultrasonic Evaluation of Adhesively Bonded CFRP-Aluminum Joints  
Seung-Hwan Lee and Oh-Yang Kwon S19-S30
- Estimation of Initial Damage in Concrete By Acoustic Emission  
Masayasu Ohtsu, Yuichi Tomoda and Taisaku Fujioka S31-S39
- Application of AE to Evaluate Deterioration of Port and Harbor Structures  
Kimitoshi Matsuyama, Akichika Ishibashi, Tetsuro Fujiwara, Yasuhiro Kanemoto, Shiro Ohta, Shigenori Hamada and Masayasu Ohtsu S40-S49
- Acoustic Emission Diagnosis of Concrete-Piles Damaged By Earthquakes  
Tomoki Shiotani, Norio Sakaino, Masayasu Ohtsu and Mitsuhiro Shigeishi S50-S59
- Observation of Damage Process in RC Beams under Cyclic Bending by Acoustic Emission  
Mitsuhiro Shigeishi, Masayasu Ohtsu, Nobuyuki Tsuji and Daisuke Yasuoka S60-S69
- Spectral Response and Acoustic Emission of Reinforced Concrete Members under Fatigue Bending  
Yasunori Sakata and Masayasu Ohtsu S70-S79
- Acoustic Emission Behavior during Tensile Deformation of Welded Steel Joints  
J. H. Huh, K. A. Lee and C. S. Lee S80-S88
- Acoustic Emission Signal Analysis in C/C Composites  
Ja-Ho Koo, Byung-Nam Kim, Manabu Enoki and Teruo Kishi S90-S94

### **Congreso Regional de Ensayos No Destructivos y Estructurales**

Oct. 27-30, 1997, Mendoza, Argentina, sponsored by Comisión Nacional de Energía Atómica and Universidad Tecnológica Nacional. The following article is reprinted from its Proceedings.

- Recent Development in Acoustic Emission Kanji Ono S95-S102
- 40th AEWG Meeting, Program and Abstracts S103-S110
- 14th International Acoustic Emission Symposium & 5th Acoustic Emission World Meeting,  
Abstracts of Oral Briefs S111-S124
- 6th AECM Symposium, Program S125-S126

## **SOURCE LOCATION IN HIGHLY DISPERSIVE MEDIA BY WAVELET TRANSFORM OF AE SIGNALS**

**Oh-Yang Kwon and Young-Chan Joo**

Department of Mechanical Engineering, Inha University  
253 Yonghyun-dong, Incheon 402-751, Korea

### **ABSTRACT**

A new technique for the location of acoustic emission(AE) sources in thin plates has been studied using wavelet transform of AE signals. The detected AE signals were pre-processed using wavelet transform to decompose the low frequency flexural wave and the high frequency extensional wave. Since the flexural wave is highly dispersive, a decomposed flexural component has been extracted for a single frequency or within a very narrow frequency band by the inverse wavelet transform. The result of source location has been compared with those by the conventional as well as the cross-correlation method.

### **INTRODUCTION**

Source location can be regarded as the most practical thus important function of AE testing of real structures since it provides a quick or real-time access to the region of interest, damaged or being damaged. Numerous studies of source location have been done since the application AE technique to the hydroproof testing of Polaris missile chamber in 1964[1], most of which are well documented in the literatures[2]. When the AE source location technique had been applied for the thick-walled structures such as nuclear reactor vessels, the conventional method based on the threshold crossing may have no problem. On the other hand, when it is applied for thin-walled structures such as aerospace structures such as composite shells or aluminum panels, the conventional method cannot be successful any more. Plate wave consists of the nondispersive extensional wave and the dispersive flexural wave. The large difference in amplitude between the extensional and the flexural mode can cause a serious problem in source location[3,4]. By introducing wavelet transform of AE signals, the low-amplitude extensional mode can be filtered out. The decomposed flexural waves have been selected for the source location based on threshold crossing. The wavelet transform appears to have a great potential for AE signal processing[5].

## WAVELET TRANSFORM

The continuous wavelet transform(CWT) is defined as the sum of the signal multiplied by scaled, shifted versions of the wavelet function  $\Psi$  over all time:

$$C(\text{scale}, \text{position}) = \int_{-\infty}^{\infty} f(t)\Psi(\text{scale}, \text{position}, t)dt \quad (1)$$

The result of the CWT are many wavelet coefficients  $C$ , which are a function of scale and position. If we choose scales and positions based on powers of two which is so called dyadic scales and positions, then our analysis will be much more efficient and just as accurate. We obtain such an analysis for actual waveform data from the discrete wavelet transform(DWT).

$$C(a,b) = C(j,k) = \sum_{n \in \mathbb{Z}} S(n)g_{j,k}(n) \quad \text{where, } (a = 2^j, b = k2^j, j \in \mathbb{N}, k \in \mathbb{Z}) \quad (2)$$

In order to be efficient and useful, a method designed for analysis also has to be able to perform synthesis(an inverse transform). The wavelet method achieves this. The analysis starts from  $s$  and results in the coefficients  $C(a,b)$ . The synthesis starts from the coefficients  $C(a,b)$  and reconstructs  $s$ . Synthesis is the reciprocal operation of analysis. For signals of finite energy, there is two formulas to perform the inverse wavelet transform:

- Continuous synthesis:

$$S(t) = \frac{1}{K_{\Psi}} \iint_{\mathbb{R}} C(a,b) \frac{1}{\sqrt{a}} \Psi\left(\frac{x-b}{a}\right) \frac{da db}{a^2} \quad (3)$$

where  $K_{\Psi}$  is a constant depending on  $\Psi$ .

- Discrete synthesis:

$$S(t) = \sum_{j \in \mathbb{Z}} \sum_{k \in \mathbb{Z}} C(j,k)\Psi_{j,k}(t) \quad (4)$$

In the above Eq. 4, let us fix  $j$  and sum on  $k$ . A detail  $D_j$  is nothing more than the Eq. 5. Let us sum on  $j$ . The signal is the sum of all the details:  $S = \sum_{j \in \mathbb{Z}} D_j$

$$D_j(t) = \sum_{k \in \mathbb{Z}} C(j,k)\Psi_{j,k}(t) \quad (5)$$

$$A_j = \sum_{j > J} D_j \quad (6)$$

The details have just been defined. Take a reference level called  $J$ . There are two sorts of details. Those associated with indices  $j \leq J$  correspond to the scales  $a = 2^j \leq 2_J$  which are the fine details. The others, which correspond to  $j > J$ , are the coarser details. We group these latter details into the Eq. 6.

An efficient way to implement this scheme using filters was developed in 1988 by Mallat[6]. The Mallat algorithm is in fact a classical scheme known in the signal processing community as a two-channel subband coder.

For many signals, the low-frequency content is the most important part since it is what gives the signal its identity. The high-frequency content, on the other hand, imparts flavor or nuance. The original signal,  $S$  passes through two complementary filters and emerges as two signals as shown in Fig. 1. The approximation,  $A$  is the high-scale, low-frequency component of the signal. The detail,  $D$  is the low-scale, high-frequency component. The filtering process, at its most basic level, looks like this:

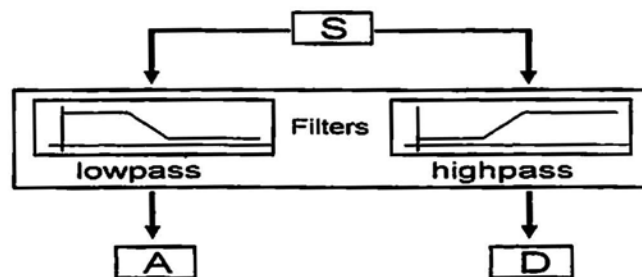


Fig. 1 The filtering process

The decomposition process can be iterated, with successive approximations being decomposed in turn, so that one signal is broken down into many lower-resolution components. This is called the wavelet decomposition tree as shown in Fig. 2.

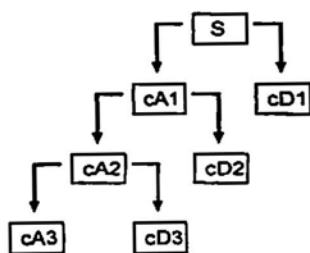


Fig. 2 The wavelet decomposition tree

$$S = A_j + \sum_{j \leq J} D_j$$

$$A_{j-1} = A_j + D_j$$

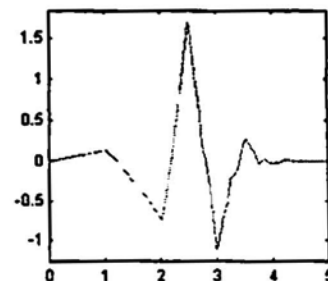


Fig. 3 Daubechies wavelet

The arrival time can be calculated using one of the decomposed wavelets, i.e. an approximation or a detail. In this study, the detected signals from each sensor were decomposed by the Daubechies[7] wavelet shown in Fig. 3 at level 5, i.e. the d5 for Al6061 plate and the a5 for CFRP laminate as shown in Fig. 4.

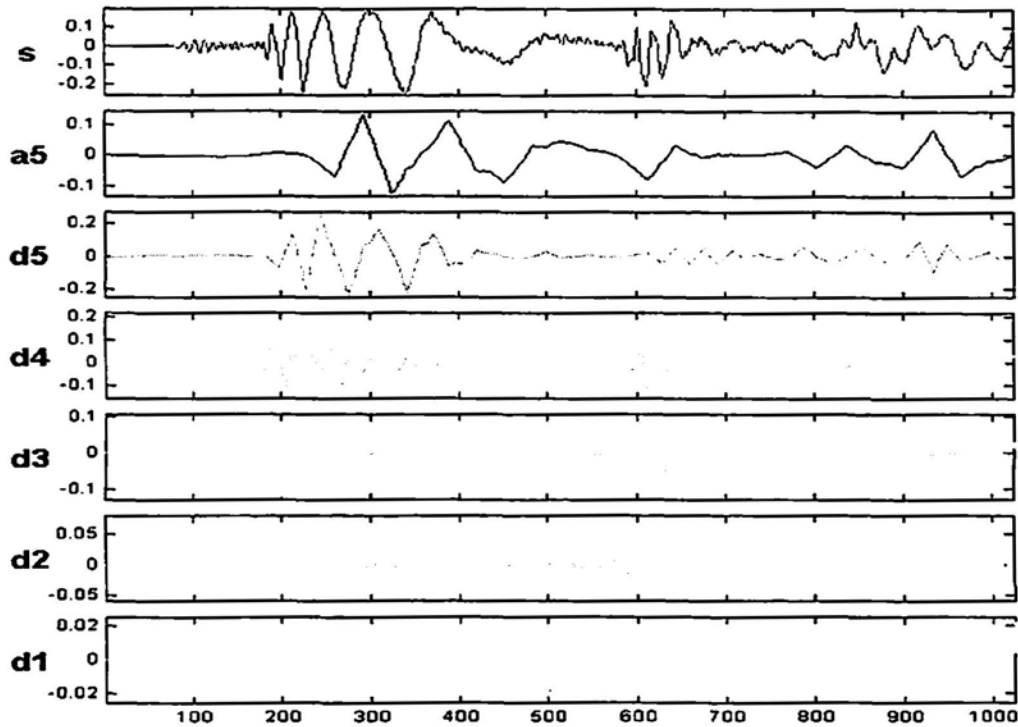


Fig. 4 The original signal(S) from Al6061 plate and the decomposed wavelets

## EXPERIMENTS

Source location was carried out on a 1200 x 1000 x 3 mm Al 6061 plate and a 650 x 650 x 4 mm cross-ply CFRP laminate. The elastic waves generated from the simulated source of pencil lead breaks(HB 0.5 Standard pencil lead; JSNDI-006). Four broadband, high fidelity, piezoelectric sensors(B1025; Digital Wave) were employed to form double triangular sensor array. Sensors were mounted on the surface of the plate by high vacuum grease. Detected signals were amplified by preamplifiers then fed into the signal conditioning module(F4000). The module controlled the filtering and gain for AE signal and the trigger level. Signals were digitized and recorded at PC through A/D boards(CS225; Gage). The conventional threshold crossing and the cross-correlation method were performed by using FWD96 software in the

apparatus. Another method of the threshold crossing with wavelet transformed(WT) signals was performed by using the program contained in the Matlab<sup>®</sup> Toolbox. Fig. 5 is a schematic diagram of the experimental setup.

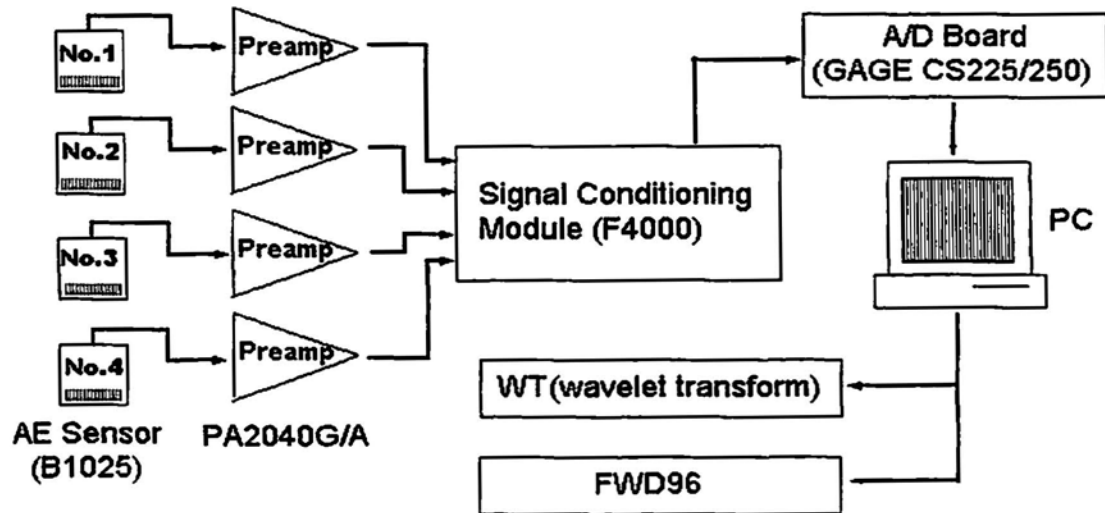


Fig. 5 Schematic diagram of the experimental setup

Table. 1 The coordinates of AE sensor location

Coordinates Sensor No.	CFRP plate (x, y)	Al6061 plate (x,y)
1	( 0, 0 )	( 0, 0 )
2	( 300.0, 0 )	( 600.0, 0 )
3	( 150.0, 259.8 )	( 300.0, 519.6 )
4	( 450.0, 259.8 )	( 900.0, 519.6 )

Table 2 The coordinates of exact AE source

Coordinates Source No.	CFRP plate (x, y)	Al6061 plate (x, y)
1	( 150.0, 86.7 )	( 300.0, 173.2 )
2	( 187.5, 108.3 )	( 375.0, 216.5 )
3	( 105.0, 30.0 )	( 210.0, 60.0 )
4	( 180.0, 165.0 )	( 360.0, 330.0 )
5	( 150.0, -43.5 )	( 300.0, -87.0 )

## RESULTS AND DISCUSSION

Results of source location in a Al6061 plate based on the conventional threshold crossing, the cross-correlation and the threshold crossing with wavelet transformed signals are shown in Fig. 6, Fig. 7 and Fig. 8, respectively. With the conventional method, the result of source location appeared to be highly affected by the level of threshold voltage. The result with 0.1V and 0.2V as the thresholds were fairly successful as shown in Fig. 5(b) and (c). On the other hand, the results shown in Fig. 5(a) and (d) appeared to be very poor with such a small change of threshold voltage as  $\pm 0.05V$ .

To get rid of the dependence on threshold voltage level, a new approach was developed and instrumented using cross-correlation.[3] the results shown in Fig.7 were obtained by using the apparatus in which the source location by cross-correlation is available. Once the frequency has been chosen properly, the result appeared not to be affected by the gain or threshold level settings.

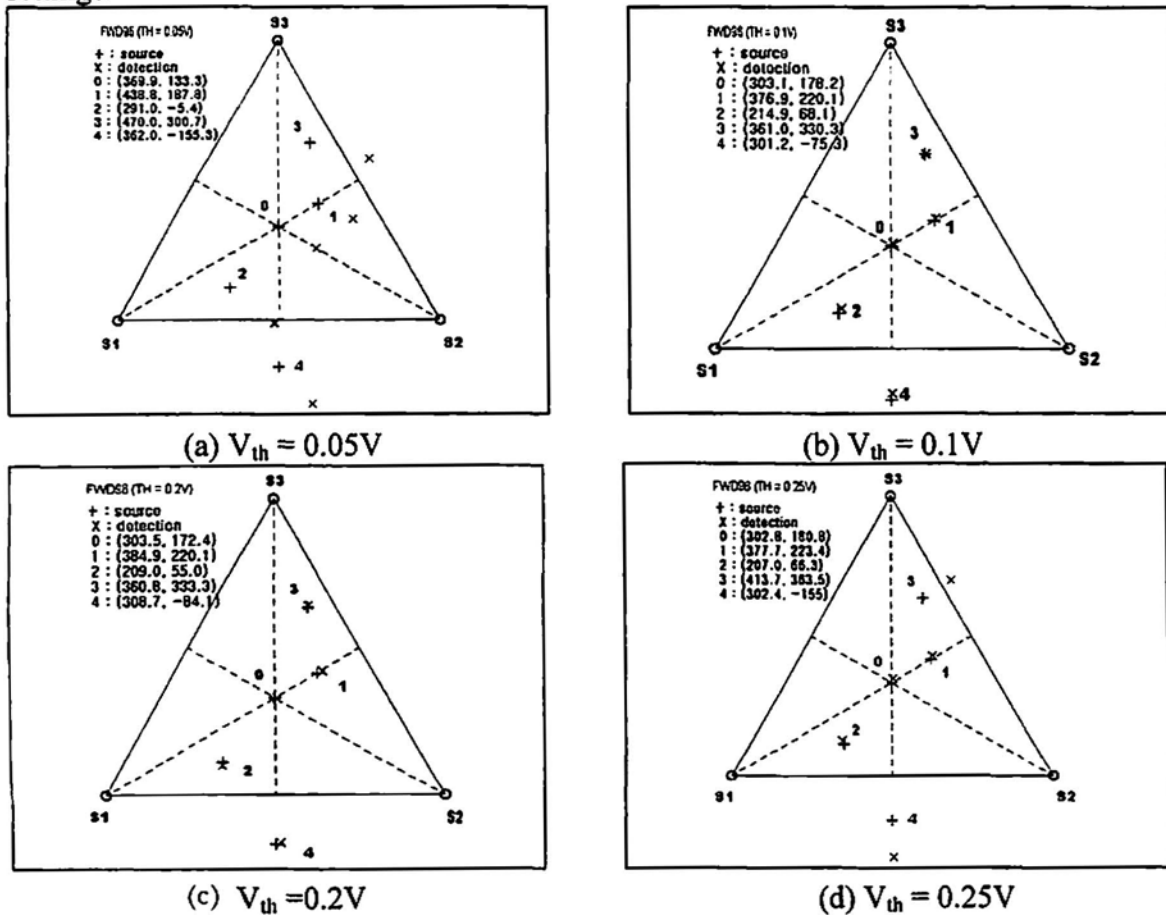
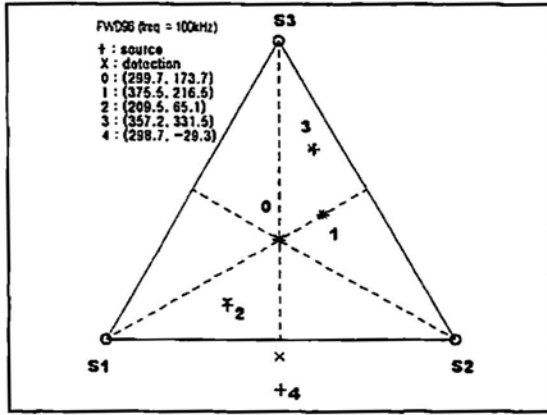
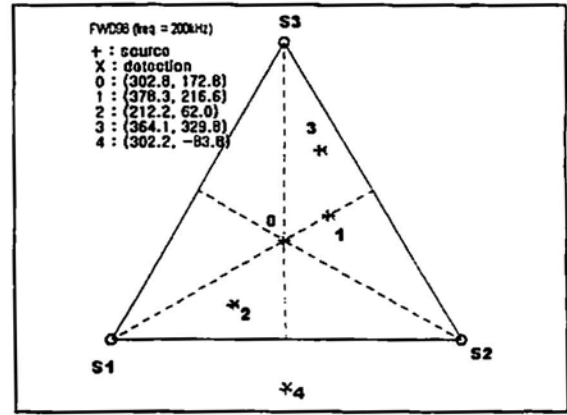


Fig. 6 Results of source location based on the conventional threshold crossing method in an Al6061 plate

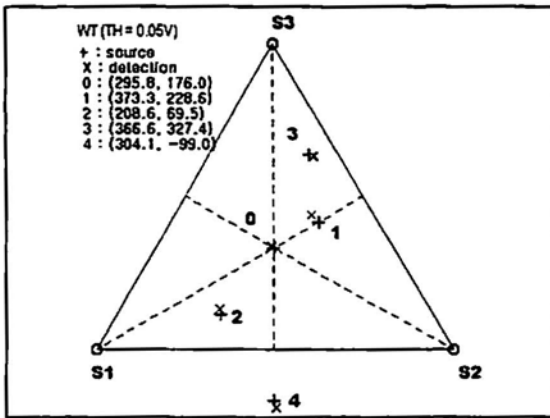


(a)  $f = 100\text{kHz}$

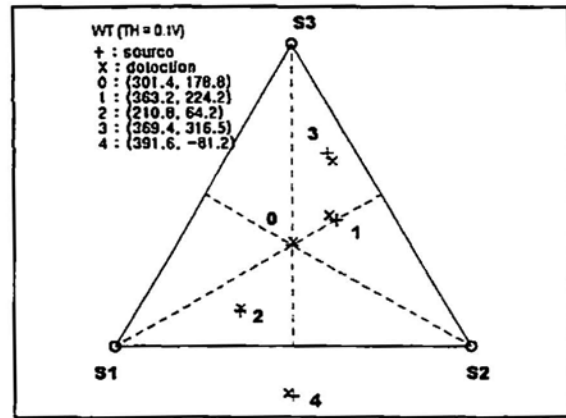


(b)  $f = 200\text{kHz}$

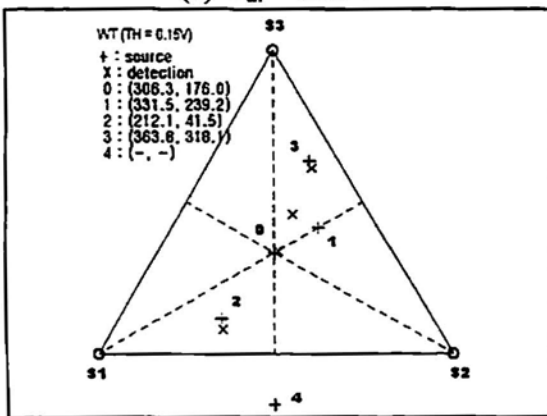
Fig. 7 Results of source location based on the cross-correlation in an Al6061 plate



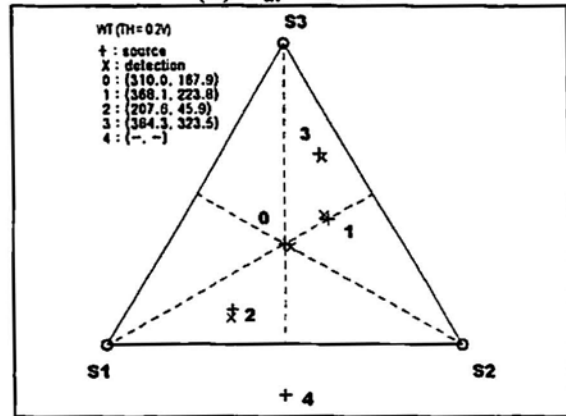
(a)  $V_{th} = 0.05\text{V}$



(b)  $V_{th} = 0.1\text{V}$



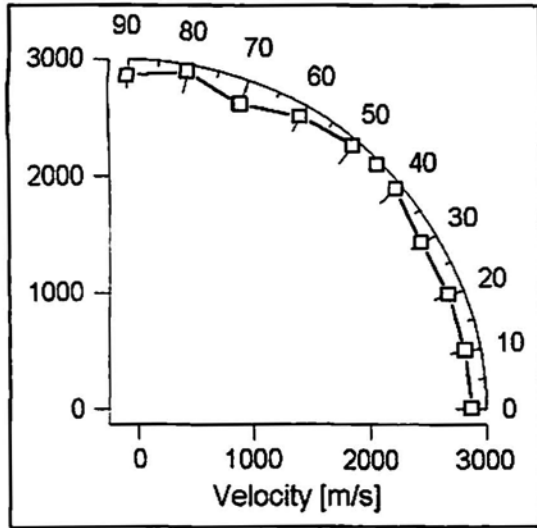
(c)  $V_{th} = 0.15\text{V}$



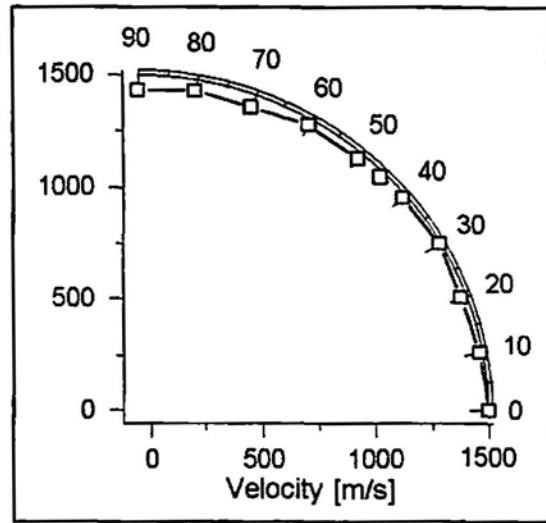
(d)  $V_{th} = 0.20\text{V}$

Fig. 8 Results of source based on the threshold crossing with wavelet transformed signals in an Al6061 plate

Another possibility for the arrival time to be independent of threshold level or gain settings based on the dispersive flexural wave has been investigated and the results are shown in Fig. 8.

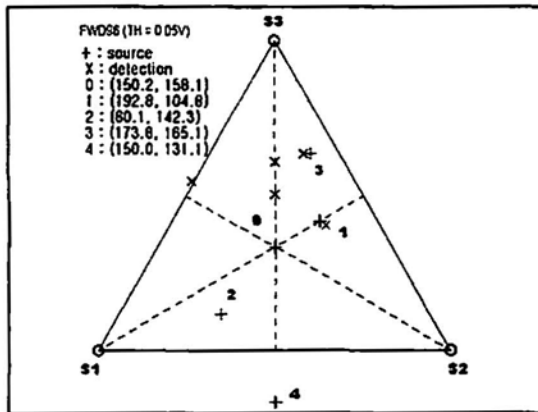


(a) Al6061

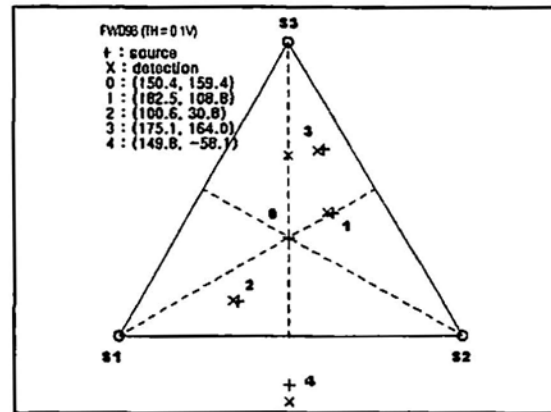


(b)  $[0/90]_{8S}$  CFRP

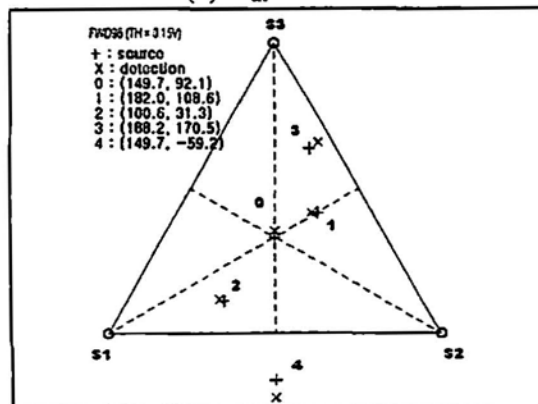
Fig. 9 Experimentally measured velocity with angle



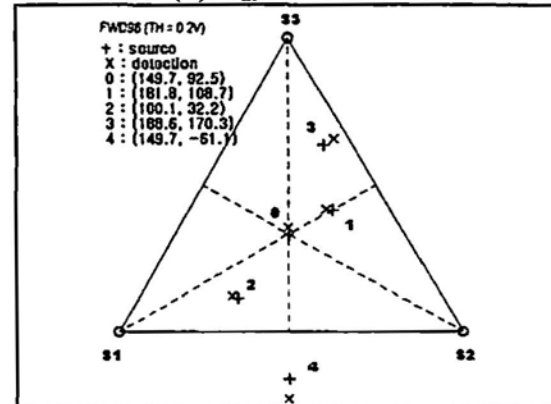
(a)  $V_{th} = 0.05V$



(b)  $V_{th} = 0.1V$



(c)  $V_{th} = 0.15V$



(d)  $V_{th} = 0.20V$

Fig. 10 Results of source location based the conventional threshold crossing method in a  $[0/90]_{8S}$  CFRP plate

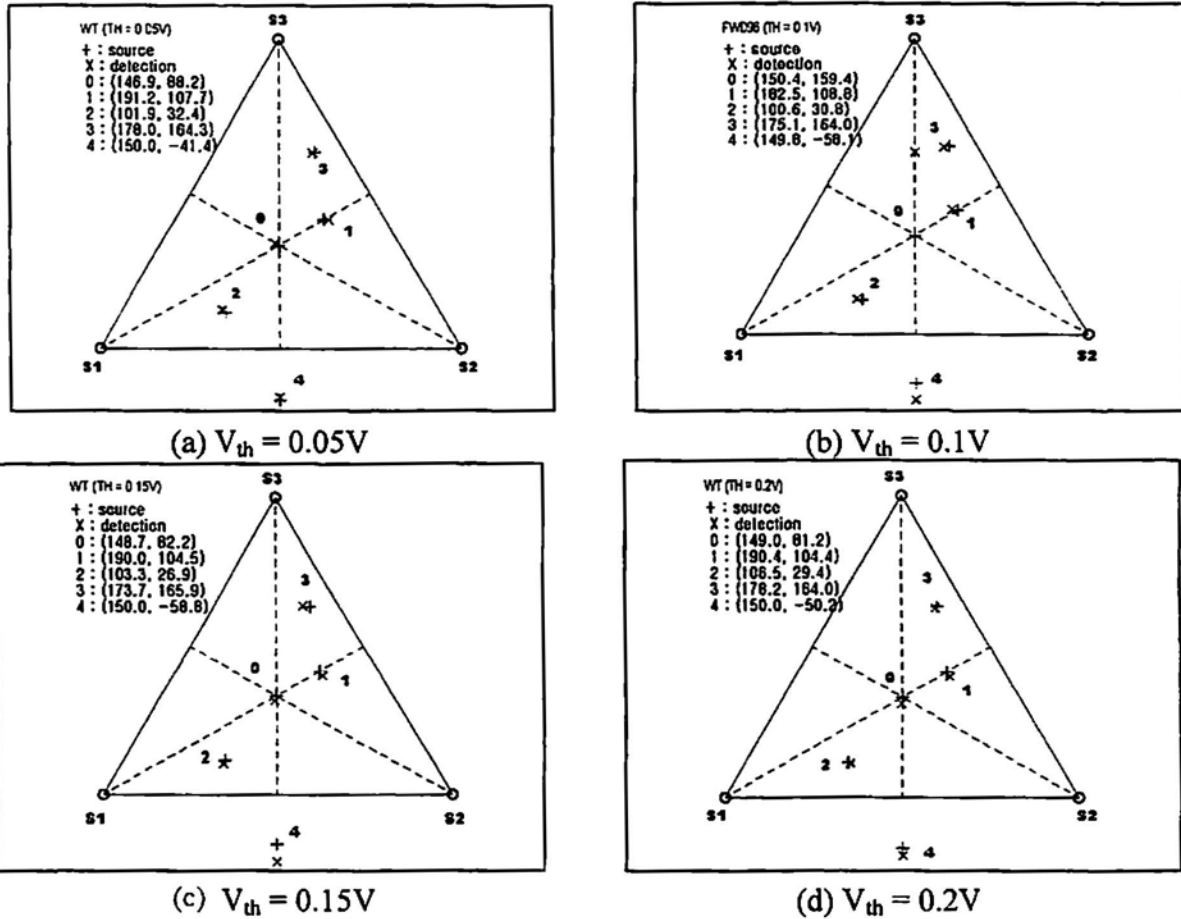


Fig. 11 Results source location based on the threshold crossing with wavelet transformed signals in a  $[0/90]_{8S}$  CFRP plate

Although the results are not as excellent as those by the cross-correlation method, they are insensitive to threshold level and most of the locations fall within the experimental error found.

The wave velocities in Al6061 and CFRP plates were experimentally measured with various angles from 0 to 90 degree as shown in Fig. 9. It was a little unexpected but the wave velocities in the  $[0/90]_{8S}$  CFRP laminate appeared not very anisotropic. Similar measurements for source location in the CFRP laminate were carried out as in the case of Al6061 plate. The wave velocities employed for source location were 2870 m/s and 1480 m/s for Al6061 and CFRP plates.

Results of source location in the CFRP plates using the conventional method and the wavelet method are summarized as shown in Fig. 10 and Fig.11, respectively. As in the case of source location in Al6061 plate, the conventional method appeared to be highly affected by the threshold level whereas the wavelet transform method did not. The result of source location by cross-correlation method was too poor to be presented here.

With the wavelet transformed signals, it is possible to trigger the location clocks on the flexural component with which we may apply the method to large real structures. Although the problem due to anisotropy was not solved, the problem due to dispersion could be overcome by isolating a single frequency or a very narrow band component using wavelet transform.

### CONCLUSION

The source location in a thin plate can be improved by introducing the wavelet transform of AE signals. The accuracy of source location appeared to be independent of threshold level or gain settings if the wavelet transformed signals are employed for the arrival time differences. The decomposed flexural wave becomes nondispersive if it has a single or a very narrow frequency band so that the method can be applied to a large scale real structures, where the high amplitude of flexural wave is utilized.

### ACKNOWLEDGEMENT

This work was supported by the Internal Research Fund, Inha University, Korea.

### REFERENCES

1. A. T. Green, C. S. Lockman, and R. K. Steele, "Acoustic Verification of Structural Integrity of Polaris Chambers", *Modern Plastics*, Vol. 41, No. 11, pp. 137-139&178&180, 1964
2. T. F. Drouillard, "Acoustic Emission - A Bibliography with Abstracts", Plenum, New York, 1979
3. S. M. Ziola and M. R. Gorman, "Acoustic Emission Source Location in Thin Plates Using Cross-correlation", *Proc. of AECM-4*, pp 411-417, July 27-31, 1992, Seattle, WA, U.S.A.
4. M. R. Gorman and W. H. Prosser, "AE Source Orientation by Plate Wave Analysis", *Journal of Acoustic Emission*, Vol. 9, No. 4, pp. 283-288, 1990
5. H. Suzuki, T. Kinjo, Y. Hayashi, M. Takemoto and Kanji Ono, "Wavelet Transform of Acoustic Emission Signals", *J. of Acoustic Emission* Vol. 14, No. 2, pp. 69-84, 1996
6. S. Mallat "A Theory for multiresolution signal decomposition: the wavelet representation", *IEEE Pattern Anal. and Machine Intell.*, vol. 11, no. 7, pp. 674-693, 1989
7. I. Daubechies, "Ten lecture on wavelets", SIAM, 1992

## **ACOUSTIC EMISSION MONITORING OF THE FATIGUE CRACK ACTIVITY IN STEEL BRIDGE MEMBERS**

**Dong-Jin Yoon<sup>1</sup>, Seung-Seok Lee<sup>1</sup>, Philip Park<sup>2</sup>,  
Sang-Hyo Kim<sup>2</sup>, Sang-Ho Lee<sup>2</sup> and Young-Jin Park<sup>3</sup>**

- <sup>1</sup> NDE Group, Failure Prevention Research Center  
Korea Research Institute of Standards and Science  
P.O.BOX 102, Yusong, Taejon 305-600, Korea
- <sup>2</sup> Department of Civil Engineering, Yonsei University
- <sup>3</sup> Institute of Construction Technology, Kolon Construction Co.

### **ABSTRACT**

Acoustic emission technique was employed for the monitoring of crack activity in steel bridge members. Laboratory experiment was carried out to identify active fatigue crack for the several test condition such as a different specimen type, a varying of cyclic load ratio. The results of this test indicated that the crack propagation characteristics for fatigue cycles did not change significantly with different type of beam. Through all of tests, load ratio of specimen affected significantly to the results such as the crack growth rate and the amount of generating AE signals. From fracture mechanics point of view, the straight curve obtained from theoretical calculation by Paris equation was well correlated to the experimental results. AE location events were not early detected although several AE hits from each sensor were generated in the early of the test. However the features of three parameters, that is, crack growth length, AE location events and cumulative AE events, showed almost same trend in their increase with the number of cycles. Although there were somewhat scattered location in the vicinity of upper flange, which were considered as environmental noises, good locations near the actual crack tip were obtained. Post filtering work was carried out to eliminate these unwanted location, good results were obtained from filtering work using AE parameters.

### **INTRODUCTION**

The deterioration of steel bridge members is caused by a combination of load and environmental factors. The unpredictable rate of deterioration makes it difficult for the

bridge engineer to plan for repair or replacement.[1] Generally most of steel bridge members are constantly subjected to cyclic loadings. The materials of structures were undergone by these fatigue loading then came to failure of structures finally. Several previous studies have showed the possibility for the applying acoustic emission technique to monitor the fatigue crack propagation in the bridge structure materials[2,3,4] and in the field testing[1,5,6]. However an useful guideline or a method of finding crack growth were not suggested in these results clearly. In addition it is very important to know and to plan for the applied load in the real structures during acoustic emission testing. Therefore the works relating to this relationship will be necessary to apply this technique to real structures. In this study, laboratory experiments for the I-beam with same materials of bridge construction were conducted to obtain and to characterize the relationship between acoustic emission signals and fatigue crack propagation. And also, in order to apply this technique to monitoring of real structures, an AE source location method to find fatigue cracks will be discussed.

## EXPERIMENTS

### Specimen preparation

In order to evaluate the effect of different types of structure, two types of specimen were prepared. Material used in these structures was bridge construction material of SWS490A. As shown in figure 1, web plate with thickness of 20mm were cut into 1200mm, 200mm in length and height respectively. And then it was welded to I-type beam using 10mm thickness plate. V-end notch was cut into 100 mm depth in the middle of plate span. Actual crack in the notch was made by fatigue test for introducing of pre-crack before each test.

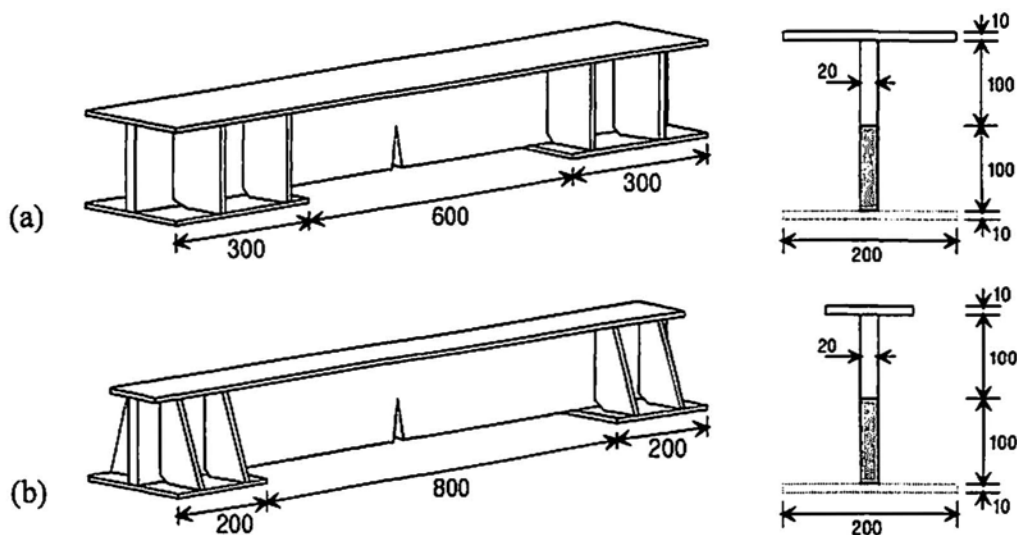


Figure 1 Preparation of test specimens (a) Type I, (b) Type II (unit : mm)

### Load control and strain measurement

Three point bending tests were conducted on a MTS closed loop hydraulic loading machine. All of test specimens were subjected to constant amplitude cyclic loading for each test at load frequency of 3 Hz. In order to eliminate environmental noise such as a hydraulic noise and rubbing sources between specimen and jig contact point, a soft and tough paper was used between support and specimen as noise insulator. Five specimens were tested in this study, three of type I and two of type II, as shown in table 1. To observe the effect of load condition, some different load ratio (min. load / max. load) and load range (difference between max. load and min. load) were applied to each specimen. To measure local average stress of near crack, four strain gauges were used. Strain measurements for each strain gauge were conducted for both static and dynamic loading condition

Table 1 Type of Specimens and load condition

Type of Specimen		Type I			Type II	
No. of Specimen		1	2	3	4	5
Load condition	Range ( $\Delta P$ : ton)	3-6(3)	3-6(3)	1.8-6(4.2)	3-5(2)/3-6(3)	1.5-5(3.5)
	Ratio (R)	0.5	0.5	0.3	0.6/0.5	0.3

### Crack growth measurement

Crack gauges were used to obtain crack growth length during the experiments. All of specimens used crack gauge (Model KG-B25, 25mm crack length, KRAK-GAGE<sup>®</sup>) which is thin film type for continuous crack growth measurement. Crack gauges were attached to web plate properly so that there is coincidence between the gauge starting crack tip and the root of the specimen notch. The output voltage from crack measurement system (Model 1078, FRACTOMAT) was fed into AE measurement system as a parameter input. Figure 2 shows AE sensor array and a crack gauge attached in the root of the notch.

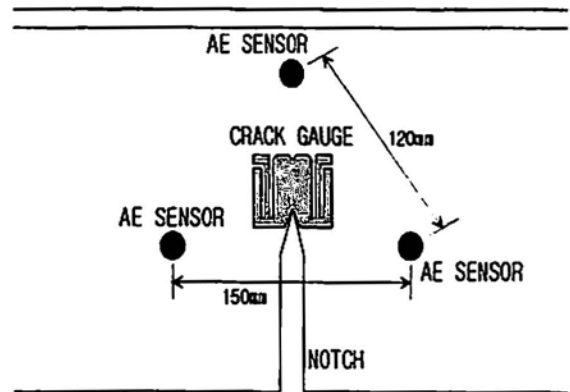


Figure 2 AE sensor array for triangular source location and a crack gauge attached in the root of the notch

### AE monitoring

The measurement of AE signals was conducted using multi-channel commercial AE equipment, SPARTAN 2000 (by PAC). All of tests used triangular source location method, using three sensors, for monitoring of crack propagation. With all sensors in place, the traditional pencil lead break test was performed for source location sensor

array. The pencil break also checked the accuracy of source location setup, indirectly determining the actual acoustic velocity in this structure. A preamplifier gain of 60dB plus post gain of 20dB and a fixed threshold of 48dB were used. Figure 2 shows the position of each sensor around pre-crack tip. AE Sensors with resonant frequency of 300 kHz were used. The preamplifier output was also fed into 4 channel digital oscilloscope, model 9354 (by LeCroy). Then, after AE waveform acquisition and storage, post-analysis of waveforms and spectrums was carried out. The schematic diagram of overall experimental setup is shown in figure 3.

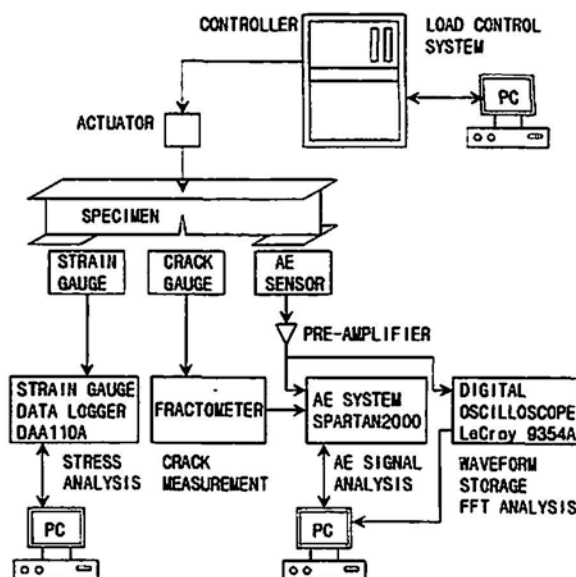


Figure 3 Schematic diagram of overall experimental setup

## RESULTS AND DISCUSSION

Figure 4 shows the crack growth length according to fatigue cycles for specimen No.3 and No.5 that is specimen of Type I and of Type II, respectively. The results of this test indicated that the crack propagation characteristics for fatigue cycles did not change significantly with different type of beam. Generally, crack growth rate showed three typical features that are smooth increase in initial stage, stable increase in second stage, and rapid increase according to increasing of number of cycles in last stage.

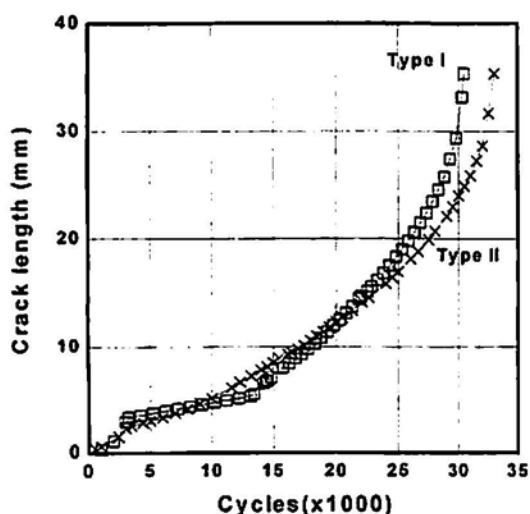


Figure 4 Crack length vs. fatigue cycle for specimen beam type

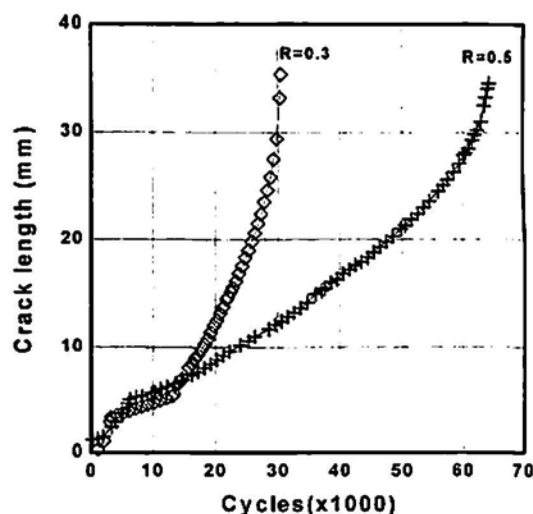


Figure 5 Crack length vs. fatigue cycle for loading ratio

Figure 5 shows the crack growth length according to fatigue cycles for specimen No.3 and No.2 which corresponds to  $R=0.2$  and  $R=0.5$  of load ratio, respectively. Through all of tests, load ratio of specimen affected significantly to the results such as the crack growth rate and the amount of generating AE signals. As shown in this figure, in case of  $R=0.3$  the number of fatigue cycles was about 2 times compared to in case of  $R=0.5$  up to crack propagation of 35mm. It also could be found that this load ratio was related to the change of stress intensity factor ( $\Delta K$ ).

Figure 6 shows the relationship between the crack growth rate ( $da/dn$ ) and the change in stress intensity factor ( $\Delta K$ ) for all five specimens. The straight curve obtained from theoretical calculation by Paris equation was well correlated to experimental results. In the early works of AE with fatigue test, most of studies dealt with relating acoustic emission to crack growth rate and to the stress intensity factor using several kinds of equations. In this study, Paris equation was used for theoretical calculation, namely  $da/dn = C(\Delta K)^m$  where  $\Delta K$  is the applied stress intensity factor and is given as  $\Delta K = \Delta\sigma\sqrt{\pi a_{av}}$  where  $\Delta\sigma$  is the magnitude of the alternating stress,  $\sigma_{max} - \sigma_{min}$ , and  $a_{av}$  is the average crack length.  $N$  is the number of cycles and  $C$  and  $m$  are constants for a given material.

Figure 7 shows the AE location events, the cumulative AE events and the crack growth length respectively according to the fatigue cycles for specimen No.1. In this experiment AE location events were not early detected although several AE hits from each sensor were generated in the early of the test. However the features of three parameters, that is, crack growth length, AE location events and cumulative AE events, showed almost same trend in their increase with the number of cycles.

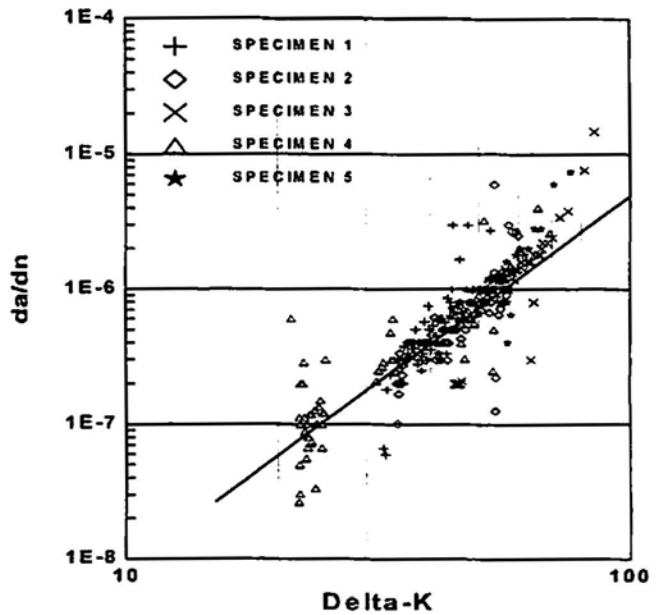


Figure 6 Crack growth rate vs. Delta-K for each specimen

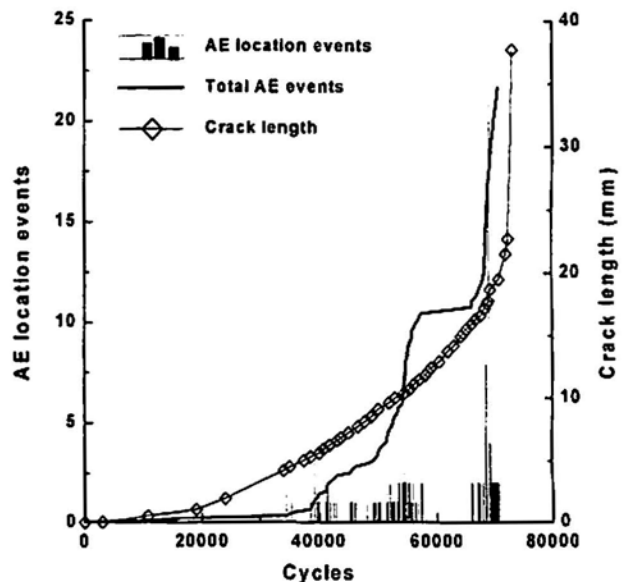


Figure 7 Crack length, AE location events and cumulative AE events vs. fatigue cycle

Figure 8 shows the result of source location during entire test of specimen No. 5. Each graph shows AE event locations in the cycle range of  $10-20 \times 10^3$ ,  $20-30 \times 10^3$ ,  $30-35 \times 10^3$ ,  $35-38 \times 10^3$ , respectively. As increasing of the number of cycles, a numerous AE events were located around the crack tip. Although there were somewhat scattered location in the vicinity of upper flange, which were considered as environmental noises, good locations near the actual crack tip were obtained. As shown in these figures, these environmental noises were considered as the noises at the upper contact point of three point contact in case of the early stage of test. On the other hand it was considered as the random locations by sources at the plastic region around crack tip in case of the last stage of test. Therefore post filtering work was carried out to eliminate these unwanted location events using several AE parameters. Figure 9 shows the typical results of post filtering works. AE parameters such as rise time, peak amplitude, event duration, etc. were used to filter out unwanted location. On the whole good results were obtained except noise signals having same features with actual crack signals unfortunately. Figure 9 shows the result of filtered output by rise time parameter, representatively. The AE event locations by noise signals were almost eliminated.

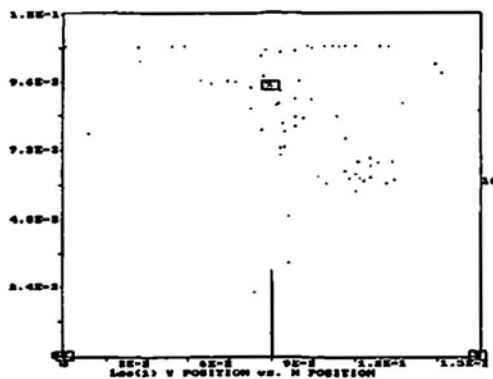


Figure 8 (a) The result of AE source location( $10-20 \times 10^3$  cycles)

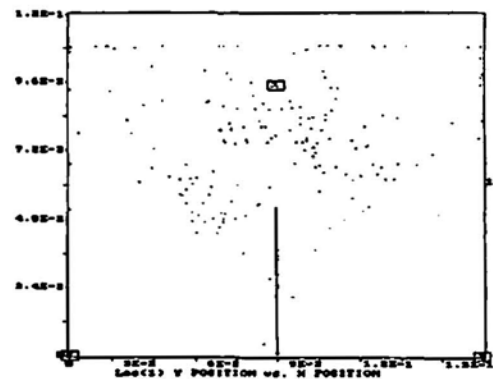


Figure 8 (b) The result of AE source location ( $20-30 \times 10^3$  cycles)

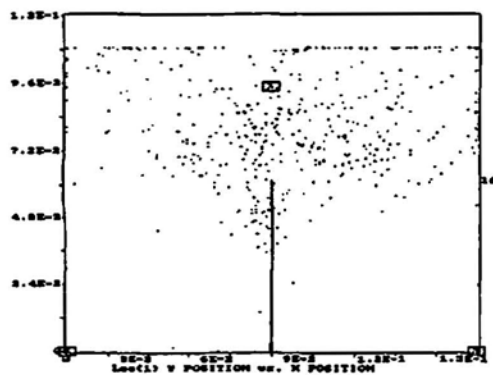


Figure 8 (c) The result of AE source location ( $30-35 \times 10^3$  cycles)

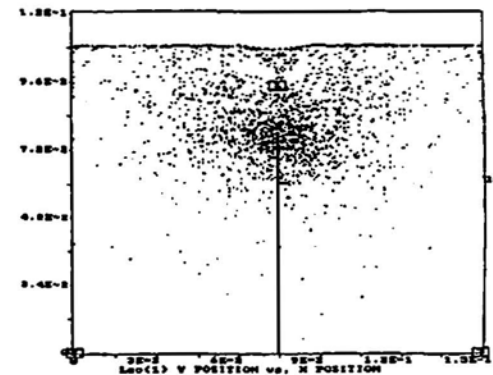


Figure 8 (d) The result of AE source location ( $35-38 \times 10^3$  cycles)

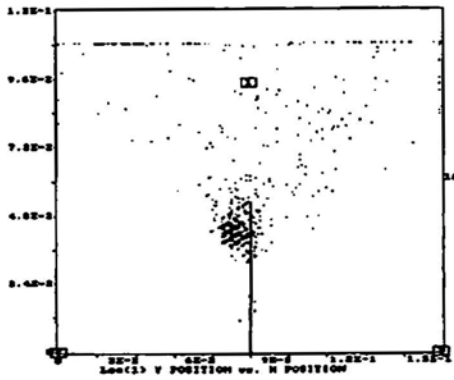


Figure 9 (a) The result of AE source location (before filtering)

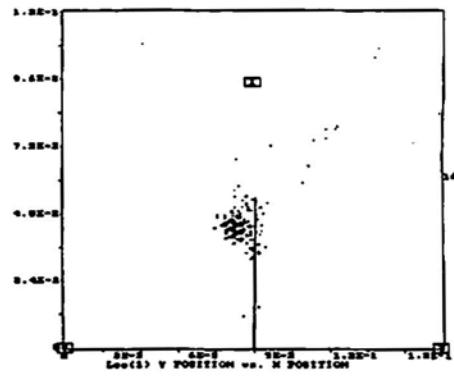


Figure 9 (b) The result of AE source location (after filtering)

In this study it was not reviewed for the relationship between fatigue crack activity and stress state in order to generate AE in actual structure. Practically it is very important to know and to plan for the applied load in the real structures during acoustic emission testing. Therefore further works relating to this will be necessary to apply this technique to real structures.

## CONCLUSIONS

Acoustic emission technique was employed for the monitoring of crack activity in steel bridge members. The crack propagation characteristics for fatigue cycles did not change significantly with different type of beam. Generally, crack growth rate showed three typical features that are smooth increase in initial stage, stable increase in second stage, and rapid increase in last stage according to increasing of number of cycles. Through all of tests, load ratio of specimen affected significantly to the results such as the crack growth rate and the amount of generating AE signals. From fracture mechanics point of view, the straight curve obtained from theoretical calculation by Paris equation was well correlated to the experimental results.

AE location events were not early detected although several AE hits from each sensor were generated in the early of the test. However the features of the crack growth length, AE location events and cumulative AE events, showed almost same trend in their increase with the number of cycles.

Although there were somewhat scattered location in the vicinity of upper flange, which were considered as environmental noises, good locations near the actual crack tip were obtained. Post filtering work was carried out to eliminate these unwanted location events, good results were obtained from filtering work using AE parameters.

## REFERENCES

1. M. Sison, J.C. Duke, G. Clemena, and M.G. Lozev, "Acoustic Emission: A Tool for the Bridge Engineer", *Materials Evaluation*, August pp.888-900, 1996
2. H.L. Dunegan, "Use of Plate Wave Analysis in Acoustic Emission Testing to Detect and Measure Crack Growth in Noisy Environment", *Proc. of Structural Materials Technology - An NDT Conference*, San Diego, pp.335-341, 1996
3. M.N. Bassim, "Detection of Fatigue Cracking in Metallic Structures with Acoustic Emission", *Proc. of 11th Int'l Acoustic Emission Symposium*, Fukuoka, Japan, pp.347-352, 1992
4. A. Ghorbanpoor and D.W. Vannoy, "Laboratory Acoustic Emission Investigation of Full Size ASTM A-588 Bridge Beams", *The 2nd Int'l Conference on Acoustic Emission*, pp.S307-S310, 1985
5. H.L. Chen and R.D. Fultineer, "Study of Fatigue Cracks in Steel Bridge Components Using Acoustic Emission", *Proc. of Structural Materials Technology - An NDT Conference*, San Diego, pp.317-322, 1996
6. A. Ghorbanpoor and T. rentmeester, "NDE of Steel Bridges by Acoustic Emission", *Natural Hazards Mitigation*, pp.1008-1013, 1988

## **ACOUSTO-ULTRASONIC EVALUATION OF ADHESIVELY BONDED CFRP-ALUMINUM JOINTS**

**Seung-Hwan Lee and Oh-Yang Kwon**

Department of Mechanical Engineering, Inha University,  
253 Yonghyun-dong, Incheon 402-751, Korea

### **ABSTRACT**

Correlation between the amount of artificial defects in bonded region and the acousto-ultrasonic parameters(AUPs) including signal amplitude and then the static strength of adhesively bonded joints of carbon fiber reinforced plastic(CFRP) laminates and Al6061 plates has been investigated. The effect of the frequency content and the bandwidth of input signals were studied using 200kHz, 650kHz, 1MHz, 2MHz pulses and 1MHz tone-burst signals. With increasing fraction of defects, the signal amplitude and AUP1 were decreased whereas AUP2 was increased. This result has been attributed to the energy transfer characteristics of bonded joints with delamination-type defects and the change of spectral content due to the defects. Considering the nature of high attenuation, a pulse signal with major frequency content at the third harmonic of thickness mode resonance, 650kHz for the dimension of specimens used in this study, has been found optimal for acousto-ultrasonic testing of CFRP-aluminum joints.

### **INTRODUCTION**

Composite materials which have excellent characteristics like high specific strength and modulus, and good fatigue resistance are used more and more as structural materials in space structures, aircrafts and ground vehicles. For such usages as in real mechanical structures, it is difficult to avoid having parts bonded with similar or dissimilar materials. In general, bonded areas have inferior mechanical properties than base materials to a great extent because of the existence of interfacial or transitional region show quite different gradients in chemical and

microstructural aspects. Therefore, bonded parts can be more critical than base structures to determine the overall integrity of mechanical structures.[1]

There are two possible methods for bonding of polymer matrix composites or fiber reinforced plastics(FRP); One is mechanical bonding using fasteners such as rivets, screws, and bolts, the other is the adhesive bonding using various adhesives. The latter method has been widely adopted since the adhesively bonded joints can extend fatigue life, reduce total weight of structures, and homogeneously transfer stresses. These characteristics play an important role in highly efficient structure such as aluminum-FRP or aluminum-aluminum bonding of aircraft structures.

Various nondestructive testing methods such as ultrasonics, acoustic emission(AE), radiographic testing have been used for the detection of defects at bonding areas. Especially detailed information about bonding interface can be easily acquired by analyzing signals which pass through defects, failures or damages of structures using acousto-ultrasonic(AU) method which inputs ultrasonic source signals and receives AE signals. [2]

## THEORETICAL BACKGROUND

### Definition of Acousto-Ultrasonic Parameters(AUPs)

AUPs has been defined from the power spectral moments,  $M_n$ , which are given as:

$$M_n = \int_b^N w(f) f^n df$$

where  $f_N$  is Nyquist frequency,  $W(f)$  is power spectral density function and  $n$  is integer. From real digital domain,  $M_n$  can be calculated as follows:

$$M_n = \sum_{i=0}^{N/2} \frac{(w_{i+1} + w_i)}{2} (i\Delta f + \frac{\Delta f}{2})^n \Delta f$$

From the above equation,  $\Delta f$  is frequency resolution, which is defined as  $\Delta f = (1/j\Delta t)$ , where  $\Delta t$  is sampling interval. For example, the zeroth moment( $M_0$ ) is defined as follows:

$$M_0 = \int_b^N w(f) df \text{ or, } M_0 = \sum_{i=0}^{N/2} \frac{(w_i + w_{i+1})}{2} \Delta f \quad (\text{in digital domain})$$

The zeroth moment or  $M_0$  means the signal energy calculated as the area under spectral density curve, which is analytically related to the mean square of voltage signals.[3, 4] The first moment( $M_1$ ) means total spectral density for each frequencies, whereas the second moment( $M_2$ ) shows the dispersion of profile slope distribution of spectral density function. The third and the fourth moments are related to skewness and kurtosis, respectively. Therefore, the odd numbered moments are related to the symmetry, and even numbered ones are to the

profile curvature of spectral density function. For applying the above theories to AU experiments, AUP1 can be defined as  $M_0$ , which means the total energy of received signals. AUP2 has been defined as  $M_1/M_0$ , which means the arithmetic mean value of spectral density for each frequencies. AUP3 is defined as  $(M_1/M_0)^5$ , which means the dispersion factor of spectral density function, whereas AUP4 as  $(M_4/M_2)^5$ , the factor that shows the profile curvature of spectral density function. The quantities of AUP3 and AUP4 are also known as the distortion factors and are theoretically the indication of the amount of high frequency content in a predominantly lower frequency content.[4-6]

## EXPERIMENTS

### Specimens

Specimens used in this study were made by joining 16-ply uni-directional CFRP laminates and 3mm-thick Al6061 plates using adhesives(9923A/B, IPCO National Ltd.). The mating surface of aluminum plates was polished with sandpapers whereas that of CFRP was just cleaned using acetone. Specimens were designed in both configuration of the single lap (SL) and the double lap (DL) joints. The bonded area was kept 1" × 1" for all specimens with predetermined fraction of artificial defects introduced as shown in Fig. 1.

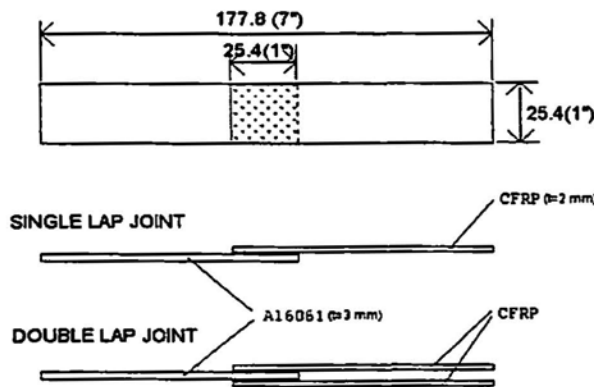


Fig. 1 Dimension and shape of specimen

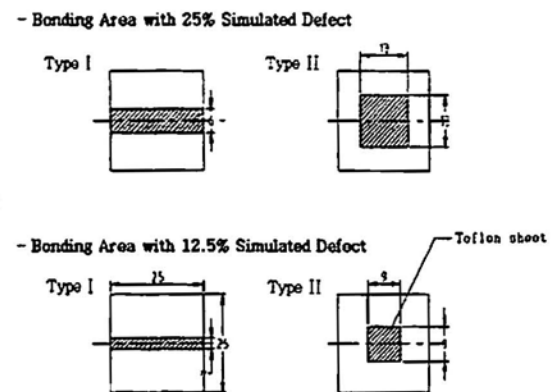


Fig. 2 Shape of bonding area with artificial defects

To introduce artificial defects, specimens have been designed by adjusting the size, location and shape of teflon sheets as shown Fig. 2. For single lap joints, the fractions of defects per total bonding area were 12.5% and 25%, whereas they were 6.25% and 12.5% for double lap joints. Specimens with double lap joints had two bonding surfaces; one was made

in the same way as the single lap joints, the other was made as a perfectly bonded surface. Therefore, the fraction of defects at double lap joints is a half of that at single lap joints. As the reference of experimental measurements, four specimens with perfectly bonded joints were included.

Table 1 Number of specimens for each type of bonding area

Type of joint	Fraction of artificial defects(%)	Bonding area with artificial defect		No. of Specimens
		bonding surface #1	Bonding surface #2	
Single lap (SL)	0	perfectly bonded	-	4
	12.5	type I	-	4
		type II	-	4
	25	type I	-	4
		type II	-	4
	Double lap (DL)	0	perfectly bonded	Perfectly bonded
6.25		perfectly bonded	type I of SL(12.5%)	4
		perfectly bonded	type II of SL(12.5%)	4
12.5		perfectly bonded	type I of SL(25%)	4
		perfectly bonded	type II of SL(25%)	4

### Instrumentation and Data Acquisition

As the specimens with bonded joints were prepared, they were inspected by ultrasonic C-scan method to confirm that specimens were made with correct size and location of artificial defects. A table-top C-scan system (UltraPac II; PAC) were used for this purpose. Only the specimens whose size and location of defects were confirmed have been used. A schematic diagram of experimental set-up is shown in Fig. 3. Source signals were made from an arbitrary waveform generator (CompuGen 840; Gage) and filtered by a tunable band-pass filter (KH3103A; Krohn-Hite Corp.). The signals were then amplified by 50dB using a broadband RF amplifier (240L; ENI) to survive in CFRP which generally exhibits high attenuation. Both tone-burst signals and pulses at 1MHz were employed at first, then pulses of 200kHz, 650kHz and 2MHz were also employed to investigate the effect of the frequency content and the bandwidth of input signals. To put input signals into specimens, a 0.5MHz ultrasonic transducer (K0.5S; Krautkrämer) for 200kHz and 650kHz pulses, an 1MHz transducer(B1S; Krautkrämer) for 1MHz pulses and tone-burst signals and a 2.25MHz transducer(KB-A) for

2MHz pulses were used. Signals propagated through the specimens to be detected by a broadband type AE sensor (WD; PAC). Detected signals were amplified by 40dB at pre-amplifier with bandpass filter(100kHz-1200kHz) or highpass filter(100kHz high), and then fed into AE DSP unit (MISTRAS 2001; PAC), where they were processed to calculate AUPs.

The bonding strength were obtained from tensile testing of the same specimens that used for the AU measurement. The correlation between the bonding strength and four AUPs and the fraction of defects has been evaluated using regression analysis.

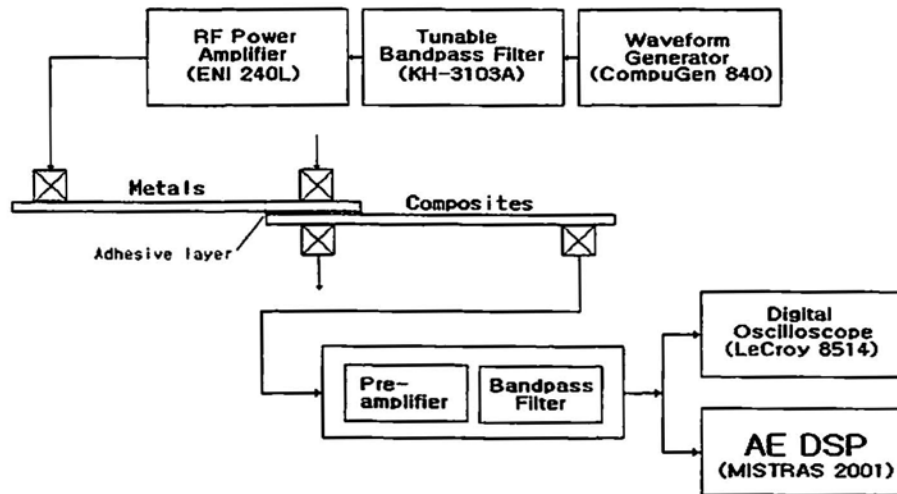


Fig. 3 Schematic diagram of experimental set-up

## RESULTS AND DISCUSSION

The results shown in Fig. 4 were obtained from the AU measurement for type I specimens of both SL- and DL-joints using an 1MHz pulse as the input signal. Amplitude and AUP1 decreased with increasing fraction of defects, whereas AUP2 increased. The decrease of amplitude and AUP1( $M_0$ ) are due to the increased attenuation as the fraction of defects increased. Similar results were obtained from the measurement for type II specimens of both SL- and DL-joints. Therefore, this tendency appeared to depend primarily on the amount of defects. When a tone-burst signal at 1MHz was employed as the input, the results were also very similar but less significant than that shown in Fig. 4. Pulse signals, which has broader bandwidth than tone-burst signals, appeared to be more efficient for AU evaluation of lap joints.

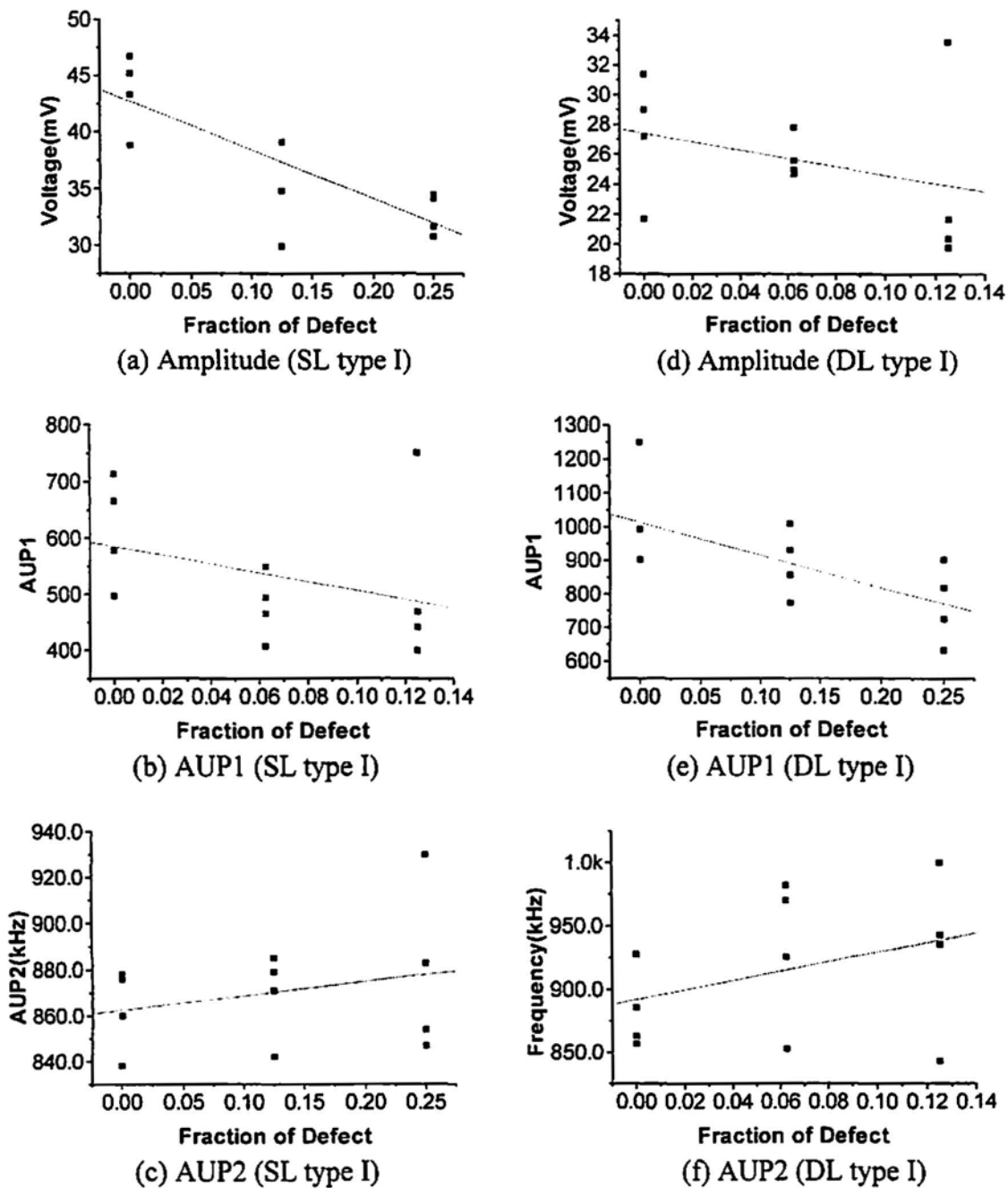


Fig. 4 Results of AU measurements for type I specimens of both single-lap and double-lapjoints using an 1MHz pulse input

In Fig. 5, the input and the detected AU signals employed to get the above results are shown with the respective power spectrum for each signal. The input was a typical pulse signal which had relatively wide band characteristics in the vicinity of 1MHz as shown in Fig. 5(b).

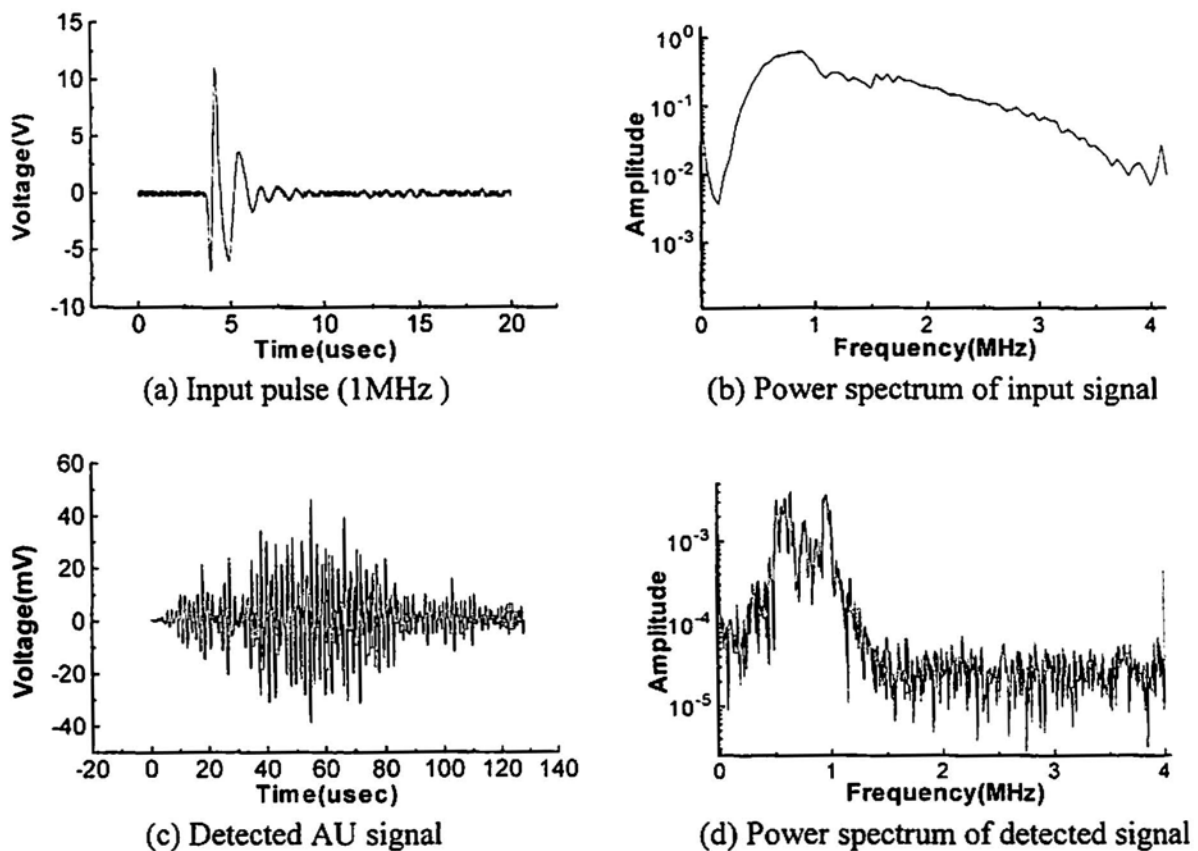


Fig. 5 Waveforms and power spectra of the input and the detected signals

On the other hand, the power spectrum of detected signal has main peak at about 650kHz and about 1MHz as shown in Fig. 5(d). Because of this result, a pulse signal whose major frequency content at about 650kHz was intensively employed in addition to the originally scheduled frequencies such as 200kHz, 1MHz and 2MHz.

Fig. 6 shows the result obtained from the AU measurement for type II specimens of DL-joints using a 650kHz pulse as the input signal. With increasing fraction of defects, amplitude and AUP1 decreased whereas AUP2 and AUP4 increased. This tendency is similar to but is also more significant than that observed in Fig. 4.

In order to understand the tendency in terms of the spectral density distribution, frequency spectra of AU detected signals from specimens with three different fraction of defects were obtained as shown in Fig. 7. It appeared that with increasing fraction of defects, the magnitude of relatively low frequency band at about 300-400kHz decreased rapidly, whereas the magnitude at about 500-600kHz was virtually unchanged. The relative change of magnitude between at lower frequency band(300-400kHz) and at higher frequency band(500-600kHz) accounts for the increase of AUP2 with increasing fraction of defects.

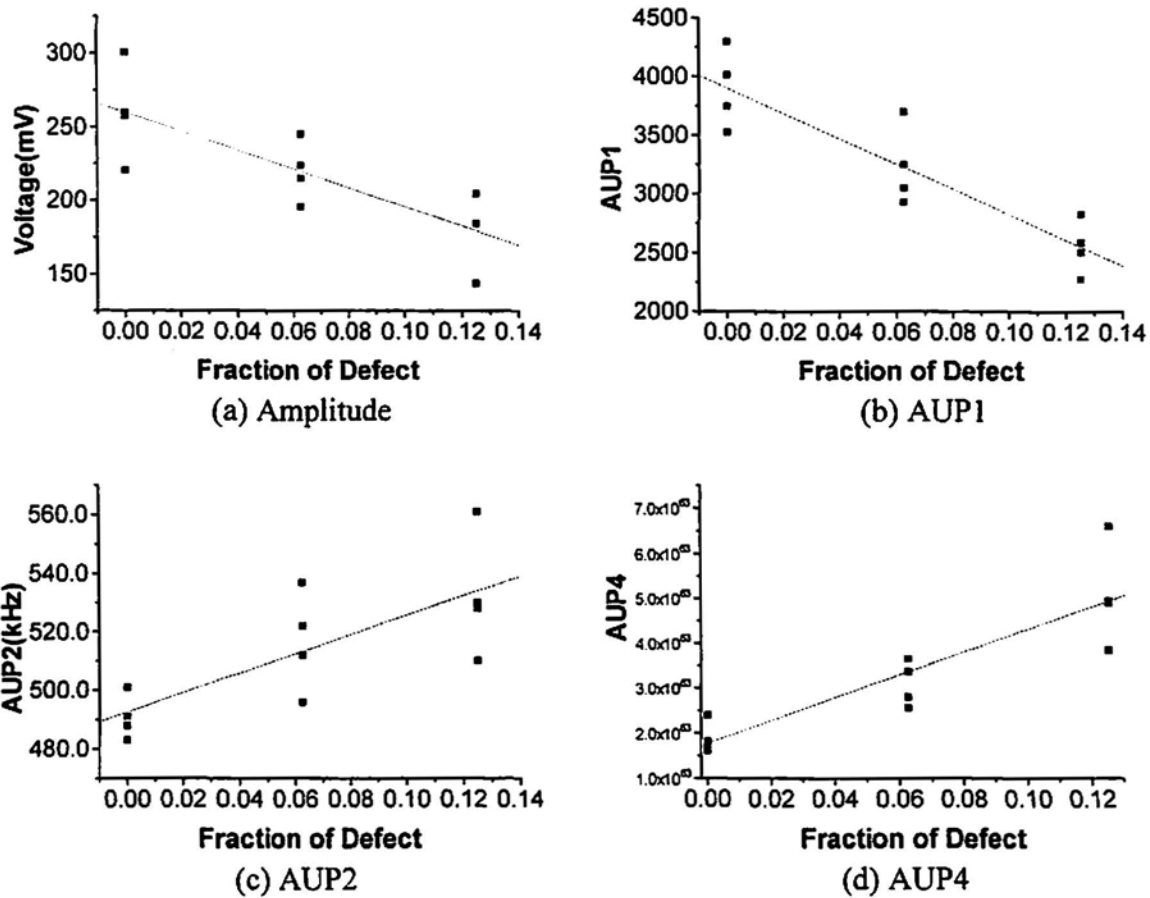
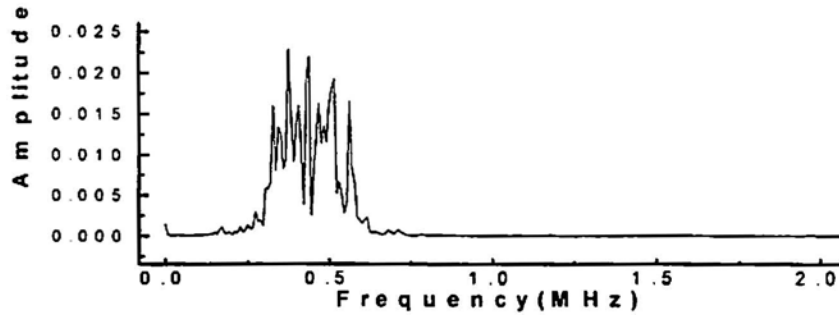


Fig. 6 Results of AU measurement for type II specimens of double-lap joints using a 650kHz pulse input

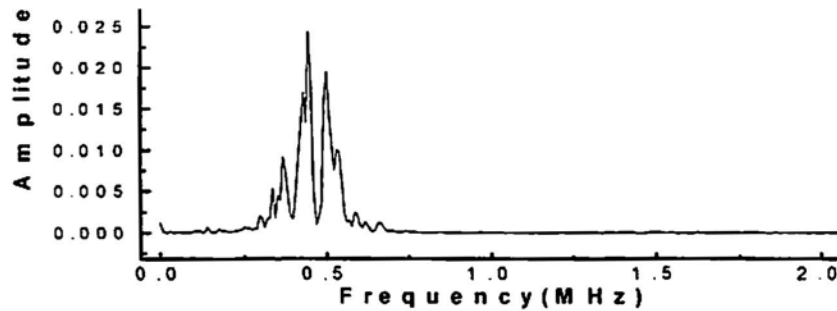
The increase of AUP4, which is related to the kurtosis, can also be expressed by comparing three spectra of Fig. 7. As compared with perfectly bonded specimens which showed relatively distributed frequency spectrum, specimens with higher fraction of defects showed spectra more or less concentrated at narrow band. This can be appeared as the increase of AUP4 since it is based on the kurtosis of spectra. The physical basis for the above phenomena can be explained in terms of the thickness mode resonant frequencies of lap joints with and without having defects at bonding area. The resonant frequency,  $f_r$  can be calculated by using the equation given as [7]

$$f_r = \frac{n v}{2 D} \quad (n=1, 2, 3, \dots) \quad (1)$$

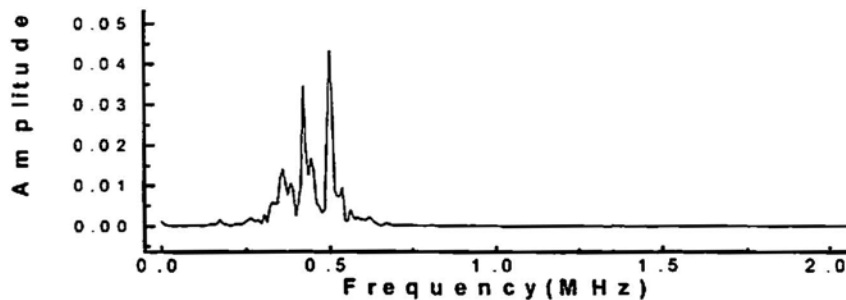
where  $n$  is the order of resonance,  $v$  is sound wave velocity in the material and  $D$  is the thickness of plates. For the specimens with joints consisted of a metal(Al6061) and a composite(CFRP), however, it is impossible to calculated the exact frequencies using eq. (1)



(a) Spectrum of AU detected signals from specimens without defects



(b) Spectrum of AU detected signals from specimens with 6.25% defects



(c) Spectrum of AU detected signals from specimens with 12.5% defects

Fig. 7 Power spectra of AU detected signals from the measurements for type I specimens of double-lap joints using a 650kHz pulse input

since the sound velocity,  $v$  is different in different materials. Therefore, the resonant frequency of specimens used in this study was assumed as a value between that of Al-Al joints and that of CFRP-CFRP joints at equivalent thickness. Table 2 shows natural frequencies of Al6061 and CFRP calculated for 5mm-thick plates.

Frequencies of 200kHz and 650kHz employed in the experiment were assumed as the apparent fundamental and the third-order resonant frequencies, respectively. It was found that the tendency of AU parameters with the fraction of defects could be measured the most efficiently using 650kHz as shown in Fig. 6.

Table 2. Calculated natural frequencies and their harmonics at 5mm-thickness (kHz)

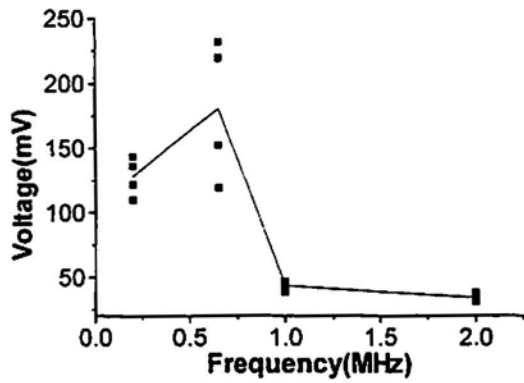
Materials	$f_1^*$	$f_2$	$f_3$	$f_4$	$f_5$
Aluminum	313	616	939	1,252	1,565
Composites	220	440	660	880	1,100

Since the specimens were designed with the artificial, delamination-type defects at the bonding area, the effective thickness of joints actually decreased with increasing fraction defects. This resulted in the decrease in thickness,  $D$  in eq. (1) and eventually resulted in the increase of resonant frequencies. This accounts for the shift of major peaks in power spectra toward higher frequency band and further for the increase of AUP2 with increasing fraction of defects.

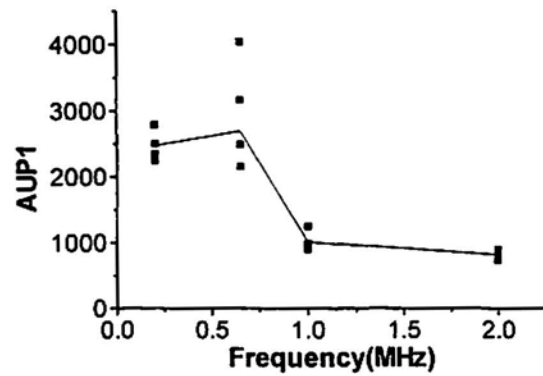
The effect of frequency content of input signals on the AU parameters has been summarized as shown in Fig. 8 for specimens with single-lap joints. Regardless of the fraction of defects, with the increasing frequency of input signals from 200kHz to 650kHz, both amplitude and AUP1 increased to the highest value and then significantly decreased to lower value with further increase in input frequency up to 1MHz and 2MHz. The amplitude of AU detected signals from the measurements using 1MHz pulse as the input signals were already close to the minimum detectable value in this configuration. Although the bandwidth of digital AE signal processing unit was limited by 100kHz to 1.2MHz, the input pulse with frequency contents higher than 1Mz appeared to be not very useful for the purpose.

## CONCLUSIONS

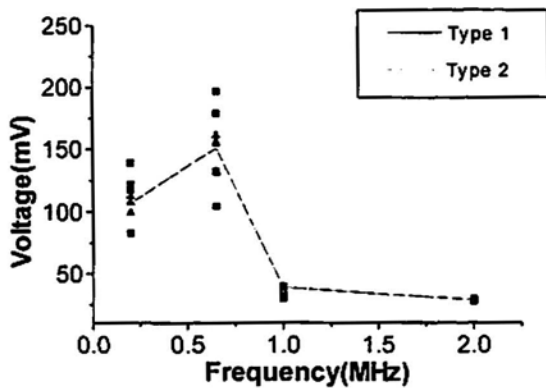
1. The wider band pulse signals appeared to be more efficient than the narrower band tone-burst signals for AU evaluation of metal-composites lap joints.
2. The signal energy transfer characteristics was highly affected by the frequency content of input signals so that the fundamental and the third-order resonant frequencies could be the optimal input frequencies.
3. The apparent correlation between the amount of defects in bonded region and the acousto-ultrasonic parameters(AUPs) is due to the change of frequency contents of AU detected signals, which can be attributed to the reduction of the affective thickness of joints with increasing fraction of delamination-type defects.



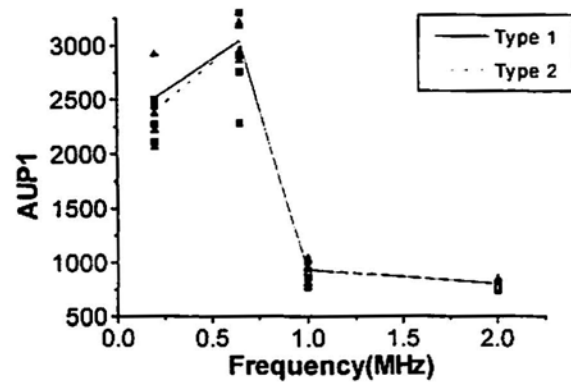
(a) Amplitude change (0% defects)



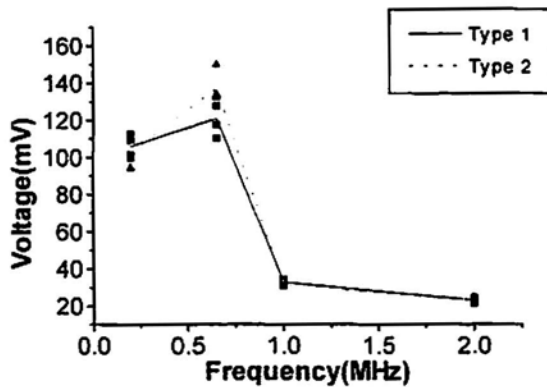
(d) AUP1 change (0% defects)



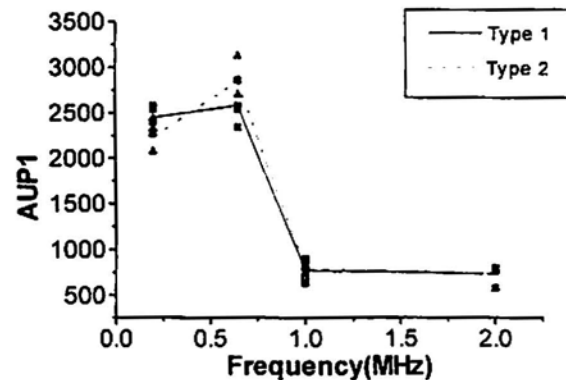
(b) Amplitude change (12.5% defects)



(e) AUP1 change (12.5% defects)



(c) Amplitude change (25% defects)



(f) AUP1 change (25% defects)

Fig. 8 The effect of frequency content of input signals on AU parameters from the measurements for specimens with single-lap joints

## ACKNOWLEDGEMENT

This study was supported by the Ministry of Education, Government of Korea.

## REFERENCES

1. G. B. Chapman, Jr., "A Nondestructive Method of Evaluating Adhesive Bond Strength in Fiberglass Reinforced Plastic Assemblies", *Joining of Composite Materials*, ASTM STP 749, K. T. Kedward, Ed., American Society for Testing and Materials, pp.32-60, 1981
2. A. Vary and K. J. Bowles, "An Ultrasonic-Acoustic Techniques for Nondestructive Evaluation of Fiber Composite Quality", *Polymer Engrg. Science*, 19(5), pp.373-376, 1979
3. A. Tiwari and E. G. Henecke, Jr., "Real Time AU-NDE Technique to Monitor Damage in SiC/CAS Ceramic Composites under Dynamic Loads", ASTM STP 1184, M.R. Mitchell and O. Buck, Eds., ASTM, Philadelphia, PA, pp. 363-375, 1994
4. P.A. Dickstein et al., "Ultrasonic Feature-Based Classification of the Interfacial Condition in Composite Adhesive Joints", *Res. Nondestr. Eval.* 2, pp.207-224, 1990
5. Michael T. Kiernan and John C. Duke, Jr., "A Physical Model for the Acousto-Ultrasonic Method", NASA CR185294, October 1990
6. Grant E. Hearn and Andrew v Metcalfe, "Spectral Analysis in Engineering: Concepts and Cases", ARNOLD, 1995
7. Y. H. Son, J. O. Lee and S. H. Lee, "Nondestructive Evaluation of Adhesive Bonding Quality by Measurements of Peak Amplitude of Simulated Stress Wave", *Journal of the Korean Society for Nondestructive*

## **ESTIMATION OF INITIAL DAMAGE IN CONCRETE BY ACOUSTIC EMISSION**

**Masayasu Ohtsu<sup>1</sup>, Yuichi Tomoda<sup>1</sup> and Taisaku Fujioka<sup>2</sup>**

<sup>1</sup> Department of Civil Engineering and Architecture, Kumamoto University,  
2-39-1 Kurokami, Kumamoto 860, Japan

<sup>2</sup> Fukuoka City Office, 2-5-31 Daimyo, Chuou-ku,  
Fukuoka 810, Japan

### **ABSTRACT**

An application of acoustic emission (AE) observation to the uniaxial compression test of concrete-core samples has been proposed and under improvement. Damage of concrete is quantitatively estimated by the rate process analysis of AE generating behaviors under compression. Because the rate of AE activity is dependent on mixture proportion and the condition of core samples, the damage is estimated relatively from the rate in comparison with that of sound concrete.

In the present paper, the damage mechanics is introduced to estimate the damage of concrete quantitatively. Concrete samples of controlled damage are prepared by freezing and thawing tests. The initial damages are determined on the basis of Loland's model. It is attempted to determine the initial damage from AE generating behaviors, correlating with the rate process analysis. Results show a promise to estimate the initial damage of concrete samples without information on the sound sample.

### **INTRODUCTION**

The damage caused by microcracking is one essential feature of concrete, and is critically related with the ultimate load-bearing capacity of concrete structures in service. The increase of aging structures and the disastrous damage due to recent earthquakes lay stress on the need for repairing and retrofitting procedures for damaged structures. For this purpose, a detailed inspection of existing concrete structures is required in advance. Core samples are often bored out to measure their uniaxial compressive strengths and Young's moduli. Thus, the damage

degree of concrete is estimated from only mechanical properties comparable with the specification, because concrete properties of the same mixture proportion and of the sound concrete are not concurrently available.

For the assessment of damaged concrete, recently the measurement of acoustic emission (AE) activity in uniaxial compression tests of core samples is proposed [1]. This is because AE generating behavior is closely associated with the presence of microcracks in concrete. To analyze quantitatively the occurrence of AE events, the rate process theory is introduced [2].

In the present paper, a practical procedure for the assessment of damaged concrete is studied. The damage evolution process under uniaxial compression is modelled by the damage mechanics [3]. It is attempted to estimate the initial damage from AE generating behaviors without information on the sound concrete.

### CONCRETE SAMPLES OF CONTROLLED DAMAGE

To prepare concrete samples of controlled damage, cylindrical specimens of dimension 10 cm diameter and 20 cm height were cast. Mixture proportion of concrete is given in Table 1. At 28 days after moisture-curing, concrete samples were subjected to freezing and thawing cycles from  $-16^{\circ}\text{C}$  to  $+6^{\circ}\text{C}$  for three hours. Damaged samples due to 100 freezing-thawing cycles, 150 cycles, 200 cycles and 250 cycles were prepared and then loaded uniaxially at 0.65 kN/sec. Results of uniaxial compression tests are summarized in Table 2. Mechanical properties were determined from the averaged values of three samples.

Table 1 Mixture Proportion

Maximum Aggregate Size (mm)	W/C (%)	s/a (%)	Unit weight ( $\text{kg/m}^3$ )				Air En-trained Agent (cc)	Slump (cm)	Air contents (%)
			W	C	S	G			
20	55	47	179	326	816	1040	196	10.2	7.0

Table 2 Mechanical properties

Number of cycles	Compressive strength (MPa)	Young's modulus (GPa)	Poisson's ratio
0 cycle	46.5	35.2	0.25
100 cycles	45.5	29.5	0.22
150 cycles	44.4	30.8	0.22
200 cycles	40.0	29.2	0.22
250 cycles	44.7	30.0	0.21

In the uniaxial compression test, strain measurement was conducted by using four strain gauges in the axial and the lateral directions. For AE measurement, mainly one AE sensor of 150 kHz resonance frequency was attached at the center of the cylindrical sample. AE events generated under compression was counted up to final failure by AE processor. For event-counting, the threshold level was set to 120 mV with 60 dB gain, and the duration of the deadtime was 2 msec. To decrease noise from contact surfaces between the sample and loading plates, teflon sheets of 0.5 mm thickness were inserted with silicon grease. Total gain of AE measurement was set 60 dB and the frequency range employed was 10 kHz - 300 kHz.

In the course of freezing and thawing cycles, dynamic Young's moduli of concrete were also measured in accordance with the JIS-A-1127 code. Variations of all mechanical properties measured are shown as relative values in Fig. 1. Dynamic moduli decrease only 8 % after 250 freezing-thawing cycles, while static Young's moduli decrease around 15 %. Because concrete contained 7 % air contents of total volume as seen in Table 1, it is realized that fairly minor damages were induced into these concrete samples. As a result, the strengths of these samples are comparable to that of sound concrete (at 0 cycle).

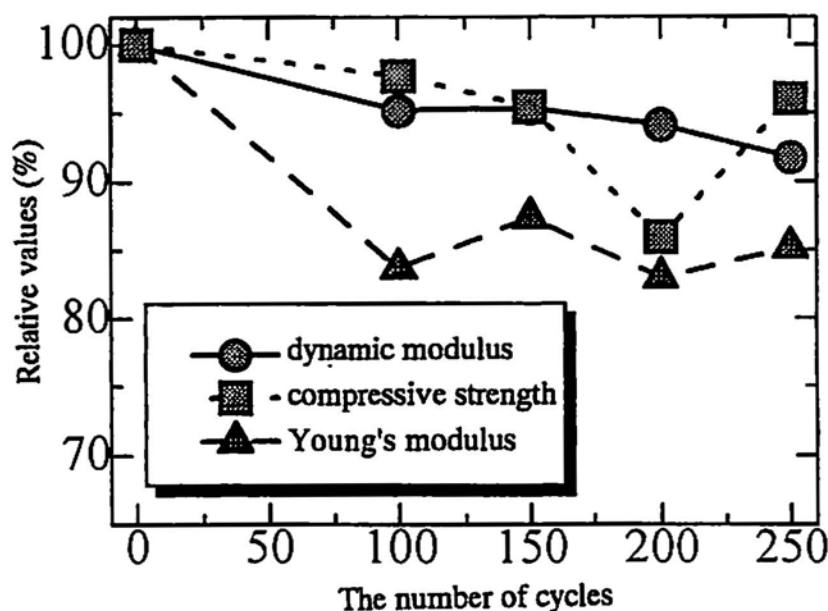


Fig. 1 Variation of mechanical properties

To quantify the damage degree induced in the samples, pore distributions were determined. From the samples, small cylindrical elements of 1 cm diameter were drilled at 3 cm depth from the surface. Then, the porosity was measured. Results are summarized in Fig. 2. It is observed that the ratio of pores over 0.05  $\mu\text{m}$  diameter increases after 100 freezing-thawing cycles, although the pores over 0.1  $\mu\text{m}$  diameter do not consistently increase with the increase of freezing-thawing cycles. This might be a reason why the strengths were comparable regardless of the freezing-thawing cycles. The minor damages of the samples were confirmed.

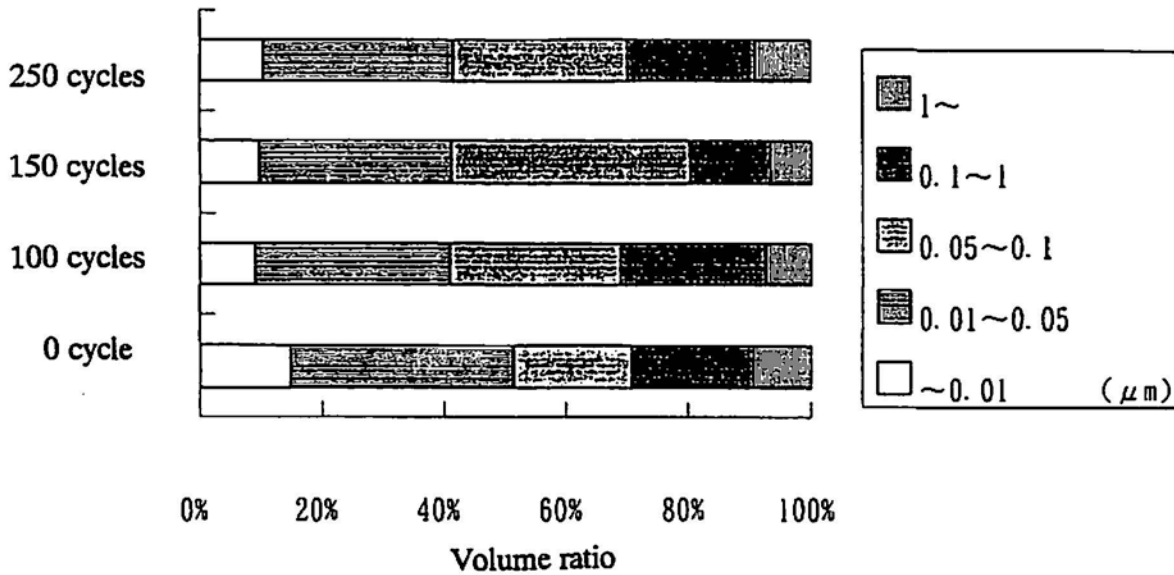


Fig. 2 Pore distribution

### RATE PROCESS ANALYSIS

When concrete contains a number of critical microcracks, active AE generation is expected in the uniaxial compression test due to crack propagation from existing defects. In contrast, AE activity in sound concrete under compression is considered to be stable and low prior to final failure. Thus, the presence of critical microcracks in concrete is closely associated with AE generating behavior under compression [4]. To formulate the AE occurrence under uniaxial compressive stress, the rate process theory is introduced [2]. The probability function  $f(V)$  of AE occurrence from stress level  $V(\%)$  to  $V+dV(\%)$  is correlated with the incremental number of AE events,  $dN$ , as follows;

$$f(V) dV = dN/N, \quad (1)$$

where  $N$  is the total number of AE events up to stress level  $V(\%)$ , which is normalized by the compressive strength:  $\sigma_c$ . To approximate high AE activity at low stress level, the function  $f(V)$  is assumed in the following hyperbolic function,

$$f(V) = a/V + b, \quad (2)$$

where  $a$  and  $b$  are empirical constants. Substituting eq. 2 into eq. 1, a relationship between the number of total AE events  $N$  and stress level  $V(\%)$  is readily obtained,

$$N = C V^a \exp (bV). \quad (3)$$

Here, C is the integration constant.

### DAMAGE EVOLUTION UNDER COMPRESSION

According to the damage mechanics [3], the state of damage is represented by introducing the scalar damage parameter  $\Omega$ . As Young's modulus of an intact material is  $E^*$ , Young's modulus  $E$  of a damaged material is expressed as  $E^*(1 - \Omega)$ . After the damage evolution by Loland [5], the damage parameter  $\Omega$  is assumed as a function strain  $\epsilon$  as,

$$\Omega = \Omega_0 + A_0 \epsilon^\lambda, \quad (4)$$

where  $\Omega_0$  is the initial damage.  $A_0$  and  $\lambda$  are empirical constants. In the uniaxial compression test, a stress-strain relation is represented as  $\sigma = E\epsilon$  and  $E = E^*(1 - \Omega)$ . Combining with eq. 4,

$$\sigma = E_0 \epsilon - E^* A_0 \epsilon^{\lambda+1}, \quad (5)$$

where  $E_0$  is Young's modulus of an initially damaged material. Assuming that  $d\sigma/d\epsilon = 0$  at the peak stress  $\sigma_c$  and the corresponding strain  $\epsilon_c$ ,

$$E_0 = E^* A_0 (\lambda + 1) \epsilon_c^\lambda \text{ and } 1 - \Omega_0 = A_0 (\lambda + 1) \epsilon_c^\lambda. \quad (6)$$

Thus, coefficient  $\lambda$  can be determined as,

$$\lambda = (\sigma_c / \epsilon_c) / (E_0 - \sigma_c / \epsilon_c). \quad (7)$$

In Table 2, Young's moduli  $E_0$  at particular freezing-thawing cycles are given. Thus, the corresponding coefficients  $\lambda$  are readily determined from eq. 7. From stress-strain relations obtained in the tests, coefficients  $\lambda$  were obtained. As referring to  $E^*$  as Young's modulus at 0 cycle, the initial damage levels  $\Omega_0$  were also determined and then empirical constants  $A_0$  were obtained from eq. 6. From these data, stress-strain relations were modelled. One result at 100 freezing-thawing cycles is given in Fig. 3 (a). The uniaxial stress-strain relation in the experiment is remarkably modelled by eq. 5. In this case, the damage evolution process in eq. 4 is estimated as shown in Fig. 3 (b). It is found that even at the peak strain  $\epsilon_c$ , the maximum damage  $\Omega_c$  induced is not greater than 0.5.

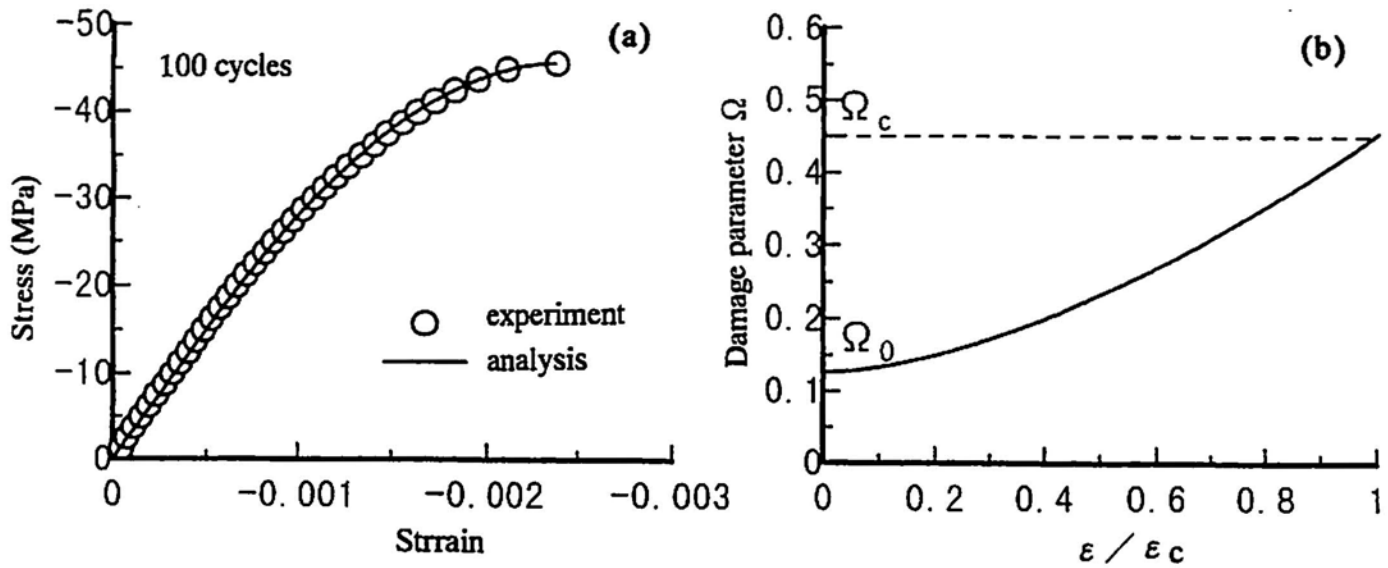


Fig. 3 (a) Stress-strain relation and (b) damage evolution process

### DAMAGE ESTIMATION BY AE

All tests were performed for three samples of the same freezing-thawing cycles. The strength, Young's modulus, the initial damage  $\Omega_0$ , and coefficient  $\lambda$  were determined as the averaged value of three. Thus, the stress-strain relations at particular freezing-thawing cycles were modelled.

Setting the total number of AE observed in a test as  $N_c$  and  $V = \sigma / \sigma_c$ , eq. 3 is rewritten,

$$N / N_c = (\sigma / \sigma_c)^a \exp[b(\sigma / \sigma_c - 1)]. \quad (8)$$

Coefficients  $a$  and  $b$  were also determined as the averaged values of three samples at the same freezing-thawing cycles. At a given strain level  $\varepsilon / \varepsilon_c$ , stress level  $\sigma / \sigma_c$  was calculated from eq. 5. Then, AE activity  $N / N_c$  was obtained from eq. 8. These results are plotted in Fig. 4 in the logarithmic scale. It is found that relations between AE activity and strain are so linear as being formulated by,

$$N / N_c = (\varepsilon / \varepsilon_c)^m. \quad (9)$$

Introducing the least square method, coefficient  $m$  is determined. Then combining with eq. 4,

$$(\Omega - \Omega_0) / (\Omega_c - \Omega_0) = (N / N_c)^{1/m}. \quad (10)$$

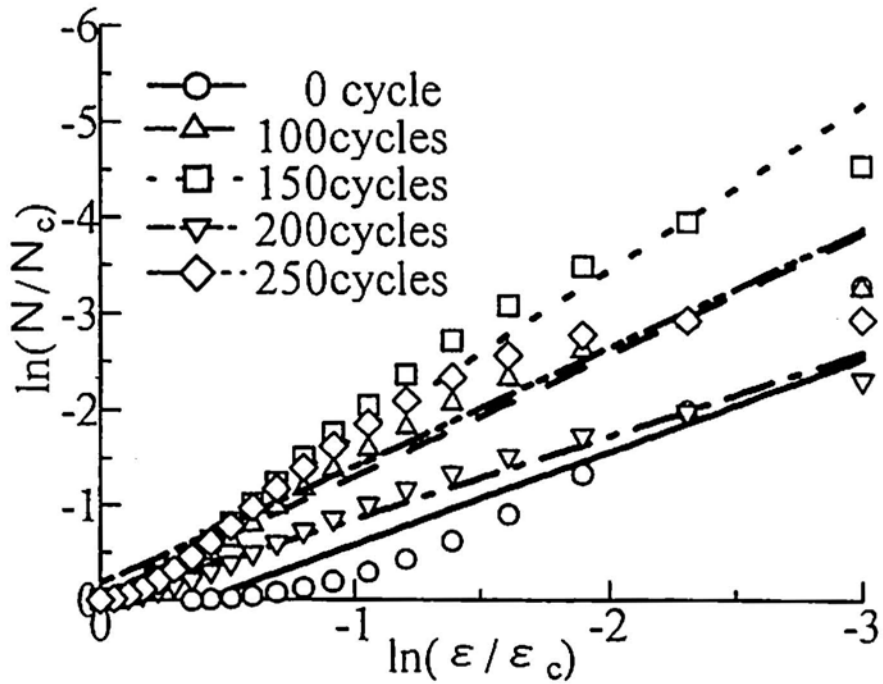


Fig. 4 Relations between AE counts and strains

As setting  $(\Omega - \Omega_0)/N^{\lambda/m} = (\Omega_c - \Omega_0)/N_c^{\lambda/m} = k$ , eventually eq. 6 leads to,

$$\Omega_0 = 1 - (\lambda + 1) k N_c^{\lambda/m}. \tag{11}$$

In order to determine the coefficient k, an empirical relation between the value,  $\Omega_c - \Omega_0$ , and the

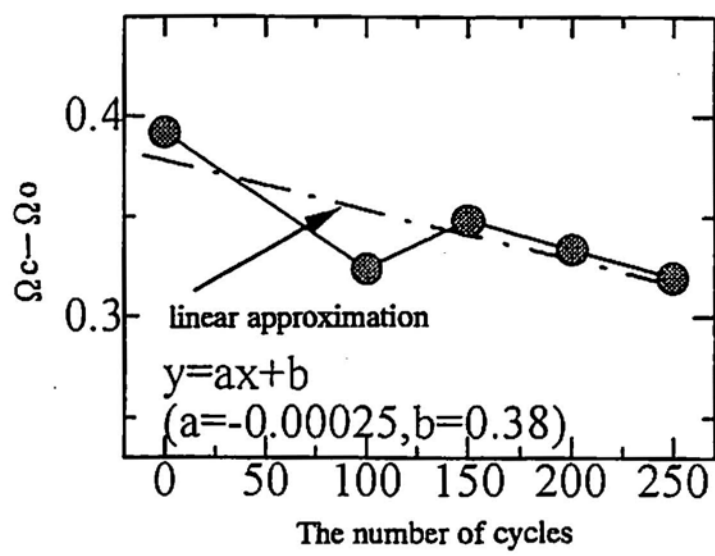


Fig. 5 Damage evolution under freezing and thawing

freezing-thawing cycles is necessary. Here, the two cases were considered. In case 1, the value was directly determined from the test results. In another case 2, the relation was approximated as shown in Fig. 5, where a linear relation is assumed.

The initial damages  $\Omega_0$  analyzed by eq. 11 were compared with the values  $\Omega_0$  actually determined from  $1 - E_0/E^*$ . Results are given in Fig. 6. It is found that the initial damages are reasonably estimated from eq. 11 in the both cases. The value,  $\Omega_c - \Omega_0$ , however, are determined empirically from the test results of damaged concrete. It implies that the procedure is still to be improved.

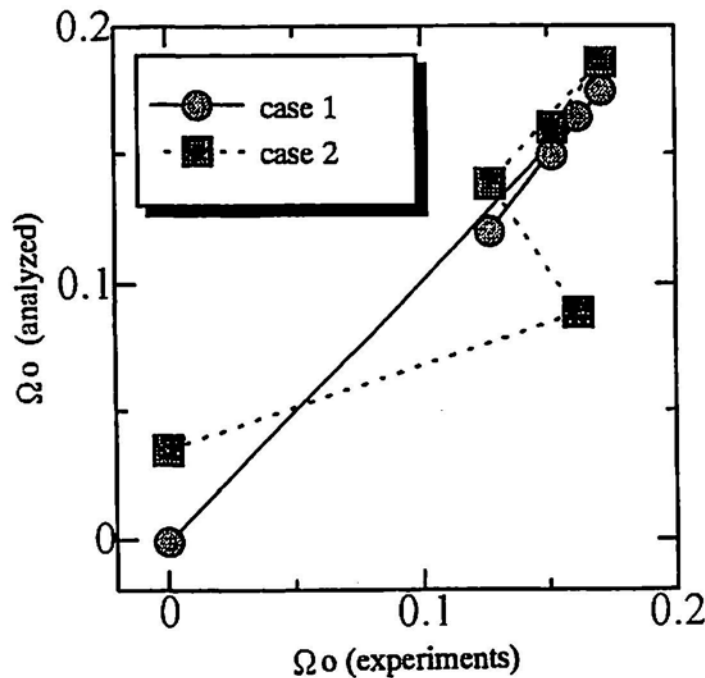


Fig. 6 Initial damage estimated

## CONCLUSION

A procedure for the evaluation of damaged concrete is studied. Stress-strain relations of concrete under compression were modelled by introducing the damage mechanics. It is attempted that the damage parameters are determined from the AE rate process analysis. Concrete samples of controlled damage are prepared by freezing and thawing tests of concrete. The following conclusions are obtained.

- (1) The initial damages are determined on the basis of Loland's model in the damage mechanics. Experimentally, the damage is estimated from the initial Young's modulus of the damaged concrete.
- (2) AE generating behaviors are analyzed by the rate process theory. It is attempted to

determine the initial damage without information on the sound concrete. Results show that the initial damages of concrete samples are reasonably estimated.

In these analyses, the value,  $\Omega_c - \Omega_0$ , are determined empirically from the test results of damaged concrete. It implies that the procedure is still to be improved.

## REFERENCES

1. M. Ohtsu, "Acoustic Emission Characteristics in Concrete and Diagnostic Applications," J. AE, Vol. 6, No. 2, pp. 99-108 (1987)
2. M. Ohtsu, "Rate Process Analysis of Acoustic Emission Activity in Core Test of Concrete," Concrete Library of JSCE, No. 20, pp. 143-153 (1992)
3. M. Kachanov, "A Continuum Model for Medium with Cracks," J. Engineering Mechanics, ASCE, Vol. 106, No. 5, pp. 1039-1051 (1980)
4. M. Ohtsu, K. Ukita and K. Yuno, "Stochastic Analysis of AE Activity in Uniaxial Compressive Test," Proc. JSCE, No. 520/V-28, pp. 13-24 (1995)
5. S. P. Shah, S. E. Swartz and C. Ouyang, Fracture Mechanics of Concrete, John Wiley & Sons, Inc., New York, Chapter 11, pp. 425-451, (1995)

## **ACOUSTIC EMISSION DIAGNOSIS OF CONCRETE-PILES DAMAGED BY EARTHQUAKES**

**Tomoki Shiotani<sup>1</sup>, Norio Sakaino<sup>1</sup>, Masayasu Ohtsu<sup>2</sup> and Mitsuhiro Shigeishi<sup>2</sup>**

<sup>1</sup> Technological Research Institute, Tobishima Corporation,  
5472 Kimagase, Sekiyado, Higashi-katsushika, Chiba 270-02, Japan

<sup>2</sup> Department of Civil Engineering and Architecture, Kumamoto University,  
2-39-1 Kurokami, Kumamoto 860, Japan

### **ABSTRACT**

Earthquakes often impose unexpected damage on structures. Concerning the soundness of the structure, the upper portion is easily estimated by visual observation, while the lower portion located in deep underground is difficult to be estimated. Thus there exist few effective methods to investigate underground structures. In this paper, a new inspection technique for damage evaluation of concrete-piles utilizing acoustic emission (AE) is proposed, and is verified by a series of experiments. Firstly, such basic characteristics as the attenuation and effective wave-guides for detecting AE underground, are examined through laboratory tests. Secondary, fracture tests of full-scale prefabricated concrete piles are conducted, and the characteristics of the AE are examined. Finally, actual concrete-piles attacked by the 1995 Great Hanshin Earthquake are investigated. Results confirm that the estimated damages by the proposed method are in good agreement with actual damaged locations. Thus, the method is very effective for the diagnosis of the concrete-piles.

### **INTRODUCTION**

After big earthquakes attacked, it is in urgent demand for infrastructures to be inspected and diagnosed for their soundness. The upper portions of the structures are comparatively easy to be estimated by visual observation, while the lower portions, foundations of structures in particular piles located in deep, are difficult to be estimated. As the techniques to investigate the soundness of piles, there exist conventionally a few methods. One of them is an impact-echo test commonly called "Pile Integrity Test (PIT)", that has been worldwide used for the quality control of cast in-

place piles. Because of the simplicity, PIT has many results, although in advance to the survey, the vicinity of head of the piles has to be exposed for producing stress waves. Boring of the piles and the borehole observation by CCD camera, are also used for the investigation.

Acoustic Emission (AE) is a stress wave generated due to the deformation and fracture. In a fracture process of concrete-piles by earthquakes, when the strain energy is released with crack propagation, and AE would be generated. In the piles once damaged, it is expected that the AE is produced due to creep deformation of piles and the increase of skin friction with consolidation settlement of the ground in loosen sand and cohesive soil. Additionally, it is reported that, in materials experienced plastic deformation, Kaiser Effect<sup>1)</sup> does not hold<sup>2)</sup>. Hence, considering these aspects on the characteristics of fracture in piles, "Damage Diagnosis Technique by Acoustic Emission in Concrete-Piles" have been developed and applied to the investigation of the piles in actual buildings. In the paper, the concept of the proposed method is reviewed, a series of the studies on basic issues of the technique is discussed and then the application is shown.

## CONCEPT OF THE TECHNIQUE

### AE Propagation

When the piles having damage are under external loading, AE from damaged portions is expected to be generated. For simplicity, we limit our attention to the motion of P-wave incident. Figure 1 shows a schematic procedure for detecting AE in concrete-piles. An AE wave radiated within piles is firstly propagated into the soil, and approaches to an interface between the soil and a wave-guide. At the interface, the incident wave is partially reflected, and partially transmitted into the wave-guide. The transmitted wave is propagated in the wave-guide, and is detected by AE sensors.

### Estimation of AE sources

AE source location is performed by the one-dimensional source location method. In the right portion of Figure 1, AE waveforms detected in AE sensors are schematically shown. Because AE source exists close to AE sensors #1, the sequence of AE arrival is sensor #1 and sensor #2. Accordingly, we obtain the arrival time difference  $\delta t$ . The location of AE source is calculated from,

$$a = \frac{l - v\delta t}{2}, \quad (1)$$

where  $l$  is the sensor spacing, and  $v$  is the wave velocity.

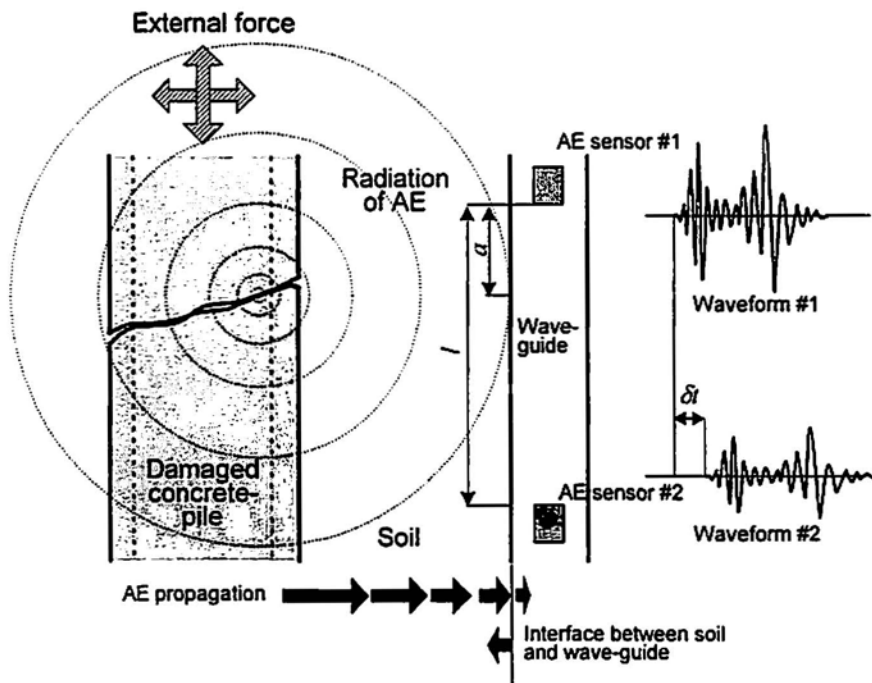


Fig. 1 Schematic procedure for detecting AE in concrete-piles

### Wave Transmission Loss at Interfaces

An interface is defined as the boundary between two media with different acoustic properties. The transmission loss of an incident wave is dependent on the difference between acoustic impedances  $Z_{\text{soil}}$  and  $Z_{\text{wave-guide}}$  which are defined as density times wave velocity. The amplitudes of the reflected and the transmitted waves,  $A_r$  and  $A_t$ , are given by

$$A_r = A_i \frac{(Z_2 - Z_1)}{Z_1 + Z_2}, \quad (2)$$

$$A_t = A_i \frac{2Z_2}{(Z_2 + Z_1)}, \quad (3)$$

where  $Z_1$  is the acoustic impedance of the medium where the wave propagates and is incident to the interface,  $Z_2$  is the acoustic impedance of the medium where the wave is transmitted from the interface, and  $A_i$  is the amplitude of the incident wave. The ratio of  $A_r/A_i$  is the coefficient of reflection,  $R$ ,

$$R = \frac{Z_2 - Z_1}{Z_2 + Z_1} . \quad (4)$$

The traditional and still widely-used wave-guides are made of metal<sup>3), 4)</sup>. It implies that an incident wave is almost reflected at the soil/metal interface, because  $Z_1$  is even smaller than  $Z_2$  in equation 4. Therefore, in the case that the wave-guides are applied to the detection of AE underground, the materials of wave-guides should be examined on their acoustic properties.

### CHARACTERISTICS OF AE PROPAGATION IN THE GROUND

A body wave radiated from a simple AE source is known as a spherical wave. In this radiation process, the AE wave loses its energy with propagation, and the attenuation is normally called “geometrical damping”, and is represented by

$$A = A_0 r^{-n} , \quad (5)$$

where  $A_0$  is the amplitude of source,  $A$  is the amplitude at the distance of  $r$  from the source, and  $n : 2$  (semi-infinite media);  $1$ (infinite media);  $1/2$ (surface wave). Furthermore, the AE wave also attenuates caused by absorption. Absorption is the result of internal friction. Considering absorption, equation 5 is modified,

$$A = A_0 e^{-\lambda r} r^{-n} , \quad (6)$$

where  $\lambda$  is the ratio of equivalent attenuation to the absorption, and is given by

$$\lambda = \frac{2\pi h f}{v} , \quad (7)$$

where  $h$  is the ratio of absorption, and  $f$  is the frequency.

#### Characteristics of Attenuation in Toyoura Sand

Due to the homogeneous distribution of the grain size, Toyoura sand is known as the standard sand. Figure 2 shows the result of AE attenuation in Toyoura sand. In the experiment, an artificial AE is generated by hitting nails of stainless steel, and is detected by AE sensors of 60kHz resonant type. In the figure, “Dry” demonstrates a result of sand of relative density 50%,

“Sat” denotes saturated sand, and “Wet” indicates sand which is drained for 24 hours after saturated. From Figure 2, AE attenuates in proportion to the logarithms of propagation distance up to a few centimeters. Beyond 1 meter, AE quickly decays. Therefore, for detecting AE of small magnitude produced by micro-crack growth, 1 meter would be the standard length for the effective AE monitoring.

### EFFECTIVE WAVE-GUIDES

Taking into account characteristics of AE propagation, new wave-guides are proposed. The wave-guide is combined “Unplasticized Polyvinyl Chloride (PVC) Pipes” with “water”. The PVC pipes is devised for the decrease of the transmission loss between soil and the outer portion of wave-guides, and water is filled in the pipes for the decrease of attenuation in propagation. AE sensors are set at proper places in the water, and they detect AE propagated in the water without notable attenuation.

### Experiment of Wave-guide

Figure 3 shows an experimental setup of wave-guides. Materials of wave-guides are aluminum and vinyl chloride. The length of wave-guides is 500mm, the diameters are 70 (vinyl chloride) and 78mm (aluminum), and the thicknesses are 11 (vinyl chloride) and 20mm(aluminum), respectively. Two AE sensors, denoted A and B, are placed in

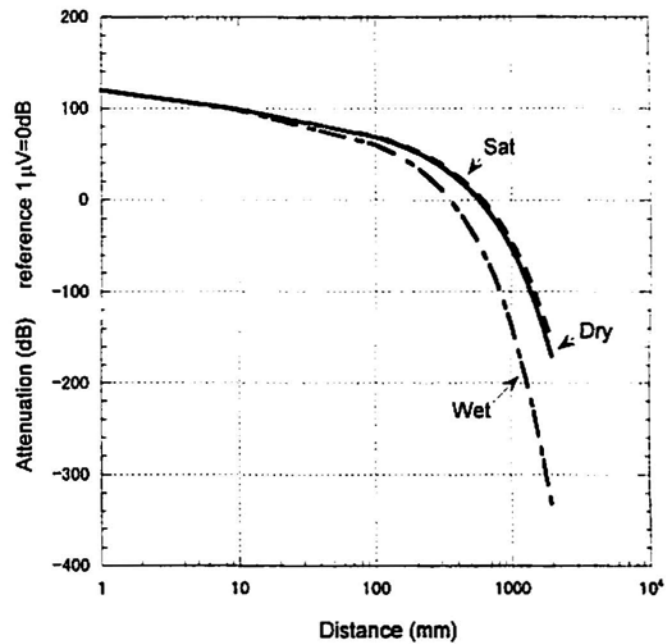


Fig. 2 Results of AE attenuation in Toyoura sand

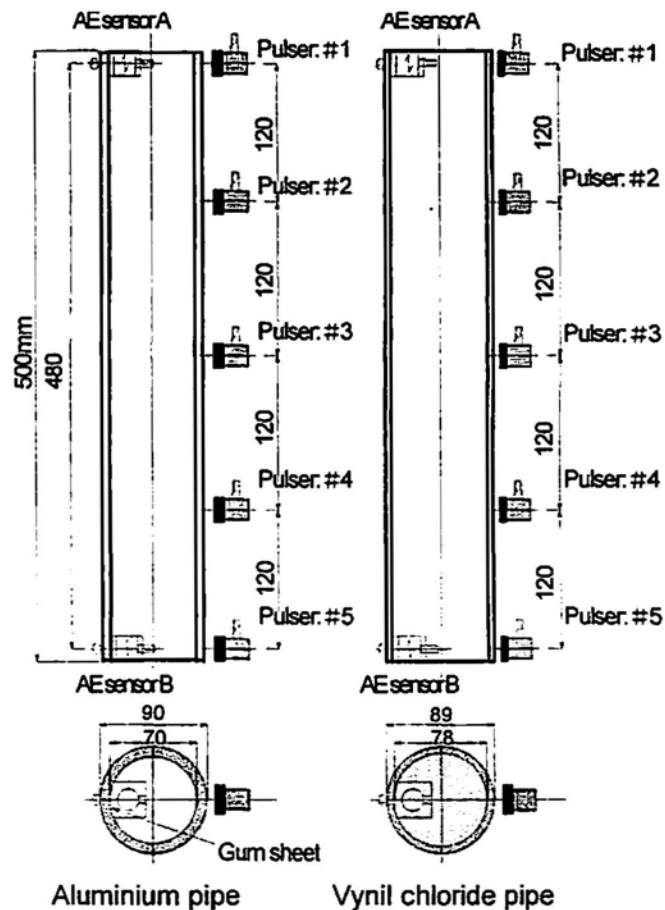
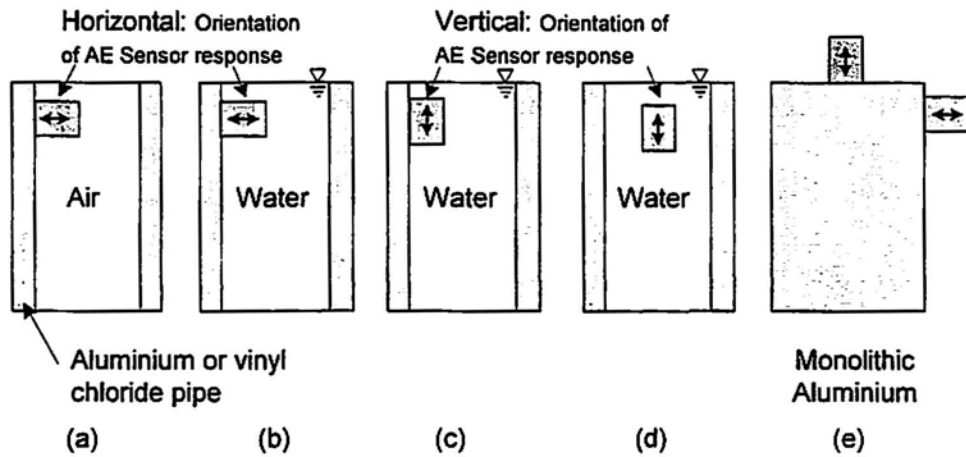
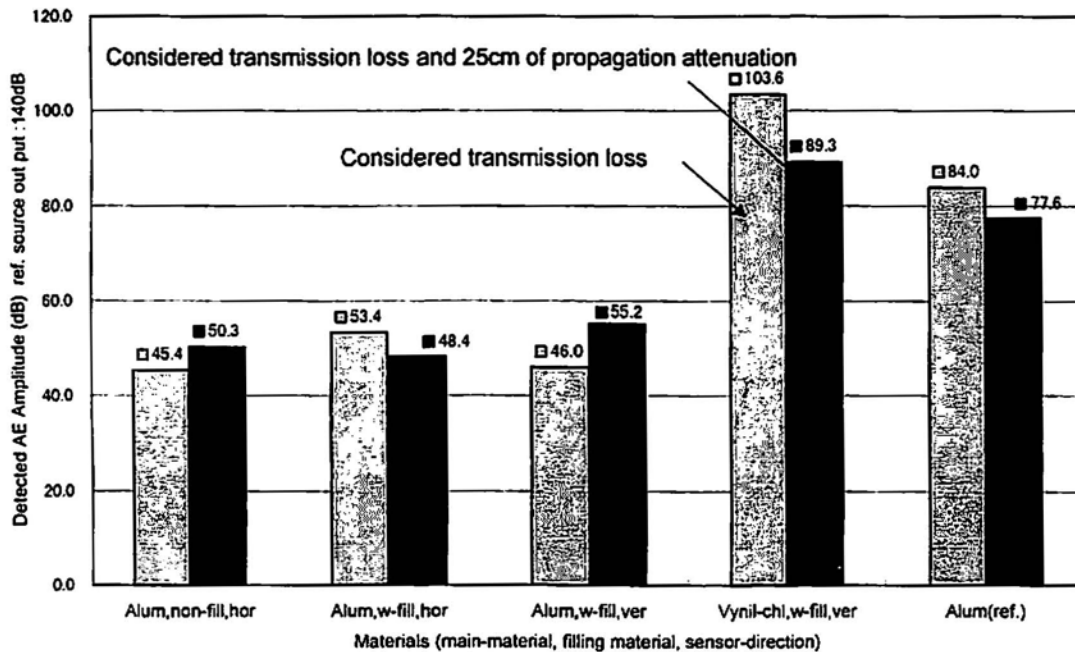


Fig. 3 Experimental setup of wave-guides



**Fig. 4 Methods for setup of AE sensors in the wave-guides**

the both sides of the wave-guides. Figure 4 shows setting methods of AE sensors in the wave-guides: (a) AE sensor on the inter wall of the pipes; (b) AE sensor in water; (c) AE sensor changed vertically; (d) AE sensor suspended in the water; and (e) AE sensors conventionally mounted. The wave-guide is set in Toyoura sand of 50% relative density. Five AE sensors of 60kHz resonant type are arranged at 3mm separated from the wave-guide as shown in Figure 3 from #1 through #5. AE measurements are performed by Pac's Mistras DSP, in which AE waves are recorded with sampling of 1MHz and 2k words.



**Fig. 5 AE amplitude detected by AE sensor of A and B on various wave-guides in Voltage**

## Experimental Results

Figure 5 exhibits the AE amplitude detected by AE sensor of A and B. Figure 5 shows by decibel term in which artificial AE output referred to 140dB. “Considered transmission loss” in the figure, shows the average of the amplitude when the artificial AE are generated at pulser #1 and #2 in Figure 3. The amplitude also includes the effect of the attenuation of AE propagation in the water. “Considered transmission loss and propagation attenuation of 25cm” shows the results of the average of the amplitude when the artificial AE are generated in the middle of the wave-guides at pulser #3. In the horizontal axis, methods of AE sensor setups and materials of wave-guide are indicated. “Alum, non-fill, hor”, for example, represents case that the wave-guide of aluminum is filled with nothing, and AE sensors are mounted horizontally. From Figure 5, the proposed wave-guides denoted as “Vinyl-chl, w-fill, ver” shows better characteristics than the monolithic aluminum, and the amplitude is twice as high as those of the aluminum pipes. Therefore, it is concluded that the proposed wave-guide combining PVC Pipes with water reveals excellent characteristic for detecting AE under the ground.

## FRACTURE TESTS OF FULL-SCALE PREFABRICATED CONCRETE-PILES

### Experimental Outline

Fracture tests of full-scale prefabricated concrete-piles are performed for examining the characteristics of AE in the fracture process. The length of pile is 7m, and the diameter is 400mm. Two types of the fracture mode are adopted. One is bending and the other is shearing. In this paper, the characteristic of AE in the shearing test is only explained.

### Test Procedure

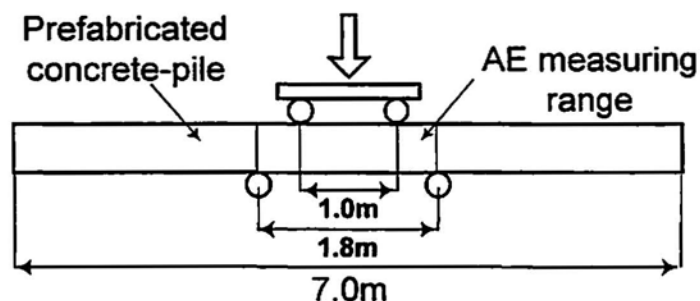


Fig. 6 Schematic configuration of the shearing test

Figure 6 illustrates the schematic configuration of the shearing test. Basically, the test is similar to 4-point bending tests. Placing the supports close to the loading points, the zone of high shear stress is concentrated in the narrow area shown in the figure. AE is monitored by six AE sensors to cover the measuring range in Figure 6. AE is previously amplified 40dB in pre-amplifier and is recorded over the threshold of 50dB.

## Experimental Results

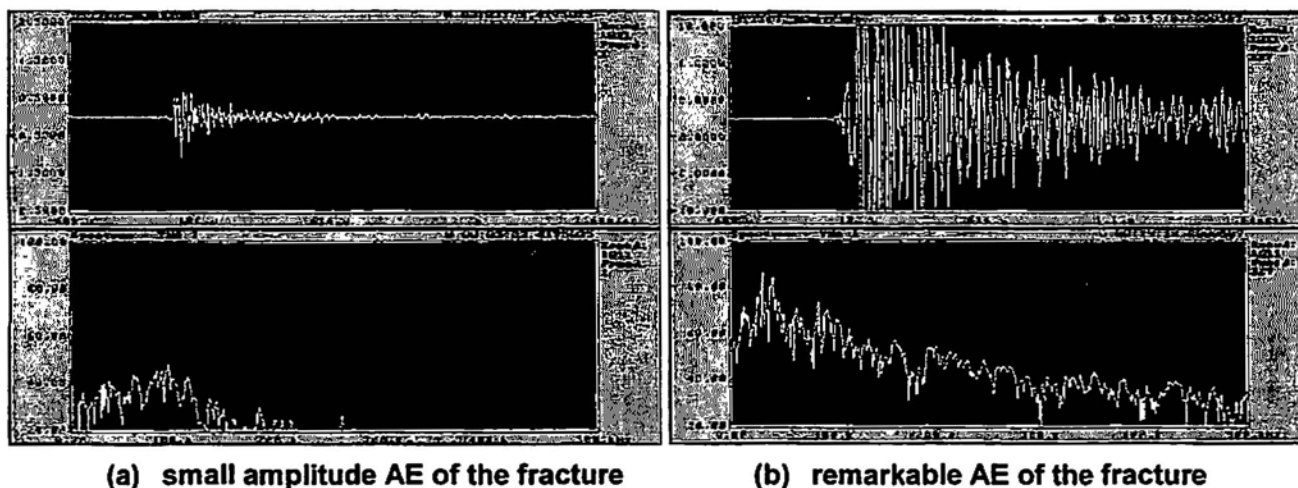


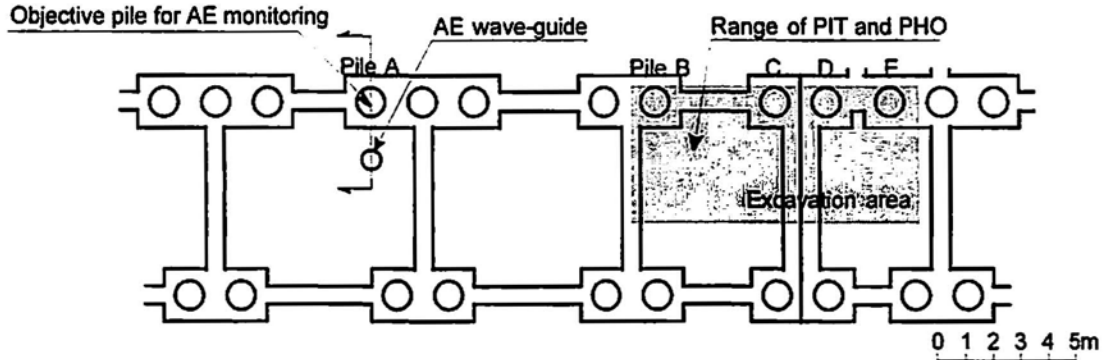
Fig. 7 AE waveforms and frequency spectra

Figure 7 shows the AE waveforms and frequency spectra. Figure 7 (a) shows the waveform and frequency spectrum that is generated by small magnitude of the fracture and observed frequently until visible crack growth. Figure 7 (b) is the waveform caused by the fracture with crack growth. In these figures, the AE wave due to micro-fracture has the short duration time and particular peak frequencies, while AE wave due to macro-fracture has the long duration time and the broad frequency contents ranging from low to high.

## APPLICATIONS

### Site and The Method for Detecting AE

The investigation was carried out at a foundation of high-rise building damaged by the 1995 Great Hanshin Earthquake located in Hyogo Prefecture. When the following inspections were performed, the upper structure was already removed. Therefore, loading by heavily machinery can easily induce AE. Figure 8 shows the plan view of investigated piles. The AE monitoring is performed by a suspended wave-guide in the monitoring well located in the vicinity of pile A. The PIT and "Pile head observation by human (PHO)" were examined in piles B, C and D.



**Fig. 8 Plan view of investigated piles**

Unfortunately, the piles investigated by AE is different from those by PIT and PHO. Figure 9 shows the geological chart of investigated ground and wave-guide configuration. In this ground, a reclamation bed of silty sand exists from surface to 3m depth, a loose sand bed lays up to 6m depth, a dense gravel bed over 30 of N-value is observed from 6 to 7m depth, and a silty sand bed is located below. AE monitoring was performed by using 5m-long aluminum wave-guide that was suspended 10m deep in the monitoring well filling up with the pure water.

**Estimated Damage Location by AE Monitoring**

Figure 10 shows AE events, weighted by ring-down counting versus the depth. In the figure, the damage location was estimated "around head of pile" and "3.5m to 4.5m (6m to 7m in the depth) below the head of pile". Although the objective piles of AE, PIT and PHO were different, estimated damage location at "head of pile" is well coincident with the results of PHO, and the fact "3.5m to 4.5m below the head of pile" also well agree with the results of PIT. It is noted that location estimated by both AE and PIT is identical to a peculiar stratum of ground beds. Generally it is reported that the weak portions of piles are introduced by the hasty change ground beds boundary, hence the estimated damage location by AE is considered to be reasonable.

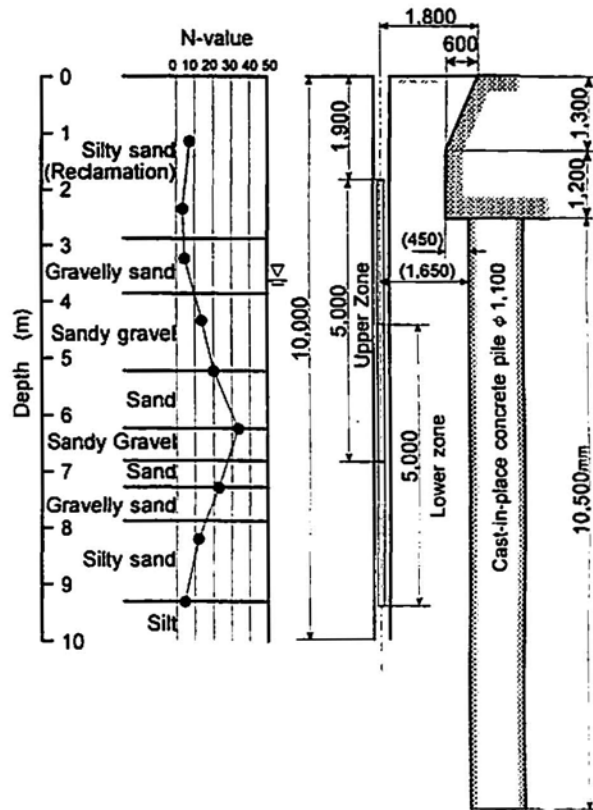


**Fig. 9 Geological chart of investigated and a wave-guide configuration**

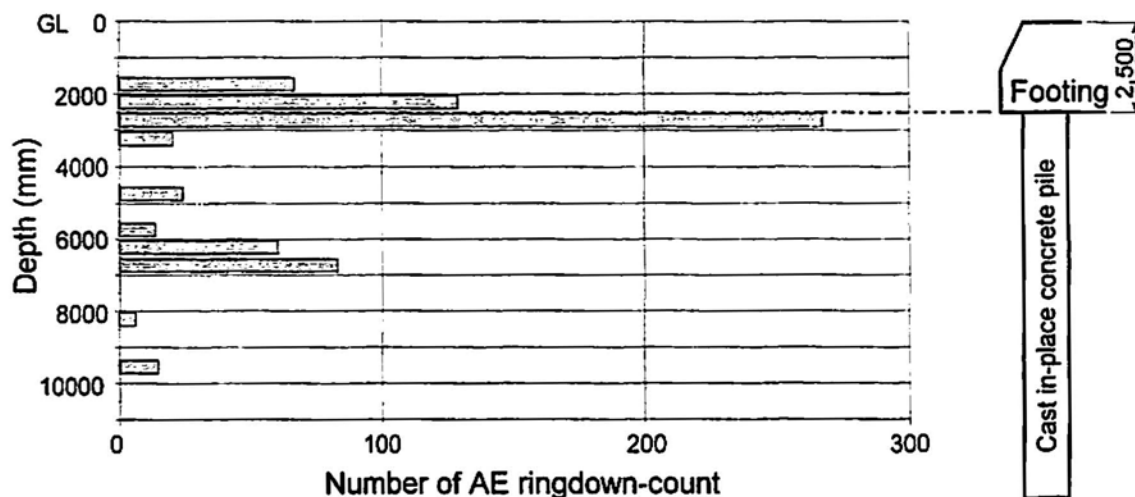


Fig. 10 AE event occurrence weighted by ringdown-counts

## CONCLUSION

A new inspection technique for damage evaluation of concrete-piles is proposed by utilizing AE, and is verified by a series of experiments. It is concluded as follow:

- 1) For detecting a small magnitude of AE produced by micro-crack growth, 1 meter would be the standard distance for the effective AE monitoring.
- 2) The proposed wave-guide combining PVC Pipes with water reveals excellent characteristic for detecting AE in the ground.
- 3) AE wave with micro-fracture has the short duration time and particular peak frequencies, while AE wave with macro-fracture has the long duration time and broad frequency contents ranging from low to high.
- 4) In an actual application, estimated damage location by the proposed AE technique is considered to be reasonable.

## REFERENCES

- 1) J.Kaiser, "Erkenntnisse und folgerungen aus der messung von geräuschen bei zugbeanspruchung von metallischen werkstoffen", *Arch. Eisenhüttenwesen* 24, pp.43-45, 1953. (in German)
- 2) S. Nagataki, T. Okamoto, T. Ayada and S. Yuyama, "Classification of cracking pattern developed in reinforced concrete members by Acoustic Emission", *Proceedings of the Symposium on Nondestructive Evaluation in Civil Engineering*, JSCE, pp.139-144, 1991.(in Japanese)
- 3) E. Lord, Jr. et al., "Utilization of steel rods as AE waveguides", *Journal of the Geotechnical Engineering Division*, ASCE, Vol.108, No.GT2, pp.300-305, Feb., 1982.
- 4) H.Geginald Hardy, Jr. et al., "Mechanical waveguides for use in AE/MS geotechnical applications", *Progress in AE IV*, JSNDI, pp.292-302, 1988.

## APPLICATION OF AE TO EVALUATE DETERIORATION OF PORT AND HARBOR STRUCTURES

Kimitoshi Matsuyama<sup>1</sup>, Akichika Ishibashi<sup>1</sup>, Tetsuro Fujiwara<sup>1</sup>, Yasuhiro Kanemoto<sup>1</sup>,  
Shiro Ohta<sup>1</sup>, Shigenori Hamada<sup>2</sup> and Masayasu Ohtsu<sup>3</sup>

- <sup>1</sup> Nippon Koei Co., Ltd. Research and Development Center  
2304 Takasaki, Kukizaki-cho, Inashiki-gun, Ibaraki 300-12, Japan
- <sup>2</sup> The Port and Harbour Research Institute, Ministry of Transport  
3-1-1 Nagase, Yokosuka-shi, Kanagawa 239, Japan
- <sup>3</sup> Kumamoto University, Department Civil Engineering and Architecture  
2-39-1 Kurokami, Kumamoto 860, Japan

### ABSTRACT

The degree of concrete deterioration is normally evaluated by uniaxial compression tests of core samples taken from existing concrete structures. The uniaxial compression test can give details on concrete strength, elastic modulus and so forth. By using AE (acoustic emission) technique with uniaxial compression tests, we can get more useful information on interior failures of the core sample. The observation of AE activity was conducted during uniaxial compression tests of concrete specimens and samples. The specimens were cast with 5, 10, 15 and 20% air content. The samples were taken from 2 harbor sites in Japan. Generating behavior of AE was studied quantitatively on the basis of rate process theory. Distribution of pores in the concrete could be measured by the porosimeter. The relation between AE activity in the uniaxial compression test of core samples and concrete property is clarified.

### INTRODUCTION

A large amount of concrete structures, in particular built in 1960's, are found to be approaching their service limit due to severe environmental conditions. Cost of maintenance for the concrete structures is predicted as very high in the beginning 21st century. Therefore, the development of diagnostic nondestructive evaluation (NDE) is urgently required.

There are many old structures in port and harbor facilities. These require proper diagnosis and timely reinforcement or repair for their continuous service. To estimate deterioration of the old concrete structure, core samples are taken from them and the uniaxial compression test is normally carried out. The uniaxial compression test can give details on concrete strength, elastic modulus etc.. However, these informations are still insufficient to evaluate the concrete deterioration.

AE (acoustic emission) is one of the NDE techniques that give useful information on internal cracking. By applying AE technique to uniaxial compression tests, information of micro cracks in the concrete can be obtain. These informations can make us to evaluate deterioration of the concrete.

In this study, an observation of AE activity was carried out during uniaxial compression testing of concrete specimens and core samples. For newly cast specimens, entrained air contents were arranged as 5%, 10%, 15% and 20%. AE measurement was carried out under the uniaxial compression test and behavior of AE was studied quantitatively on the basis of rate process. Distribution of pores in the specimens could be measured by the mercury porosimeter. A relation between pore volume and result of rate process was investigated. The concrete core samples from 2 harbor sites (port-A and port-B, which were constructed in 1963, 1906 respectively.) in Japan were tested. AE measurement, the rate process analysis, and the pore distribution were studied. It is clarified that results of the rate process analysis are strongly related to characteristic of the pore distribution in deteriorated concrete. Considering the relationship and the mechanism of the concrete deterioration, AE technique could be available for evaluating deterioration of concrete structure.

### RATE PROCESS ANALYSIS

The Kaiser effect is well known as an irreversible AE generating behavior under uniaxial compression. It results from the fact that cracks nucleated due to prior loading do not propagate until the load exceeds the previous level in the next loading. However, limited success is reported in respect to the determination of the previous load level, because it depends highly on the loading path and history. In usual cases, AE activity under uniaxial compression test is observed from low stress level. This is because the loading path is not identical to the previous path. It leads to a conclusion that some critical micro-cracks in one loading path may propagate due to stress increase. When concrete contains a number of critical micro-cracks, active AE generation is expected from low stress level due to new crack propagation. In contrast, AE activity in concrete of few micro-cracks is considered to be stable and low at stress level as in Fig. 1. Thus, the amount of critical micro-cracks in concrete could be evaluated by monitoring AE activity under the uniaxial compressive stress.

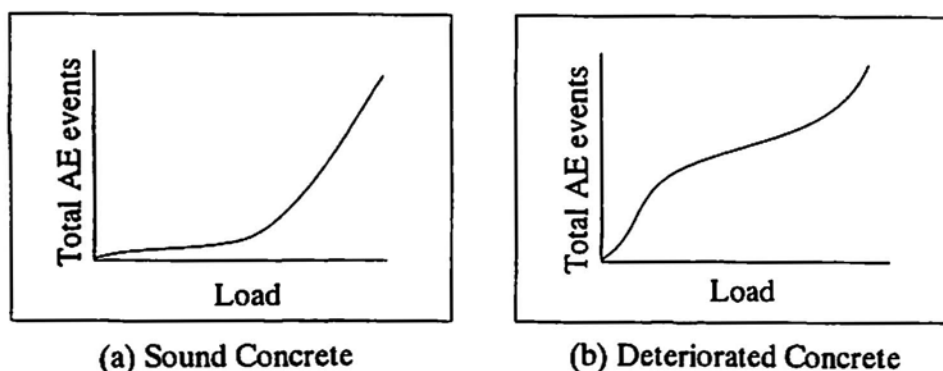


Fig.1 AE activities of concrete

To quantify the AE activity in the uniaxial compression test, the rate process theory was introduced by Ohtsu [1]. His method is described below ;

The probability function  $f(V)$  of AE occurrence from stress level  $V(\%)$  to  $V(\%) + dV(\%)$  is assumed, as follows:

$$f(V)dV = dN/N \tag{1}$$

where  $N$  is accumulated AE events up to stress level  $V(\%)$ , which is normalized by the strength. Here, the probability function  $f(V)$  is defined as the following hyperbolic function,

$$f(V) = a/V + b \tag{2}$$

where  $a$  and  $b$  are empirical constants. In the conventional rate process theory, the probability function  $f(V)$  is usually assumed as constant, which is called a rate. Whereas Eq.2 suggests two possible relations between the probability of AE occurrence and stress, introducing the hyperbolic term,  $a/V$ . The relation is illustrated in Fig.2. In the case that the value ' $a$ ' is positive, the probability of AE occurrence is high at low stress level. In contrast, the probability is very low at low stress level when the value ' $a$ ' is negative. Since the discrepancy of ' $a$ ' is considered to be dependent upon the amount of critical micro-cracks, the deterioration due to micro-cracking could be quantitatively evaluated on the basis of the value ' $a$ '.

From Eq.1 and 2, a relationship between the number of total AE events  $N$  and stress level  $V(\%)$  is obtained,

$$N = CV^a \exp(bV) \tag{3}$$

where  $C$  is an integration constant.

In the case that  $f(V)$  is constant, we obtain

$$N = C \exp(bV) \tag{4}$$

Eqs. 3 and 4 represent the relation between AE event and stress level. In the analysis, experimental data on AE events versus stress is approximated by Eq.3 or Eq.4 and empirical constant  $a$ ,  $b$ , and  $C$  are determined by the least-square error analysis.

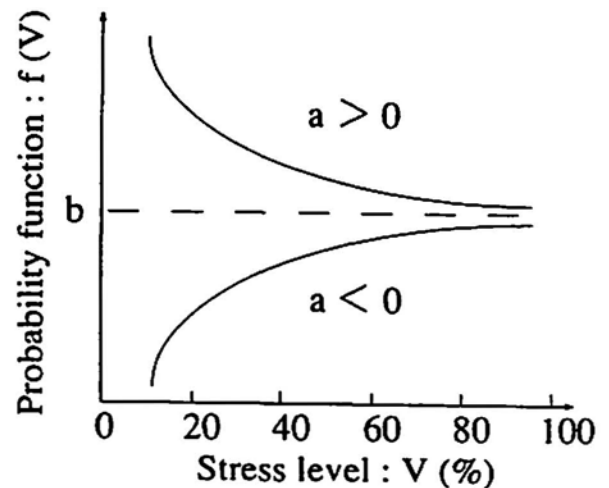


Fig.2 Assumed relations :  $f(V)$  vs.  $V(\%)$

## PORE DISTRIBUTION OF CONCRETE

Pore distributions of concrete are summarized in Fig. 3 [2]. Pores of concrete can be classified into the primary pore and the secondary. The primary pore is generated under construction and hardening of concrete, while the secondary pore is generated after hardening of concrete.

In the primary pore distribution, concrete has several radius of pore as given below :

Gel pores : under 3.0 nm	Capillary pores : 3.0 nm ~ 10 $\mu$ m
Entrained air : 10 $\mu$ m ~ 1.0 mm	Entrapped air : over 1.0 mm

At any stage of hydration, the hardened paste consists of hydrates of such compounds as, collectively referred to as gel, crystals of  $\text{Ca}(\text{OH})_2$ , minor components, unhydrated cement, and the residue of the water-filled spaces in the fresh paste. These voids are called capillary pores, but within the gel itself there exist interstitial voids called gel pores.

Entrained air in concrete is defined as air intentionally incorporated by means of suitable agent. This air is clearly distinguished from accidentally entrapped air.

In the secondary pore distribution, concrete has some radius of pore as given below :

Pores by drying shrinkage : 0.005 ~ 1.0 $\mu$ m,	Pores by freezing and thawing : 1.0 ~ 100 $\mu$ m
Mortar cracks : 1 $\mu$ m ~ 10 $\mu$ m,	Bond cracks : 10 ~ 150 $\mu$ m

These pore volume in concrete should be changed due to an extent of the concrete deterioration.

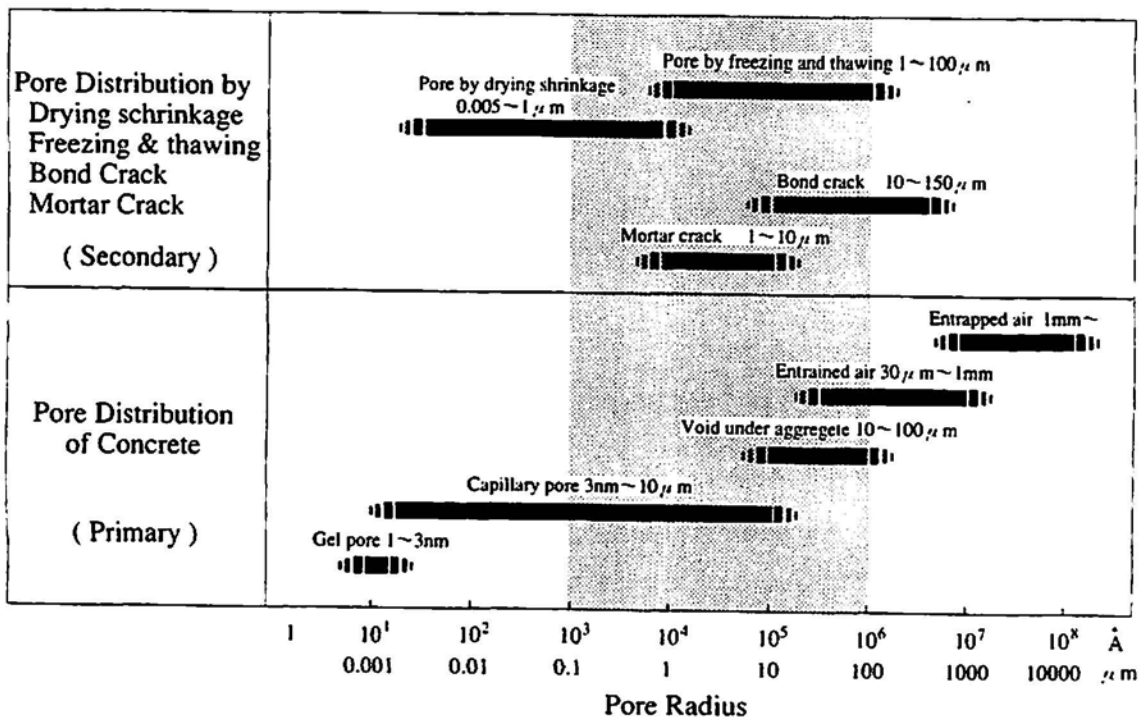


Fig.3 Pore distributions of concrete

## BASIC EXPERIMENT

### Test Procedure

#### (1) Specimens

Mix proportions employed are indicated in Table 1. Based on the mix proportions of Table 1, the entrained air contents were arranged as 5%, 10%, 15%, 20% by using air-entrained admixture. For the uniaxial compression test, cylindrical specimens of 10 cm radius and 20 cm height were cast and moisture-cured for 90 days.

Table1 Mix proportions of concrete

Unit Weight (kg per 1 m <sup>3</sup> of concrete)				
Water	Cement	Sand	Gravel	Air(%)
178	223	855	983	5.0

#### (2) Experiments

During the uniaxial compression test, AE events were counted up to the final failure. AE sensor of 150 kHz resonant frequency was attached at the center of a core sample. To decrease noise from contact surfaces between the specimen and loading plates, Teflon sheets of 0.5 mm thickness were inserted. Total gain of AE measurement was set to 60 dB.

The pore distribution of concrete were measured by means of the mercury porosimeter. The porosimeter with 400 MPa maximum pressure was used. After vacuum pumping on the specimens, mercury was let in. Pore size distribution was calculated according to the Washburn equation assuming cylindrical pore shape :

$$P = -4 g \cos d / D$$

P : pressure, g : surface tension of mercury

d : contact angle mercury-pore

D : radius of pore

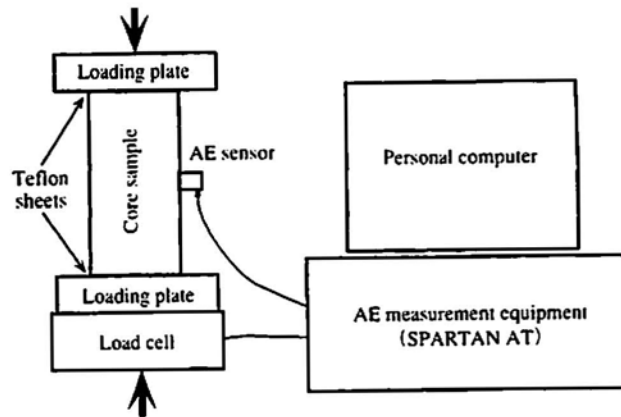
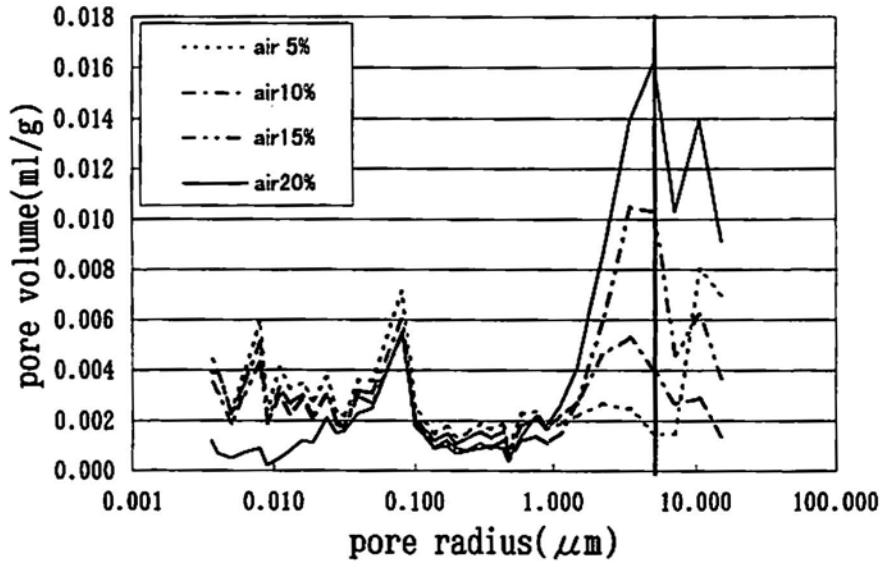


Fig.4 AE test setup

**Result**

**(1) Pore distribution**

Pore distribution of the specimens is shown in Fig. 5. Over 1.0  $\mu\text{m}$  pore radius differences of pore volume are remarkable. In general, entrained air has typically a radius of about tens to hundreds  $\mu\text{m}$ . The pore radius over 1.0  $\mu\text{m}$  in Fig. 5 corresponds to the range of pore radius of general entrained air.



**Fig.5 Pore distribution of the specimens**

A relation between pore volume of radius from 3.4 to 5.0  $\mu\text{m}$  and strength is shown in Fig. 6. It is found that the relationship is linear. It means that the pore volume of particular radius is one of causes which influence the strength of concrete.

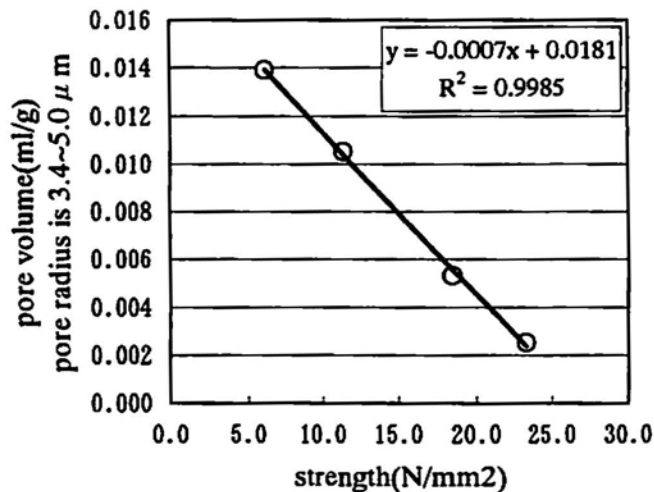


**Fig.6 Relation between pore volume and strength**

Fig. 7 shows relation between 'a' value in Eq. 3 and the pore volume of pore radius from 3.4 to 5.0  $\mu\text{m}$ . The higher pore volume is, the larger 'a' value is obtained. This means that high AE activity at low stress level derives from the increase of the pore volume, and 'a' value becomes larger.

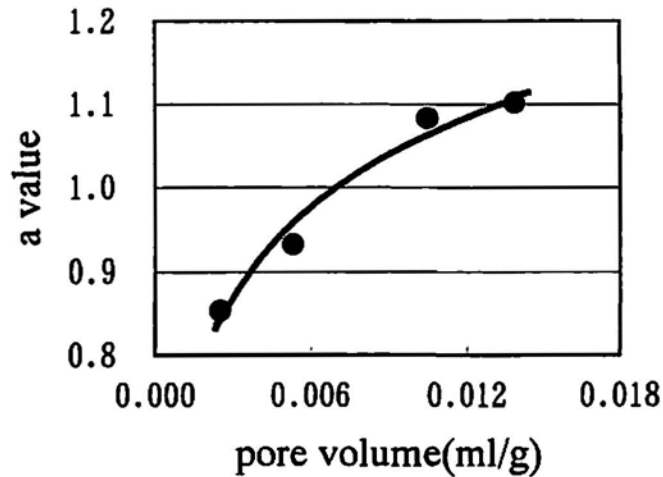


Fig.7 Relation between 'a' value and pore volume

## EXPERIMENT OF CORE SAMPLES FROM STRUCTURES

### Test Procedure

#### (1) Objective

AE data was obtained from concrete core samples of two ports - port-A and port-B. Port-A was constructed in 1963. Concrete core samples were extracted from upper, middle and lower parts of prestressed concrete bridge located at sea-side and land-side. Port-B was constructed in 1906 and was restored in 1924, because of the Kanto earthquake in 1923. Concrete core samples were extracted at splash zone and under the sea of reinforced concrete caisson. Damage estimation of port-A and port-B by visual inspection and compressive strength of cores are given in Table 2.

Table2 Damage estimation at Port-A and Port-B

Name	Locations	Visual Inspection			Uniaxial Compression Test
		Cracks of Concrete	Corrosion of Reinforcing Bar	Striooing of Concrete	Ave. of Compressive Strength (N/mm <sup>2</sup> )
Port-A	Sea side	○	○	○	43.5
	Land side	○	×	×	42.8
Port-B	Splash zone	×	×	×	22.9
	Under the sea	×	×	×	29.5

○ : Exist    × : Not Exist

Although port-A is not older than port-B, some characteristics of deterioration were recognized at port-A. In the port-B, any particular deterioration were not observed by visual inspection.

## (2) Experiments

The uniaxial compression test and AE measurement were carried out as the basic experiment. The mercury porosimeter was applied to evaluate pore distribution.

## Result

### (1) Characteristic of Pore Distribution

Pore distributions at cover concrete of port-A and port-B are summarized in Fig.8 [3]. The ratios of the pore volume of 0.1 ~ 100  $\mu\text{m}$  radius to total pore volume of 0.005 ~ 100  $\mu\text{m}$  radius are indicated. In the port-A, sea-side concrete has the pore volume more than the land-side concrete. Concrete of middle and lower parts show higher ratio of pore volume than concrete of upper part. In the port-B, the ratio of pore volume at splash zone is higher than that of pore volume in the sea.

The pore volume of 0.1 ~ 100  $\mu\text{m}$  radius is coincident with the pore radius of bond crack and mortar crack as shown in Fig. 3 (shade zone).

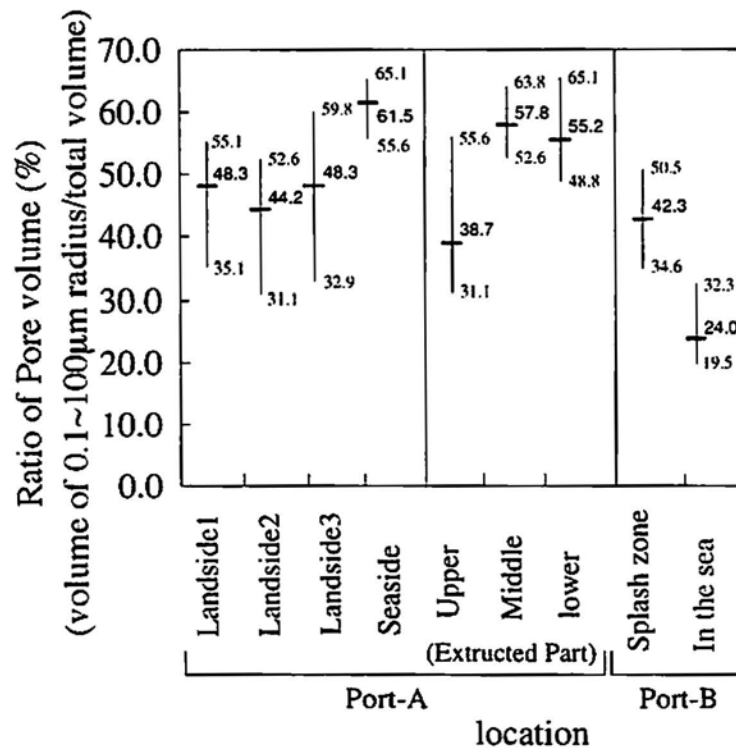


Fig.8 Pore distribution (port-A,B)

### (2) Pore Distribution and 'a' Value

Fig.9 shows a relationship between the ratio of the pore volume of 0.1 ~ 100  $\mu\text{m}$  radius to the total pore volume of 0.005 ~ 100  $\mu\text{m}$  radius and 'a' value calculated by the rate process analysis. Concrete that has more the pore volume of 0.1 ~ 100  $\mu\text{m}$  radius shows high value of 'a'. Comparing between port-A and port-B, the range of 'a' value and the ratio of pore volume of port-A are varied wider than those of port-B.

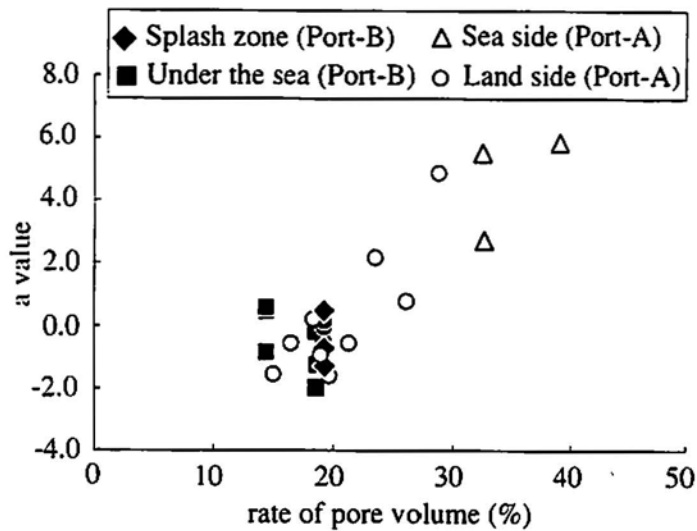


Fig.9 'a' value and Rate of pore volume

### DISCUSSION

Environmental conditions of port-A was clarified as below :

- (1) Corrosion was seen at sea-side and lower part.
- (2) Corrosion was not seen at land-side and upper part.
- (3) The minimum temperature is below -10 degree Celsius.

Considering these environmental conditions, 'a' value and the pore ratio, it is considered that deterioration of port-A concrete occurred due to freezing-thawing process and then corrosion of reinforced bar was introduced as shown in Fig.10.

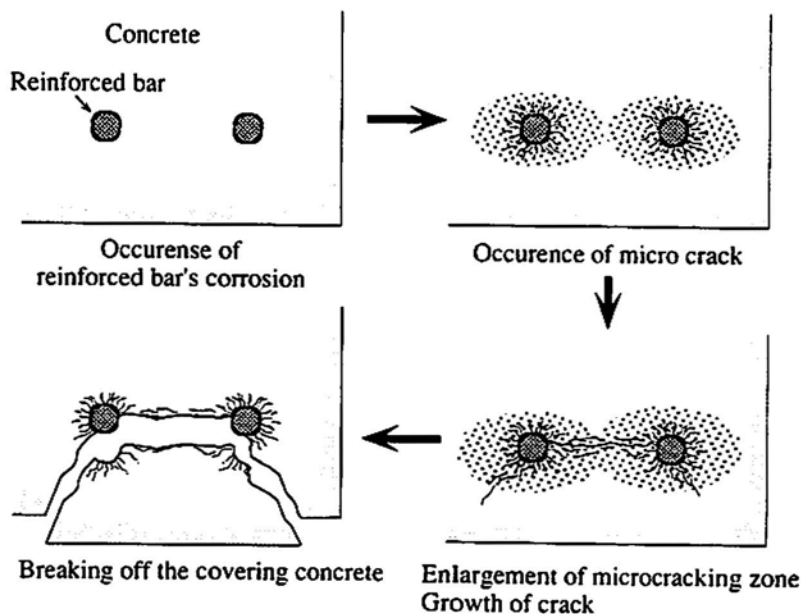


Fig.10 Mechanism of concrete deterioration

Environmental conditions of port-B was clarified as below :

- (1) Cracks and corrosions of reinforced bar did not exist.
- (2) Port-B has been used over 70 years.
- (3) Climate around port-B is not as cold as port-A.

Considering these environmental conditions, 'a' value and the pore ratio, port-B could be estimated to be slightly influenced by exposure condition.

## CONCLUSIONS

- (1) Increase of the pore volume made AE activity high at low stress level, and 'a' value increase in the experiments of cast specimens.
- (2) Freezing-thawing and corrosion result in the high ratio of pore volume of 0.1 ~ 100  $\mu\text{m}$  radius in concrete of Port-A.
- (3) There is a consistent relationship between the ratio of the pore volume of 0.1 ~ 100  $\mu\text{m}$  radius to the total pore volume of 0.005 ~ 100  $\mu\text{m}$  radius and 'a' value calculated by the rate process analysis.

AE measurement under the uniaxial compression gives useful information on micro-cracks in the core sample. The 'a' value could be applied to evaluate the extent of deterioration of concrete. Thus, the rate process analysis of AE measurement and the uniaxial compression test could supply not only compressive strength and young's modulus but also 'a' value that could evaluate the extent of concrete deterioration quantitatively.

## REFERENCES

- [1] M. Ohtsu, "Rate process Analysis of AE activity in Uniaxial Compression Test of Core Sample", *Progress in AE V, JSNDI*, 1990, pp.479-486.
- [2] J. Yamada, "Intelligible knowledge of cement and concrete", *Kajima publisher*, 1987, pp.145.
- [3] A. Ishibashi, "Concrete Core Testing of Harbor Structures using AE Rate Process Analysis", *The First US-Japan Symposium on Advances in NDT*, 1996, pp.49-54.

## **OBSERVATION OF DAMAGE PROCESS IN RC BEAMS UNDER CYCLIC BENDING BY ACOUSTIC EMISSION**

**Mitsuhiro Shigeishi<sup>1</sup>, Masayasu Ohtsu<sup>1</sup>, Nobuyuki Tsuji<sup>2</sup> and Daisuke Yasuoka<sup>3</sup>**

<sup>1</sup> Department of Civil Engineering & Architecture, Kumamoto University,  
2-39-1 Kurokami, Kumamoto 860, Japan

<sup>2</sup> Graduate School of Kumamoto University,  
2-39-1 Kurokami, Kumamoto 860, Japan

<sup>3</sup> Osaka Branch, Daiho Corporation,  
Shinkou Building #2, 2-2-5 Higashi-Tenma, Kita-ku, Osaka 530, Japan

### **ABSTRACT**

Reinforced concrete (RC) structures are generally applied to construction of buildings and bridges, and are imposed on cyclic loading incessantly. It is considered that detected acoustic emission (AE) waveforms are associated with the damage degree and the fracture mechanisms of RC structures. Therefore, the cyclic bending tests are applied to damaged RC beam specimens. To evaluate the interior of the damaged RC beams, the AE source kinematics are determined by 'SiGMA' procedure for AE moment tensor analysis. By using 'SiGMA' procedure, AE source kinematics, such as source locations, crack types, crack orientations and crack motions, can be identified. The results show the applicability to observation of the fracture process under cyclic bending load and evaluation the degree of damage of RC beam.

### **INTRODUCTION**

A phenomenon, acoustic emission (AE) is the propagation of elastic waves generated from a source in an elastic material. AE source is a micro-motion caused by rapid dislocation of mass. The most typical AE source is the release of internal energy due to propagation of an existing crack. Further, contact of the faces and friction at the existing crack surfaces are also sources of AE. AE behavior, activity, waveforms contain its source mechanisms and the conditions of medium during propagation. Accordingly, in the case that AE waveforms are appropriately detected and theoretically analyzed, it is expected that the existence and expansion of damaged domain could be evaluated.

AE technique enables real-time and wide-range surveillance of structures without

intermission. Furthermore, the behavior of a material / structure could be observed under dynamic loading. In consequence of these advantages of AE technique, research on diagnosis of interior condition and behavior of a material / structure by using AE technique has been actively performed in concrete and structural engineering [1].

Reinforced concrete (RC) beams / slabs are extensively employed in construction of bridges and structures. RC beams / slabs are liable to be damaged because they are always imposed on cyclic loading. It is considered that detected AE waveforms and their parameters are associated with both the fracture mechanisms of RC structures and the damage degree due to cracking in concrete body and slipping of reinforcement.

In this research, the fracture process of RC beams under cyclic bending is observed, and then SiGMA moment tensor analysis is applied to diagnosis of damaged degree of RC structures.

### CYCLIC BENDING TEST OF RC BEAMS

Two RC beam specimens reinforced by a single steel bar are used. Configuration of the specimen is shown in Fig. 1. These are designed to bear static 44.1 kN bending. The measured ultrasonic velocity which propagates in concrete is 4 770 m/s. The specimen has a square section of 100 mm and a length of 400 mm, and one through-thickness notch 1 mm wide is prepared at the center of span at the bottom surface.

Type A contains a deformed steel bar of 10 mm diameter at depth 15 mm. A round steel reinforcement of 10 mm diameter is embedded in Type B.

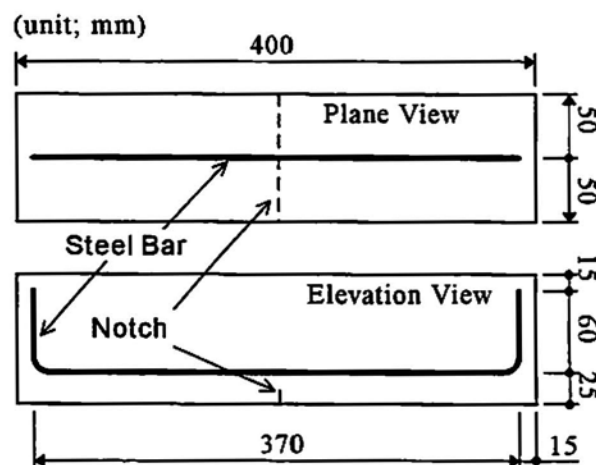


Figure 1. Configuration of RC beam specimen

To examine the applicability of AE waveform analysis using SiGMA procedure, cyclic bending tests of RC beams were carried out. AE waveform analysis has already been applied to observation of RC beam fracture under cyclic bending [2]. However, semi-static load was simply applied to specimens intermittently. In this experiment, the low-level cyclic load was applied continuously. The experimental setup of the four-pointed bending test is shown in Fig. 2.

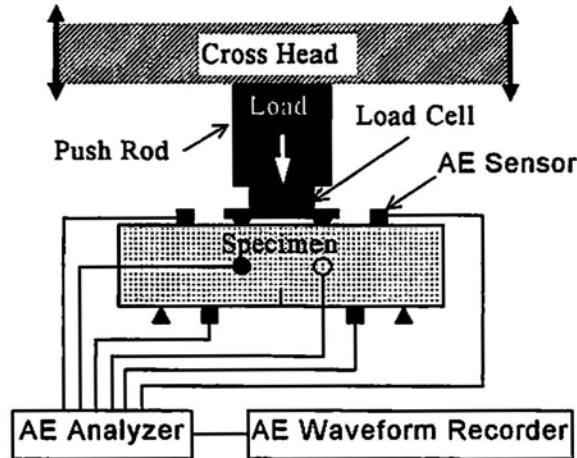


Figure 2. Experimental setup of cyclic bending test

Before cyclic bending test, the static load (22.05 kN) corresponding to 50 % of bending strength was applied to both specimens. After pre-load is removed, cyclic load from 0.98 kN to 22.05 kN was applied to RC beam specimens 100 times automatically. The loading speed of the cross head was set to 10 mm/s.

During the test, AE waveforms were continuously recorded at 6-channel AE measurement system. AE sensor locations are shown in Fig. 3. AE waveforms were detected at 6 AE sensors, which are attached to the top surface (# 1 and # 2), the facing side (# 3), the bottom surface (# 4 and # 5) and the back side (# 6) of the specimen. These sensors have flat response in the wide frequency-band up to 1 MHz.

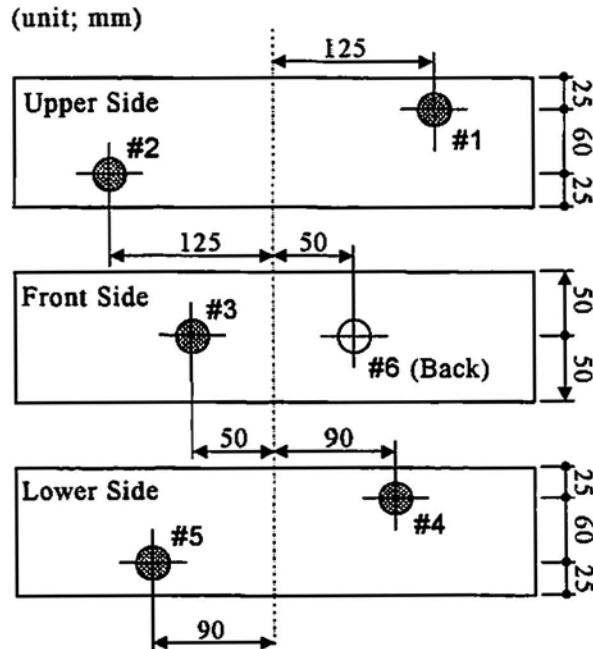


Figure 3. Arrangement of AE sensors

When a signal, of which threshold level was over 120 mV, due to arrival via sensor #1, the system enforced all channels to start recording AE signals. The high-pass filtering over 3 kHz was employed for recording AE waveforms. Total amplification of the measurement was 60 dB gain. AE signal was digitized into 2 048 words in length at 2 MHz sampling rate. Digital data were stored into the hard disk.

## SIGMA MOMENT TENSOR ANALYSIS

### Generalized Theory of Acoustic Emission

For quantitative AE waveform analysis, theoretical treatment is summarized as a generalized theory of AE [3]. Mathematically a micro-cracking of the AE source is modeled by a dislocation of internal surfaces as shown in Fig. 4.

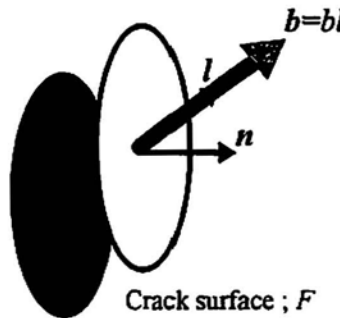


Figure 4. Dislocation model for micro-crack

The crack surface  $F$  is nucleated at location  $y$  due to dynamic fracturing. An internal face with normal vector  $n$  virtually consists of two planes in coincident motion. Due to micro-fracturing, dislocation vector  $b$  between the two planes is defined. Dynamic motion of dislocation  $b$  generates elastic wave which is observed at surface of the body.

When crack motion direction  $b$  is parallel to normal vector  $n$ , a tensile crack is nucleated. Otherwise, a mixed-mode or shear crack is occurred. The angle between the direction  $b$  of crack and the normal direction  $n$  is not equal to zero and is less than 90 degree.

Thus, crack kinematics are defined by normal vector  $n$  and crack motion direction  $l$  ( $b=bl$ ). A physical quantity defined by two orientations is mathematically called a tensor. Conveniently, the following tensor is defined from the two vectors,

$$m_{pq} = C_{pqjk} l_j n_k \quad (1)$$

Here  $C_{pqjk}$  are elastic constants. Then, AE waveform  $u_i$  at location  $x$  corresponding crack motion on crack surface  $F$  is represented by using moment tensor  $m_{pq}$ ,

$$u_i(x, t) = \int_F G_{ip,q}(x, y, t) m_{pq} * S(t) dS \quad (2)$$

Where  $G_{ip,q}$  is the spatial derivative of Green's function and  $S(t)$  represents the source-time

function (crack kinetics) and the notation \* means the convolution integral.

### SiGMA Procedure

Fig. 5 shows a view of AE waveform detected by an AE sensor placed at a boundary surface.

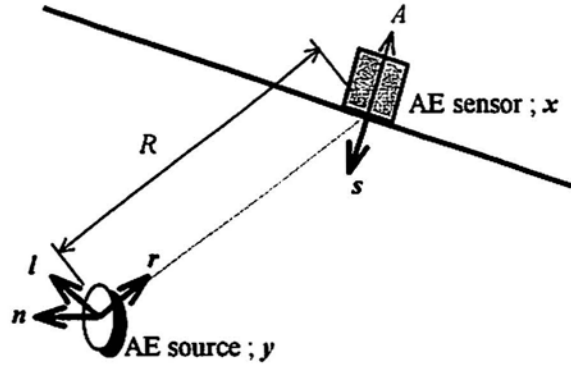


Figure 5. AE waveform observation

To process AE waveform data promptly, a simplified moment tensor inversion procedure is developed by the use of only P wave amplitude [4]. A procedure named as SiGMA (simplified Green's function for moment tensor analysis) is developed. Selecting the P wave portion from the full-space Green's function of homogeneous and isotropic material, Eq. 2 is simplified,

$$A = C \operatorname{Re}(s, r) \frac{\gamma_p \gamma_q m_{pq}}{R} \quad (3)$$

Here,  $C$  is the material constant,  $\operatorname{Re}(s, r)$  is the reflection coefficient due to directions  $s$  of sensor sensitivity and direction  $r$  of wave incidence from the source as shown in Fig. 5.  $R$  is the distance between the source and the sensor, and  $\gamma$  is the direction cosine of  $r$ . The moment tensor  $m_{pq}$  can be represented by using the normal  $n$  to crack surface and direction  $l$  of crack displacement in an isotropic material,

$$m_{pq} = \lambda l_k n_k \delta_{pq} + \mu (l_p n_q + l_q n_p), \quad (4)$$

where  $\lambda$  and  $\mu$  are Lamé constants.

When elastic wave due to one AE event is detected at more than six sensors, the parameters concerned with source location and the amplitudes of the first motion are known. Hence, the independent six component of moment tensor can be determined by solving the simultaneous equations of Eq. 3 at each observation point.

Information about crack kinematics can be obtained from the eigenvalue analysis of the moment tensor. The eigenvalues,  $E_n$  and the eigen vectors,  $e_n$  are determined from Eq. 4,

$$\begin{aligned}
m_{pq}[e_1 \ e_2 \ e_3] &= \begin{bmatrix} E_1 & 0 \\ & E_2 \\ 0 & & E_3 \end{bmatrix} [e_1 \ e_2 \ e_3] \\
&= \begin{bmatrix} \frac{l_k n_k}{1-2\nu} + 1 & & 0 \\ & 2\nu \frac{l_k n_k}{1-2\nu} & \\ 0 & & \frac{l_k n_k}{1-2\nu} - 1 \end{bmatrix} [l + n \ l \times n \ l - n]
\end{aligned} \tag{5}$$

Note that all vectors are normalized in the calculation. Making reference to Fig. 6, original magnitudes of the vectors can be reproduced from the following equations,

$$\varepsilon_1 = \sqrt{2 + 2l_k n_k} \cdot e_1, \tag{6}$$

$$\varepsilon_3 = \sqrt{2 - 2l_k n_k} \cdot e_3, \tag{7}$$

$$l_k n_k = (E_1 + E_3 - 2E_2)/(E_1 - E_3). \tag{8}$$

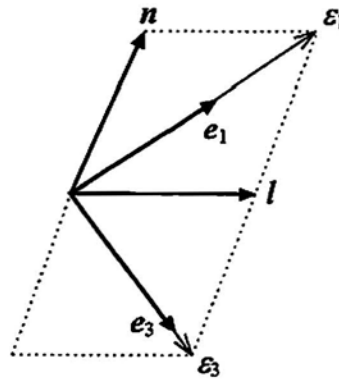


Figure 6. Crack orientations and eigen vectors of moment tensor

Thus, the direction of the normal  $n$  to the crack surface and the direction  $l$  of the crack motion can be recovered,

$$l = (\varepsilon_1 + \varepsilon_3)/2, \tag{9}$$

$$n = (\varepsilon_1 - \varepsilon_3)/2. \tag{10}$$

A quantitative classification of the crack type into shear mode, tensile mode and mixed mode is developed. The eigenvalues of the moment tensor are decomposed into a shear component, a deviatoric component (CLVD) and a hydrostatic component [5]. These components are given in Fig. 7. AE sources consist generally of a mixed mode with tensile and shear components. Setting the ratio of shear component as  $X$ , that of CLVD component as  $Y$  and that of hydrostatic component as  $Z$  with respect to the maximum eigenvalue of the moment tensor, all eigenvalues

are uniquely decomposed,

$$\begin{cases} 1.0 = X + Y + Z \\ E_2 / E_1 = -0.5Y + Z \\ E_3 / E_1 = -X - 0.5Y + Z \end{cases} \quad (11)$$

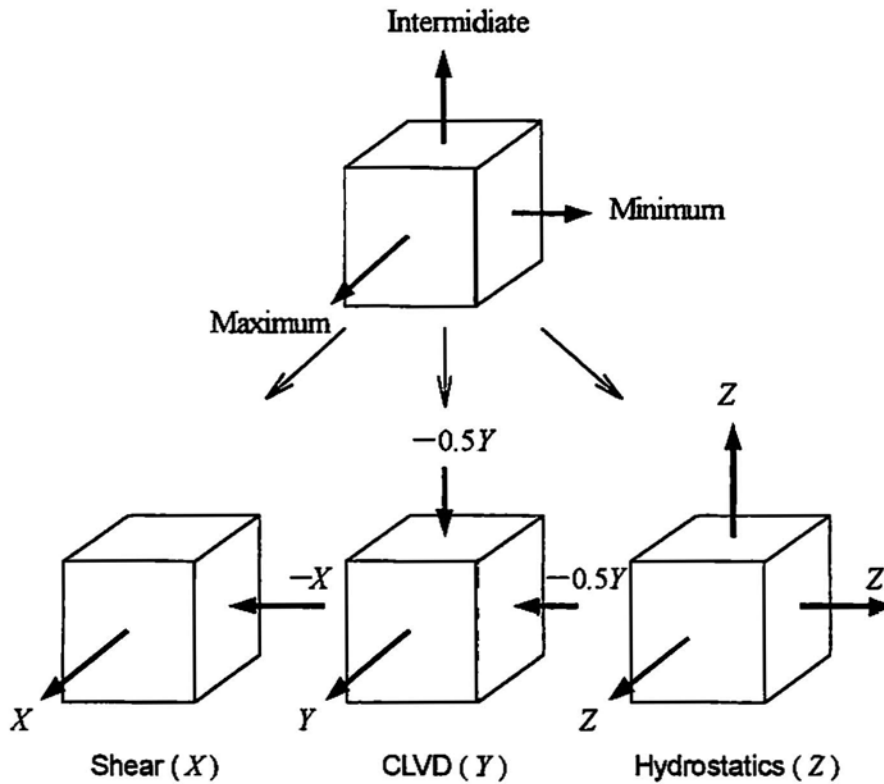


Figure 7. Eigenvalue decomposition of the moment tensor

In the case that the moment tensor components are determined from detected AE waveforms, information on locations, types and directions of cracks is determined by a SiGMA procedure of AE sources. The experimental verification of this procedure in two-dimensional problem has already reported [6].

Furthermore, confirmation of the SiGMA procedure solutions is conducted by a post analysis [7]. When a moment tensor and a location of an AE source are known, the first portion of the elastic wave at the observation point can be simulated by Eq. 2. As the verification, the SiGMA solutions determined from the detected AE waveforms are compared with those calculated from the simulated waves. Then, poor solutions are discarded.

### DAMAGE PROCESS OBSERVATION

The analyzed results in the pre-loading test are shown in Figs. 8 and 9. An arrow symbol indicates an AE source classified into a tensile crack of which shear component ratio  $X$  is smaller

than 30 %. The direction of the arrow directs the crack opening direction. In contrast, a cross symbol indicates a shear-type AE source or a mixed-mode AE source of which shear component ratio  $X$  is greater than 30 %. Each line directs either the crack normal  $n$  or crack displacement  $l$ . The dotted lines and the broken lines show the observed visible crack on the front side (dotted lines) and the rear side (broken lines).

The difference of damage degree resulting from the shape of reinforcement is clearly observed. The visible cracks propagate a little and a few of micro-cracks are produced at the tip of notch in Type A (reinforced by deformed steel bar). In contrast, the visible many cracks grow and almost reach the top of the specimen in Type B (reinforced by round steel bar). The micro-cracks (AE sources) are widely distributed around the visible cracks. It could be concluded that Type B is already damaged considerably at this step.

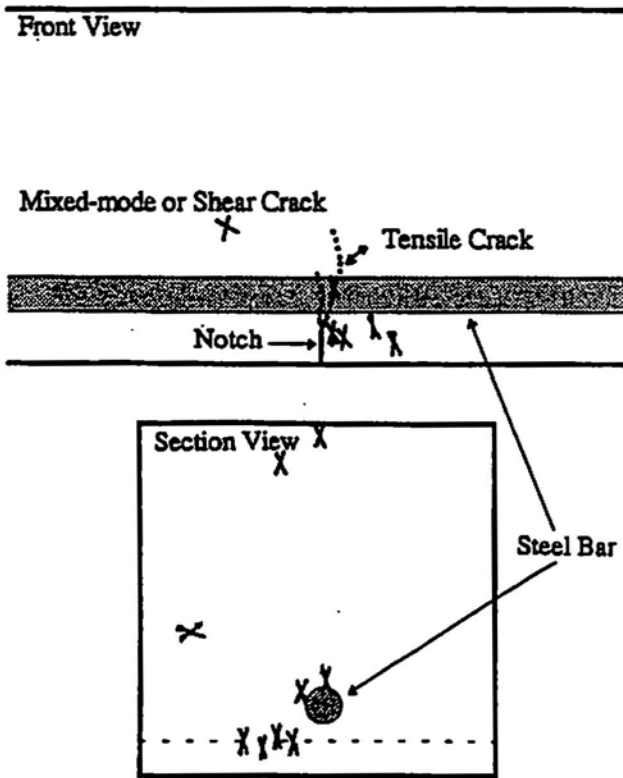


Figure 8. Results of Type A at pre-loading

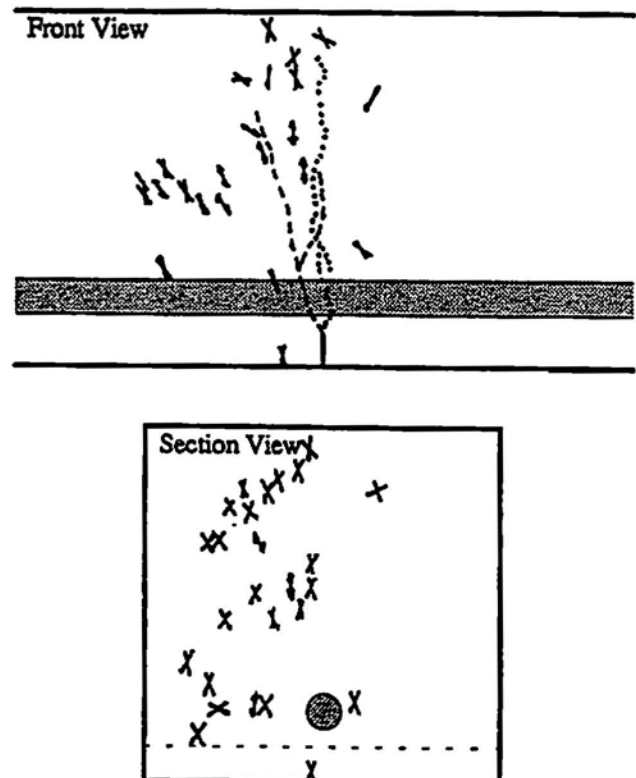


Figure 9. Results of Type B at pre-loading

Results under the cyclic loading test are shown in Figs. 10, 11, 12 and 13. Until the 15th loading, micro-cracks are mainly generated in the compressive stress zone at the upper in Type A. Some micro-cracks are also created near the reinforcement, indicating the slipping off. In the case of Type A, most micro-cracks are generated along the visible cracks after the 15th loading. Thus, the deformed bar surely contributes to prevent from cracking.

In the case of Type B, before the 15th loading, further propagation of visible cracks is hardly observed. However some micro-cracks are scattered in the wide area. This means probably that the fracture process zone is spreading out step by step. At the final step in Fig. 13, the area, where the micro-cracks are generated, further spreads out.

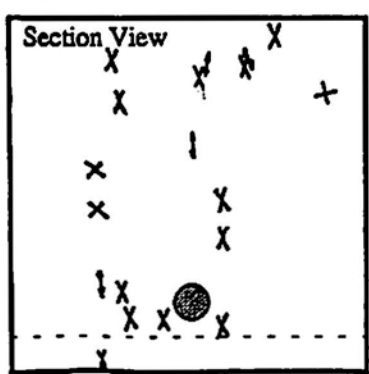


Figure 10. Results of Type A at 15th loading

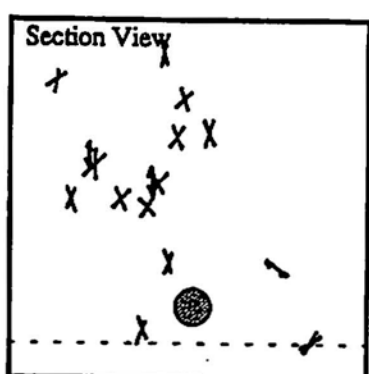
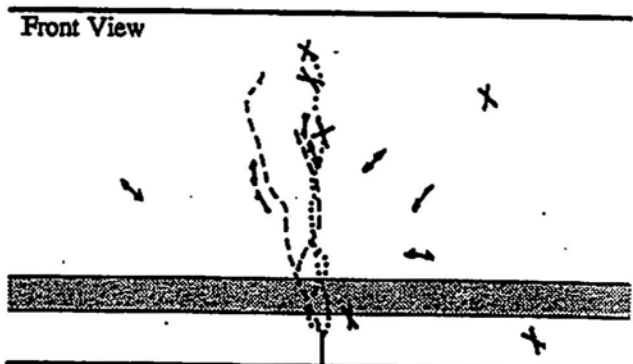


Figure 11. Results of Type B at 15th loading

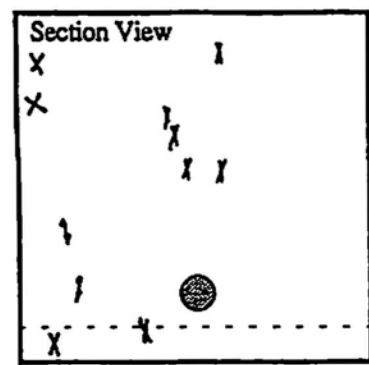
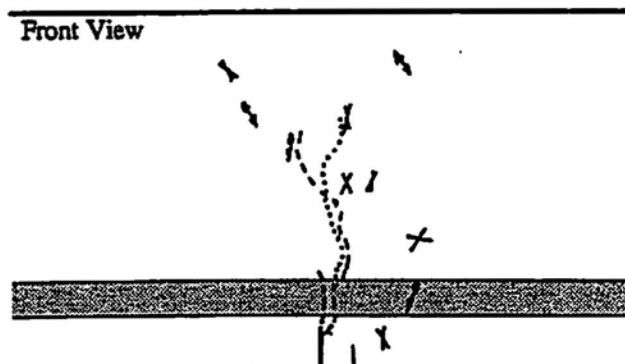


Figure 12. Results of Type A at 100th loading

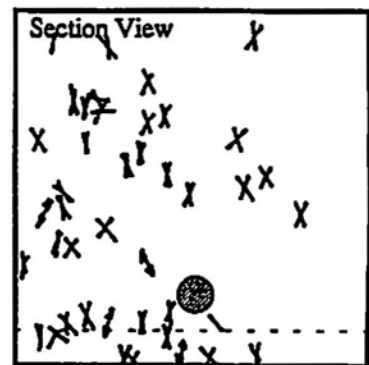
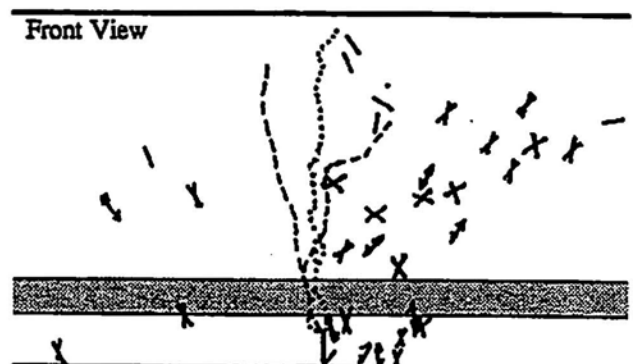


Figure 13. Results of Type B at 100th loading

## CONCLUSIONS

For the on-site investigation of civil structures, the inspection, which could be performed without stopping the service, is meaningful as well as non-destructive. Considering the advantages of AE technique, it is expected that AE technique is applicable to monitoring the damaging process and estimating the deteriorated degree in RC structures. To examine the applicability of AE waveform analysis using SiGMA procedure, cyclic bending tests of RC beams are carried out and dynamic AE measurement is performed. Then, the following conclusions are obtained:

- 1) The difference of damage degree resulting from the shape of reinforcement is clearly observed.
- 2) At early step (until 15th loading) in cyclic bending test, micro-cracks are mainly generated in the compressive stress zone at the upper in RC beam specimen containing a deformed steel bar (Type A). Some micro-cracks are also created near the reinforcement, indicating the slipping off. Most micro-cracks are generated along the visible cracks after that. Thus, the deformed bar surely contributes to prevent from cracking.
- 3) In the case of RC beam specimen containing a round steel bar (Type B), propagation of visible cracks is hardly observed at early step (before the 15th loading). However some micro-cracks are scattered in the wide area. This means probably that the fracture process zone is spreading out step by step. At the final step, the area, where the micro-cracks are generated, further spreads out.

## REFERENCES

1. M. Ohtsu, "The History and Development of Acoustic Emission in Concrete Engineering", *Concrete Library of JSCE*, No. 25 (1995)
2. S. Yuyama, T. Okamoto, M. Shigeishi and M. Ohtsu, "Quantitative Evaluation and Visualization of Cracking Process in Reinforced Concrete by a Moment Tensor Analysis of AE", *Material Evaluation*, Vol. 53, No. 6, pp. 751-756 (1995)
3. M. Ohtsu and K. Ono, "A Generalized Theory of Acoustic Emission and Green's Functions in a Half Space", *Journal of AE*, Vol. 3, No. 1, pp. 124-133 (1984)
4. M. Ohtsu, "Determination of Crack Orientation by Acoustic Emission", *Material Evaluation*, Vol. 45, No. 9, pp. 1070-1075 (1987)
5. L. Knopoff and M. J. Randall, "The Compensated Linear Vector Dipole: A Possible Mechanism for Deep Earthquakes", *Journal of Geophysical Research*, Vol. 75, No. 26, pp. 4957-4963 (1970)
6. M. Shigeishi and M. Ohtsu, "Observation of Mixed-Mode Fracture Mechanics by SiGMA-2D", *Journal of Acoustic Emission*, Vol. 11, No. 4, pp. 57-63 (1994)
7. M. Ohtsu, K. Arao and S. Yuyama, "Post-Analysis of SiGMA Solutions for Error Estimation in Reinforced Concrete Members", *Progress in Acoustic Emission VII*, pp. 411-416 (1994)

# SPECTRAL RESPONSE AND ACOUSTIC EMISSION OF REINFORCED CONCRETE MEMBERS UNDER FATIGUE BENDING

Yasunori Sakata<sup>1</sup> and Masayasu Ohtsu<sup>2</sup>

- <sup>1</sup> Faculty of Engineering, Department of  
Civil Engineering, Kyushu-Tokai University  
9-1-1 Toroku, Kumamoto 862, Japan
- <sup>2</sup> Faculty of Engineering, Department of Architecture  
and Civil Engineering, Kumamoto University  
2-39-1 Kurokami, Kumamoto 860, Japan

## ABSTRACT

Durability of concrete structures is an important problem in concrete engineering. Nondestructive testing to estimate defects in concrete structures is desired to maintain their durability. The reinforced concrete (RC) structures subjected to fatigue bending is known to gradually deteriorate for a long term.

Several nondestructive testings are applied to estimate the defects in concrete structures. Only one method, however, could not evaluate readily the deterioration degree, because the phenomenon is very complicated. Thus, the combined method seems to be promising to estimate the deterioration degree of RC structures subjected to fatigue.

In this paper, the method to estimate the deterioration degree of RC members under fatigue bending is studied experimentally, by using ultrasonic spectroscopy and acoustic emission (AE) method. The results show that both methods are useful and the combined method is promising to estimate the deterioration degree of RC members under fatigue bending.

## INTRODUCTION

Conventionally, concrete structures are considered to be durable. But, some concrete structures recently arise very fast deterioration due to salt attack, alkali-aggregate

reaction, freezing and thawing, fatigue, and so forth. Therefore, inspection of these concrete structures is so important as to maintain the durability. To estimate the defects and the durability of concrete structures, non-destructive testing methods<sup>1)</sup> have been developed. There are the ultrasonic velocity method, the ultrasonic spectroscopy and the impact echo method, the acoustic emission, the infrared thermography, the radar, the half cell potential, the X-ray and the  $\gamma$ -ray. However, the estimation of the deterioration degree of structures under fatigue process is not easy. Because any single method is directly effective, a combined method is to be developed. Thus, tests of RC beam subject to fatigue bending are performed by using the ultrasonic spectroscopy<sup>2), 3)</sup> and the acoustic emission method.<sup>5)</sup>

### MEASURING SYSTEM

A measuring system<sup>2)</sup> to obtain spectral responses is shown in Fig.1. Sinusoidal sweep-mode signals generated by a signal generator are driven into a transmitter through an amplifier. These signals are converted into elastic waves that propagate through a specimen. Arriving at a receiver, elastic waves are converted again into electric signals. The signals are monitored through a preamplifier by an oscilloscope and stored in a digital recorder. Transducers employed for both a transmitter and a receiver are AE sensors of broad band type with 1 MHz resonance frequency. The system has a smooth and flat response in the low frequency range(See Fig.3). The sensitivity below 10 kHz is fairly low. The amplitude scales of the spectral responses are relative, because the amplification is adjusted to keep spectral responses not saturated in the measuring scale. For AE measurement, a system consisting of AE sensor, pre-amplifier, and discriminator is employed. For the location of AE events, two sensors are applied.

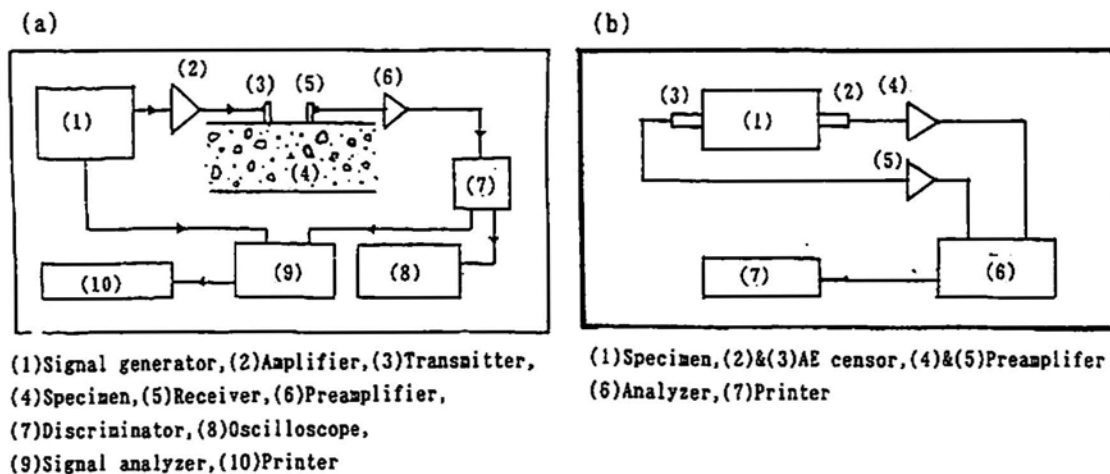
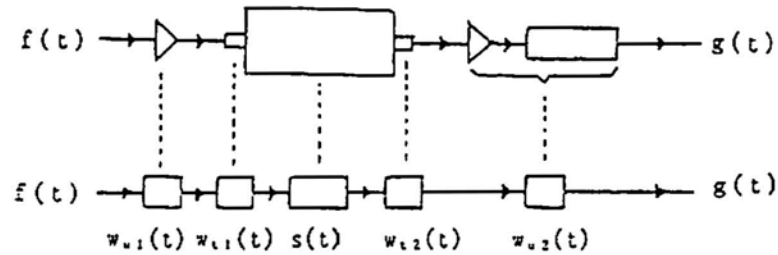


Fig.1 Measuring system for spectral responses (a) and acoustic emission (b).



$f(t)$ : Incident wave due to signal-generator  
 $w_{u1}(t)$ : Transfer function of the amplifier  
 $w_{t1}(t)$ : Transfer function of the transmitter  
 $s(t)$ : Transfer function of the specimen  
 $w_{r2}(t)$ : Transfer function of the receiver  
 $w_{u2}(t)$ : Transfer function of the pre-amplifier and discriminator  
 $g(t)$ : Detected wave

Fig.2 Transmission path of ultrasonic waves and corresponding transfer functions

### THEORY ON SPECTRAL RESPONSE<sup>2)</sup>

On the basis of the linear system theory, the measuring system is summarized as shown in Fig.2. In the time domain it is represented as,

$$g(t) = f(t) * w_{u1}(t) * w_{t1}(t) * s(t) * w_{r2}(t) * w_{u2}(t), \quad (1)$$

where a notation \* means the convolution integral. All transfer functions are denoted in Fig.2. The effect of a coupling agent is included in  $w_{t1}(t)$  and  $w_{r2}(t)$ . Response functions  $G(f)$ ,  $F(f)$ ,  $W_{u1}(f)$ ,  $W_{t1}(f)$ ,  $S(f)$ ,  $W_{r2}(f)$  and  $W_{u2}(f)$  are Fourier transforms of  $g(t)$ ,  $f(t)$ ,  $w_{u1}(t)$ ,  $w_{t1}(t)$ ,  $s(t)$ ,  $w_{r2}(t)$ , and  $w_{u2}(t)$ , respectively. Then Eq.1 is transformed into the frequency domain.

$$G(f) = F(f) \cdot W_{u1}(f) \cdot W_{t1}(f) \cdot S(f) \cdot W_{r2}(f) \cdot W_{u2}(f). \quad (2)$$

The aim of this research is to obtain specimen response  $S(f)$ . To determine  $S(f)$  from  $G(f)$ ,  $G(f)$  must be calibrated by  $G_0(f)$ .

$$S(f) = G(f) / G_0(f) \quad (3)$$

$$\text{where } G_0(f) = F(f) \cdot W_{u1}(f) \cdot W_{t1}(f) \cdot W_{r2}(f) \cdot W_{u2}(f). \quad (4)$$

Examples of the response functions  $G(f)$ ,  $G_0(f)$  and  $S(f)$  are shown in Fig.3, which was obtained from a plain concrete specimen.  $G_0(f)$  has a fairly smooth response over the frequency range, while  $G(f)$  has particular peak frequencies. As a result, spectral

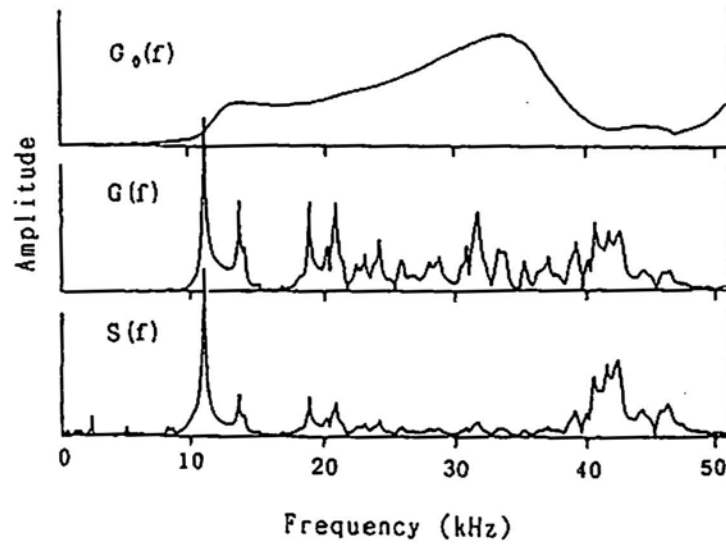


Fig.3 Response function  $G(f)$ ,  $G_o(f)$  and  $S(f)$ .

response  $S(f)$  is not much different from  $G(f)$ . Thus, ultrasonic spectral responses of concrete members are discussed only in term of  $G(f)$ .

### EQUIVALENCE BETWEEN SPECTRAL RESPONSE AND FOURIER SPECTRUM

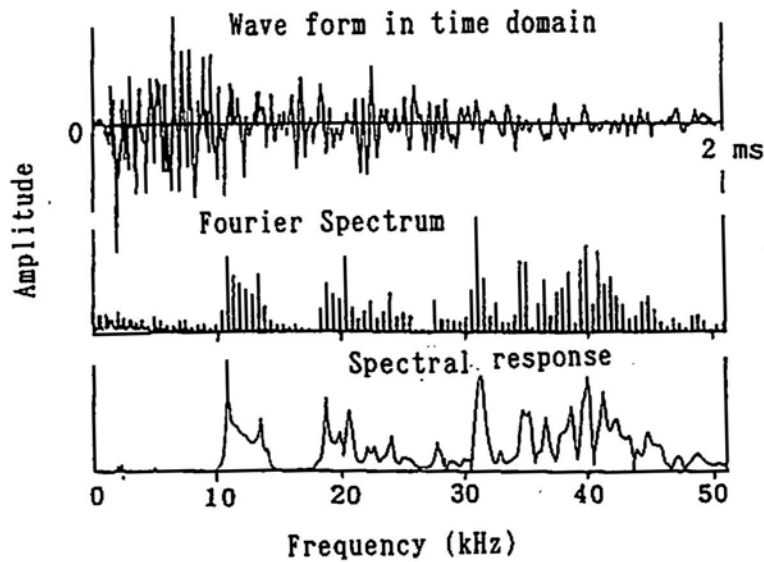


Fig.4 Comparison between Fourier spectrum due to impulse input and spectral response by sweep-mode input.

Sinusoidal signals of sweep-mode and constant amplitude are driven from a signal generator. An output of a time-amplitude curve is referred to as a spectral response. The curve is theoretically equivalent to the Fourier spectrum due to the impulse signal. In eq.1, in the case of  $f(t)$  equal to the delta function, Fourier transform  $F(f)$  becomes constant. A comparison between the spectral response obtained by the sweep-mode input and Fourier spectrum by an impulse are shown in Fig.4. In this case, the spectral response and Fourier spectrum are measured for the range 0 ~ 51.2 kHz. It is known that the spectral response by the sweep-mode input is effected by the duration time of the sweep-time. To reduce the effect of sweep-time, the sweep-time must be set longer than 1 second<sup>2)</sup>. In this experiment, the duration time to measure the spectral responses is 10 seconds.

### SUMMARY OF EXPERIMENT<sup>2)</sup>

The size of specimens is shown in Fig.5. The specimen of dimension 15 x 20 x 120 cm is reinforced with steel bar of 13 mm diameter (SD295). Stirrup bars are used of 4 mm diameter with 10 cm spacing. For concrete, the maximum size of coarse aggregate is 25 mm. Water-cement ratio W/C is 60 %. The strength of concrete is 26.5 MPa. Under loading, the one-dimensional AE location was conducted. Spectral responses were measured at both the compressive side and the tensile side. The ratios of cyclic loads to static failure load are 75, 80 and 85 %. AE and spectral responses were measured at particular cycles from 0 to  $2.5 \times 10^6$  cycles.

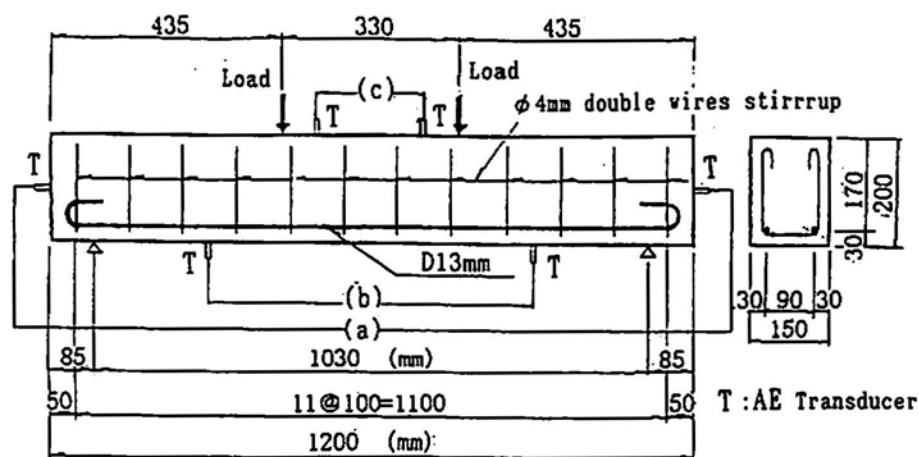


Fig.5 A sketch of the specimen and the sensor arrangement.

## RESULTS AND DISCUSSION

The relationships between the load cycles and AE counts observed under loading at these cycle stages are shown in Fig.6. AE counts are normalized by the number observed at 1000 cycles. AE counts increase rapidly in the case of high load level while, in low load level, AE counts are gradually increasing. Those imply that the measuring of AE counts is available to estimate cyclic load level for the structures. In the distribution of AE location under cyclic loading process, more AE events are relatively generated near the principal cracks, although many AE events are observed in the whole region. This is because most principal cracks were generated at the earlier stage, and AE events due to friction between steel bar and concrete are continuously generated.

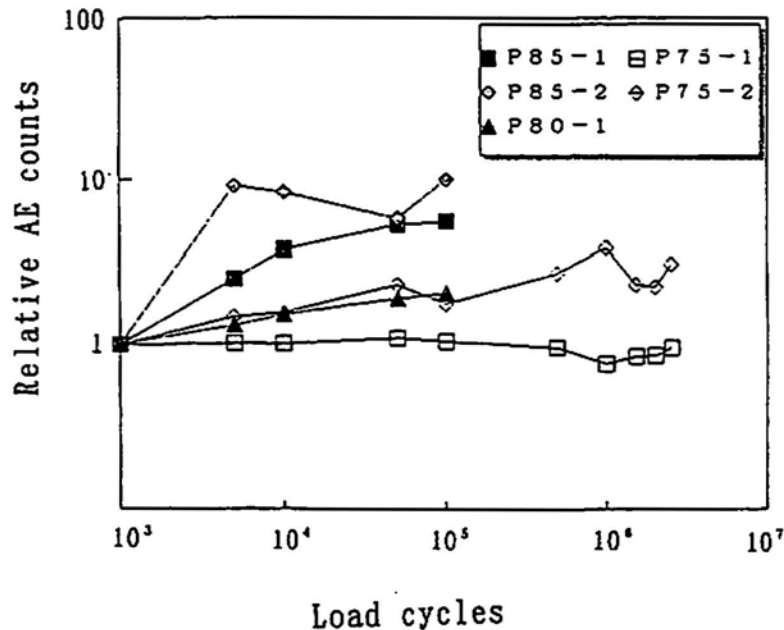


Fig.6 Relationships between AE counts and load cycles.

The examples of the amplitude distribution of AE events are shown in Fig.7. The cases of broken specimens near load cycles  $10^5$  are given in Fig.7 (a) and (b), and Fig.7(c) is the case of unbroken specimen even at  $2.5 \times 10^6$  cycles. In high load level, some types of amplitude distribution had been observed. In Fig.7(a), the amplitude distribution shifts to the high amplitude region with increasing of load cycles. The other side, in Fig.7(b), the amplitude distribution grow up with load cycles in all range. In the case of low load level, the amplitude distribution does not shift. It is considered that the deterioration of RC beam under cyclic load does not develop, and only AE events due to the friction between steel bar and concrete are generated.

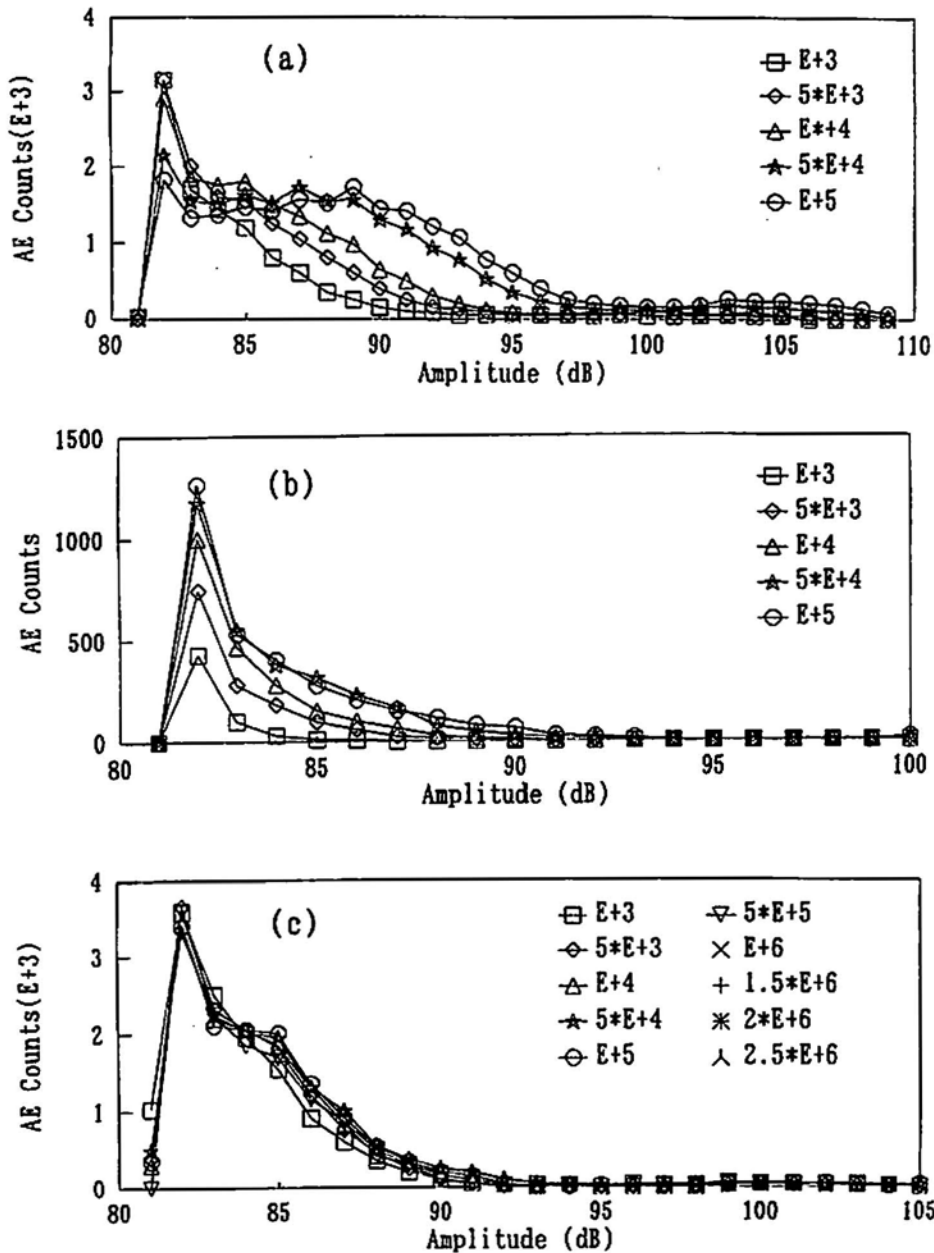


Fig.7 Amplitude distributions of AE waves with increase of load cycles.

Therefore, the monitoring of the amplitude distribution is also available to estimate the deterioration degree of the RC beam subjected to fatigue bending.

Spectral responses in the frequency range 1 ~ 400 kHz with increasing of load cycles obtained at compressive side of RC beam are shown in Fig.8. Before loading, the responses is dominant in high frequency range. The spectral responses in the high frequency zone gradually decrease with increase of load cycles. This is because concrete gradually deteriorate due to cyclic bending load. The tendency is particularly remarkable in the high frequency range. On the other hand, the shifts

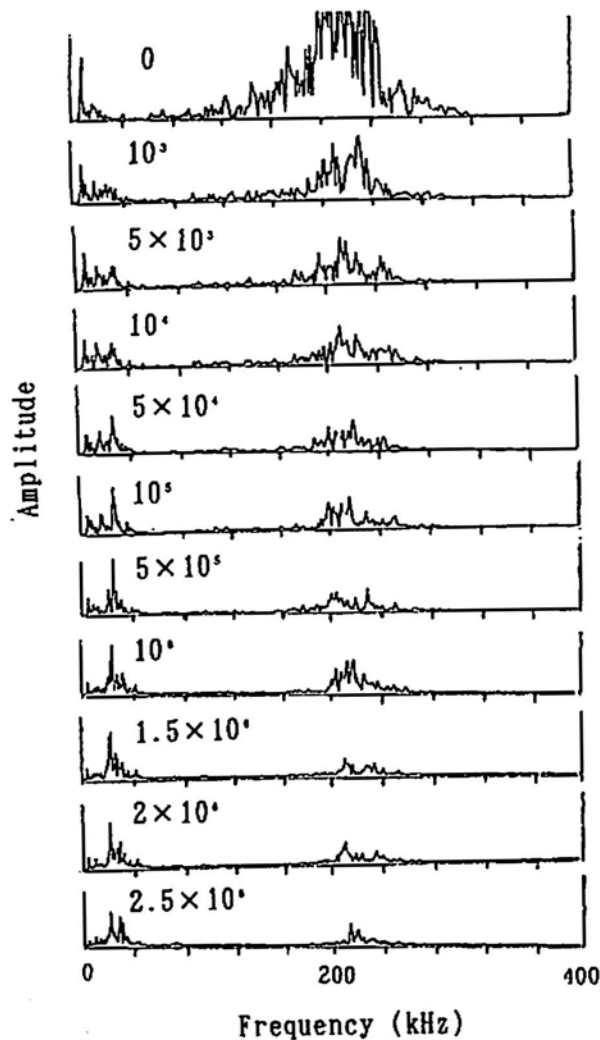


Fig.8 Spectral responses with increase of load cycles.

of peak frequencies with increase of load cycles were observed in the low frequency range under 20 kHz. Therefore, the shift of peak frequencies with increase of load cycles is applicable to estimate the deterioration degree of RC beam subjected to fatigue bending.

Relationships between accumulated ultrasonic energies obtained from integrated spectral responses and load cycles are shown in Fig.9. Relative ultrasonic energies obtained from integrated spectral responses in the frequency range 1 ~ 400 kHz after calibrating by the response curve of measuring system. In the case of high cyclic load level, the energies decrease all the way with increase of load cycles. On the other hand, in the case of low cyclic load level, the energies is decrease in fast stage, and then keep constant levels.

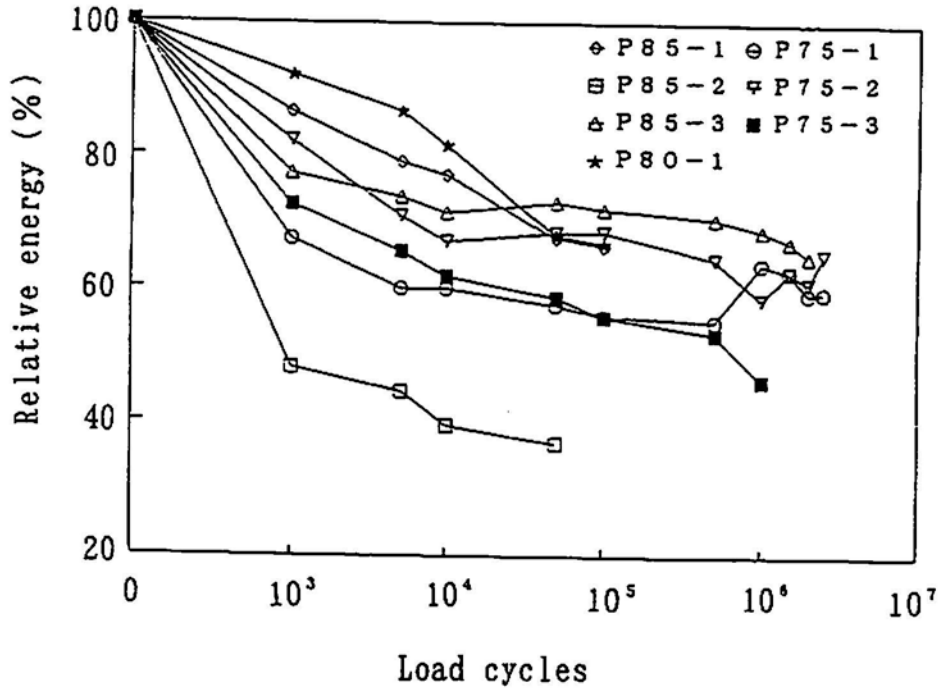


Fig.9 Relationships between relative energy and load cycles

### CONCLUSION

To estimate the deterioration degree of RC beam subjected to fatigue bending, the spectroscopy and the AE method are applied. The results show that the both methods are available to estimate the deterioration of RC beam subjected to fatigue bending. Thus, the combined method is in progress.

- 1) AE counts increase rapidly under the high cyclic load level with increase of load cycles, while, those in the low cyclic load level keep almost constant.
- 2) In the high cyclic load level, the amplitude distribution shift to the larger amplitude region with increase of load cycles. In the low cyclic load level, the distribution keep constant.
- 3) The spectral responses obtained from RC beam subjected to fatigue bending decrease gradually with increase of load cycles.
- 4) Using the ultrasonic energy, the variation of spectral responses is quantitatively estimated. In the high cyclic load level, ultrasonic energies decrease rapidly in all the way of fatigue bending. On the other hand, in the low cyclic load level, the energies decrease rapidly in the early stage, but then keep stable. Thus, the tendency could be available for evaluating the deterioration degree under fatigue.

## REFERENCES

1. Special issue on nondestructive testing of concrete, JCI, Concrete Journal, Vol.27, No.3, 1989.3
2. Y.Sakata and M.Ohtsu, Crack Evaluation in Concrete Members Based on Ultrasonic Spectroscopy, ACI Material Journal/Nov.-Dec.1995, pp.686-699
3. Y.Sakata and M.Ohtsu, Evaluation of Internal Defects in Concrete Structure by Ultrasonic Spectroscopy, Proceedings of JSCE, 1992.2, No.442, V-16, pp.71-80
4. Y.Sakata and M.Ohtsu, Spectral Responses and Acoustic Emission on RC-Member Subjected to Fatigue Bending, Proc.JCI, 1997, Vol.19, No.1, pp.1339-1344
5. M.Ohtsu, Rate Process Analysis of Acoustic Emission Activity in Core Test of Concrete, Proceedings of JECE, 1992.2, No.442/V-16, pp.211-218

## ACOUSTIC EMISSION BEHAVIOR DURING TENSILE DEFORMATION OF WELDED STEEL JOINTS

J. H. Huh, K. A. Lee and C. S. Lee

Center for Advanced Aerospace Materials,  
Pohang University of Science & Technology, Pohang 790-784, Korea

### ABSTRACT

An investigation has been carried out to study the acoustic emission (AE) behavior during tensile deformation of welded steel joints of low-carbon low alloy steel. The results indicate that the AE characteristics of the base metal is distinctly different from those of the heat affected zone (HAZ) and the weld metal. For the base metal consisting of ferrite-pearlite microstructure, most of the AE events are produced near the yield point, mainly due to the dislocation movements during the deformation. However, For the HAZ and the weld metal, a second AE peak with higher energy is evident after yielding, in addition to the AE peak occurring around the yield point. This second AE peak is attributed to the existence of martensite and, its amplitude is proportional to the volume fraction of the martensite. The sources of the second AE peak were the debonding of ferrite-martensite interfaces and the micro-cracking of brittle martensite plates, as rationalized by the microstructural and the frequency spectrum analysis.

### INTRODUCTION

The structural steels used for the construction of modern buildings have been developed to improve the strength, ductility and weldability, which enhances the resistance to the earthquakes and strong winds. In recent years the steels treated via the thermo-mechanically controlled process (TMCP) are especially attractive for their high strength and high toughness due to their fine grain sizes and low carbon contents [1]. During welding three zones are usually generated in the steel joints, namely, the base metal, the heat affected zone (HAZ) and the weld metal. Mechanical properties, especially the toughness [2], are seriously deteriorated in those regions with evidently coarsened grains (typically in the heat-affected zone (HAZ) and the weld metal) because of coarsened grains and transformed microstructures.

An acoustic emission (AE) method, one of the non-destructive evaluation techniques, widely utilized in recent decades to inspect the safety of atomic power plants, bridges and fuel tanks owing to its capability of real time monitoring [3]. Since AE is very sensitive to some specific micro-events in local areas, *e.g.* dislocation movement and multiplication, microcrack initiation and growth, and interfacial cracking, the AE method is useful in

identifying the origin, magnitude and distribution of the source that causes the characteristic AE events. Advances have been made in studies using the AE method in characterizing the deformation behavior [4-6], the interfacial debonding/cracking [7-8] and the micro-void coalescence or crack growth [9] in steels and other non-ferrous alloys. Although several studies have been made on the mechanical behavior of welds by use of AE [10-11], information is still lacking for a better understanding of the correlation between the AE behavior and microstructure in steel welds. This study is aimed to investigate the AE behavior during tensile deformation of welded steel joints and to correlate the AE behavior with the specific microstructures in the base metal, the HAZ and the weld metal.

## EXPERIMENTAL PROCEDURES

The TMCP steel (PILAC-BT33) used in this work was supplied by Pohang Iron and Steel Company in the form of 48mm thick plate. The nominal composition of this steel is shown in Table 1. A submerged arc welding (SAW) method was used to weld the steel joints, with an arc voltage of 36 V, a welding current of 980 A and a heat input of 92 kJ/cm. No heat-treatment was conducted after welding.

Table 1. Chemical composition of TMCP steel (PILAC-BT33).

Element	C	Si	Mn	P	S	Cr	Ti	Fe
wt %	0.14	0.23	1.23	0.0117	0.003	0.033	0.15	Bal.

The tensile sheet specimens were prepared according to the relevant ASTM code and they had a width of 6.25 mm, a thickness of 3 mm and a gauge length of 25 mm. The specimens of the welded joints were cut from the base metal, the HAZ and the weld metal regions, respectively, with the tensile axis in the rolling direction. To simulate the microstructural changes in the HAZ and the weld metal, another batch of samples were heated to 760 °C, 800 °C, 830 °C and 860 °C, respectively, for 1.5 hours and then quenched into water, to produce different amount of transformed martensite. They are hereafter referred to as HT<sub>1</sub>, HT<sub>2</sub>, HT<sub>3</sub> and HT<sub>4</sub>, respectively. The volume fraction of the martensite was measured using the Mössbauer analysis to be 26%, 43%, 61% and 82%, respectively, corresponding to the increase in heating temperatures given above. The tensile tests were conducted at room temperature using an Instron 1361 testing machine with a cross-head speed of 0.27 mm/min. Scanning electron microscopy was also utilized for fractographic analysis.

The AE analysis was carried out using the AE detector (AEDSP-32/16) made by PAC Co., with the sensor R15. The data processing was done under the condition of a pre-amplification of 40 dB plus a main amplification of 40 dB, giving a total amplification of 80 dB. The sensor was coupled to the polished jig by a thin layer of vacuum grease under a constant pressure. To remove the noise from actuator, *etc.*, a threshold amplitude was specified to be 30 dB, which was determined in the preliminary tests by using an oscilloscope. The jig pin was coated with a layer of grease to minimize the friction between the specimen and the jig. The AE data acquisition was realized by the MISTRAS 2001 program. A schematic diagram of the testing and acoustic emission recording system is shown in Fig. 1.

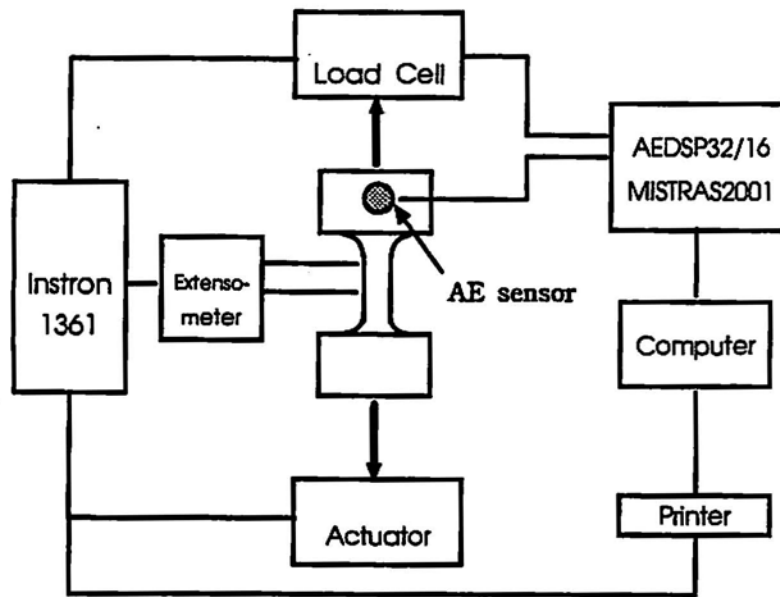


Fig. 1. Schematic diagram showing tensile and AE tests.

## RESULTS AND DISCUSSION

### Microstructures and tensile properties

The microstructures of the weld joints in different regions are shown in Fig. 2. The base metal is composed of ferrite and pearlite (Fig. 2a). The microstructure in the HAZ is characteristic of very coarse grains (Fig. 2b), which also includes the martensite-austenite (M-A) constituent, upper bainite and martensite formed during the heating-cooling cycle of welding. In the region of the weld metal, the microstructural constituents similar to those in the HAZ may also exist, but typically an area of coarse columnar microstructure is observed (Fig. 2c), which is chiefly due to the temperature gradient formed during the cooling process while being welded.



Fig. 2. Optical micrographs showing three different regions of welds ;  
(a) base metal (b) HAZ and (c) weld metal.

Table 2 summarizes fundamental tensile properties of specimens representing the base metal, the HAZ and the weld metal, respectively. For the specimens in the HAZ, the yield strength (Y.S.) is about 9% lower and the elongation is about 15% lower than the base metal, presumably due to the grain coarsening and the transformed constituents-induced embrittlement. In the weld metal, the elongation is about 10% lower than the base metal, which is probably caused by the structural inhomogeneity occurring in the coarse columnar solidification area or in the segregated central area.

Table 2. Tensile properties of the welds in different regions.

	Base metal	HAZ	Weld metal
Y.S. (Mpa)	421	383	402
U.T.S. (Mpa)	527	477	498
Elongation (%)	26.8	22.8	24.1

### The AE characteristics of the welds

As one of main AE parameters, the AE energy rate (frequently represented as a root-mean-square voltage) measured during the tensile tests is shown in Fig. 3 together with the corresponding tensile curve, for the specimens representative of different regions in the welded joint. In the base metal (Fig. 3a), most of the AE events occur around the yielding stage and the energy rate peak is detected around the yield point. By contrast, the AE behavior in the HAZ and the weld metal is quite different from that in the base metal. As is seen in Fig. 3 b - c, the AE events are evidenced not only around the yield point, but also in the post-yielding stage. A second and higher peak of the AE energy rate is detected in the post-yielding stage.

Fig. 4 shows the AE amplitude distribution for the tensile specimens taken from different regions of the welds. Only amplitudes above 30 dB are plotted due to the threshold set at this value. It is found that, for all three regions, most AE events occur around the yield point but with relatively low amplitudes (30-35 dB). For the specimens in the HAZ and the weld metal, however, the AE events with higher amplitudes (typically around 54 dB) are also evidenced (Fig. 4, b-c), in contrast to the case in the base metal in which the high-amplitude AE events are basically not detectable. Therefore the specimens in the HAZ and the weld metal are characteristic of the appearance of the second AE peak with high amplitudes occurring in the post-yielding stage.

It is found by Scruby [12] that the AE signals due to the dislocation movement reach to the maximum near the yield point and then gradually decrease. In view of similar AE features, the AE peak around the yield point for the present cases is also assumed to be related to the onset of large amount of dislocation movements. On the other hand, the 2<sup>nd</sup> AE peak has also been documented in some previous investigations[5, 7-8, 13-14] and its origin has been identified as the interaction of moving dislocations with precipitates [5], the serrated flow [14] and the debonding of second phase particles or inclusions or precipitates from the matrix [7-8, 13]. Considering the present microstructural constitution, it is highly probable that the 2<sup>nd</sup> AE peak appearing in the HAZ and the weld metal might be attributed to the existence of martensite. To examine this assumption, the AE investigations have further been conducted on another batch of TMCP steel samples heat-treated to result in different amount of martensite.

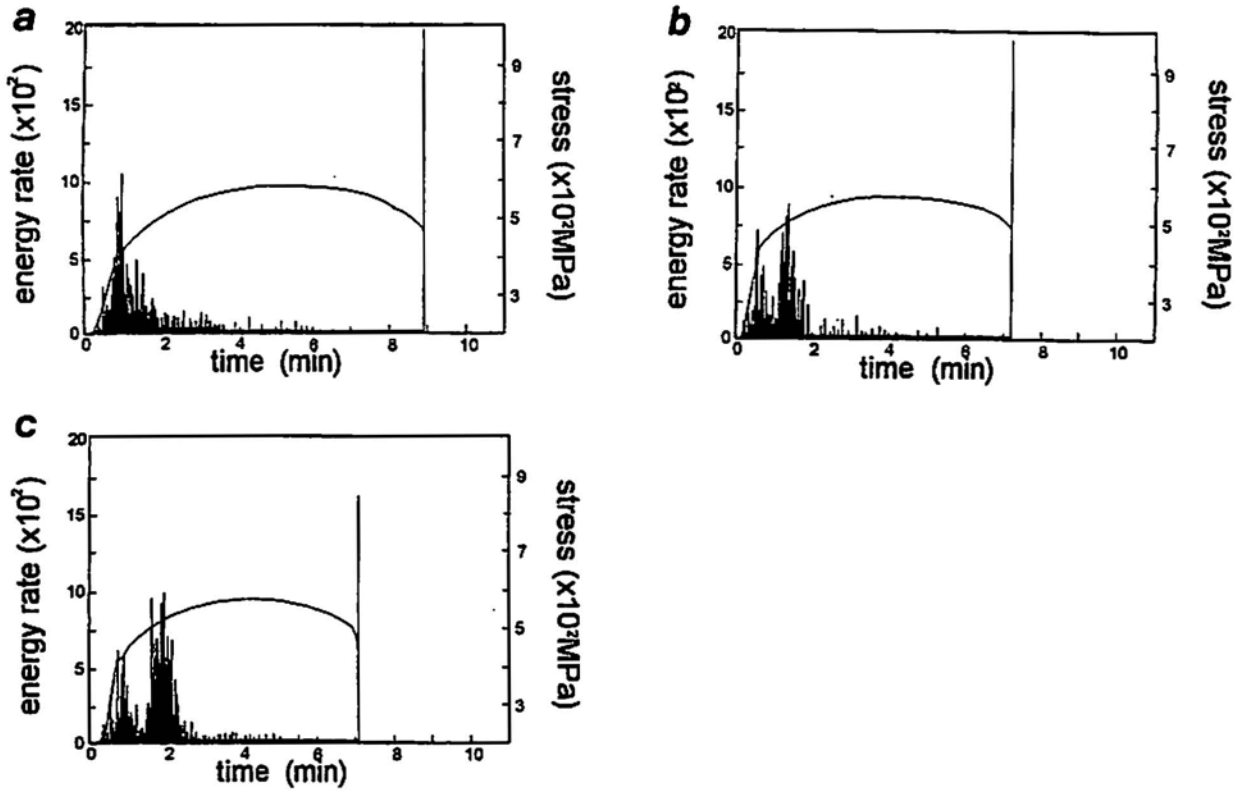


Fig. 3. AE energy rate produced during the tensile deformation of welds ;  
 (a) base metal (b) HAZ and (c) weld metal.

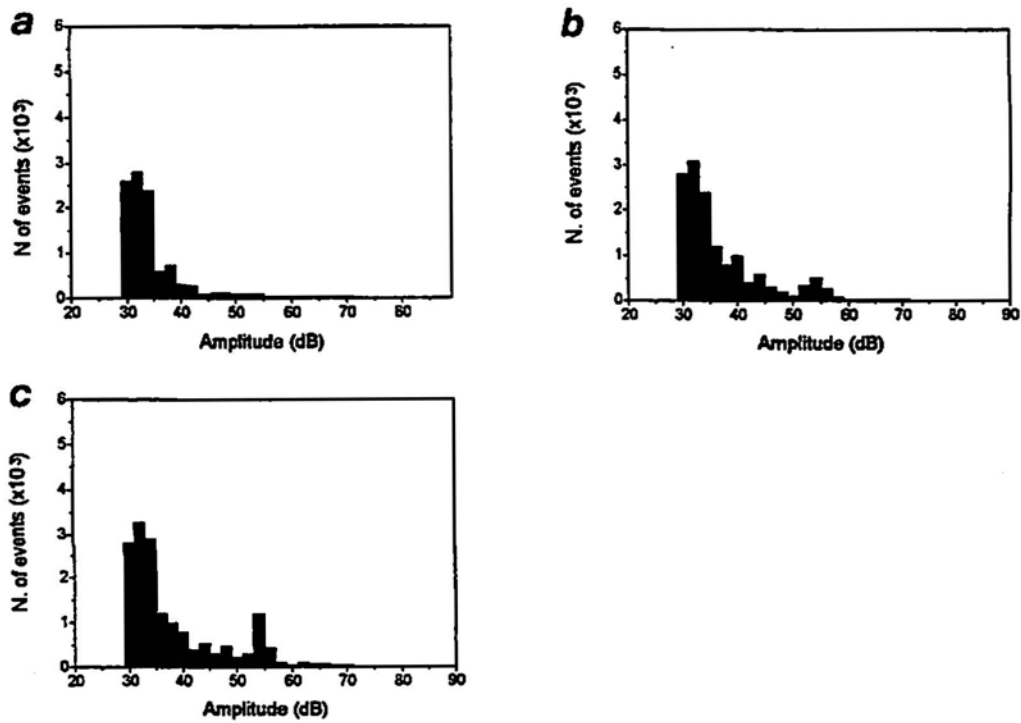


Fig. 4. AE amplitude distribution produced during the tensile deformation of welds ;  
 (a) base metal (b) HAZ and (c) weld metal.

The AE amplitude distribution during the tensile tests has been analyzed for the specimens with different martensite volume fractions of 26%, 43%, 61% and 82% and the results are given in Fig. 5. It is found that all the heat-treated specimens exhibit similar characteristics with the distribution of HAZ and weld metal (Fig. 4 *b-c*). As is indicated in this figure, in addition to the low-amplitude heavy AE activities occurring around the yield point, there are quite a lot of AE events occurring at amplitudes higher than 50 dB, characteristic of the second AE peak. The general trend for the second peak of the heat-treated specimens is that the amplitude and the number of events both increase with increasing the volume fraction of the martensite.

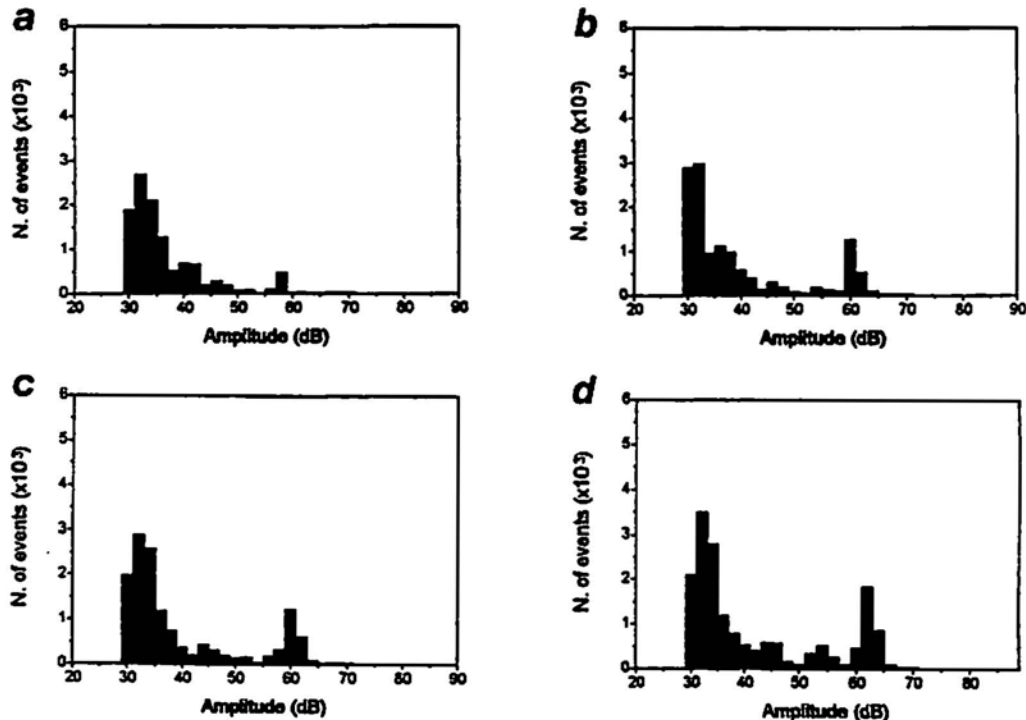


Fig. 5. AE amplitude distribution for heat-treated specimens ;  
(a) HT<sub>1</sub> (b) HT<sub>2</sub> (c) HT<sub>3</sub> and (d) HT<sub>4</sub>.

As an example, Fig. 6 shows the SEM micrographs taken from the tensile specimens of the heat-treated steel. It is evidenced that microcracks can be found both at the ferrite-martensite interface (Fig. 6*a*) and in the interior of martensite (Fig. 6*b*).

Combining with the AE characteristics shown above, it is justified that the occurrence of the 2<sup>nd</sup> AE peak is attributed to the existence of the martensite in which the micro-cracking events occur due to the ferrite-martensite interfacial debonding and/or the martensite plate cracking itself. This point is supported by a previous AE investigation on the carburized steels [15], which identifies the 2<sup>nd</sup> AE peak with higher amplitude as originated from the intergranular cracking.

The difference in the strength level between ferrite and martensite is assumed to be mainly responsible for the cracking *via* the ferrite-martensite interfacial debonding. Moreover, the residual stresses resulted from the inhomogeneous contraction due to cooling and expansion during martensitic transformation may also contribute to the interfacial cracking. Therefore the interface is highly potential for the initiation of microcracks and

hence, the AE from these regions possesses an evidently higher energy than in the case where just plastic deformation occurs.

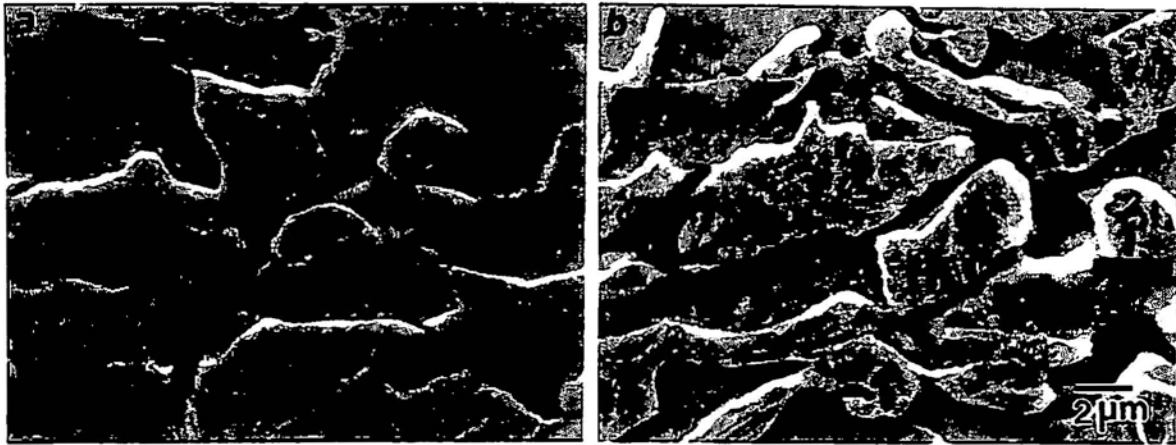


Fig. 6. SEM micrographs for the heat-treated specimens after tensile deformation. Cracks were observed (a) at interfaces between martensite and ferrite, and (b) inside the martensite phase.

#### Fast Fourier transformation (FFT) analysis

Using FFT method to analyze the frequency spectrum for the AE waves is important because different deformation or damage processes usually correspond to different frequency spectrums [9]. In the present study this method is employed to analyze the AE signals detected in the specific cases of the ferrite deformation and the ferrite-martensite interfacial cracking. The results are given in Fig. 7 as typical examples.

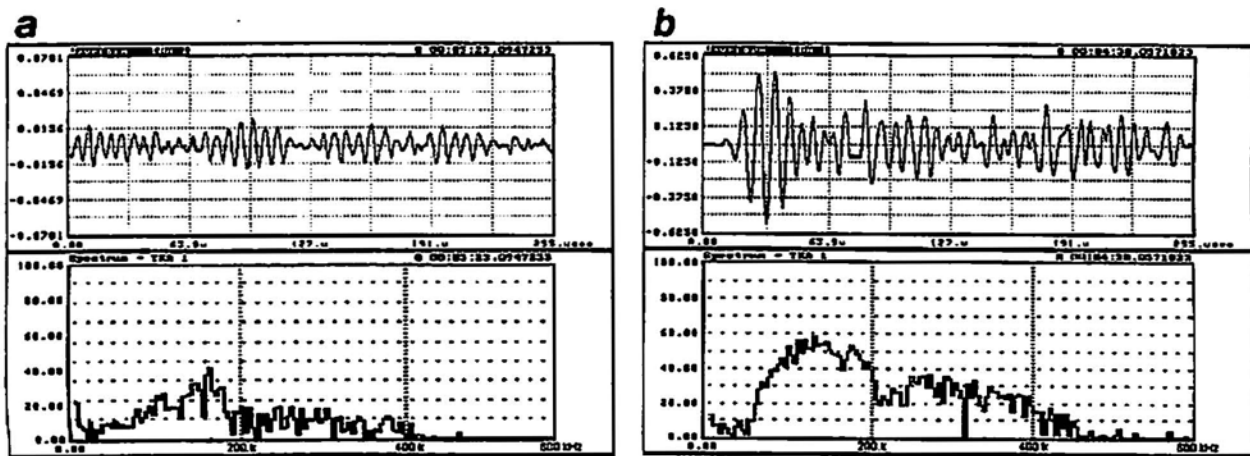


Fig. 7. AE waveform (upper part) and frequency spectrum (lower part) for (a) ferrite deformation and (b) cracking at F/M interfaces.

In the case of ferrite deformation (Fig. 7a), the AE wave is characterized by long rise time (rise time = the time required to reach the maximum amplitude) and low amplitude.

This is in accordance with the present fractographic observation that the base metal fractures in a typical ductile mode. The frequency corresponding to the peak is about 175 kHz. By contrast, in the case of the ferrite-martensite interfacial cracking (Fig. 7b), the AE wave is characterized by short rise time and high amplitude (approximately 5 - 10 times that of the former case). This is also in agreement with the fact that a brittle fracture occurs with a high energy releasing rate in the steel with the martensitic microstructure. The frequency for the peak is about 110 kHz, obviously lower than in the case of ferrite deformation. It is clarified that the results on the frequency spectrum analysis further confirm the arguments on the two distinct types of AE origins stated in earlier sections.

## CONCLUSIONS

(1) In the base metal region of the weld joint, most AE events are associated with the dislocation movement during the yielding and only one AE peak is found around the yield point. In the HAZ and the weld metal, in addition to the 1<sup>st</sup> AE peak around the yield point, a 2<sup>nd</sup> peak appears in the post-yielding stage and is related to the microcracking events at the ferrite-martensite interface and/or within the martensite.

(2) The AE behavior of the heat-treated steel with different martensite contents is also characterized by the existence of the 2<sup>nd</sup> AE peak. The AE amplitude and the number of events both increase as the volume fraction of martensite increases. Cracks are found both at the ferrite-martensite interface and in the interior of martensite.

(3) When the ferrite matrix deforms, the AE wave is characteristic of long rise time, low amplitude. However, when the ferrite-martensite interfacial cracking occurs, the AE wave is characteristic of short rise time and high amplitude.

## ACKNOWLEDGEMENT

The authors wish to acknowledge the financial support of the Pohang Iron & Steel Co. Ltd. (POSCO). The authors are also thankful to Dr. Hee-Don Jeong (RIST) for his helpful discussion of this work.

## REFERENCES

1. A. J. DeArdo, "Proc. of Intl. Conf. on Microalloying", Iron and Steel Society, Pittsburgh, pp. 15 (1995)
2. T. Haze, S. Aihara and H. Mabuchi, "Accelerated Cooling of Rolled Steel", TMS, Warrendale, (1986)
3. "Non-Destructive Testing Handbook, 2<sup>nd</sup> Edition", Vol. 5, American Society for Non-Destructive Testing, Columbus, (1981)
4. H. N. G. Wadley, C. B. Scruby, P. Lane and J. A. Hudson, "Influence of microstructure on acoustic emission during deformation and fracture of Fe-3.5Ni-0.21C steel", Met. Sci., Vol. 15 pp. 514-524 (1981)
5. C. B. Scruby, H. N. G. Wadley and K. L. Rusbridge, Mater. Sci. Eng., "Origin of acoustic emission in Al-Zn-Mg alloys II : Copper-containing quaternary alloys", Vol. 59, pp. 169-

183 (1983)

6. K. A. Lee and C. S. Lee, "Acoustic emission characteristics associated with microstructures and plate orientations of an Al-Li 8090 alloy", Mater. Sci. Eng. A, in print, (1997)
7. C. H. Heiple, S. H. Carpenter and M. Carr, J. Mater. Sci., 15, pp. 587 (1981)
8. S. M. Cousland and C. M. Scala, Mater. Sci. Eng., "Acoustic emission during the plastic deformation of aluminium alloys", Vol. 57, pp. 23-29 (1983)
9. B. Raj, B. B. Jha and P. Rodriguez, Acta Metall., "Frequency spectrum analysis of acoustic emission signal obtained during tensile deformation and fracture of an AISI 316type stainless steel", Vol. 37, pp. 2211-2215 (1989)
10. C. B. Scruby and K. A. Stacey, "Acoustic emission measurements on PWR welded material with inserted defects", J. of Acoustic Emission, Vol. 7, pp. 81-93 (1988)
11. P. G. Bentley, and M. J. Beesley, J. of Acoustic Emission, "Acoustic emission measurements on PWR weld material with inserted defects using advanced instrumentation", Vol. 7, pp. 59-79 (1988)
12. C. Scruby, H. Wadley and J. E. Sinclair, "The origin of acoustic emission during deformation of aluminum and aluminum-magnesium alloy", Phil. Mag., 44A, pp. 249 (1981)
13. M. Wu and S. H. Carpenter, J. Acoustic Emission, 11, pp. 5 (1983)
14. Y. Xu, Z. Zou and F. Du, "Relationship between the second acoustic emission peak and the serrated flow of aged Al-Zn-Mg-Cu alloy", Phys. Stat. Sol., A155, pp. 305-319 (1996)
15. B. Raj and T. Tayakumar, J. of Acoustic Emission, "Acoustic emission during tensile deformation and fracture in austenitic stainless steels", Vol. 7, S1-S12 (1988)

## **ACOUSTIC EMISSION SIGNAL ANALYSIS IN C/C COMPOSITES**

**Ja-Ho Koo, Byung-Nam Kim, Manabu Enoki and Teruo Kishi**

Research Center for Advanced Science and Technology, University of Tokyo,  
4-6-1 Komaba, Meguro-ku, Tokyo 153, Japan

### **ABSTRACT**

In the case of materials in which plane wave velocity varies along the direction of the propagation, satisfactory algorithm to locate acoustic emission (AE) source has to be developed. Therefore, for the first, we measured the wave velocity in C/C composites and made empirical equation for the relation between the direction and the velocity. Anisotropic location algorithm using this equation and the Successive Over Relaxation (SOR) method were used to find the position of AE source. Then, we study crack propagation mechanism of 2-D C/C composite by using AE method during the tensile loading of CT specimen. From these results we found that the effect of sub-bundle breaking mechanism is dominant than other mechanisms in 2D C/C composites with 8-harness satin structure and after maximum stress non-fractured bundles remained.

KEY WORD : AE, Anisotropic, Location, C/C composites

### **I . INTRODUCTION**

C/C composites have very high resistance of heat transfer, thermal shock and low specific gravity ( e.g.,  $2.25 \text{ g/cm}^3$  in the case of graphite single crystal). High strength and stiffness of C/C composites make them be an attractive material for aerospace industry.[1 - 4] However for the importance of usage, more high reliability is requested than other materials. On the purpose of making the reliability high, various methods are performed, for example, prediction of life time, measurement of weibull modulus and development of processing, nondestructive evaluation, etc. In these various methods nondestructive evaluation method can monitor the behavior of propagated or propagating cracks.[5]

In this study, 2D C/C composites with 8-harness satin structure has been examined by AE signal analysis that is one of the nondestructive evaluation methods. In the field of AE signal analysis, one of the important technique is calculating of location of the AE source. But, in the case of materials in which plane wave velocity varies along direction of the propagation,

satisfactory algorithm has not been developed yet. Therefore, for the first, we made empirical equation about the relation between direction and velocity and calculated 2-dimension location of AE source by using the equation and SOR method that had been used by Sato et al [6]. Then, we study crack propagation mechanism of 2-D C/C composite by using of AE method during the tensile loading of CT specimen.

## II . Two Dimensional Location in Anisotropic Medium

The longitudinal wave velocities in 2D C/C composites with 8-harness satin structure were measured from 0° to 45° in the interval of 5°. The results are shown in Fig. 1. Because this composites have 45° symmetry in the variation of wave velocity as shown in Fig. 2, only between 0° and 45° curve fitting was performed. The result equation is as following.

$$V = V_0 \left\{ 1 - a \cdot \exp\left(-\frac{b}{\theta^2}\right) \right\} \quad (1)$$

where  $\theta$  is the angle of the direction of propagation for the longitudinal wave,  $V$  is the longitudinal velocity of the direction ( $\theta$ ),  $V_0$  is the longitudinal velocity of the direction of fiber,  $a$  and  $b$  are constants.

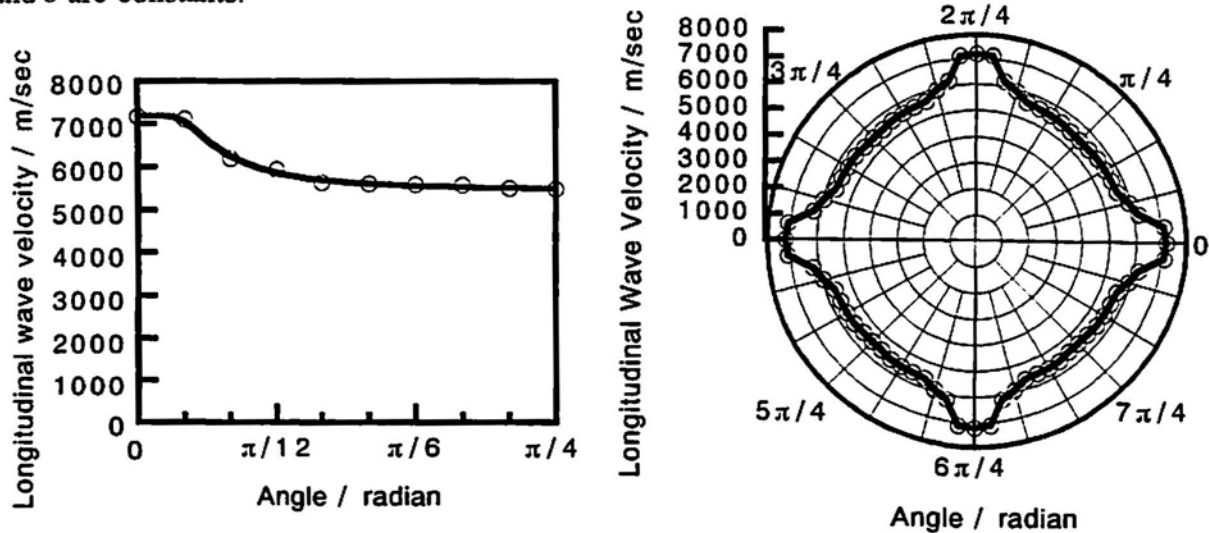


Fig.1 Relation between wave velocity and angle. Fig. 2 Symetry of wave velocity and angle.

The denotation for numerical analysis is as followings.  $(x, y)$  is location of AE source,  $t$  is time of AE occurrence,  $(X_i, Y_i)$  is location of  $i$ -th sensor,  $T_i$  is arrival time of first longitudinal wave to  $i$ -th sensor,  $t_i$  is arrival time of first longitudinal wave of  $i$ -th sensor,  $D_i$  is distance between  $(x, y)$  and  $(X_i, Y_i)$ ,  $V_i$  is longitudinal wave velocity in direction of between  $(x, y)$  and  $(X_i, Y_i)$ . For the first, if  $(x, y)$  and  $t$  are numerical approximated values,  $t_i$  becomes as following.

$$t_i = t + D_i / V_i \quad (2)$$

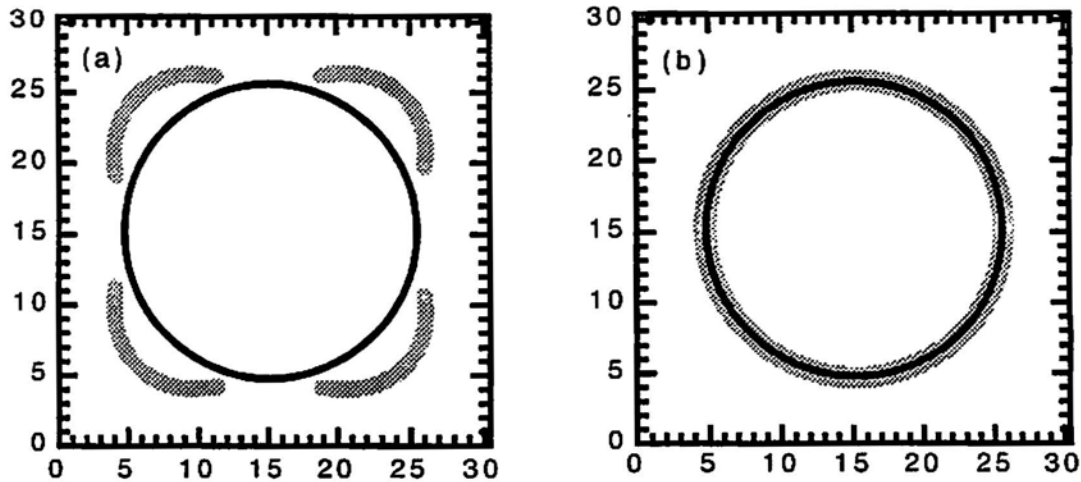


Fig.3 Simulation comparing (a)isotropic algorithm with (b)anisotropic algorithm ( dimension of medium is 30.4 x 30.4 mm, black is the position of AE sources, grey is the position of output ).

At this time, if the sum of square of  $(T_i - t_i)$  is larger than given error range, by using the successive over relaxation method  $t$ ,  $x$  and  $y$  are becomes  $t + \Delta t$ ,  $x + \Delta x$  and  $y + \Delta y$ . Then new value of  $t_i$  can be calculated from corrected  $t$ ,  $x$ ,  $y$ .

Fig. 3 is the result of comparing isotropic algorithm with anisotropic algorithm. If AE signal is generated on the black circle in the medium that has the same wave velocity distribution as shown in Fig. 2, each arrival time of the signal is different in four AE sensors. Fig. 3 (a) is the result of the case inputting the arrival time table to isotropic algorithm and Fig.3 (b) is the case inputting the arrival time table to anisotropic algorithm. Maximum error in (b) is 0.0164 mm. As this value is very small, we applied this anisotropic algorithm to practical CT specimen.

### III . FRACTURE MECHANISM OF 2-D C/C COMPOSITES

#### 1. Experimental Procedure

In order to apply the location evaluation method mentioned above, thin CT specimen (32 x 30 x 5, mm) of 2D C/C composites with 8-harness satin structure was selected. The length of notch was 22 mm. The kinds of specimen is four. The misorientation angles of the fiber on the notch are 0°,15°,30°,45° (to be called each by type 1, type 2, type 3, type 4 ). During tensile loading, load and COD were measured. AE signal was detected by using of AE analyzer(DCM140, JTT) with 4 AE sensors(M304A, Fuji Ceramics Co.). Two kinds of tests were performed. One of two tests is performed using the pre-amplifier with the gain of 11 dB and 54 dB.

#### 2. Results and Discussion

For type 1, in the case of using 54dB pre-amplifier as shown in Fig. 4 (a), too many large AE signals ( $> 4.5 \text{ V}$ ) were generated and saturated the limit of pre-amplifier capacity. The saturated AE signals are in the hashed range. In order to analyzing this area, 11dB pre-amplifier was used. The result is shown in Fig. 4 (b). When using 54dB pre-amplifier, it is supposed that AE signals ( $< 4.5 \text{ V}$ ) is due to matrix cracking, debonding and fiber pull-out but the other AE signals ( $> 4.5 \text{ V}$ ) is due to fiber breaking and sub-bundle breaking. When using 11dB pre-amplifier, it is supposed that AE signals ( $< 1.5 \text{ V}$ ) is due to fiber breaking and AE signals ( $>$

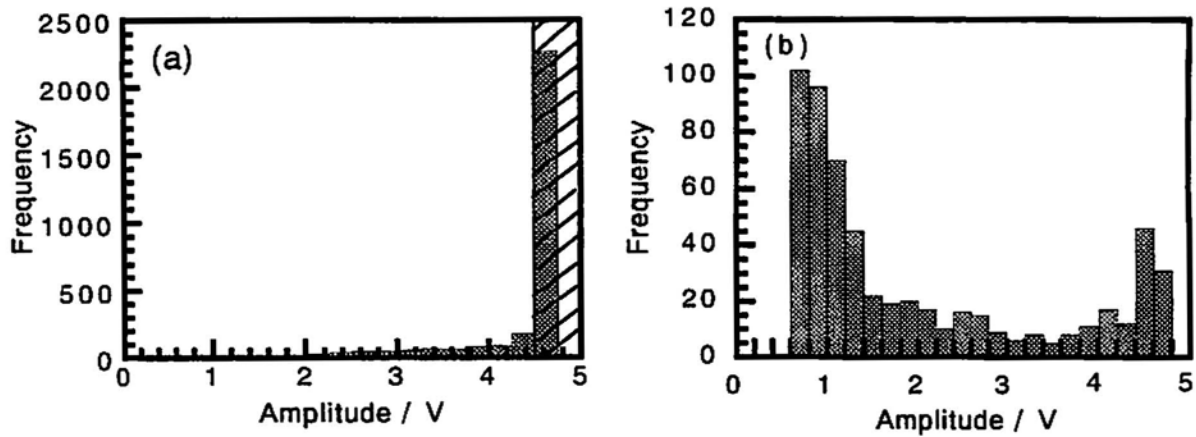


Fig. 4 AE Amplitude distribution ( (a) in the case using 54dB pre-amplifier, (b) in the case using 11dB pre-amplifier ).

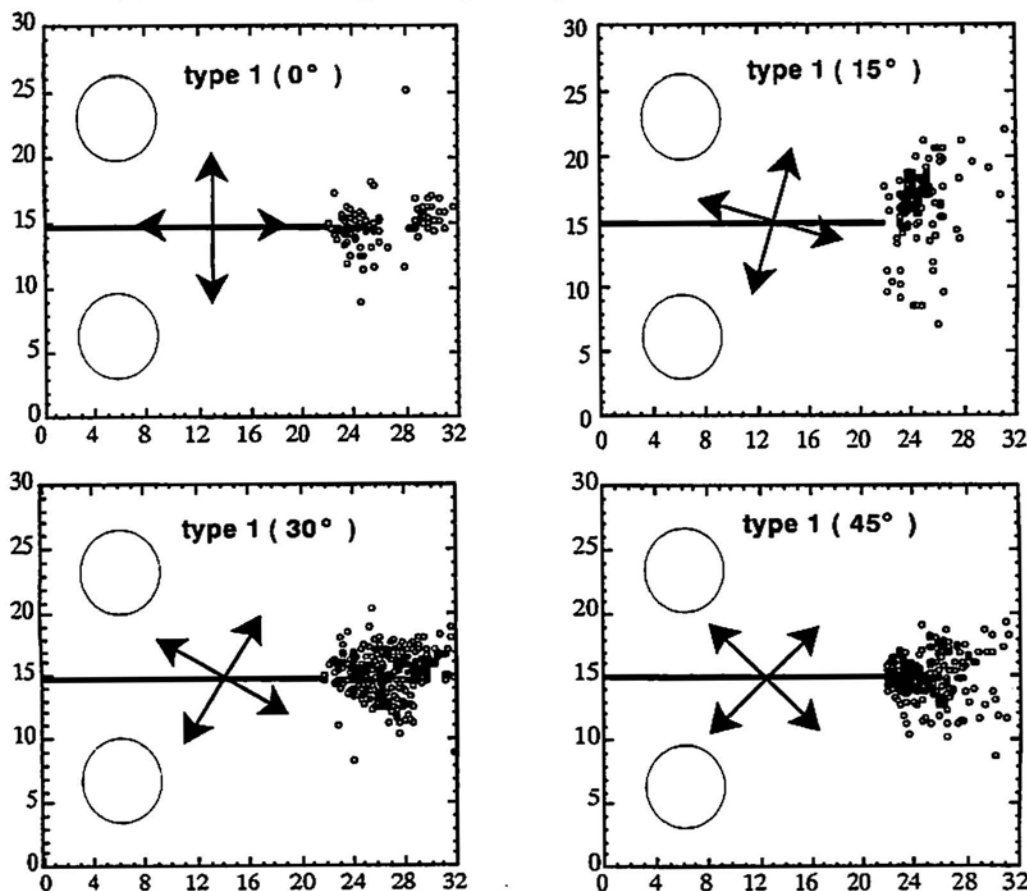


Fig. 5 Location of CT test ( arrow is the direction of the fiber ).

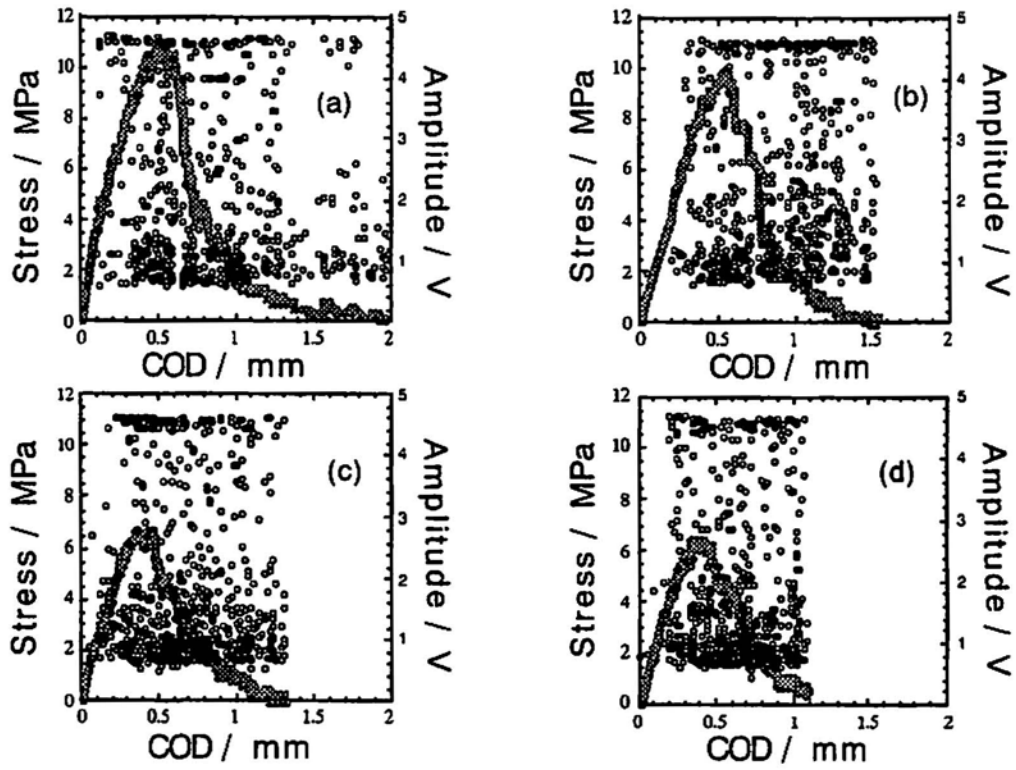


Fig. 6 Stress-COD curves and AE amplitude ; (a) type 1 (b) type 2 (c) type 3 (d) type 4.

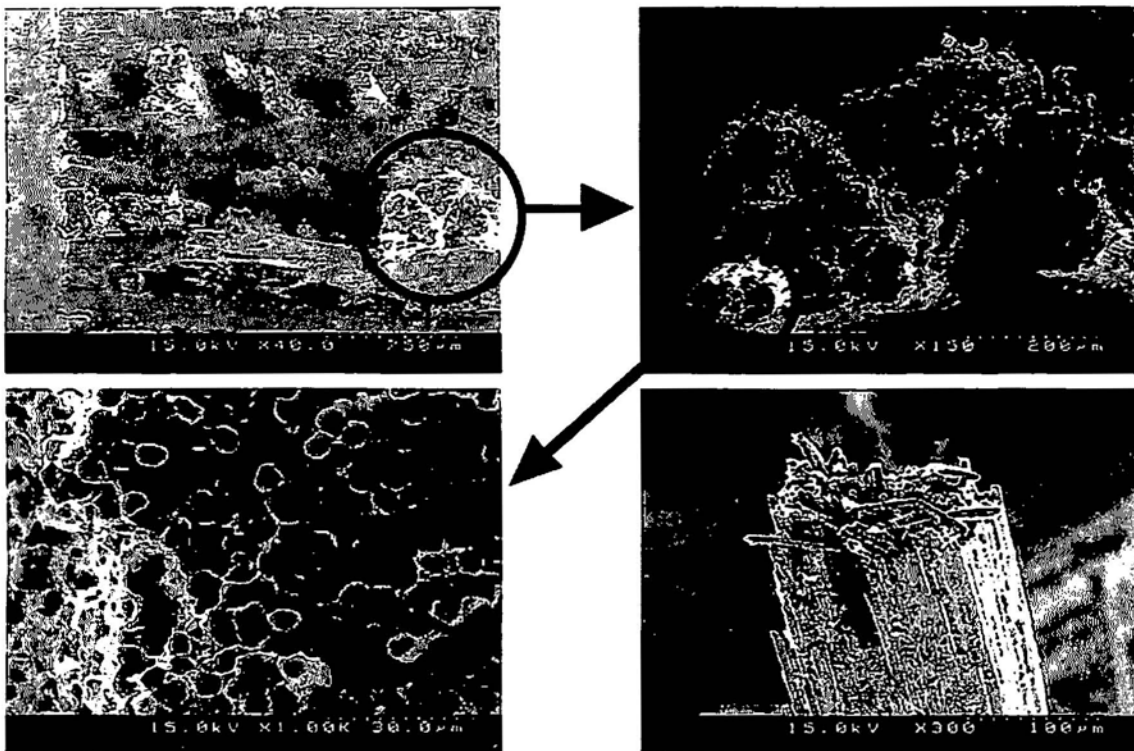


Fig.7 Fracture surfaces of CT specimen for type 1.

1.5 V and  $< 4.5$  V ) is due to sub-bundle breaking and AE signals ( $> 4.5$  V ) is due to saturated AE. Therefore, in order to analyze large AE signal, we used 11dB pre-amplifier in Fig. 5, Fig. 6 and Fig. 7.

Fig. 5 is the result of location using two dimensional anisotropic algorithm. Four types all show AE location in front of notch tip. Fig. 6 is the result of CT Test with AE analyzer. Type 1 has the highest maximum stress and type 4 has the lowest maximum stress. We did AE source characterization. The radius of source of large ( $> 4.5$  V ) AE signal was calculated by invers operation. The radius of a fiber is  $3.5\mu\text{m}$  but the result radius range is in about from  $50\mu\text{m}$  to  $200\mu\text{m}$ . The radius of sub-bundle shown in SEM photograph of Fig. 7 is also in that range.

#### IV. CONCLUSIONS

Two dimensional anisotropic location algorithm using empirical equation for wave velocity in C/C composites was developed to find the position of AE source. The propriety of application to practical materials was proved by the simulation checking the algorithm. The maximum error between the source position and the result position by anisotropic location algorithm was 0.0164 mm in anisotropic medium whose dimension was  $30.4 \times 30.4$  mm . In practical CT test, the good location result that showed the direction of fiber was obtained by the anisotropic algorithm. On the other hand we found the fact that the effect of sub-bundle ( the radius range is in about from  $50\mu\text{m}$  to  $200\mu\text{m}$  ) breaking mechanism on fracture is dominant than other mechanism in 2D C/C composites with 8-harness satin structure by AE source characterization and SEM observation.

#### REFERENCES

1. D. Belitskus, "Fiber and Whisker Reinforced Ceramics for Structural Applications", Marcel Dekker, Inc., pp. 315 (1993)
2. O.L.Blakslee, D.G.Proctor, E.J.Seldin, G.B.Spence and T.Wang, J.Appl.Phys., Vol. 41, 8, pp. 3373 (1979)
3. E.Fitzer and A.Gkogkidis, Prepr.Am.Chem.Soc.Div.Pet.Chem., Vol. 29, pp. 506 (1984)
4. B.Broquere, Proc.4th Int.Conf.SAMPE, pp. 279 (1984)
5. T. Kishi, A. Koma, Y. Komiya, H. Ohkushi, H. Tanoue, M. Ohtsuka, "Evaluation System of Materials", Tokyo Univ. Press (1987)
6. Y. Sato, K. Katsuyama, Mining and Preservation ,Vol. 31, No. 6, pp. 11 (1985)

# RECENT DEVELOPMENT IN ACOUSTIC EMISSION

Kanji Ono

Department of Materials Science and Engineering, Box 951595  
University of California, Los Angeles, California 90095-1595, USA  
e-mail: ono@ucla.edu

This review paper presents recent development in the field of acoustic emission (AE). The topics covered include AE source simulation analysis applied to composite samples, guided wave AE, pattern recognition analysis for AE signal discrimination, moment tensor analysis with application to concrete, and new generation AE instrumentation.

## 1. Introduction

Recently, Drouillard appraised the history of the first half century of acoustic emission (AE)<sup>(1)</sup>. AE field in the past 30 years has evolved from late 1960's main thrust of aerospace applications with special attention given to metal welds. In the 1970's, nuclear applications became the mainstay and composite applications started to emerge. The Three Miles Island accident stymied the nuclear applications, and composite applications of AE took off in the 1980's. The most recent trend appears to be the proliferation of faster digital instruments and the diversity of applications resulting from user-friendly AE instrumentation. General current summary of AE is given in Ono<sup>(2)</sup>.

I examined in 1994<sup>(3)</sup> the status of acoustic emission research and applications from papers collected by a database, known as INSPEC over the period of 1989 to 1993. In order to obtain an overall picture of AE studies, the titles and abstracts of about 1000 AE papers were evaluated. Selected papers were summarized to provide representative status of each segment of the field. Breakdown was: research (600 papers); applications (160 papers); signal detection, generation and processing (180 papers) and others (60 papers). It was noted that composite and ceramic materials were studied actively, but metals were researched just as much with emphasis on fracture and fatigue. Fewer applications papers were published, but certain areas had strong activities, as in signal detection and signal processing methods.

In preparation for this presentation, a similar search, though with less systematic evaluation, was conducted. Overall impression was that comparable activities are in progress (about 950 papers in four years) except metals activities are down. For this review, however, I will concentrate on several specific topics; AE source simulation analysis applied to composite samples, guided wave AE, pattern recognition analysis for AE signal discrimination, moment tensor analysis with application to concrete, and new generation AE instrumentation.

## 2. AE Source Simulation Analysis

Breckenridge et al.<sup>(4)</sup> standardized the calibration of AE sensors using a capacitive transducer to capture the initial arrival of a displacement signal produced by the fracture

of a glass capillary. This allowed the development of quantitative comparison of AE experiment with theories of the wave propagation. Hsu et al.<sup>(5)</sup>, Sachse and Pao<sup>(6)</sup>, the Harwell group<sup>(7,8)</sup> and Kishi and coworkers<sup>(9)</sup> led the growth of deconvolution (or source inversion) methods to determine AE-source characteristics in metals, ceramics and composites. Noise was a serious problem in the inversion scheme and the difficulties in calculating Green's functions for useful geometries was the fundamental obstacle. Ohtsu and Ono<sup>(10,11,12)</sup> have proposed alternate techniques based on source simulation. Takemoto and coworkers<sup>(13,14)</sup> have combined the source simulation concept with radiation pattern and source location analysis techniques for the fracture mechanism characterization in composites taking the viscoelastic nature of the matrix into account.

Acoustic emission has been widely used to study various types of microfracture in fiber reinforced composites<sup>(15,16)</sup>. Hsiao et al.<sup>(17)</sup> experimentally measured the out-of-plane displacements due to a step-wise point unloading (pencil lead breaking) on polyethylene and polymethyl methacrylate, and recognized both the response delay and amplitude attenuation. Weaver et al.<sup>(18,19)</sup> proposed a comprehensive method to calculate the displacement component of viscoelastic waves. Here, the wave relaxation was accounted for successfully by including frequency independent relaxation function,  $R(t)$ . They demonstrated a good agreement between experimental and theoretical responses to a monopole excitation.

In order to examine the fracture modes and dynamics in fiber-reinforced composites, Suzuki et al.<sup>(13,14)</sup> have developed an AE monitoring system for the source location and for fracture mode analysis based on the radiation pattern of the P-wave. (See Fig. 1) A displacement-sensitive sensor on one of the channels was utilized to obtain the source waveform using a computer algorithm in time domain incorporating a waveform simulation scheme. By combining the available information, detailed characterization of microfracture processes can be performed.

In this approach, the method of Ohtsu and Ono<sup>(10)</sup> was extended to calculate the displacement component of viscoelastic waves for dipole problems, taking the concept of Weaver et al.<sup>(18,19)</sup> into account. The proposed method

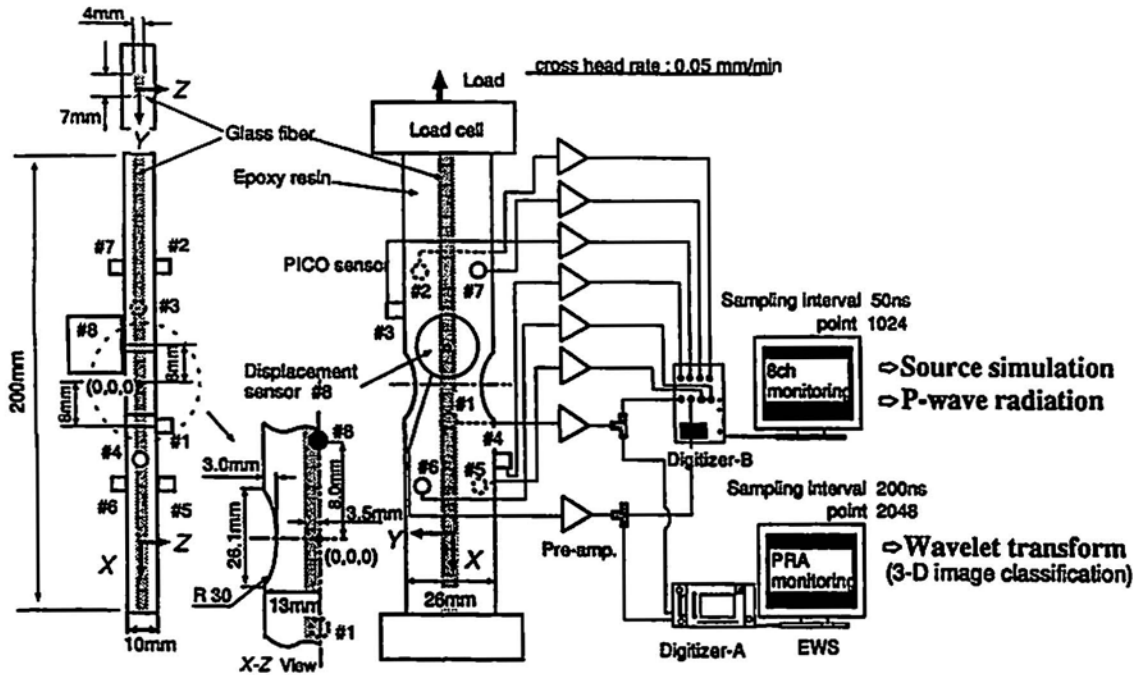


Fig. 1 Experimental setup for 10-channel AE monitoring during the tensile test of a composite sample<sup>(14)</sup>.

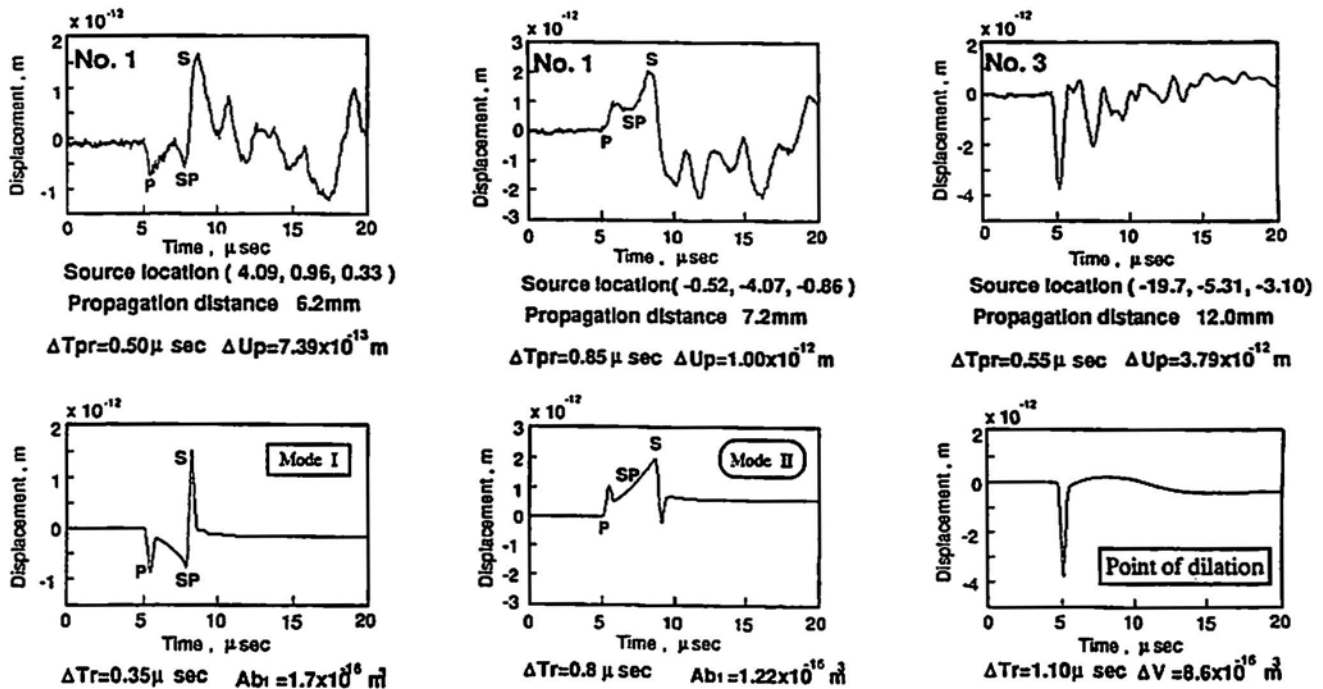


Fig. 2 Comparison of detected and simulated waves for Mode-I fiber fracture, Mode-II disbonding and dilatation center<sup>(14)</sup>.

modified the elastodynamic response by introducing the wave attenuation term,  $\exp[-\alpha(x-x')]$ , and by using the relaxation function. This concept is expressed by the following equation for displacements  $U_i$  at  $(x,t)$  due to a source at  $(x',t')$  in the half-space as:

$$U_i(x,t) = \exp[-\alpha(x-x')] \cdot T_{ij}(x,t; x',t') \cdot Ab_j(x',t') \cdot R(t),$$

where the symbol \* denotes a convolution integral in time.  $T_{ij}(x,t; x',t')$  represents the Green's function of the second kind for an isotropic elastic medium and  $Ab_j(x',t')$  is the source function or the time transient of crack volume (A being the source area), respectively. A and  $b_j$

represent the crack area and discontinuity vector (Burgers vector equivalent), respectively.  $T_{ij} \cdot Ab_j$  gives the surface displacement in a non-dissipative medium. Suzuki et al.<sup>(13)</sup> established its validity for fiber fracture in a model specimen. This was refined in Suzuki et al.<sup>(14)</sup>, which examined the complicated fracture dynamics in more realistic glass-fiber reinforced plastics. Figure 2 illustrates the waveforms, both experimental and simulated of three types of fracture thus identified; namely, Mode-I fiber fracture (in a longitudinal fiber-bundle reinforced sample), Mode-II disbonding and dilatation (in a transverse fiber-bundle sample).

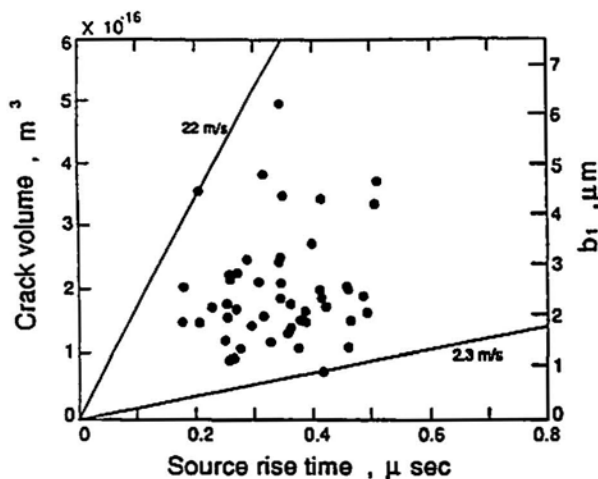


Fig. 3 Source parameters for fiber fracture in a unidirectional composite sample<sup>(14)</sup>.

Figure 3 shows a cross-plot of two source parameters for fiber fracture in a longitudinal fiber-bundle sample. The source rise time for fiber fracture is in the range of 0.17 to 0.5  $\mu\text{s}$ , and the crack volume or  $Ab_1$ , is 0.7 to 5  $\times 10^{-16} \text{ m}^3$ . Assuming the AE is produced by the fracture of a single fiber of 10  $\mu\text{m}$  diameter, crack opening displacement  $b_1$  becomes 1.0 to 6.4  $\mu\text{m}$ . This discontinuity corresponds to 1/8 to 1/2 of the fiber diameter, and suggests that fiber pull out does not occur in these composites. Indeed, we did not observe any AE signals by Mode-II fiber pull-out. Slope of  $b_1$  vs.  $\Delta T$ , gives the crack velocity on the fracture surface, and it reaches the maximum of 22 m/s. As the source function is approximated by a sinusoidal ramp function, peak crack velocities reach about 55 m/s.

### 3. Guided Wave AE

There has been awareness that guided wave propagation must be incorporated into AE studies (e.g., Pollock<sup>(20)</sup>), especially in connection to thin-walled pressure vessels and waveguides. With more wide-spread uses of AE in aircraft and aerospace structures, in which thin skins are common, consideration of guided acoustic modes has become unavoidable in the interpretation and analysis of AE with respect to source-location accuracy and identification of source mechanisms. Gorman<sup>(21)</sup> and Gorman and Prosser<sup>(22)</sup> reported on the effects of guided-wave AE propagation in plates and pointed out that the two primary propagation modes in AE signals are the extensional and flexural plate modes. The predominant particle motion for the extensional mode is in the plane of the plate, while the main motion of the flexural-mode is out-of-the-plane component. A source with in-plane displacements (especially symmetric about the midplane) generates AE signals with strong extensional components. Mode-I fatigue cracks in metals, longitudinal fiber fracture in the 0° plies and matrix cracks in the 90° plies of a composite laminate are typical examples. (Also pencil-lead breaks on sample edges.) Out-of-plane source motion such as delamination

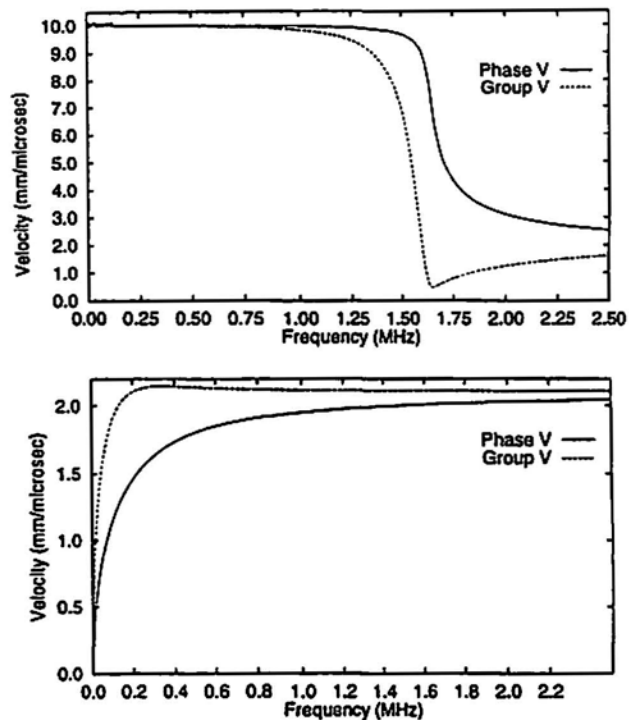


Fig. 4 The phase and group wave velocities vs. frequency for a unidirectional composite laminate, 1 mm thick<sup>(23)</sup>. The extensional wave (top); The flexural wave (bottom).

or particle fracture (or pencil-lead breaks) on the surface produces AE signals with strong flexural components.

These wave modes are dispersive and the velocity changes with frequency as shown in Fig. 4 for a unidirectional composite laminate, 1 mm thick<sup>(23)</sup>. Over the frequency range of 10 kHz to 1 MHz common in AE experiments, the extensional mode propagates with a faster velocity and suffers little dispersion. The flexural mode is slower and is highly dispersive below 500 kHz. A typical waveform generated by a pencil-lead break and detected in a composite plate with a broadband sensor identifying these two modes is shown in Fig. 5<sup>(24)</sup>. Prosser<sup>(24)</sup> measured the attenuation of these two modes as 42 dB/m (at 410 kHz) and 83 dB/m (at 85 kHz), respectively. The higher value for the flexural waves resulted primarily from the dispersion effect.

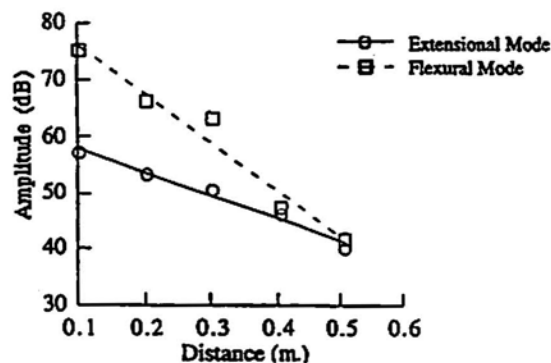


Fig. 5 Peak amplitude versus propagation distance for extensional and flexural modes in an 8-ply quasi-isotropic carbon fiber composite<sup>(24)</sup>.

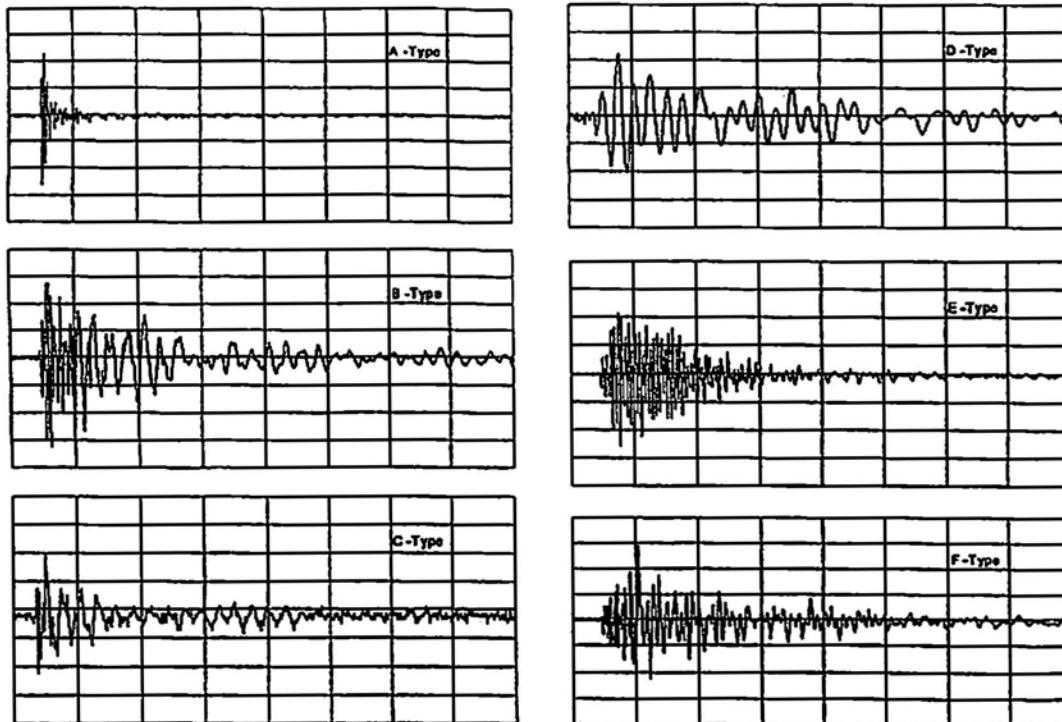


Fig. 6 Typical waveforms of six signal types from quasi-isotropic carbon fiber samples. A-type: fiber fracture; B: fiber/matrix fracture; C: transverse matrix fracture; D: delamination; E: splitting; F: angle-ply matrix crack. 41  $\mu\text{s}/\text{div}$ .

Proper uses of the varying velocities improve the accuracy of source location. Conventional single-frequency, threshold-crossing schemes for arrival time determination and source location can lead to large location errors when applied to thin structures. This is due to the mixing of two or more modes that travel at different velocities. Simulation of AE signals using pencil-lead breaks coupled with the orientation of the breaks assists in identifying the AE source mechanisms. Ono and Huang<sup>(25,26)</sup> employed in-plane and out-of-plane pencil-lead breaks (together with microscopy) to distinguish AE signals from fiber fracture, delamination and longitudinal and transverse matrix cracks. (cf. Fig. 6) These were then used as the basis for their pattern recognition analysis. However, the use of pencil-lead breaks to simulate AE signals should be approached with caution since, in most practical test configuration, only out-of-plane pencil-lead breaks can be produced. This is documented on AE testing of cylindrical composite vessels by Downs and Hamstad<sup>(27)</sup>.

Guided wave propagation in isotropic plates have been studied intensively in the literature using a variety of techniques<sup>(28,29)</sup>. Wave motion in composite plates is more complicated due to their anisotropy and inhomogeneity. Only two-dimensional cases and three-dimensional case with surface loading<sup>(30,31)</sup> have been studied in detail. Approximate solutions have been developed for wave propagation in anisotropic plates<sup>(32,33)</sup>. Retaining only the lowest Lamb-wave modes, approximate theories may be used to analyze AE data at low frequencies<sup>(34)</sup>.

Guo et al.<sup>(23)</sup> investigated Lamb waves produced by various microfracture sources in unidirectional and cross-ply composite laminates. The experimental measurements and theoretical calculations are compared and are found to

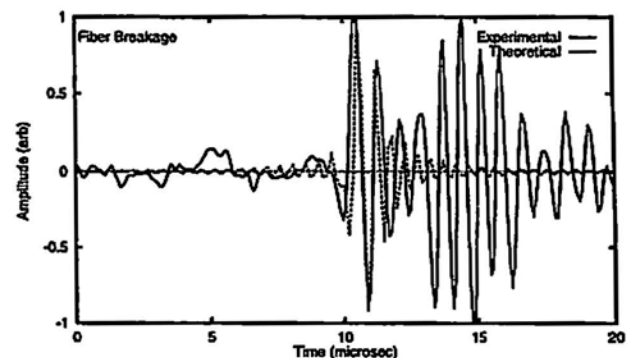


Fig. 7 Experimental measurements and theoretical calculations of Lamb waves produced by fiber fracture in a unidirectional laminate<sup>(23)</sup>.

agree well in the time domain as shown in Fig. 7 for fiber fracture in a unidirectional laminate.

#### 4. Pattern Recognition Analysis

When AE signals are recorded, either in analog or in digital form, one recognizes visually the existence of certain waveform categories. This can be time consuming as the number of AE signals is often large, but manual waveform classification has been done for some time. With digital signal analysis techniques, the procedure for classifying different waveforms and correlating them to underlying microfracture processes has become less labor intensive. Review on this topic by Ono and Huang<sup>(25)</sup> provides the basic concept and an application to the characterization of composite microfracture. They used Tektrend's ICEPAK software package, which includes five statistical and neural network classifiers. Of these, k-

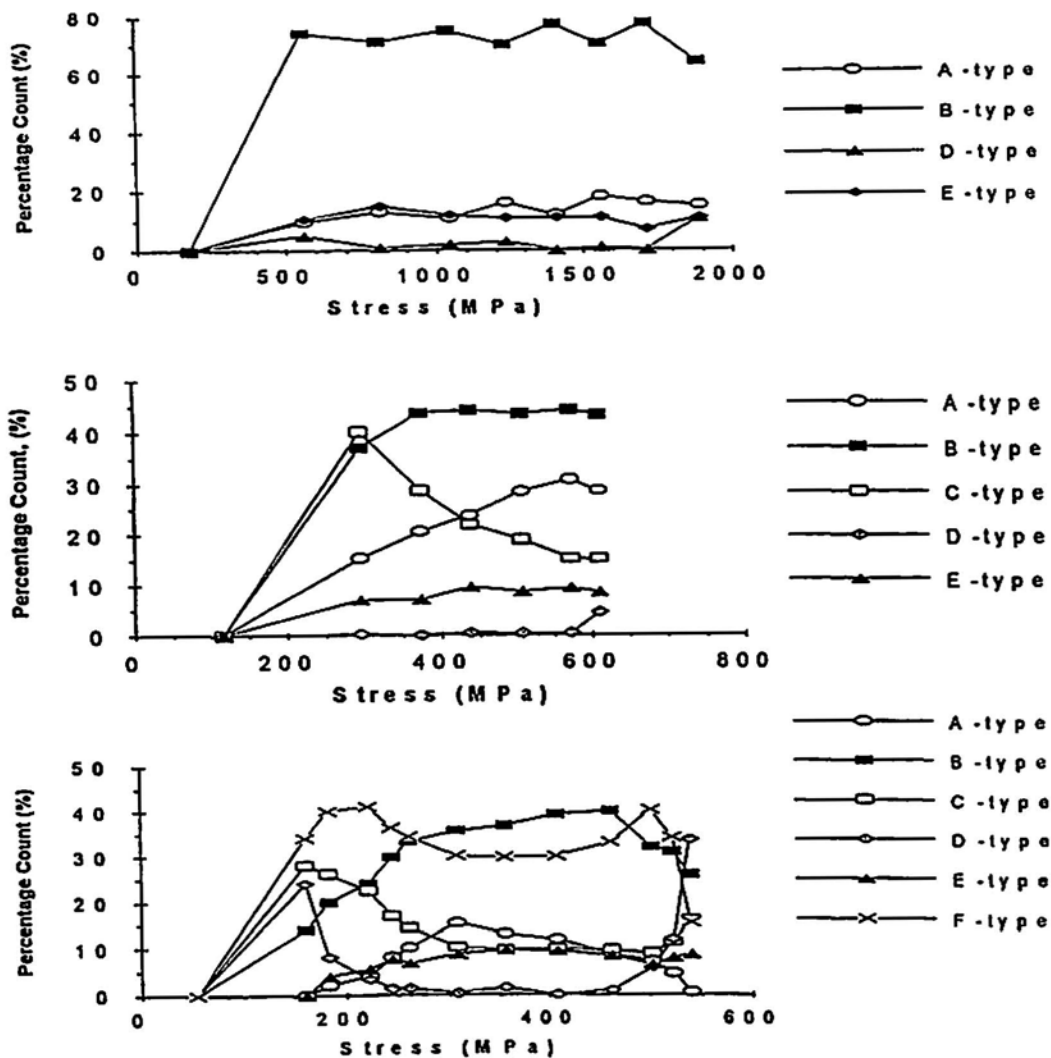


Fig. 8 Percentage counts of signal types plotted against stress<sup>(25)</sup>. Top: unidirectional; middle: cross-ply and bottom: quasi-isotropic laminates.

nearest neighbor classifier was most effective<sup>(25,26)</sup>. ICEPAK's neural network classifier was slow at that time due to the lack of computational power of 386/486 processors, but this limitation no longer applies. By using this analysis procedure, Ono and Huang<sup>(25)</sup> classified up to 8000 events per test in studying the evolution of different microfracture processes in composite samples. Percentages of six signal types shown in Fig. 6 varied as the applied load increased to fracture. The changes are shown for unidirectional, cross-ply and quasi-isotropic laminates in Fig. 8. Note the increase of Type-D events just before the final fracture in all three cases.

More recently, three other software packages designed for classification or for noise discrimination of AE signals have become available from US and German sources. One (PAC-PARS) has a similar standard approach as ICEPAK, while the other two use frequency spectral features. Vallen's VisualClass uses staggered time windows for multiple FFTs and the results are used as features for classifier. These should be useful for any AE users interested in classifying recorded waveforms. However, effects of wave dispersion and attenuation need to be considered carefully in employing these procedures when

the distance between AE source and sensor varies widely. Wideband (but not necessarily high fidelity) sensors and electronics are also needed to discriminate different signal features as waveform and spectral features are drastically altered with narrow-band sensors.

Another powerful tool for signal discrimination is wavelet transform<sup>(35)</sup>. Wavelet transform allows the determination of frequency spectrum as a function of time with optimized resolutions in time and frequency using short waveform segments or wavelets as the basis functions. Resultant mapping of wavelet coefficients in the frequency-time coordinate plane provides more informative characterization of transient signals than the power-density spectra from usual Fourier transform. Suzuki et al.<sup>(35)</sup> performed wavelet transform on AE signals from a longitudinal glass-fiber reinforced composite sample under tensile loading (see e.g., Fig. 9). Obtained spectrograms were classified into four types and compared to known fracture dynamics results with excellent correlation.

### 5. Moment Tensor Analysis

Ohtsu and Ono<sup>(12)</sup> recognized that in practical structures only external surfaces are available for transducer place-

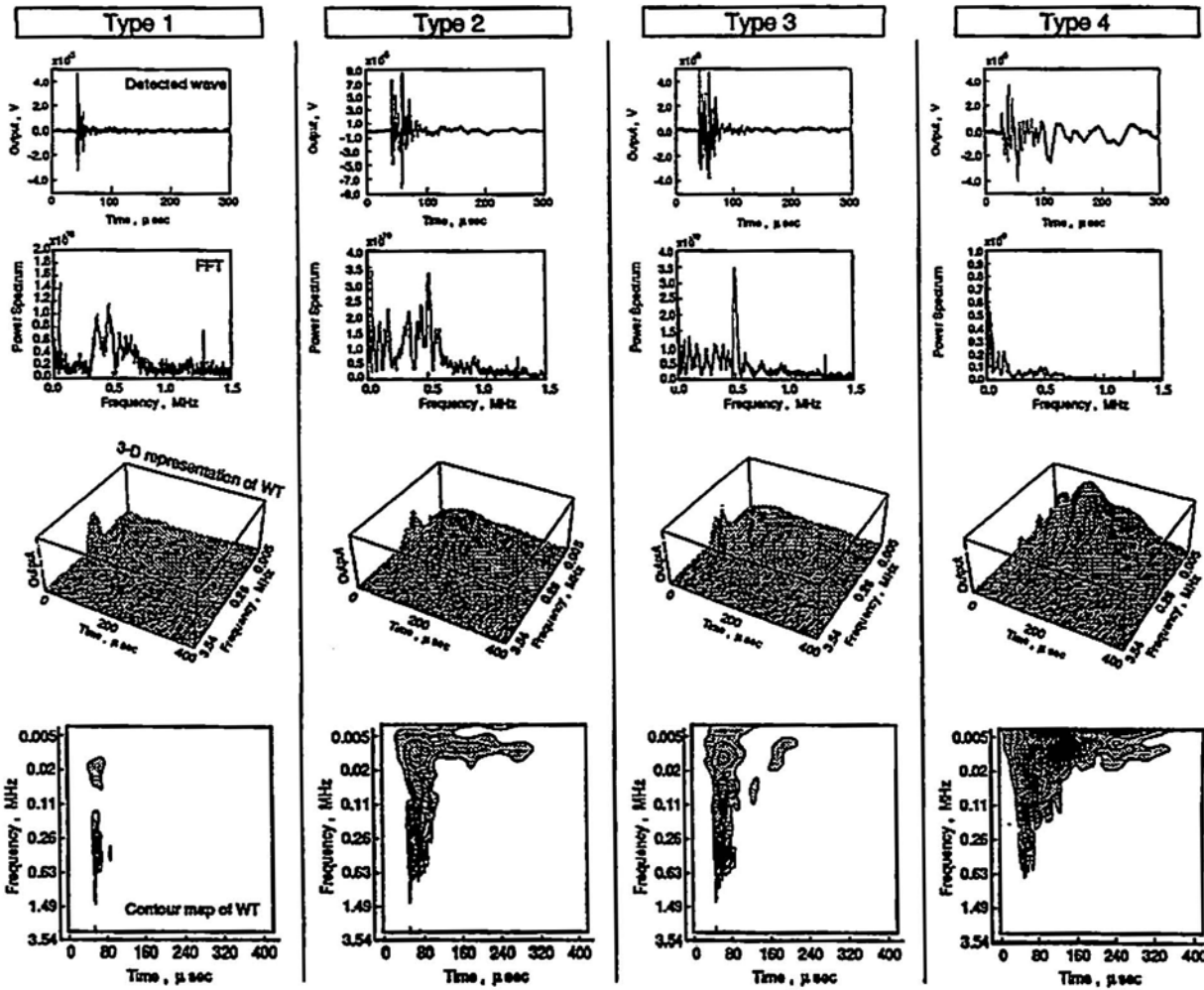


Fig. 9 Examples of AE waveforms and their Fourier Transform and Wavelet Transform<sup>(35)</sup>. Types 1 to 4 are AE signals from a glass-fiber composite sample using a PAC-PICO sensor and represent Mode-I fiber fracture, two kinds of Mode-I matrix fracture and Mode-II strain gage exfoliation.

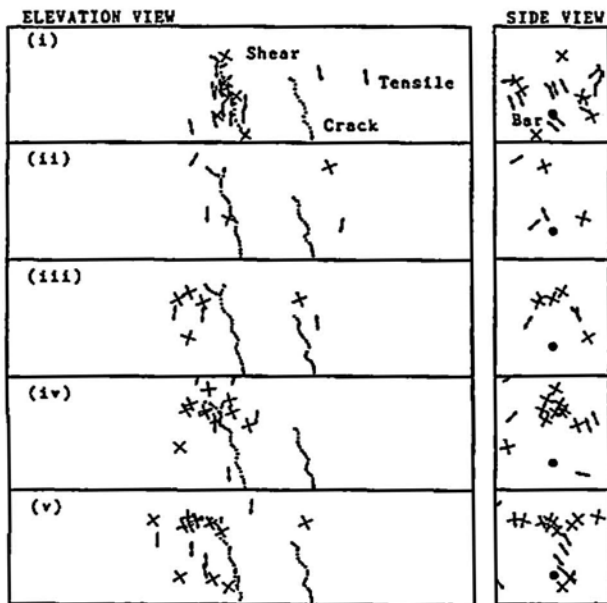


Fig. 10 Crack distribution plot at 5 stages of a concrete bend test<sup>(38)</sup>. A cross indicates a shear or mixed crack and an arrow a tensile crack. Dotted lines are the crack paths.

ment and that late arriving waves are compromised by many factors. They formulated on the basis of the generalized theory of Ohtsu and Ono<sup>(11)</sup> an approach relying on the amplitude of initial p-wave arrivals to obtain the orientation of crack motion, now referred to as Moment Tensor Analysis. Ohtsu<sup>(36,37)</sup> developed this concept into a structural monitoring system and along with many coworkers applied to laboratory and full scale concrete structure evaluation<sup>(38,39)</sup>. By using at least 4 or 6 sensors, 2-D or 3-D analysis can be performed, producing crack classification based on tensile or shear types, location, orientation as well as other AE parameters. An example of the resultant crack distribution plot is given in Fig. 10, obtained from 4-point bend testing of a notched steel-reinforced-concrete beam. In the initial linear load-displacement segment (below 50% of the maximum load), many tensile cracks are seen near the crack path. Before or at the start of non-linear segment, cracks are mostly shear-type and are ahead of macro-cracks. Here, tensile cracks are defined as containing less than 40% shear component. This method has been successful in identifying crack development in full-scale concrete structures and should prove its utility in evaluating civil infrastructures.

## 6. New Generation AE Instrumentation.

In the last few years, improved AE instruments have appeared in the marketplace from manufacturers in the US, Germany and Japan. One is based on PC plug-in boards with controlling software (PAC-Mistras). This system has a digital processing IC on each board, which processes AE data for two channels/board and provides conventional AE parameters and waveform data. The second instrument (Vallen-AMSY4) similarly provides conventional AE parameters and waveform data, but in a dedicated hardware design with AE parameters and waveform data being processed in separate modules. Surgeon et al.<sup>(40)</sup> evaluated some aspects of the performance of these two systems (albeit one generation older versions) and found that one excels in speed while the second derives advantages in operational flexibility from dedicated hardware designs. Both have been improved over the past year. Two other more specialized instruments are primarily for obtaining waveform data. One of them (Digital Wave) analyzes the data on the basis of plate-wave theory, while the second (JT of Japan) evaluates the AE source characteristics of cracks in compact tension test geometry.

These new generation AE equipment has vastly upgraded the processing capability and throughput. By combining with pattern recognition and other signal analysis procedures, automated "intelligent" processing of AE signals should become reality before too long.

## 7. Conclusion

This brief review highlights some of recent innovation in the AE field. While the first-principle prediction of AE signals is still beyond our reach in most practical applications, some understanding has started to emerge under well-controlled conditions.

With new advances in AE hardware, software and theory-based guidance, the often criticized empirical nature of AE results is finally changing. These tools will allow one to minimize uncertainty in physical interpretation of AE phenomena.

## Acknowledgment

This work was supported by the AFOSR under grant F49620-93-1-0320 (Ajit Mal, Principal Investigator) monitored by Dr. Walter Jones.

## References

- 1 - Drouillard, T.F., *J. Acoustic Emission*, **14**, 1-34 (1996).
- 2 - Ono, K., "Chapter 68: Acoustic emission", *Encyclopedia of Acoustics*, Volume Two, ed. Malcolm J. Crocker, John Wiley, New York, (1997), pp. 797-809.
- 3 - Ono, K., *Journal of Acoustic Emission*, **12**, 177-198 (1994).
- 4 - Breckenridge, F.R., C.E. Tschiegg, and M. Greenspan, *J. Acoust. Soc. Am.*, **57**, 626-631 (1975).
- 5 - Hsu, N.N., J.A. Simmons, and S.C. Hardy, *Materials Evaluation*, **35**, 100-106 (1977).
- 6 - Sachse, W. and Y.H. Pao, *Ultrasonics Intl 81-Conf Procs*, IPC Science and Tech. Press, Surrey, England, (1981), pp. 116-122.
- 7 - Wadley, H.N.G., C.B. Scruby, and G. Shrimpton, *Acta Metallurgica*, **29**, 399-414 (1981).
- 8 - Scruby, C.B., G.R. Baldwin, and K.A. Stacey, *Intl J. Fracture*, **28**, 201-222 (1985).
- 9 - Ohira, T. and T. Kishi, *Progress in AE*, eds. M. Onoe et al., Japan Soc. NDI, Tokyo, pp. 208-217 (1982).
- 10 - Ohtsu, M. and K. Ono, *J. Acoustic Emission*, **3**, 27-40 (1984).
- 11 - Ohtsu, M. and K. Ono, *J. Acoustic Emission*, **5**, 124-133 (1986).
- 12 - Ohtsu, M. and K. Ono, *NDT International*, **21**, 143-152 (1988).
- 13 - Suzuki, H., M. Takemoto and K. Ono, *J. Acoustic Emission*, **11**, 117-128 (1993).
- 14 - Suzuki, H., M. Takemoto and K. Ono, *J. Acoustic Emission*, **14**, 35-50 (1996).
- 15 - Awerbuch, J. M.R. Gorman and M. Mudhukar, *Proc. First Int'l. Symp. on AE from Reinforced Plastics*, Soc. Plastics Industry, New York, Session 2, (1983) pp. 1-30.
- 16 - Kawamoto, K. and K. Ono, *Proc. 3rd Int'l Symp. on AE from Reinforced Composites*, Amer. Soc. Nondestr. Testing, Columbus, OH, (1989), pp. 230-239.
- 17 - Hsiao, C.P., R.A. Kline, and K. A. Grasse, *Proc. IEEE Ultrasonic Symp.*, IEEE, New York, (1986), pp. 1005-1008.
- 18 - Weaver, R.L., W. Sachse and L. Niu, *J. Acoust. Soc. Am.*, **85**, 2255-2261 (1989).
- 19 - Weaver, R.L., W. Sachse and L. Niu, *J. Acoust. Soc. Am.*, **85**, 2262-2267 (1989).
- 20 - Pollock, A.A., *Progress in AE III*, Japan Soc. NDI, Tokyo, (1986), pp. 708-721.
- 21 - Gorman, M. R., *J. Acoust. Soc. Am.*, **90**, 358-364 (1991).
- 22 - Gorman, M.R. and W.H. Prosser, *J. Acoustic Emission*, **9**, 283-288 (1991).
- 23 - Guo, D., A. Mal and K. Ono, *J. Acoustic Emission*, **14**, S19-S46 (1996).
- 24 - Prosser, W.H., *J. Acoustic Emission*, **14**, S1-S11, (1996).
- 25 - Ono, K. and Q. Huang, *Progress in Acoustic Emission VII*, eds. T. Kishi et al., Japan Soc. NDI, Tokyo, (1994), pp. 69-78.
- 26 - Ono, K. and Q. Huang, *Advanced Structural Fiber Composites*, *Proc. Topical Symp. III on Advanced Structural Fiber Composites*, 8th CIMTEC, ed. Vincenzini, P., TECHNIA, Faenza, Italy, (1995) pp. 551-558.
- 27 - Downs, K.S., and Marvin A. Hamstad, *J. Acoustic Emission*, **14**, S61-S73 (1996).
- 28 - Knopoff, L., *J. Appl. Phys.*, **29**, 661-670 (1958).

- 29 - Pao, Y. H., *Elastic Waves and Nondestructive Testing of Materials*, ed. Y. H. Pao, AMD Vol. 29, ASME, New York, (1978), pp. 107-128.
- 30 - Green, E. R., *J. Appl. Mech.*, **60**, 217-223 (1993).
- 31 - Lih, S.S., and A.K. Mal, *Composites*, **27B**, 633-641 (1996).
- 32 - Reddy, J. N., *ASME J. Appl. Mech.*, **51**, 745-752 (1984).
- 33 - Sun, C. T., and T. M. Tan, *J. Astronautical Science*, **32**, 269-284 (1984).
- 34 - Lih, S.S., and A.K. Mal, *Wave Motion*, **21**, 17-34 (1995).
- 35 - Suzuki, H., T. Kinjo, Y. Hayashi, M. Takemoto and K. Ono, *J. Acoustic Emission*, **14**, 69-84 (1996)
- 36 - Ohtsu, M., *NDT International*, **22**(1), 14-20 (1989).
- 37 - Ohtsu, M., *Res. Nondestr. Eval.*, **6**, 169-184 (1995).
- 38 - Shigeishi, M. and M. Ohtsu, *Progress in AE VIII*, eds. T. Kishi et al., Japan Soc. NDI, Tokyo, (1996), pp. 205-210.
- 39 - Yuyama, S., T. Okamoto, M. Shigeishi and M. Ohtsu, *Materials Evaluation*, **53**, 347-354 (1995).
- 40 - Surgeon, M., M. Wevers, P. De Meester, and K. Ono, *Trends in NDE Science and Technology*, Proc. 14th World Conf. on NDT, vol. 1, eds. C.G. Krishnadas Nair et al., New Delhi, India, (1996), pp. 143-148.

# Program and Abstracts of the 40th AEWG Meeting

June 9-11, 1997 at Infrastructure Technology Institute, Northwestern University, Evanston, Illinois; David W. Prine, Program Chair.

## MONDAY, JUNE 9, 1997

### AE PRIMER

Introduction to AE, Alan G. Beattie, Sandia National Laboratories

Metals and Alloys, Harold L. Dunegan, Dunegan Engineering Consultants, Inc. (DECI)

AE from Composites, Yolanda L. Hinton, NASA Langley Research Center

AU and Its Application to Wood Products, Frank C. Beall, University of California, Forest Products Lab.

Geotechnical Applications of AE, H. Reginald Hardy, Jr., Penn State University

AE Testing of Pressure Vessels and Piping, Allen T. Green, Acoustic Technology Group

## TUESDAY, JUNE 10, 1997

APPLICATIONS #1; SESSION CHAIR: David W. Prine, Infrastructure Technology Institute, Northwestern Univ.

### 1a. AE Detection of Cracking in Pipe Socket Welds, Bryan Morgan, Pacific Gas & Electric Co.

Small bore pipe socket welds in fossil and nuclear power plants are prone to vibration induced cracking. This is particularly a problem for small bore pipe vents and drains cantilevered off large pipes. Fluid flow fluctuations and attached rotating equipment resonant with fundamental frequencies from the small bore pipe cantilever. Typically the small bore pipe is attached to the main piping using a socket weld. The weld geometry exhibits a high stress concentration and can result in cracking at the weld root. The socket geometry makes a non-destructive inspection using either ultrasonics or radiography very difficult. In the laboratory, stainless steel pipe specimens with socket weld cracks were stressed to material plastic yield while monitoring for AE. This showed that a significant amount of AE was generated during elastic bending, and could be used to differentiate cracked and non-cracked specimens. The cumulative AE signal energy at relatively low stress levels provided a means of identifying the cracked specimens.

### 1b. Field Data on Testing of NGV Containers Using Proposed ASTM Standard E070403-95/1, Roy D. Fultineer, Jr., Spencer Testing Services

Spencer Testing Services has inspected approximately 1500 natural gas vehicle containers over the last two years comprised of Type II, Type III, and Type IV containers. These are composite pressure vessels with metal or plastic liners and working pressures up to 3600 psi. In service inspection of these containers is not regulated by any federal authority, however, owners of these containers are anxious to reduce the risk of in service failures. We feel we can successfully remove any structurally damaged container from service with the utilization of ASTM E070403-95/1. This standard has three levels of container acceptance criteria: a three year retest, a one year retest, and a remove from service recommendation. A three year retest indicates a cylinder with no apparent problems. A one year retest indicates a container that produced low levels of acoustic emission (AE) and needs to be retested. A remove from service recommendation indicates that the container did not meet the minimum requirement to remain in service. We have found that six containers did not meet the acceptance criteria for a three year retest. Two of these containers were recommended to be taken out of service, and the four remaining containers were recommended for a one year retest. The two containers removed from service had damage in areas which could not be visually examined. One of the containers removed from service was taken to the manufacturer for further evaluation. The container was pressurized and monitored with AE during this reevaluation and the data received matched almost exactly with the field data. It was found that containers mounted in a

manner that would expose their composite wraps to degrading factors produced more AE activity than containers that were fully isolated. It has also been shown through the testing of these containers that AE monitoring is a feasible method for testing the composite wrap for damage which may result in a loss in structural integrity.

1c. The Use of Portable Wireless Acoustic Emissions Systems for Bridge Monitoring, Lozev, M.G., Virginia Transportation Research Council; Washer, G., Federal Highway Association; Carlos, M. and Miller, R., Physical Acoustics Corporation

A portable, battery powered, multi channel, all digital signal processor acoustic emission system with built-in real time filtering and wireless communications features has been used for bridge inspections.

1d. Underground Pipeline Leak Detection Using Acoustic Techniques, Carlyle, J.M., New Jersey Institute of Technology; Tafuri, A.N., U.S. Environmental Protection Agency; Watts, D.J., New Jersey Institute of Technology; and Yezzi, J.J, Jr., U.S. Environmental Protection Agency

Volumetric and pressure change techniques work well for detecting the presence of leaks, but they do not determine the location of leaks (so that they can be repaired). Reacting to this need, the Strategic Environmental Research and Development Program initiated a project to develop passive acoustic leak location instruments and techniques. The Department of Defense, the Department of Energy, and the Environmental Protection Agency are all participating in the building of an experimental pipeline facility at Edison, NJ, to test new acoustic pipeline leak detection concepts under realistic field operating conditions.

Research work under this project during the past year has established that acoustic techniques readily detect small leaks in underground pipelines, and that a variety of acoustic techniques are available to meet a number of difficult field circumstances. We have shown that it is possible to locate a 0.03 gal/hr leak in a buried 2" diameter steel water line under field conditions using a 25 foot sensor spacing (by enhancing the leak signal using a newly developed method). In addition, we have characterized the leak source process (finding that turbulence, two phase flow, jetting and geysering are distinct sources), and have also developed several styles of artificial leak sources.

This paper will provide an overview of some of some of the more important findings of the project to date, and will also present our plans for future work under the program.

1e. Waveform-Based AE for Damage Evaluation of FRP-Reinforced Glued-Laminated Wood Beams  
Marsh, K., and Landis, E., Department of Civil and Environmental Engineering, University of Maine

We are studying damage and failure mechanisms in glulam beams with an FRP reinforcement in the tension zone. We re considering an energy approach to estimate the relative effects of damage mechanisms such as interface shear failure, wood tension failure, and wood-FRP interface debonding on the overall load-deformation response of the beam. Waveform-based AE techniques are being applied to estimate the energy released by the different damage mechanisms based on the corresponding energy of the AE source. In order to do this, two basic AE analysis routines are being developed. First, AE source location estimation techniques for bulk waves in layered orthotropic media, and second, a routine to estimate the energy released by the AE source. The goal is to match specific AE event properties to corresponding changes in the beam's load-deformation response.

1 f. Acoustic Emission During Rotary Cutting of Coal, Hardy, H.R., Jr., Pennsylvania Mining and Mineral Resources Research Institute; Shen, H.W., Department of Mineral Engineering, Pennsylvania State University; and Khair, A.W., Mining Engineering Department, West Virginia University

Studies are presently under way by the authors to investigate the character of the bit-coal interaction during coal cutting and its influence on the size and shape distributions of the generated dust. An important aspect of these studies is the use of acoustic emission (AE) and associated artificial intelligence techniques for remote monitoring of coal cutting operations. Recent papers by the authors have provided a general outline of the overall study, and the preliminary results of linear, single-bit cutting. The present paper will focus on the test facilities, experimental techniques, and results associated with the rotary, single-bit cutting studies. The cutting studies were carried out using the West Virginia University laboratory-scale shearer facility in Morgantown, West Virginia. The coal specimens were initially cast in plaster of Paris. During testing, a rotating bit was advanced into the coal while AE signals were monitored. Bit rotation speed and advance rate were controlled. All mechanical operations were carried out within a closed test chamber to allow a detailed analysis of particle size and shape to be undertaken.

1 g. An Evaluation of the Performance of Acoustic Emission Systems, Surgeon, M., Wevers M., and De Meester, P., Katholieke Universiteit Leuven; and Ono, K., University of California - Los Angeles

Two AE systems were evaluated. These are Vallen AMS-3 and PAC MISTRAS. Characteristic features were compared and, in particular, the data acquisition speed and ease of use were examined. Strong and weak points based on our personal experiences will be reported.

APPLICATIONS #2; SESSION CHAIR: Kanji Ono, University of California, Los Angeles

2a. Analysis of AE Data from a Rocket Motor Case: Key Questions in AE Source Location, Maochen Ge, Natural Resources Canada, Mineral and Energy Technology

To make AE a credible and practical NDT tool, there are two essential conditions. First, the location accuracy must be drastically improved from the current level and be predictable for the given application. Secondly, the location process must be robust and can be automated. Otherwise, large scale and daily industrial applications would be very difficult, if not impossible.

The priority is to solve two long existed problems, phase association and unsophisticated location algorithms. Without phase association, serious errors are introduced into arrival time data which makes the accurate location impossible. With the unsophisticated location algorithms, it is difficult to implement the necessary means to reduce the impact of initial errors. The severe effect of these two problems are vividly demonstrated by the analysis of the AE data from a rocket motor case. It also demonstrates with the same data that the solutions to these problems are available and that, with these solutions, the AE source location accuracy in the NDT industry will immediately advance to a new level. A particular advantage of these solutions is that they do not require the additional hardware technology and are compatible with all existing ones used in the NDT industry. Therefore, the major improvement of the AE source location accuracy in the NDT industry can be achieved with a minimum price.

To make the automated AE monitoring truly practical, the other important issue is to develop a comprehensive data analysis and source location package. In addition to those general characteristics requested for a sophisticated source location code, such as efficient in calculation, no restrictions on sensor locations and numbers, flexible on regression methods, and easy to incorporate different velocity models, four other features are essential based on the study of the AE data from the rocket motor case and the extensive experience in automated rockburst monitoring. These features are phase association, which allows one to process and organize arrival time data and its critical role has been extensively discussed in the paper; effective surface ray tracing technique, which is the key to be able to use those sophisticated algorithms originally used for

extended media for shell-type structures, reliability assessment on event data and event locations, which allows the AE data to be used confidently and selectively; and a superior convergence character

The achievable source location accuracy in any application is fundamentally governed by the geometry of sensor arrays. A carefully planned array is, therefore, the single most important factor which would secure a long term source location accuracy. Array planning also allows one to evaluate whether the projected accuracy is achievable, a problem showing increased importance in modern AE applications.

#### 2b. Evaluation of Prototype Retrofit of a Steel Bridge Using AE and Strain Gages, David W. Prine, Infrastructure Technology Institute, Northwestern University

The development of a retrofit design aimed at retarding or eliminating fatigue crack growth in a large bridge can be a very difficult and expensive procedure. Analytical techniques frequently do not provide sufficient accuracy when applied to complex structural details. The California Department of Transportation (CALTRANS) recently awarded a contract to the Infrastructure Technology Institute (ITI) of Northwestern University to apply experimental state of the art NDE technology to the Interstate 80 bridge over the Sacramento River near Sacramento California (Bryte Bend). ITI researchers installed over 90 strain gages on the structure and monitored the results of both live traffic loading and controlled load tests using state of the art field monitoring equipment. Acoustic emission monitoring was also applied in conjunction with the strain gage monitoring to aid in characterizing the retrofits effect on existing active fatigue cracks. Tests were run on the bridge prior to and immediately following the installation of two different retrofit designs. Both live traffic and test loads applied under bridge closure were utilized for the tests. The load testing during bridge closure include both static and dynamic loading. The combined test results (strain and AE) clearly showed that one retrofit design was superior to the other. This paper will discuss the installation of the gages, the equipment used, the test procedures, and the results obtained. This work clearly proved the cost effectiveness of utilizing experimental techniques to gain improved understanding of retrofit performance.

#### 2c. The Role of the Shear Wave in AE Testing of Plate-Like Structures, Harold L. Dunegan, Dunegan Engineering Consultants, Inc. (DECI)

It has been observed while conducting experiments on bars and plates, using acoustic emission transducers and instrumentation, that a very strong signal having a characteristic velocity of a shear wave in the material is always present. It was first assumed that this signal corresponded to the first arrival of a dispersive anti-symmetrical lamb wave. It became apparent that this signal was still present for an in-plane source (breaking a pencil lead at the center edge of a plate) that produced pure symmetrical lamb waves with no evidence of the anti-symmetrical mode. In an attempt to better determine the identity of these signals, two shear plates with vertical and horizontal polarization were bonded to the end of a 12.5 mm. thick bar. They were used as both receivers and transmitters and AE transducers of different types were used in different orientations to receive signals from these transmitted shear waves, as well as pencil lead breaks. It is shown that a high frequency shear wave is created for both out-of-plane (OOP) and in-plane (IP) source inputs to the bar, and that AE transducers mounted to the surface of a plate are effective in detecting shear waves of both orientations. This paper presents experimental results that confirm these conclusions.

#### 2d. Attenuation of AE Signals in Composite Plates, William H. Prosser, NASA Langley Research Center

The increased understanding of the nature of AE signal propagation as guided acoustic modes in many practical testing geometries such as plates, shells, pipes, tubes, and rods has led to significantly improved AE analysis capabilities in laboratory testing. This so-called, Modal AE approach has yielded improved source location accuracy and has also provided the capability to differentiate signals from different source mechanisms (including extraneous noise) in coupons

and small scale structures. However, to apply these concepts to the testing of large structures, careful consideration must be given to the propagation behavior of the different guided modes over longer distances of propagation. Attenuation of the different modes must be characterized and corrections in amplitude measurements made to account for signal losses of the different modes. This includes signal loss in both the virgin material and that due to structural elements such as joints, stiffeners, or coatings. As an example, measurements of far field, peak amplitude attenuation are presented for the extensional and flexural plate modes propagating in two different thicknesses of a composite material. Even though the flexural mode contains much lower frequency components, its signal loss is much larger than that of the extensional mode. This is due to the significant dispersion of the flexural mode which causes a spreading of the signal in time over increasing propagation distances. The material studied is a candidate for cryogenic hydrogen propellant tanks on the prototype of a Reusable Launch Vehicle (X-33). As such, the effects on the attenuation of the plate modes due to bonded cryogenic foam insulation, which will be used on these tanks, were also evaluated. The presence of this cryogenic foam insulation had no measurable effect on the propagation of the extensional plate mode. However, it caused further severe attenuation of the flexural plate mode.

2e. Considerations for Time-of-Arrival Measurements Based on Lamb Wave Theory, Miller, R.K., Pollock, A.A., and Almeida, A.F., Physical Acoustics Institute

Operating in the very low millimeter-Mega Hertz (mmMHz) range, of the Lamb Wave dispersion curves, has been shown as one method of separating flexural and extensional wave modes. Ideally, this method should make the choice of a characteristic velocity easier resulting in accurate source location. However, this method only focuses on using the group velocities of the first extensional mode and ignores the reality that this mode may disappear into the normal background noise one encounters in actual Acoustic Emission (AE) tests. In addition, the method is only useful for very thin plates.

An investigation is underway to better understand the effects of both the group and phase velocities and how best to make measurements for realistic AE applications. Other methods are being examined that are more applicable to real-world structures. In particular is the use of. (1) the "Triple Point" (for metals); and (2) very high mmMHz values that allow the user to focus on the Rayleigh wave speed as a characteristic velocity.

2f. AE Analysis and Applications Using Moment Tensor, Yuyama, S., Nippon Physical Acoustics; and Carlos, M., Physical Acoustics Corporation

Moment Tensor analysis provides insight into the step-like movement associated with a single AE source event, in both magnitude and direction. Coupled with waveform based arrival time analysis from each sensor and location determination, a complete description of location, orientation, movement direction and source characterization can be accomplished. The purpose of this presentation is to describe the moment tensor process and several useful applications on structures.

2g. Dispersion Compensation in Acoustic Emission Pipeline Leak Location, Rewerts, L.E., Roberts, R.A., and Clark, M.A., The Center for NDE, Iowa State University

This paper addresses leak location in liquid-filled pipelines using acoustic emission time-of-flight measurements. Conventional data processing for time-of-flight-based acoustic emission event location perform less than optimally in this application due to the multiple-mode dispersive propagation characteristics of liquid filled pipes. This paper will summarize on-going work to analyze the propagation characteristics of liquid filled pipes, and develop model-based data processing for source location which accounts for the multi-mode dispersive nature of the transmission line.

Model simulation of pipeline propagation responses will be presented, along with corroborating experimental measurements. The functioning of cross-correlation source location data processing will be outlined, and degradation in algorithm performance arising from dispersive pipeline

propagation will be demonstrated. Potential approaches to data processing which incorporate *a priori* knowledge of the pipeline transmission dispersion characteristics will be presented. Particular attention is given to time-space transform methods which seek to isolate individual mode contributions to measured leak noise signals.

### **WEDNESDAY, JUNE 11, 1997**

**SIGNAL PROCESSING; SESSION CHAIR:** Harold L. Dunegan, Dunegan Engineering Consultants, Inc. (DECI)

**3a. The Use of Neural Networks to Discriminate Defect Signals from Noise, Pollock, A.A., Almeida, A.F., and Miller, R.K., Physical Acoustics Institute**

Neural Networks provide a means of developing classifiers that can potentially discriminate different types of AE sources. A recent research program provided an excellent opportunity to collect true defect signals as well as typical background noise during the testing of railroad tank cars. A description of the classifier training and results will be given.

**3b. Collecting AE Activity Graphs into an Atlas - A Proposed Format, Nordstrom, R. and Brunner, A.J., EMPA Dubendorf, Switzerland; and Bohse, J., BAM, Germany**

Comparison of AE results from different materials is limited by the great deal of variable dependencies involved in AE testing, including sensor, signal analysis and type of data representation desired. To find AE results that can be meaningfully and usefully compared, the types of AE formats that have been published were reviewed. It was found that a large number of AE papers contain a graph that represents AE activity, often as a first step in the analysis. However, there was a large variety of formats of these AE activity graphs that made comparison between materials and tests meaningless. A specific version of the AE activity graph is defined along with three graphs showing AE intensity. Examples from several materials, mostly fiber-reinforced composites, are presented from tests run at EMPA and BAM. How this collection of AE activity and intensity graphs, together with information on test materials and test parameters can be built into an AE-atlas and what its uses would be are discussed.

**3c. Wideband and Narrowband Acoustic Emission Waveforms from Extraneous Noise During Fatigue of Steel Samples, Hamstad, M.A. and McColskey, J.D., National Institute of Standards and Technology**

An extensive study of extraneous acoustic emission (AE) generated during fatiguing of steel samples has been performed. AE waveforms were emphasized instead of traditional AE parameters. Typically, four resonant sensors and four wideband high-sensitivity sensors were used to gather eight waveforms for each AE event. The fatigue tests were conducted in a servo-hydraulic fatigue test machine, using hydraulic grips. Specimen variables included two different thicknesses and different lateral dimensions of the plate-like samples. In addition to grip-based extraneous noise sources, artificial noise sources were also examined. Acoustic signals from both solid and air-transmitted artificial sources were studied. The extraneous AE was contrasted to an AE event from a sharp fatigue crack.

**3d. Wavelet Transform of AE Signals, Suzuki, H., Aoyama Gakuin University; Hayashi, Y., Shizuoka University; Takemoto, M., Aoyama Gakuin University; and Ono, K., University of California - Los Angeles**

A new analysis technique for AE signals will be presented and examples of applications illustrated. Although computationally intensive, wavelet transform allows one to separate different frequency components more accurately than windowed Fourier transform. Program listing is available for adaptation to different AE applications such as triangulation and power spectra specific parameters.

3e. Wave Propagation Effects Relative to AE Source Distinction of Wideband AE Signals from a Composite Pressure Vessel, Downs, K.S., Lockheed Martin Astronautics; and Hamstad, M.A. University of Denver

Numerous acoustic emission waveforms were recorded using wideband, non-resonant sensors during the initial proof pressurization ramp of a graphite/epoxy pressure vessel following a single controlled impact. The waveforms exhibited a variety of characters and frequency spectra. Some of the observed differences will be presented, and potential source distinctions will be discussed.

3f. PolyMODAL® AE Waveform Analysis Application, Yan, W., and Carlos, M., Physical Acoustics Corporation

PolyMODAL™ Waveform software Toolbox combines AE waveform signal processing with classical wavemode analysis to provide a complete AE test and analysis from waveform, acquisition to location analysis and data interpretation. An application example will be presented and each step in the analysis process detailed.

3g. AE Instrument, Worldwide Services Certification/Standards Issues, Carlos, M., Mitchell, J., Lowenhar, E., and Cole, P., Physical Acoustics Corporation

Standards and certifications in the Acoustic Emission industry are no longer buzzwords. They are now an essential ingredient to conducting worldwide business in terms of developing and qualifying AE instruments and carrying out AE testing services. Certifications to be discussed include ISO-9001, CE Mark, Intrinsic Safety for equipment development and manufacture, ISO-9002, ISO-9712 for Testing Services.

SENSORS/CERTIFICATION; SESSION CHAIR: Maochen Ge, Natural Resources Canada, Mineral and Energy Technology

4a. Sensitivity and Noise Models for AE Sensors, Vahaviolos, S.J., Carlos, M.F., and Lowenhar, E., Physical Acoustics Institute

The various AE "pick-ups" used for detection of low amplitude short duration and high frequency mechanical disturbances are presented. It will be shown that in order to optimize the detection of AE source waves proper impedance matching, crystal orientation and selection of preamplifier properties are necessary.

Mason's piezoelectric circuit theory models are extended and presented. These circuits are then simplified for use near or/and resonance of the piezoelectric crystal. For wideband models it is shown that cable impedance is "deadly" under high frequency and high impedance (wide band high fidelity) AE applications.

The electric current of a piezoelectric crystal is evaluated using various simplifications as based on a practical thin disk operating in a thickness mode. This current is then related to the stress wave generated by an AE source. The complete noise model of an AE transducer is presented. The effect on the noise from external components is thoroughly investigated. Optimum characteristics are obtained at resonance using a "peaking" external inductor and an FET OP-AMP as the charge amplifier. It is shown that the S/N degrades linearly with external electrostatic cable noise charge. The sensitivity of the detector is presented using the model of the "lattice." It is shown for noise voltages of 250  $\mu$ V a PZT-5 detector (transducer) could detect minimum displacements of interatomic distances. At the end a complete AE detection and processing system is detailed. Comparisons for sensitivity and noise rejection of an industrial AE sensor and "home made" one will be shown.

**4b. Improved Signal-to-Noise Wideband Acoustic/Ultrasonic Contact Displacement Sensors for Wood and Polymers, Marvin A. Hamstad, University of Denver - Department of Engineering and National Institute of Standards and Technology**

Research leading to a significant improvement in the signal-to-noise sensitivity of wideband acoustic/ultrasonic contact displacement sensors for wood and polymers is described. Design principles for such high-sensitivity sensors are reviewed. Comparisons of response between ceramic and polymer piezoelectric elements are made on low modulus specimens. A new, practical high-sensitivity sensor is characterized and its signal-to-noise sensitivity is compared to that of an existing commercial wideband, displacement sensor. The comparisons were made for polymer, maple, and redwood samples. Optimization of the piezoelectric element in the new sensor is considered. The typical increased sensitivity of the new sensor is about 30 dB over the existing commercial sensor.

**4c. Automated Sensor Testing (AST) and Low Noise Preamplifiers for AE Testing, Lowenhar, E., Carlos, M.F., and Vahaviolos, S.J., Physical Acoustics Corporation**

Automated Sensor Testing (AST) describes a unique sensor testing capability built into an AE system that allows a user to characterize the pulsing sensor as well as its neighboring sensors, on a structure, before, during and after an AE test. The use of AST allows the user to determine uniquely; if sensor coupling has remained consistent, if the sensor has fallen off, or if the cable has been removed, on a sensor by sensor basis.

Low noise preamplification of the AE signal from the sensor is extremely important in terms of duplicating the exact response from the AE sensor without being affected by external interfering sources. Low noise design includes maximizing signal-to-noise ratio in terms of boosting signal by amplification and filtering and reducing background noise, electronic circuit noise and external electrical noise generated from high Electromagnetic generation sources such as welders and high energy inductive devices.

Technical details about both of these important AE test factors will be discussed.

**COMMERCIAL PRESENTATIONS**

**BUSINESS MEETING**

**AWARDS BANQUET, Omni Orrington Heritage Ballroom**

**THURSDAY, JUNE 12, 1997; ASTM-E07.04 MEETING**

**FRIDAY, JUNE 13, 1997; ASTM-E07.04 MEETING**

# ABSTRACTS OF ORAL BRIEFS

## 14th International Acoustic Emission Symposium & 5th Acoustic Emission World Meeting

August 9 - 14, 1998, Big Island, Hawaii, USA

ORAL BRIEFS #1 Session Chair: Yakichi Higo (Precision And Intelligence Laboratory, Tokyo Institute of Technology)

Effect of Fatigue Crack Growth Rate on Detected Acoustic Emission in Bridge Steels  
David McColskey (National Institute of Standards and Technology)

Results will be presented on an in-progress acoustic emission (AE) study of fatigue-crack generated AE conducted on as-received A36, A588, A572, A514 and field-aged A7 bridge steels and as-received 2024-T351 aluminum. The materials were machined into samples that typically measured 203mm x 406mm x 25mm thick. A 25mm long notch was cut in the center of each sample. The samples were fatigue cycled (0.3Hz) at constant DK (stress intensity) values in order to gather AE data while maintaining constant crack growth rates of  $2 \times 10^{-8}$  m/cycle ( $10^{-6}$  in/cycle) and  $2 \times 10^{-7}$  m/cycle ( $10^{-5}$  in/cycle). These low fatigue crack growth rates (and lower) are representative of actual fatigue crack growth rates realized on bridge structures. Acoustic emission signals were monitored using four wideband high-sensitivity sensors developed at NIST-Boulder and four commercial resonant sensors, coupled to a digital waveform-based acoustic emission system. Eight digital waveforms were gathered for each recorded AE event. Only the AE generated during the peak 10-15 % of the loading cycle were incorporated in the presented data. The collected AE waveforms were reviewed to separate the real crack-based events from the events generated by extraneous sources. The average number of real crack-based AE events per cycle was determined from the reviewed data. The data for steel clearly demonstrates that a number (0.01 events per cycle to 0.91 events per cycle) of real, crack-based AE events were generated during the higher fatigue crack growth rate. However, the lower fatigue crack growth rate data indicated almost no generation of real crack-based AE events.

Acoustic Emission Monitoring of a Pressure Test of a Model Nuclear Reactor Containment Vessel.

A. G. Beattie (Sandia National Laboratory, now at Physical Acoustics Corp. Corrales, NM)

A mixed-scale steel model of a boiling water reactor (BWR) containment vessel was pressurized to failure. The instrumentation included an acoustic emission source location system. The real time AE monitoring predicted the failure but not its location. Post test analysis showed general agreement between the location of acoustic emission sources and the regions of distortion and failure. The analysis also gave the pressure dependence of different emitting regions. The

emphasis of this talk will be on the post test analysis of the acoustic emission data and the results of this analysis. The overall performance of the model itself will not be discussed.

**ORAL BRIEFS #2 Session Chair: Mikio Takemoto (Aoyama Gakuin University)**

**Acoustic Emission Characterization on Failure in Toughened Resin Carbon Fabric Composite**  
Toshiyuki Uenoya (Technology Research Institute of Osaka Prefecture, Izumi, Osaka, Japan)

Acoustic emission (AE) technique is used to characterize the progression of internal micro failure during the deformation of toughened composite materials. Cyclic short-term tensile creep tests were performed on two types of plain woven carbon-fiber fabric/epoxy laminate specimens with a center circular hole notch. During each test, AE activity was monitored using various AE intensities, which were analyzed in detail. Also, an AE analysis method is utilized to recognize the fracture mechanism during a tensile straining and to characterize the evolution of internal failure. Simultaneously, thermoelastic stress analysis (TSA), which can offer 2-dimensional distribution pattern of the failure, was employed to examine the development of damage. AE source were active at different locations near the center hole and the majority of the AE was practically found to originate in damaged regions which were determined through TSA. AE location and highly concentrated AE events demonstrated that the damage was bigger in size and more serious in the unmodified-matrix material than the modified-matrix material.

Felicity effect of AE from the laminated composites appeared at a normalized applied stress larger than about 0.55 for each material whereas the initiation of damage detected by using TSA technique was at a normalized stress larger than about 0.6. Although AE technique can not illustrate the detailed damage distribution as compared with TSA technique, the AE evolution responded more sensitively to the damage initiation and development in the composites than the change of TSA information.

An employed correlation criterion between AE amplitude and rise-time of AE signals is based on a similar concept to a rising-slope criterion proposed by one of the authors. The AE analysis almost perfectly distinguished various source mechanism of AE signals of the laminated composites, which was favorable to explain the effect of matrix-modification on the AE characteristics of fracture in the composite material, also the damage evolution due to toughening matrix material.

**Acoustic Emission Observation of Fatigue Damage Development in Laminates Within Loading Cycles**

Y. A. Dzenis (University of Nebraska-Lincoln, Lincoln, NE 68588-0526)

Fundamental relation between overall damage and failure process in laminates under cyclic loading and damage development within cycles is addressed. Development of damage in an un-notched graphite-epoxy laminate subjected to low-cycle fatigue loading is studied by acoustic emission analysis. Overall time history of acoustic emission is separated into emission during loading and unloading portions of the loading cycles. Histories of the locations of the AE sources and distributions of the acoustic events over the stress range are analyzed. Qualitatively different time histories and distributions over the stress range are obtained for the emission generated during loading and unloading. It is concluded that most of the new damage is developed during the loading portions of the cycles. The emission during unloading is attributed to friction

between crack faces, with possible exception for the emission at highest stresses. The location distribution of the AE sources during loading is fairly random to failure, indicating that the dominating fracture process in an un-notched laminate is scattered damage development. The time history of the new damage exhibits initial, steady, and final damage development stages. The new damage is developed over the entire stress range with higher damage rates at higher stresses. This latter result may explain the observed effects of cycle shape on the overall behavior of laminates under cyclic loading.

ORAL BRIEFS #3: Session Chair: Masayasu Ohtsu (Kumamoto University)

Application of Acoustic Emission for the Slope Failure Monitoring in Pyroclastic Flow Area  
Tetsuro Fujiwara (Nippon Koei Co. Research and Development Center, Ibaraki 300-12 JAPAN),  
Keiichi Monma (Public Works Research Institute, Ministry of Construction, Government of  
Japan, Tsukuba-city, Ibaraki 305 JAPAN), and Akichika Ishibashi (Nippon Koei Co.)

The Shirasu, which is widely distributed over southern Kyusyu, is characterized by gray soft rock derived from pyroclastic flow sediment. In Shirasu area, slope stability is frequently disturbed by heavy rain, and Shirasu slope failures caused some deaths every year. It has become very important to predict these disasters. This paper on application of acoustic emission technique in the field of Shirasu slope failure prediction presents the experimental findings on the real scale slope (4m x 5m) and laboratory tests.

In applying AE technique to monitor ground motions, so called wave-guides, which are devices designed to transmit elastic waves are often used. With the aid of wave-guides we have conducted slope failure on the real scale slope, to study the applicability of AE technique in detecting ground movements and in predicting slope failures. On the other hand the slope monitoring by video camera and other sensors (inclination meters and deformation meters) to compare and analyze AE data was carried out.

The slope failure in this experiment is caused by the slope foot cutting and water penetration. AE technique could predict the occurrence of slope failure about thirty minutes before it. It was found that a minute ground motion can be clearly monitored by AE event. This finding identifies potential of AE for Shirasu slope failure predictions .

Structural Integrity and Remnant Life Evaluation from Acoustic Emission Monitoring  
Brian R. A. Wood and Robert W. Harris (Metacoustics Pty. Ltd, Blacktown, New South Wales,  
2148, Australia.)

It is now in excess of 30 years since modern acoustic emission techniques (AE) have been employed in industry. In that period great advances have been made in both AE instrumentation development and applications including basic functions such as defect/leak/source detection and location, and some source identification.

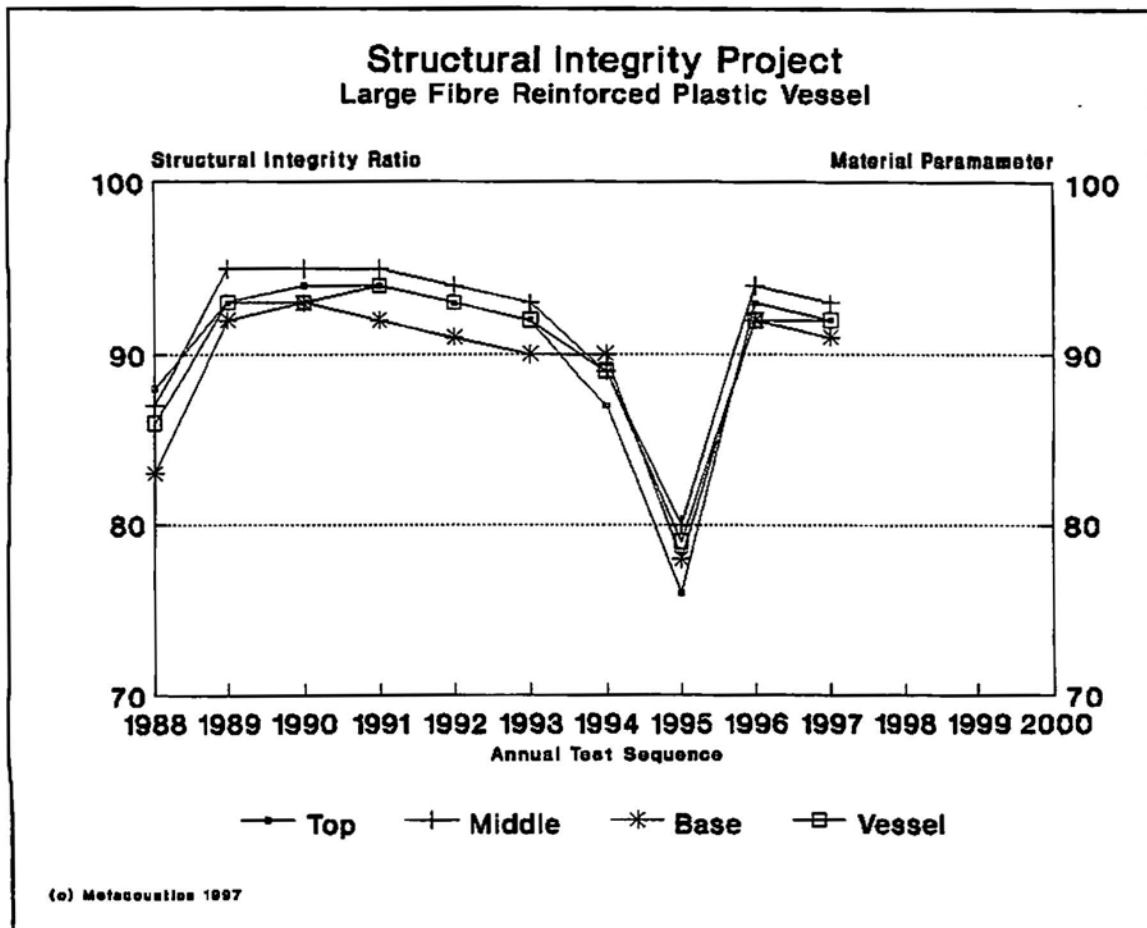
The industrial community which, in many countries, has been permitted to operate under a Self-Regulation Criteria, in some instances has demonstrated a tendency to use economic and convenience constraints to determine their operating scenarios. The desire to make manufacturing plants and structures more productive, has resulted in them being operated under conditions which exceed those envisaged during the initial design. While these plants and

structures still operate efficiently and safely, the real structural integrity and remnant life evaluation is unknown.

The changes in operating philosophies have created a need for more precise and sophisticated monitoring and analysis techniques to provide specific information about structures, manufacturing plant, and operating techniques. The application of selected acoustic emission and signal/waveform analysis techniques combined with a range of physical parameter measurements, has resulted in an analysis technique which can be used for the evaluation of structural integrity and remnant life of any monitored structure. The technique has been successfully used on civil structures, industrial plants and mining equipment and on metal, composite and geological materials.

The proposed paper will discuss the bases employed in the monitoring techniques employed, and describe a variety of industrial applications and case studies where the approaches have been used to demonstrate the successful application of the technique.

This paper will present the culmination of results obtained in over 30 years of research and industrial application which has resulted in the development of these techniques. While the data used spans 30 years, the research is current and this is the first time that this information has been published in the public domain.



ORAL BRIEFS #4 Session Chair: Yasuhiko Mori (College of Industrial Technology, Nihon University)

#### Reciprocity Calibration of Acoustic Emission Transducers

Hajime Hatano (Department of Applied Electronics, Science University of Tokyo)

The present paper reviews and discusses the background, methodology and application fields of absolute calibration of acoustic emission transducers by means of the reciprocity method. In acoustic emission measurements, transducer calibration is of significant importance, not just for quantitative evaluation, but also for mutual comparison of data obtained by different laboratories. For characterizing and calibrating acoustic emission transducers, a number of methods utilizing various mechanical sound sources, for instance, a falling steel ball, a breaking pencil lead, a gas jet, a sand blast, and an electric spark, appeared in the literature. However, by these methods it was difficult to obtain absolute sensitivity, because the characteristics of the sound sources were not clear enough, and the reproducibility from test to test was inadequate. A seismic surface pulse method was developed by Breckenridge and his collaborators, wherein the fracturing of a glass capillary is employed for the sound source and a capacitive transducer is used for the reference.

Calibration of acoustic emission transducers by the reciprocity method was proposed more than two decades ago, and has since been employed by transducer manufacturers and laboratories. The procedure for reciprocity calibration has been specified as NDIS 2109 by the Japanese Society for NonDestructive Inspection. Recently, in addition to the magnitude of sensitivity, phase characteristics and impulse responses were obtained. Frequency characteristics of amplitude and phase of absolute sensitivity were measured on the basis of the newly derived complex reciprocity parameters, and the impulse responses were determined through inverse Fourier transform. An outstanding advantage of the reciprocity method is that absolute sensitivity, including frequency characteristics and impulse responses, both to the Rayleigh wave and longitudinal wave, can be determined by means of purely electrical measurements without the use of mechanical sound sources or reference transducers.

#### Finite Element Prediction and Experimental Measurement of Lamb Wave AE Signal Reflections in Finite Plates

W. H. Prosser (NASA Langley Research Center, Hampton, VA), M. A. Hamstad (University of Denver), J. Gary, and A. O'Gallagher (National Institute of Standards and Technology, Boulder, CO)

A dynamic finite element method (DFEM) has been developed at NIST Boulder which allows the prediction of acoustic emission (AE) waveforms in plates. Previous research has confirmed the validity of this technique for predicting the direct arrivals of AE signals in both thin and thick isotropic metal plates. Effects on AE waveforms of a number of variables such as source characteristics (both rise time and spatial distribution), plate thickness, and finite element cell dimensions have been previously investigated. In this current work, the capability of the DFEM for predicting AE signals in finite plates including the effects of reflections and mode conversions from lateral boundaries was experimentally confirmed. Both in-plane and out-of-plane simulated AE sources (pencil lead breaks) were modeled which preferentially generate the lowest order symmetric and anti-symmetric Lamb modes, respectively.

Experimental measurements were made with an absolutely calibrated NIST AE sensor. For the out-of-plane source, several different source, receiver, and plate geometries were considered such that reflections at both normal and oblique incidence angles were obtained. The superposition of multiple reflections was also studied. For all cases, the DFEM predicted waveforms were in excellent agreement with experimental measurements. Likewise, for the in-plane sources, reflections at normal and oblique incidence angles were considered. In addition, the DFEM predicted, and experiments confirmed, symmetric Lamb modes which were created by the mode conversion of shear and Rayleigh waves interacting with the plate edge and corner, respectively. Again, excellent agreement between the DFEM predictions and experiment was obtained. This ability to predict AE signals including reflections is a major advantage in comparison to most analytical approaches which can only be used for infinite plate geometries. Furthermore, AE signals in most realistic test geometries, especially laboratory coupons used for materials characterization, are heavily influenced by reflected signal components.

#### Inspection of Steel Bridges with Acoustic Emission

Arup Maji (Department of Civil Engineering, University of New Mexico, Albuquerque, NM 87131)

Acoustic emission (AE) monitoring as a prospective method of inspecting large steel bridges discussed. The application of Acoustic Emissions for structural inspection has been difficult due to extraneous noise, attenuation of P-waves, and the subjectivity of various AE parameters used. A new approach to evaluating AE signals involves the use of dispersive guided plate waves (Lamb waves) that can be detected over long distances, and have relatively little attenuation. The dispersive nature of these can be an indicator of the distance traveled by the wave, and hence determine the source location. Laboratory experiments also confirmed that since individual components of a structure tend to vibrate in specific modes, AE sources associated with those modes also repeat themselves at the time interval corresponding to those specific frequencies. Hence, by associating the AE repetitions with the structural modes it may be possible to identify the areas where the AE signals originate. Laboratory scale bridge tests and field testing on an existing highway bridge provide valuable insight into the possible use of Lamb waves and vibration modes for locating AE sources in large structures.

#### AE Research in the Petrochemical Industry

Joseph Krynicki (Exxon, Petroleum Environmental Research Forum)

The current industrial practices of acoustic emission testing (AET) have limited reliability for on-stream use in discriminating sources of background noise from corrosion and crack growth energy release. Therefore, a joint industry program, "Advanced Acoustic Emission for On-stream Inspection", was initiated through PERF (Petroleum Environmental Research Forum). The objective of this program is to develop and implement advanced AET technology in a way that will enable reliable use of AET during on-stream inspections. These inspections should identify corrosion and crack growth of structural integrity significance.

The program is divided into three focus areas: accurate source location, quantitative AE/FFS relationship, and reliable source discrimination. The program is pursuing these efforts with theoretical and supporting experimental efforts. Issues regarding background noise and

monitoring at elevated temperatures (850° F) are also included. This presentation will discuss program objectives, technical challenges, and invite the participation of technical experts.

**ORAL BRIEFS #5 Session Chair: Karyn Downs (Lockheed Martin Astronautics)**

**Acoustic Emission Responses of Thermal Barrier Coatings During Four Point Bend Tests**  
C. K. Lin (Institute of Materials Engineering, National Taiwan Ocean University, Keelung 202, Taiwan, ROC), U. Senturk (The Thermal Spray Laboratory, Department of Materials Science and Engineering, SUNY, Stony Brook, NY 11794-2275), R. Lima, P. Y. Lee, and C. C. Berndt (SUNY at Stony Brook)

Thermal barrier coatings (TBCs) with different preparing conditions (with and without bond coat, with and without cooling) were air plasma sprayed onto mild steel substrates. The bond coat and ceramic coating were NiCrAlY and yttria-stabilized zirconia respectively. In situ acoustic emission (AE) were used to monitor crack growth and propagation of thermal barrier coatings during the four point bend tests. The load-displacement curve obtained from the four point bend tests can be separated into three different stages (elastic and plastic regions, and unloading). Meanwhile, AE characteristics such as ring down counts, event duration, peak amplitude, and energy were recorded and analyzed to evaluate different cracking mechanisms. It is noticed that most AE activities were detected during the plastic region of the load-displacement curve. Most macrocracks presented at this region as well. It is also observed that TBCs with bond coat prepared without cooling of substrates during spraying exhibited the fewest AE activities (cracks) during the tests.

**Sources Of Acoustic Emission From Rubbing Surfaces**

R. J. Boness, S. H. Benabdallah and T. Liu (Royal Military College of Canada, Kingston Ontario, Canada)

This paper is concerned with the measurement and subsequent analysis of acoustic emission (AE) signals obtained during the sliding wear testing of both lubricated and un-lubricated combinations of steel and silicon nitride surfaces. In the systematic wear testing of advanced engineering materials, wear maps are frequently used to determine regions of high levels of wear. These regions, on a wear map, are normally specified in terms of the operating parameters, load and sliding speed, and are further identified by the dominant wear process occurring. However in cases in which more than one wear mechanism is present during a given test, the transition from one wear process to another may not be detected. In this work SEM and microscopic examination of the worn surfaces confirm that the time dependent nature of the acoustic signal is able to detect the predominant wear process occurring and the presence of wear reducing additives. Further third body abrasive wear tests show that both wear and acoustic emission signals increase with alumina particle concentration added to the lubricant. For the steel surfaces a direct empirical relationship between integrated rms signal and the wear volume removed from the test ball in a ball-on-cylinder test apparatus has been obtained. Consequently, acoustic emission monitoring offers a novel method for studying the complex wear mechanisms that exist between loaded surfaces in relative motion.

**Unique Mineral Engineering Applications Of AE/MS Techniques**  
H. Reginald Hardy, Jr. (The Pennsylvania State University)

For some 30 years the Penn State Rock Mechanics laboratory has been involved in basic and applied studies involving the application of Acoustic Emission/Microseismic (AE/MS) techniques. This paper will first briefly review a number of earlier field related studies, including those associated with the evaluation of the mechanical stability of geologic structures such as mines, gas storage reservoirs and work slopes. The main thrust of the presentation, however, will deal with a number of recent, and somewhat unique, mineral engineering applications. These include the study of fluid flow through broken rocks, flotation control in mineral processing, the Kaiser effect in salt, and the monitoring of coal and rock cutting.

**Acoustic Emission Signal Generation During Resistance Spot Welding**  
Chang-Sheng Chien, Elijah Kannatey-Asibu, Jr. (Dept. of Mechanical Engineering and Applied Mechanics, The University of Michigan, Ann Arbor, MI 48109-2125)

Resistance spot welding has been used for several years as a reliable technique for joining sheet metal. It is the primary method by which sheet metal parts are joined in the automotive industry. The quality of the resulting welds can be monitored using non-destructive testing (NDT) techniques such as ultrasonic detection, radiography, and acoustic emission (AE). AE is the elastic energy that is spontaneously released by materials when they undergo deformation. AE can also be thought of as the naturally generated ultrasound created by local instabilities within a material. Acoustic emission differs from other non-destructive testing methods in two significant respects. First, the energy that is detected is released from within the material rather than being supplied by the NDT method. Second, AE is capable of detecting the dynamic, real-time response of processes.

Earlier work involving AE monitoring of resistance spot weld quality has been based primarily on total AE counts and threshold, for expulsion detection. To date, no analytical work has been done to model AE signal generation during resistance spot welding (RSW). This paper models AE signal generation during resistance spot welding. It focuses on analysis of AE generation during phase transformation, nugget expansion, and expulsion, and is based on a one-dimensional heat flux for both constant and sinusoidal input currents. With this as basis, a model is developed for the nugget pressure. This is then used to model AE generation during nugget growth and expulsion. Since AE is capable of detecting the dynamic, real-time response of processes, the signal modeled can be used as a basis for weld quality control.

The results show that with sinusoidal input, the initial stages of nugget growth is discontinuous. The discontinuous melting is due to the fact that the heat is initially dissipated faster than is supplied. Once the average temperature is raised to a level that the heat dissipation is slower than the heat input, continuous melting begins to occur. The initial discontinuous melting results in several AE signals from melting being generated.

## Amplitude and Frequency Characteristics of Simulated Acoustic Emission Signals as a Function of Propagation Distance in Thick-Walled Composite Tubes

David McColskey (National Institute of Standards and Technology, Boulder, CO)

Results will be presented from an in-progress study of certain aspects of propagation changes of acoustic emission (AE) signals in filament wound thick walled E-glass/graphite-epoxy hybrid composite tubes. The tubes have an outside diameter of approximately 30 cm, a wall thickness of approximately 1.6 cm and lengths of up to 3 m. Acoustic emission was monitored with 6-8 wideband high-sensitivity sensors connected to digital storage oscilloscopes or to a digital waveform-based acoustic emission system. The AE signals were bandpassed from 15 kHz to 500 kHz or from 50 kHz to 1 MHz, in the two different systems. Characteristics of simulated AE were measured on the tubes under several conditions: 1) without nitrile rubber liner, 2) with nitrile rubber liner, 3) with nitrile rubber liner and water filled, and 4) with nitrile rubber liner, water filled and internally pressurized. Acoustic emission signals were generated on the tube surface using the standard pencil lead break method. The generated signals were captured and stored for analysis. Initial results indicate an increase in the attenuation of AE with increasing distance from the source as well as with increase in internal pressure. The multiple paths to the sensors modify normal distance attenuation characteristics. Typical waveform signals and frequency spectra will be presented to demonstrate changes in characteristics of signals as a function of propagation distance and internal conditions.

ORAL BRIEFS #6 Session Chair: Roger Hill (The Nottingham Trent University)

### Investigation of Crack Formation in Salt Rock

Th. Spies (Federal Institute for Geosciences and Natural Resources), J. Eisenblätter and Gerd Manthei (Gesellschaft für Materialprüfung und Geophysik)

The suggested paper deals with the application of acoustic emission measurements in salt mining especially in the case of the disposal of hazardous waste underground. Salt rocks reveal a large variety of geomechanical behavior. Anhydrite and salt clay are examples for brittle behavior resulting in the formation of fracture. On the other side, rock salt and some potash minerals are capable of creep deformation without occurrence of fracture in a large range of the conditions of state. This is one reason, why rock salt is considered as a favorable host rock for the safe disposal of hazardous waste underground. Nevertheless, creep deformation of rock salt will be accompanied by dilatancy due to cracking if a certain level of deviatoric loading has been crossed. These so-called 'microcracks' are small fractures of single grains or grain boundaries. As a consequence of increasing density of microcracks, creep failure, e.g. the formation of larger fractures, can occur and permeability can increase in the long-range. For the assessment of the stability of underground cavities and also for the assessment of the hydraulic integrity of the rock salt, dilatant material behavior in the rock has to be identified.

For this purpose a variety of geotechnical investigation methods can be applied but for the direct detection of cracks, acoustic emission measurements in situ are necessary. Event rates and signal amplitudes can be determined using one probe only. This can characterize the temporal development of crack formation in a very limited part of a mine, for instance in a single pillar. To monitor larger areas multichannel-equipment is used. The spatial and temporal variations of the event rates, the locations of acoustic emission events and their magnitudes are determined to characterize crack formation more precisely.

A 24-channel equipment operating in the frequency range from 1 to 100 kHz will be briefly described. The results to be discussed have been obtained in German salt mines. The determination of event magnitudes using maximum signal amplitudes will be emphasized. It is usually observed that acoustic emission events are located in the vicinity of the cavities in the rock salt showing larger accumulations in pillars and in the roof between cavities. In presence of anhydrite layers in the rock, acoustic emission activity is also observed farer away from the cavities, in the rock salt as well as in the anhydrite. For both types of activity differences in the spatial-temporal variations of locations and magnitudes will be outlined and the geomechanical implications will be discussed.

#### **Absolute Measurement of Transient Dynamic Normal Velocity of Surface by Broad Band Velocity Sensor**

**Byoung-Geuk Kim and Sekyung Lee (Korea Research Institute of Standards and Science),  
Manabu Enoki and Teruo Kishi (The University of Tokyo)**

Several broad-band sensing technologies have been developed so that surface motions can be detected without any deformation. So far, any technology for broad-band sensing of the transient dynamic normal velocity of surface, in particular for direct sensing without additional processing, has not been reported. In the present work, broad-band and direct sensing of the transient dynamic normal velocity of an object surface and evaluating its absolute value were realized by using a sensor fabricated with a piezoelectric polyvinylidene fluoride (PVDF) film and a polyvinyl chloride (PVC) back-load and a PVC wear plate. The transient output signal from the sensor obtained by test employing well-defined steplike force, at the epicenter of a steel plate, showed very good agreements with the dynamic normal velocity calculated by using a Green's function and a simulated source function. The output was proportional to the dynamic normal velocity of surface, and the frequency-dependent sensitivity for the velocity was flat within the deviation of - 3.8 dB for the average in the frequency range up to 2 MHz. The transient dynamic normal velocity of surface could be absolutely determined by using the sensor calibrated by theoretical one.

#### **Set Of Parameters For Acoustic Emission Instruments**

**O.B.Tarutin (The Institute For High Pressure Physics RAS, Russia)**

The passive acoustic emission measurement is one of the popular method of non-destructive diagnostics. History of creation of the instruments for AE testing brings us a lot of the AE signal parameters. Several of them are common for different instruments, but another change from one to another. The philosophy of the parameters introducing reflects both attempts to measure physically based values and, for another hand, technological level of corresponding years, which limited the possibilities to realize parameters desired. As a result, there are no universal method for AE testing, there are no common parameters set for AE instruments, and AE diagnostics itself is a mixture of science and art. Last years give us new possibilities to process AE signal, so, it is a time to reconsider parameters of AE signal, moving from technologically restricted to more physically grounded ones. Permanent acoustic emission is connected with leaks through defects like holes, splits. Its intensity is characterized by the average amplitude of permanent AE signal. First devices rectified both halves of the signal's oscillation and averaged it with the help of RC-chain. This type of averaging gives mean amplitude. In electrical engineering, another

method of averaging is used. It is based on the equality of power dissipation for AC signal and so-called effective DC one. In this case one must calculate mean of squared AC signal and extract square root. Such method is known as RMS (Root Mean Squares). But, designers of several AE instruments named with RMS another procedure. So, now we have an expression "True RMS" in several instruments to underline the Root Mean Squares algorithm. Third useful averaging algorithm is mean logarithm of fully rectified AE signal. Sometimes it is called ASL. All three methods are used in AE instruments. In analog systems, the mean amplitude takes minimum electronic components. From physical viewpoint, RMS is proportional to square root of the signal's energy, but the mean amplitude and ASL have no direct physical sense. In general, RMS lies closer to peaks of AC signal, ASL - closer to X axis and the mean amplitude lies between them.

The averaging algorithm tightly connected with practically used characteristic, the noise level. When preparing the AE instrument for measurement, user adjusts so-called level to be above the noise, but not far from it in order to sense even pure AE signals. User decreases the level until the instrument begins to indicate random noise peaks, ones per several seconds. This noise value is often presented in the AE instrument's manual. Physically this level strictly depends on the noise value, frequency range and noise distribution. The RMS lies closer to the noise level, then other two average values: the mean amplitude and ASL. So, there are two arguments to establish the RMS as common parameter for AE instruments.

Pulse acoustic emission is associated with cracks in material of objects investigated. Acoustic wave propagates from its source to sensors and reaches its in different arrival time. When arrival time for each sensor is known, one can calculate a location of the source. Usually the arrival time is detected, when electric signal from the sensor first crosses the threshold level up. It is clear and corresponds to most direct way of the acoustic wave propagation. But, two factors darkens the situation. In order to increase sensitivity, so-called resonant sensors are used for acoustic pulses measurement. According to physical resonance, the sensor selects oscillations with narrow frequency range from wide frequency range of acoustic wave and it provides better signal to noise ratio, because the noise is proportional (not directly) to the frequency bandwidth. Due to resonance, an amplitude of electric signal does not directly correspond to the acoustic vibration velocity amplitude, but the amplitude increases step by step, pumped by the vibration. The better resonant characteristics, the better sensitivity and, unfortunately, the longer time interval from acoustic pulse start to maximum amplitude of electric signal. Moreover, there is no direct connection between acoustic and electric maximums. Second factor is accuracy dependence on propagation length. The more distance, the lower amplitude of acoustic wave. Taking into account, that the level for all sensors approximately the same, we obtain, that electric signal on closest to the source sensor will cross the level just after pulse's beginning, but on the farthest sensor it will cross the level closer to maximum of amplitude, several oscillations after pulse's beginning. It will cause certain error in the location calculation. To obtain more accurate calculations, it is worth to recommend to use arrival time of the maximum of electric signal. The maximum of electric signal is one of the most physically based and simply measured parameter. There is one remark. When the signal's amplitude is comparable with noise, an error of amplitude measurement arises because of the noise and signal superposition. To minimize the error, it is worth to subtract the noise from data measured, but take into account a nonlinear rule of addition random noise with the signal. Several AE instruments provide registration of noise just before the pulse beginning, it can help to subtract the noise. A problem of noise superposition with the signal touches not only the maximum amplitude, but every parameter of low signal, depended on the amplitude: so-called MARSE and energy.

In first AE devices, an integral parameter (amplitude by duration) of the acoustic pulse was measured as a square of an "envelop" of electric signal in axes amplitude vs time. The envelope was created by RC-chain and approximately equal to the integral of amplitude by time. Now this parameter is known as MARSE. It is easy to measure MARSE, but this parameter has no direct physical sense. Advanced technology allows to measure more physically based parameter, true energy: integral of squared amplitude by time. It is directly proportional to the acoustic pulse energy. Nevertheless, MARSE can be used to compare pulses from the same source with same shape. MARSE depends on the shape of pulse at the same energy. So, there is a reason to choose a "true energy" as an integral parameter in future devices.

Traditionally, the timing points of acoustic pulse (crest) are measured with digital counts technique, based on the points, where the signal crosses the level. Well known are "Peak timeout", SCETO, "dead time". Despite of its simplicity, this method gives good results. Dead time blocks the measurement in a channel after previous pulse execution for two reasons, to allow an acoustic ring to die out and to initialize an electronic environment of the channel to be ready to next pulse. In one AE instrument the dead time is called rearm time. In contemporary instruments, there are no technical reason to allocate time for the rearm, so, it is possible to decrease the dead time down to zero and to do continuous measurements.

There are pulse counting parameters in several AE instruments: peak count from start to maximum, from start to end and so on. When using resonant sensor, such counts reflects resonant frequency of the sensor itself and practically no more. With wide-band sensor (non resonant) counts can present dominant frequency of the acoustic pulse. But, from contemporary point of view, it is better to digitize the wave and calculate frequency distribution with Fast Fourier Transform. Many parameters and technical characteristics of AE instruments depend on type of the sensors used. Resonant one has up to 40 dB peaks and pits on a response-frequency plot. It makes several parameters of AE instruments unusable and does not use, for example, flatness of amplitude-frequency characteristic of an amplifier. Wide band sensors can inspire physical sense into most parameters and can use good electrical characteristics of the instruments. We can expect new types of sensors, based on another physical principles, which could combine good acoustic to electric response with lower noise, than it is possible today.

#### **An Investigation Of The Thermal Damage In Aluminum Alloy By Laser Ultrasonic And Conventional NDT Techniques**

**A. Maslouhi, R. D. Leblanc (Université de Moncton) and D. S. Forsyth, A. Fahr (Institute for Aerospace Research NRC)**

Aluminum alloy (AA7050-T7451) has applications in aircraft structures that can be subjected to abnormally high temperatures as a result of accidental hot exhaust leaks or engine fires. The conventional method of assessing the mechanical properties of heat-damaged parts requires both hardness and electrical conductivity measurements and can not be used on in-service parts because of indentations created by hardness testing procedures. The state of in-service parts is currently determined by assuming that the alloy is in the fully-annealed condition, and replacement is indicated if the conductivity value falls outside the manufacturer-specified range for AA7050-T7451. The cost of repair and replacement under this criterion is extremely high. A non-destructive inspection technique is necessary to properly assess the extent of the heat-damage, thus providing a scientific basis for repair or replacement of the affected zones. The effect of exposure of 7050 aluminum alloy to high temperatures has been studied using ultrasonic techniques. Contact, immersion, and laser ultrasonic techniques were used. The

relationships of parameters of ultrasonic propagation with static material properties and material microstructure were evaluated. Pattern recognition techniques were used in conjunction with immersion ultrasonic measurements to distinguish between different heat treatments. It was shown that attenuation measurements at high frequencies can provide an indication of material microstructure and thus mechanical properties of 7050 aluminum.

The results show that ultrasonic wave attenuation measurements using laser generation and detection at high frequencies are sensitive to precipitate phase changes in the AA7050 alloy, and therefore can provide some indication of mechanical degradation due to high temperature exposure. Overall, laser ultrasonic measurements provide valuable information that can compliment electrical conductivity tests in characterizing heat-affected zones of aluminum aircraft structures

### **Oral Briefs not presented at the Conference**

#### **Identification of Acoustic Emission Sources Using a Neural Network**

Xi-qiang Liu (University of Science and Technology of China, Beijing, China), Zhizhen Zheng, Ping Shen, Xuanhui Yang (Center for Earthquake Data and Information, State Seismological Bureau, Beijing, China)

An artificial neural network (ANN) algorithm has been applied to the automatic picking of local acoustic emission P and S phase. For a set of local three-component acoustic emission data, a variety of features for signal detection and phases identification were analyzed in terms of sensitivity and efficiency. To compare the performance of these attributes in discriminating the local P and S phases, eight attributes are discussed in this study. They are Rectilinearity (Jurkevics, 1988), Planarity (Jurkevics, 1988), Long-axis incidence angle (Jurkevics, 1988), Short-axis incidence angle (Jurkevics, 1988), Degree of polarization (Cichowicz, 1993), Ratio of horizontal power to total power, Ratio of short-term average (STA) to long-term average (LTA) (Allen, 1978), Changes of autoregressive (AR) coefficients (Haykin, 1991). Comparing the performance of each feature indiscriminating the local P and S phases, five features were selected as input attributes of the ANN P and S phases picker: (1) degree of polarization, (2) the ratio between short-term average and long-term average, (3) the ratio between horizontal power and total power, (4) auto-regressive model coefficients, and (5) the short-axis incidence angle of polarization ellipsoid. The five attributes were calculated in the frequency band of 2 to 8 Hz with a 2.5-sec moving window. This choice of frequency band and window length is appropriate for local micro-acoustic emission monitoring. The result of preliminary training and testing with a set of local acoustic emission recording show that the ANN P and S phases picker can achieve a good performance in identification and onset-time estimation for local P and S phases. In overall result, 83% correct rate of phases identification has been achieved by the trained ANN P and S phases picker, 75% of them are precisely picked with less than 0.10 sec onset time error. We believe that the method presented here is a promising approach to automatic phases identification and onset-time estimation.

A genetic algorithm has been applied to the automatic location of local marine array full wave train acoustic log. On the basis of identified phases and known 3-D velocity structure, we calculate theory travel time in 3-D velocity structure. In the process of conversion, we use the genetic algorithms. Considering large parameter space in the initial iterations and small parameter space in the final iterations, this paper gives mutation probability which is a large value in the initial iterations and small value in the final iterations. The formation of the mutation probability is linear and exponential with iterations. It is found that the exponential function is a

more effective method. Using the exponentially reduced mutation probability, the acoustic emission location is obtained through genetic algorithms. The residual of the source location is very small.

The objective of the work described in this article is to implement the artificial neural network for the P and S phases picking and genetic algorithms for accurate location, which is an important task for local location of acoustic emission source.

**Acoustic Emissions During Anelastic Strain Recovery of Cores from Deep Boreholes**  
Lawrence W. Teufel (Sandia National Laboratories and New Mexico Institute of Mining and Technology, Socorro, New Mexico 87801)

Several studies have proposed that microcracks in rock may, in some manner, be related to the pre-existing *in situ* stress field at depth, and that the distribution of microcracks in a rock sample may be related to its unloading history. This hypothesis was tested by monitoring acoustic emissions and compressional wave velocity measurements during anelastic (time-dependent) strain recovery measurements on sandstone, siltstone, and chalk cores, immediately after the cores were retrieved from 2.7 to 3.2 km deep boreholes. Strain recovery occurred in all of the cores, and acoustic emissions were always detected. The acoustic emission rate decreased exponentially with time, similar to the strain relaxation behavior of the cores. The cumulative number of acoustic emission events was linear with volume expansion of the cores. No significant decrease in velocity occurred during strain relaxation, monitored 6-52 hours after the cores were cut, because the strains were small (less than 300 microstrains). However, laboratory measurements of compressional velocity on relaxed, air-dried cores show a well-defined anisotropy in low porosity cores, which has a strong preferred orientation of the principal recovery strains. The slowest velocity was in the direction of maximum expansion. The field and laboratory results suggest that a statistically aligned microcrack population evolves during strain relaxation, with microcracks opening more in the direction of maximum strain recovery. It is proposed that the degree of anisotropy is dependent on the relative difference in the magnitude of the *in situ* stresses and corresponding strain relaxation, as well as the degree of heterogeneity of the rock. In high porosity rocks the fractional increase in porosity due to relaxation microcracks is much smaller. Therefore, differential expansion of a core, due to opening of relaxation microcracks with preferred orientations, does not produce a measurable anisotropy.

**Pattern Recognition of Artificial Neural Network to Waveform Data**  
Shifeng Liu (Nondestructive Testing Lab, Mechanical Engineering Department, Tsinghua University, Beijing 100084, P. R. China)

Pattern recognition of artificial neural network is being applied for some waveform data. The data were taken from acoustic emission monitoring of pressure vessels and underground pipelines, from acousto-ultrasonic testing of composite materials. The characteristic data for the input of neural network were obtained from original waveform data by the various methods respecting to the different individual data characteristics. The pre-processing methods include some advanced modern spectrum analysis methods. The neural networks are basically BP networks with some significant modifications such as single data group training for the data type of shortage of good quality data.

# **AECM-6 Symposium Program**

1 JUNE 1998: EDUCATIONAL SEMINAR, Introduction to Acoustic Emission in Composite Materials

2 - 4 JUNE 1998: San Antonio, Texas

## **CARP CODES AND PROCEDURES**

John Teti Plenary Lecture: Acoustic Emission: A Mature NDT Technology with Worldwide Applications and Standards S. Vahaviolos, Physical Acoustics Corporation

Acoustic Emission Testing of Carbon Fiber Composite Offshore Drilling Risers  
C. Barnes, G. Ramirez, University of Texas at Austin

Acoustic Emission Testing of ASME Section X FRP Pressure Vessels  
M. Droge, Dupont

Recommended Procedure for Determination of Design Strain Limit in FRP Specimens  
P. Ziehl, T. Fowler, University of Texas at Austin

Standard Test Method for Acoustic Emission Examination of FRP Fan Blades  
T. Crump, Dupont

## **RESEARCH AND DEVELOPMENT IN COMPOSITE TESTING**

Acoustic Emission Source Simulation for Integrity Evaluation of UD-GRFP's with Different Filter/Matrix Interfacial Quality  
K. Ono, University of California at Los Angeles; T. Kinjo, H. Suzuki, M. Takemoto, Aoyama Gakuin University (Japan)

## **APPLICATIONS OF CARP TESTING**

Keynote Speaker: Waveform Analysis of Acoustic Emission in Composites  
William Prosser, NASA Langley Research Center

Neural Network Burst Pressure Prediction in Fiberglass/Epoxy Pressure Vessels Using Acoustic Emission E. Hill, Embry-Riddle Aeronautical University; M. Fisher, Lockheed Martin

Acoustic Emission Testing - A Composite Tank Manufacturer's Experiences  
J. Richter, Tankinetics

Design and Acoustic Emission Testing of FRP Equipment  
C. Garza, Dow Chemical

Acoustic Emission Evaluation of Field Tests on FRP Materials Using the Three Way System  
S. Botten, Independent Testing Lab

Acoustic Emission of Large Scale Composite Aerospace Structures  
P. Cole, Physical Acoustics Ltd (United Kingdom)

## **ACOUSTIC EMISSION DEVELOPMENT IN APPLICATIONS**

Fracture Mode Classification in Locally Loaded Cross-Ply CFRP Coupons using Wavelet Transform  
Y. Mizutani, K. Nagashima, M. Takemoto, Aoyama Gakuin University (Japan); K. Ono, University of California at Los Angeles

**Acoustic Emission Testing of GRP Composites Progressively Damaged by Fatigue and Environmental Exposure**

J. Hale, G. Kotsikos, University of Newcastle upon Tyne (United Kingdom)

**ACOUSTIC EMISSION IN CONCRETE APPLICATIONS**

**Keynote Speaker: Quantitative Evaluation of Crack and Damage in Concrete by Acoustic Emission** M. Ohtsu, Kumamoto University (Japan)

**Acoustic Emission Application for Diagnosis of Deteriorated Concrete of Harbor Structures**  
A. Ishibashi, K. Matsuyama, Nippon Koei Ltd (Japan)

**Crack Extension in Concrete by SiGMA**  
M. Munwam, M. Ohtsu, Kumamoto University (Japan)

**Acoustic Emission Characteristics of Full-Scale Concrete-Piles Under Bending and Shear Load**  
T. Shiotani, Tobishima (Japan)

**Bedrock Observation by Captured Acoustic Emission**  
T. Shiotani, Tobishima (Japan); K. Monma, Public Works Research Institute (Japan)

**Acoustic Emission Monitoring of Reinforced Concrete Structures**  
C. Barnes, University of Texas at Austin

**Acoustic Emission Monitoring of Prestressed Concrete Girders**  
T. Fowler, University of Texas at Austin; L. Yepez, Universidad Catolica de Guayaquil (Ecuador)

**Evaluation Criteria for Acoustic Emission Examination of Reinforced Concrete Structures**  
M. Ohtsu, Kumamoto University (Japan); S. Yuyama, Nippon Physical Acoustics (Japan);  
T. Okamoto, Nihon Cement (Japan); T. Kishi, The University of Tokyo (Japan)

**Property Evaluation of Thermal-Sprayed Metallic Coatings for Acoustic Emission Analysis**  
A. Ishida, M. Takemoto, Aoyama Gakuin University (Japan); K. Ono, University of California at Los Angeles

**Panel Session: Discussion on CARP subjects**

---

**1997 SUBSCRIPTION RATE for Volume 15**

Base rate for one year (combined issues)	\$ 96.00
Add Postage of U.S. - Book rate	\$ 8.00
All others - Book rate	\$ 11.00
Western Europe/S. America - Air mail rate	\$ 25.00
All others - Air mail rate	\$ 30.00

Add \$5 without payment upon order. Payment must be in U.S. dollars drawn on a U.S. bank. Bank transfer accepted, but with \$10 surcharge to the A.E. Group account (Account No. 080-03416470) at

Sumitomo Bank of California  
San Fernando Valley Office  
15250 Ventura Blvd, Sherman Oaks, CA 91403-3262

Notify us of such a transfer as the bank cannot sometimes give us the name of the payer. One volume of four issues per year. Index included in the last issue. Back issues available at \$50 per volume for Vols. 1-3, \$90 per volume

for Vols. 4-8, \$96 per volume for Vols. 9-14. US surface postage \$8 per volume. For Canada and overseas surface delivery, add \$11 and for air mail, add \$30 per volume (will be adjusted for multi-volume order).

All orders should be sent to (or Fax 1-818-990-1686)

Acoustic Emission Group  
Suite 106, 16350 Ventura Blvd.  
Encino, CA 91436 USA

For inquiry through Internet, use the following address:

ono@ucla.edu

Editor-Publisher Kanji Ono Tel. (310) 825-5233  
Cover Design Robin Weisz (UCLA Publications)  
Production Pace Publication Arts

Publication Date of This Issue: 14 September 1998.

# Index to Volume 15

## Contents

Page 1-18	Wideband and Narrowband Acoustic Emission Waveforms from Extraneous Sources during Fatigue of Steel Samples <i>M.A. Hamstad and J.D. McColskey</i>
Page 19-32	Fracture-Mode Classification Using Wavelet-Transformed AE Signals from a Composite <i>Tetsuo Kinjo, Hiroaki Suzuki, Naoya Saito, Mikio Takemoto and Kanji Ono</i>
Page 33-42	Nondestructive Evaluation of Fiberglass-Reinforced Plastic Subjected to Localized Heat Damage Using Acoustic Emission <i>H. Nayeb-Hashemi, P. Kishino and N. Saniei</i>
Page 43-52	An Investigation of Lüders Band Deformation and the Associated Acoustic Emission in Al - 4.5% Mg Alloys <i>D. L. Armentrout and S. H. Carpenter</i>
Page 53-61	Modal Analysis of Acoustic Emission Signals <i>H.L. Dunegan</i>
Page 63-68	An Acoustic Emission Tester for Aircraft Halon-1301 Fire-Extinguisher Bottles <i>Alan G. Beattie</i>
Page 69-78	AE Detection of Cracking in Pipe Socket Welds <i>Bryan C. Morgan</i>
Page 79-87	Feature Extraction of Metal Impact Acoustic Signals For Pattern Classification by Neural Networks <i>Shahla Keyvan and Rodney G. Pickard</i>
Page S-i	<b>Conferences and Symposia</b>
Page S1-S94	Fourth Far-Eastern Conference on NDT
Page S95-S102	Congreso Regional de Ensayos No Destructivos y Estructurales
Page S103-S110	Program and Abstracts of the 40th AEWG Meeting
Page S111-S124	Abstracts of Oral Briefs, 14th International Acoustic Emission Symposium & 5th Acoustic Emission World Meeting
Page S125-S126	Program of the 6th AECM Symposium
Page 62	Meeting Calendar
Page 68	Cover Photograph
Page I-1	Index to Volume 15

## Authors Index

A.F. Almeida	S107, S108	A.J. Brunner	S108
D.L. Armentrout	43	M. Carlos	S104,S107,S109
Alan G. Beattie	63, S111	S. H. Carpenter	43
S. H. Benabdallah	S117	Chang-Sheng Chien,	S118
C. C. Berndt	S117	M.A. Clark	S107
J. Bohse	S108	P. Cole	S109
R. J. Boness	S117	P. De Meester	S105

K.S. Downs	S109	A. Maslouhi	S122
H.L. Dunegan	53, S106	Kimitoshi Matsuyama	S40
Y. A. Dzenis	S112	J.D. McColskey	1, S108, S111, S119
J. Eisenblätter	S119	R. (K.) Miller	S104, S107, S108
Manabu Enoki	S90, S120	J. Mitchell	S109
A. Fahr	S122	Keiichi Monma	S113
D. S. Forsyth	S122	Bryan C. Morgan	69, S103
Taisaku Fujioka	S31	H. Nayeb-Hashemi	33
Tetsuro Fujiwara	S40, S113	R. Nordstrom	S108
Roy D. Fultineer, Jr.	S103	A. O'Gallagher	S115
J. Gary	S115	Shiro Ohta	S40
Maochen Ge	S105	Masayasu Ohtsu	S31, S40, S50, S60, S70
Shigenori Hamada	S40	Kanji Ono	19, S95, S105, S108
M.A. Hamstad	1, S108, S109, S115	Philip Park	S11
H.R. Hardy, Jr.	S105, S118	Young-Jin Park	S11
Robert W. Harris	S113	Rodney G. Pickard	79
Hajime Hatano	S115	David W. Prine	S106
Y. Hayashi	S108	A.A. Pollock	S107, S108
J. H. Huh	S80	William H. Prosser	S106, S115
Akichika Ishibashi	S40, S113	L.E. Rewerts	S107
Young-Chan Joo	S1	R.A. Roberts	S107
Yasuhiro Kanemoto	S40	Naoya Saito	19
Elijah Kannatey-Asibu, Jr.	S118	Norio Sakaino	S50
Shahla Keyvan	79	Yasunori Sakata	S70
A.W. Khair	S105	N. Saniei	33
Byoung-Geuk Kim	S120	U. Senturk	S117
Byung-Nam Kim	S90	Ping Shen	S123
Sang-Hyo Kim	S11	H.W. Shen	S105
Tetsuo Kinjo	19	Mitsuhiro Shigeishi	S50, S60
Teruo Kishi	S90, S120	Tomoki Shiotani	S50
P. Kisnomo	33	Th. Spies	S119
Ja-Ho Koo	S90	M. Surgeon	S105
Joseph Krynicki	S116	Hiroaki Suzuki	19, S108
Oh-Yang Kwon	S1, S19	A.N. Tafuri	S104
E. Landis	S104	Mikio Takemoto	19, S108
R. D. Leblanc	S122	O.B. Tarutin	S120
P. Y. Lee	S117	Lawrence W. Teufel	S124
Seung-Hwan Lee	S19	Yuichi Tomoda	S31
Sekyung Lee	S120	Nobuyuki Tsuji	S60
Sang-Ho Lee	S11	Toshiyuki Uenoya	S112
Seung-Seok Lee	S11	S.J. Vahaviolos	S109
K. A. Lee	S80	G. Washer	S104
C. S. Lee	S80	D.J. Watts	S104
R. Lima	S117	M. Wevers	S105
C. K. Lin	S117	Brian R. A. Wood	S113
T. Liu	S117	W. Yan	S109
Xi-qiang Liu	S123	Xuanhui Yang	S123
Shifeng Liu	S124	Daisuke Yasuoka	S60
E. Lowenhar	S109	J.J. Yezzi, Jr.	S104
M.G. Lozev	S104	Dong-Jin Yoon	S11
Arup Maji	S116	S. Yuyama	S107
Gerd Manthei	S119	Zhizhen Zheng	S123
K. Marsh	S104		

# Notes for Contributors

## 1. General

The Journal will publish contributions from all parts of the world and manuscripts for publication should be submitted to the Editor. Send to:

Professor Kanji Ono, Editor - JAE  
6531 Boelter Hall, MSE Dept.  
University of California  
Los Angeles, California 90095-1595 USA  
FAX (1) 818-990-1686  
e-mail: ono@ucla.edu

Authors of any AE related publications are encouraged to send a copy for inclusion in the AE Literature section to:

Mr. T.F. Drouillard, Associate Editor - JAE  
11791 Spruce Canyon Circle  
Golden, Colorado 80403 USA

All the manuscripts will be reviewed upon submission to the Editor. Only papers not previously published will be accepted. Authors must agree to transfer the copyright to the Journal and not to publish elsewhere, the same paper submitted to and accepted by the Journal.

A paper is acceptable if it is a revision of a governmental or organizational report, or if it is based on a paper published with limited distribution.

An abstract of about 200 words is needed for Research and Applications articles, while it should be shorter than 100 words for other articles.

The language of the Journal is English. All papers should be written concisely and clearly.

## 2. Page Charges

No page charge is levied. Fifty copies of off-prints will be supplied to the authors free of charge.

## 3. Manuscript for Review

Manuscripts for review need only to be typed legibly; preferably, double-spaced on only one side of the page with wide margins and submitted in duplicate.

The title should be brief. Except for short communications, descriptive heading should be used to divide the paper into its component parts. Use the International System of Units (SI).

References to published literature should be quoted in the text citing authors and the year of publication. These are to be grouped together at the end of the paper in alphabetical and chronological order. Journal references should be arranged as below. Titles for journal or book articles are helpful for readers, but may be omitted.

H.L. Dunegan, D.O. Harris and C.A. Tatro (1968), *Eng. Fract. Mech.*, 1, 105-122.

Y. Krampfner, A. Kawamoto, K. Ono and A.T. Green (1975), "Acoustic Emission Characteristics of Cu Alloys under Low-Cycle Fatigue Conditions," NASA CR-134766, University of California, Los Angeles and Acoustic Emission Tech. Corp., Sacramento, April.

A.E. Lord, Jr. (1975), *Physical Acoustics: Principles and Methods*, vol. 11, eds. W. P. Mason and R. N. Thurston, Academic Press, New York, pp. 289-353.

Abbreviations of journal titles should follow those used in the ASM Metals Abstracts. In every case, authors' initials, appropriate volume and page numbers should be included. The title of the cited journal reference is optional.

Illustrations and tables should be planned to fit a single column width (87 mm or 3.3") or a double width (178 mm or 7"). For the reviewing processes, these need not be of high quality, but submit glossy prints or equivalent with the final manuscript. Lines and letters should be legible.

## 4. Review

All manuscripts will be judged by qualified reviewer(s). Each paper is reviewed by one of the editors and may be sent for review by members of the Editorial Board. The Board member may seek another independent review. In case of disputes, the author may request other reviewers.

## 5. Electronic Media

In order to minimize typographical error, the authors are encouraged to submit a floppy disk copy of the text. We can read Macintosh and IBM PC formats. Those who can connect to INTERNET can send the text portion to "ono@ucla.edu". This will greatly shorten the time of communication.

## 6. Color Photograph

We can print color photographs needed to enhance the technical content of an article. Because of the cost, the author is asked to pay \$350 per page.

## Contents

Page 1-18	Wideband and Narrowband Acoustic Emission Waveforms from Extraneous Sources during Fatigue of Steel Samples <i>M.A. Hamstad and J.D. McColskey</i>
Page 19-32	Fracture-Mode Classification Using Wavelet-Transformed AE Signals from a Composite <i>Tetsuo Kinjo, Hiroaki Suzuki, Naoya Saito, Mikio Takemoto and Kanji Ono</i>
Page 33-42	Nondestructive Evaluation of Fiberglass-Reinforced Plastic Subjected to Localized Heat Damage Using Acoustic Emission <i>H. Nayeb-Hashemi, P. Kisnomo and N. Saniei</i>
Page 43-52	An Investigation of Lüders Band Deformation and the Associated Acoustic Emission in Al - 4.5% Mg Alloys <i>D. L. Armentrout and S. H. Carpenter</i>
Page 53-61	Modal Analysis of Acoustic Emission Signals <i>H.L. Dunegan</i>
Page 63-68	An Acoustic Emission Tester for Aircraft Halon-1301 Fire-Extinguisher Bottles <i>Alan G. Beattie</i>
Page 69-78	AE Detection of Cracking in Pipe Socket Welds <i>Bryan C. Morgan</i>
Page 79-87	Feature Extraction of Metal Impact Acoustic Signals For Pattern Classification by Neural Networks <i>Shahla Keyvan and Rodney G. Pickard</i>
Page S-i	<b>Conferences and Symposia</b>
Page S1-S94	Fourth Far-Eastern Conference on NDT
Page S95-S102	Congreso Regional de Ensayos No Destructivos y Estructurales
Page S103-S110	Program and Abstracts of the 40th AEWG Meeting
Page S111-S124	Abstracts of Oral Briefs, 14th International Acoustic Emission Symposium & 5th Acoustic Emission World Meeting
Page S125-S126	Program of the 6th AECM Symposium
Page 62	Meeting Calendar and Recent Books on AE
Page 68	Cover Photograph
Page I-1	Index to Volume 15